TU Clausthal

Reactive transport modeling of fluid-rock interactions associated with carbonate diagenesis and implications for reservoir quality prediction

Dissertation

to be awarded the degree

Doctor of Engineering (Dr.-Ing.)

submitted by

M.Sc. Ying Xiong

from Sichuan, P.R. China

approved by the Faculty of

Energy and Economic Sciences,

Clausthal University of Technology

Date of oral examination

July 5, 2022

Dean

Prof. Dr. mont. Leonhard Ganzer

Chairperson of the Board of Examiners

Prof. Dr. rer. pol. Inge Wulf

Supervising tutor

Prof. Dr.-Ing. habil. Michael Zhengmeng Hou

Reviewer

Prof. Dr. rer. nat. Bernd Lehmann

Acknowledgments

First of all, I would like to extend my deepest gratitude to my supervisor Prof. Dr.-Ing. habil. Michael Zhengmeng Hou for his constant guidance, support and motivation in my academic studies in TU Clausthal (TUC). Particularly, Prof. Hou helped me acquire the skills for planning and independently solving some scientific research problems. Without his patient instruction and insightful advice, the completion of this thesis would not have been possible. My sincere gratitude also goes to Prof. Dr. rer. nat. Bernd Lehmann for his constructive review and suggestions on my work.

Next, I would like to show my appreciation to the working group of Prof. Hou for a good sense of teamwork. Special thanks give to Dr. Jianxing Liao for his guidance in my initial study of numerical simulation method, and Mrs. Karin Peya for her administrative support. Dr. Ke Li, Mr. Ye Yue and Mr. Jiashun Luo are thanked for their help in daily life and making life here interesting and fun. The China Scholarship Council (CSC) is also thanked for the financial Aid.

Besides, I am very grateful to Prof. Xiucheng Tan and Prof. Di Xiao from Southwest Petroleum University (SWPU), China. Discussions with them helped me broadened my understanding of this field of research and improve my dissertation. I should also give my appreciation to the joint training program for overseas teachers between SWPU and TUC for providing me a precious opportunity for studying here.

Last but not least, I am deeply indebted to my beloved family members who have always been supporting me without a word of complaint. Their moral support and comfort helped me out of the difficult times when I felt worried and confused, offering me everlasting optimism to move forward.

Ying Xiong

Clausthal-Zellerfeld, July 2022

Abstract

Diagenesis research is an important basis for hydrocarbon reservoir characterization and exploration in sedimentary rocks. The diagenetic products-based classical geological methods have shortcomings in quantitative characterization of the evolution of diagenetic geo-bodies and physical properties (porosity-permeability) of reservoirs at multiple spatial-temporal scales, which limits the prediction of precise diagenetic trends. Reactive transport modeling (RTM) is an emerging approach for diagenesis research, with the unique capability of quantification and forward modeling of the coupled thermo-hydro-chemical diagenetic processes. Using TOUGHREACT simulator, this thesis investigates the two most important fluid-rock interactions in carbonate rocks, i.e., dolomitization and karstification, based on generic model analyses and a case study in the Ordos Basin, China.

The reflux dolomitization (mineral replacement reaction of calcite by dolomite) in evaporated seawater environment is modeled as a kinetic process. Increased dolomite, decreased calcite and dynamic gypsum evolution (precipitation followed by dissolution) are observed during simulation. The gypsum precipitation, which occurs in the dolomitization front zone, is likely related to the combination of released Ca^{2+} during dolomitization (2 mole $CaCO_3$ replaced by 1 mole $MgCa(CO_3)_2$) and SO_4^{2-} in the solution. Collectively controlled by pore-increment via dolomitization and pore-infill by gypsum cementation, the rock porosity-permeability trend displays a dynamic variation of slight decrease followed by substantial increase. Sensitivity analyses suggest that higher brine salinity, temperature, reactive surface area and brine injection rate accelerate the reaction rate, while the degree of dolomitization can only be enhanced under conditions of higher brine salinity and temperature, as well as fine-grained rock fabric such as in micrite. The eogenetic karst process is modeled in a one-dimensional vadose meteoric water-rock system. There is a downward decreasing trend in carbonate dissolution and rock porosity due to the decrease in calcite solubility and enrichment of Ca^{2+} and HCO_3^- in the deeper part. The duration of subaerial exposure and rainfall recharge significantly determine the karst-affected depth and porosity increment. The atmospheric carbon dioxide concentration has a minor impact on the extent of karst, but it facilitates the

dissolution rate under high pCO_2 conditions. The influence of atmospheric pCO_2 variation over geological time on the porosity increment has also been reconstructed. The differences in dissolution rates and extent of karst between limestone and dolostone can be interpreted as the result of different rate-determining reaction mechanisms, i.e., thermodynamically controlled calcite and kinetically controlled dolomite.

Integrated geological and RTM study shows that the Ordovician Majiagou Formation reservoir in the Ordos Basin displays a typical characteristic of early diagenesis-control where the major reservoir porosities were formed during the syngenetic to early diagenetic stage. The reflux dolomitization occurred mainly in the restricted-evaporative environment, giving rise to a maximum 7.3% porosity increment of lagoon-facies micrite. Cyclic depositional sequences and lithofacies, and intercalated gypsum layers resulted in different brine fluxes and rock reactivities, and eventually multistage reflux dolomitization events that are featured by varying degrees of dolomitization and heterogeneous distribution of dolomite zones. The eogenetic karst developed mainly in the shoal-facies grainstone due to its relatively high paleo-topographic position and high-frequency sea level fluctuations. The dissolution lens and high-porosity zone concentrate at the core part of shoals. The duration of subaerial exposure and meteoric water leaching ranges between 30–110 ka, leading to porosity increments of 1.5–6.7% (average 3.1%) in shoal-facies grainstone. Further exploration of the Majiagou Formation reservoir should particularly focus on sedimentary environment and paleo-geomorphology that have significantly affected the occurrence and distribution of dolomitization and karstification.

In summary, this study makes an attempt to quantitatively characterize the diagenetic fluid-rock interactions and to reconstruct the diagenesis-porosity evolution of carbonate reservoirs through an emerging RTM approach. Some controversies in carbonate diagenesis research, which cannot be well explained by classical geological methods, have also been discussed. The results are helpful to better understand the spatial-temporal distribution and co-evolution of diagenesis-mineral-porosity during the complicated diagenetic processes with their potential controlling factors, and to reduce the uncertainty of reservoir quality prediction.

Table of contents

List of figures

List of tables

1 Introduction

1.1 Motivations and objectives

Carbonate rocks are important hydrocarbon reservoir rocks and have attracted great attention of petroleum geologists since the rise of petroleum industry. It is estimated that around 50–60% of the world's conventional oil and gas resources are reservoired in carbonate rocks (Burchette, 2012). In comparison with clastic rocks, carbonate rocks are more sensitive to diagenesis because the formation and preservation of most secondary pores in carbonate rocks are directed controlled by diagenetic fluid-rock interactions. In the past few decades, the study of diagenesis has been an important basic work for carbonate reservoir characterization and exploration, with the fundamental goal of precisely predicting the influence of diagenesis on reservoir quality and heterogeneity at multiple spatial-temporal scales. With the development of oil and gas exploration, the accuracy of reservoir heterogeneity characterization is increasingly required, and the classical description and conceptual diagenetic models based on observational results can no longer meet the requirements of precise prediction of high-quality reservoirs. As such, quantifying diagenesis with relevant fluid-rock interaction processes has become a rising field of research and is attracting an increasing attention.

The study of diagenesis has a long history with various methods. The current approaches for carbonate diagenesis study (e.g., petrographic observation, mineralogical and geochemical analyses of drilling core samples) are mostly diagenetic products-based. Although these methods help to trace the origins and chemical properties of diagenetic fluids and reveal the diagenetic environment through qualitative description and elemental-isotopic signals of rock samples, they cannot provide quantitative constraints of the diagenesis-mineral-porosity co-evolution. Meanwhile, these methods are more or less limited in terms of spatial-temporal resolution (Xiao et al., 2018), which introduces great uncertainties to reservoir quality prediction, especially in areas that are poorly explored or away from well control. Besides, there remains some controversies regarding carbonate diagenesis that cannot be well explained by the current classical research approaches.

Numerical simulation (represented by reactive transport modeling; RTM) of diagenetic fluids-rock interactions is an emerging method for diagenesis study. Preliminary studies in the past two decades have shown that this approach is effective to quantitatively/semi-quantitatively evaluate the diagenetic processes and their impacts on reservoir properties, and hosts broad development and application prospects because of its economic efficiency and flexible spatial-temporal resolution (Xu et al., 2004; Xiao et al., 2018). At present, the RTM approach has been applied in both natural diagenesis (including carbonate and clastic rocks) at geological scale and artificial diagenesis at production scale (e.g., Whitaker and Xiao, 2010; Gabellone et al., 2016; Zhang et al., 2019; Hamon et al., 2021). Nevertheless, these findings will never be the final conclusions for RTM study of diagenesis, as there is always a contradiction between the complexity of real geological diagenetic events and the simplification of setting models. Thus, ever since the RTM method was applied in diagenesis study, a constant objective has been setting up geological and numerical models and parameters more closely to the diverse real geological environments.

To enrich the fluid-rock interactions theory associated with carbonate diagenesis and to reduce uncertainty of reservoir quality prediction, this thesis provides forward modeling of the two important diagenetic processes (i.e., dolomitization and karstification) using RTM approach, focusing on the spatial-temporal evolution of minerals and porosity, diagenetic trend and their potential controlling factors. The results are used and try to explain some of the controversies in current diagenesis study. RTM simulation of diagenesis has also been employed in a case study (the Ordovician Majiagou Formation, Ordos Basin, China), which helps to reconstruct the diagenesis-porosity evolution of carbonate rocks in a more accurate way than previous studies, and also provides new clues for further prediction of high-quality reservoirs.

1.2 State of the art and scientific challenges

1.2.1 Overview of carbonate diagenesis

(1) Definition and classification

The formation of sedimentary rocks goes through two main stages. The first stage includes

weathering, transport, deposition, and other geological processes that predate burial of sediments, which is broadly defined as sedimentation and involves a variety of physical, chemical, and biological processes. The second stage involves various post-sedimentation (i.e., during burial) geological processes, known as diagenesis and metamorphism. Therefore, the carbonate diagenesis refers to any physical, chemical and biological process that alters carbonate rocks after sedimentation (until metamorphic conditions are reached) (Nader, 2017). In terms of the duration and process, the sedimentation stage is characterized by short time and rapid progress, while the diagenesis experienced prolonged time and slow progress. No matter what the sedimentary rocks look like today, they are the result of a long period of diagenetic alteration. In general, the study of diagenesis of sedimentary rocks includes the multiple diagenetic process and their controlling factors, involving various issues such as lithification of initial loose sediments, element redistribution and mineralization, and rock porosity evolution. Particularly, for carbonate rocks, when the ambient conditions of the rocks and intrinsic fluids change, or upon migration of extrinsic fluids into a rock-mass, processes such as dissolution, precipitation, and mineralogical and porosity-permeability changes may occur. These issues are directly related to the spatial-temporal distribution and evolution of mineral and hydrocarbon resources in sedimentary rocks, and the basic theory of the formation process of sedimentary rocks. Therefore, investigation of carbonate diagenesis has become a fundamental task for the exploration and development of hydrocarbon carbonate reservoirs.

The classification of diagenesis of sedimentary rocks can be varied. According to the type of driving force, diagenesis can be divided into physical-dominant processes (e.g., compaction), chemical-dominant processes (e.g., mineral precipitation, dissolution and replacement) and biological-dominant processes (e.g., bacterial sulfate reduction and biomineralization) (Huang, 2010). In terms of the influence on hydrocarbon reservoirs, diagenesis can be constructive (reservoir spaces increase), destructive (reservoir spaces decrease) or retentive (reservoir spaces adjustment and preserve) (Zhang et al., 2014). According to the different lithofacies of sedimentary rocks, diagenesis can also be divided into carbonate diagenesis, sandstone diagenesis, mudstone (shale) diagenesis, etc. (Bjørlykke and Jahren, 2012). In addition to the above classification schemes, considering the sensitivity of carbonate to the variations in

ambient environmental conditions and pore fluid properties, the most common classifications of carbonate diagenesis are based on diagenetic environment (realm) and diagenetic stage (relative time).

(2) Diagenetic environments (realms)

The concept of "diagenetic environment" is used to characterize the environmental conditions and pore fluid properties under which the diagenesis occurs, which is also frequently named "diagenetic realms" (Fig. 1.1). Due to the coverage of new sediments, diagenetic environment is distinct from the sedimentary environment, including physical properties (e.g., temperature, pressure and flow pattern of pore water), chemical properties (e.g., water composition, pH and Eh values) and biochemical properties. The diagenetic environment changes continuously as the sediments are buried or briefly exposed and then burial, or tectonically uplifted to the surface after burial. As such, the physicochemical conditions controlling the diagenetic process are also changing, and the most important controlling factor is the properties of pore water.

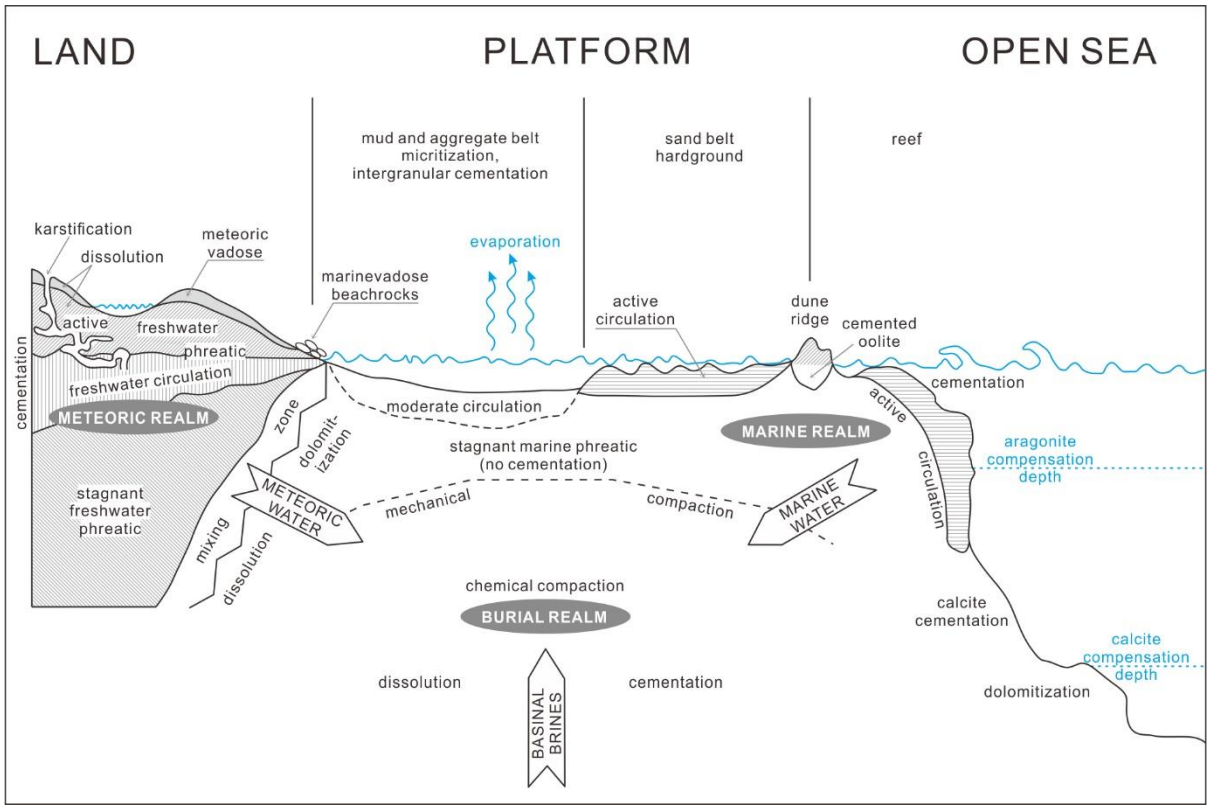

Figure 1.1 Schematic representation of the major carbonate diagenetic realms and related processes in a carbonate platform (modified after Moore, 2001; Nader, 2017).

Carbonate sediments can be involved in several types of pore fluid condition including marine seawater, meteoric freshwater and burial fluid. Each pore fluid type could result in specific fluid-rock interactions that can be identified by unique mineral assemblages, rock fabrics and geochemical indicators. Meanwhile, each digenetic realm, which is inherently associated with the prevailing type of fluid, constitutes a unique diagenetic environment. According to the properties (origins) of the pore fluid and whether it fills with the pore spaces, five types of diagenetic environment of carbonate rocks can be classified: seawater environment, meteoric water environment, seawater-meteoric water (mixing water) environment, burial environment and telogenetic environment (Fig. 1.1).

Seawater diagenetic environment is also called submarine diagenetic environment. Generally, the supratidal zone is in the sub-environment of vadose seawater and the intertidal-subtidal zone is in the sub-environment of phreatic seawater. Seawater diagenesis occurs in an early syngenetic stage just after the sediments deposition, and is characterized by pervasive cementation (e.g., isopachous fibrous aragonite/calcite cementation), mineral replacement (e.g., evaporative pumping- and shallow seepage reflux-related dolomitization) and biological effects (e.g., bioturbation and microbial-related micrite envelope).

Meteoric diagenetic environment is associated with the intermittent short-term exposure (generally less than 1 Ma) of carbonate sediments during the periods of relative sea level fall. Bounded by water-table (phreatic surface), the meteoric diagenetic environment consists of a vadose zone in the upper part and a phreatic zone in the lower part. According to the saturation state of $CaCO_3$ in the pore water, the vadose sub-environment can be further divided into a dissolution zone that is featured by fabric-selective dissolution and karstification caused by undersaturated meteoric water, and a precipitation zone that is featured by minor meniscus, pendent and spelean cementation. The phreatic sub-environment comprises three distinct zones: an upper dissolution zone where the (high pCO_2-containing) pore water is still unsaturated with regard to carbonate and moldic and vuggy porosities are well developed; a mid-precipitation zone where the pores are filled with $CaCO_3$-saturated water and active water circulation promotes rapid cementation (e.g., equant calcite cement) and porosity destruction; a lower

stagnant zone where the equilibrium between pore water and $CaCO_3$ has been established and cementation is weakly developed due to the absence of water circulation and replenishment.

Mixing water diagenetic environment is the mixing zone between the seawater phreatic sub-environment and the meteoric phreatic sub-environment. In humid climate, the carbonate shelf and carbonate platform could have a wide mixing zone. The best known diagenesis in mixing water environment is mixed-water dolomitization. However, in the past two decades, the mixed-water dolomitization model has been intensively questioned in terms of thermodynamics, and researchers have gradually realized that the mixed-water model cannot explain the genesis of thick-bedded and massive dolostone in geological formations. It should be also noted that the seawater, meteoric water and mixing water environments are all at surface/near-surface settings, within which the diagenesis occurs without coverage of now sediments and has a relatively small influencing depth. As such, these three diagenetic environments are collectively called the near-surface diagenetic environment.

Following the accretion of overlying sediments, the initial carbonate sediments are subjected to burial diagenetic environment when they are at depths beyond the reach of near-surface diagenetic processes. Generally, burial diagenetic environment can be further divided into shallow-medium-deep burial sub-environments. Burial diagenesis is typically represented by the pervasive compaction and pressure solution. In addition, in some areas with special basin thermal evolution history and tectonic events, diverse diagenetic processes, such as mineral dissolution (e.g., organic acids-related burial dissolution), cementation (e.g., fractures/fault controlled calcite, dolomite and gypsum/anhydrite precipitation) and replacement (e.g., basinal brines- and hydrothermal-driven dolomitization) might also occur. These burial diagenesis can be distinguished from near-surface diagenesis by particular petrological features and geochemical indicators.

Finally, telogenetic environment refers to the re-exposure of carbonate rocks to near-surface diagenetic environment (mostly meteoric water environment) due to regional tectonic uplift after medium-deep burial and mineral stabilization. Under the action of CO_2-containing surface water or groundwater, carbonate rocks are easily subjected to weathering, dissociation,

transport and redeposition, forming various karst landforms, cave systems and porous rocks.

(3) Diagenetic stages

Diagenetic stage is generally used to describe the evolution of different diagenetic processes (diagenetic sequences) and the temporal characteristics of diagenetic alteration. Since the temporal factor in the geological history is a relative one, there are many schemes for the division of diagenetic stages proposed by different researchers, with different terms and emphasis, and the classification standards have not been unified yet.

Typically, the diagenetic stages of carbonate rocks can be simply classified into eogenesis, mesogenesis and telogenesis, which imply information of both the temporal characteristics and environmental conditions of the diagenetic processes. To be specific, eogenesis refers to the diagenetic processes that occur just after sediments deposition and before burial, involving marine, meteoric water and mixing water diagenetic environments. Alternatively, eogenesis is frequently described as early diagenesis. Mesogenesis is commonly used to describe the various diagenetic processes that occur under long-term burial conditions. Finally, telogenesis refers to the diagenetic processes that occur under surface/near-surface conditions when the carbonate rocks are tectonically uplifted after burial and (once again) subject to meteoric diagenetic environment.

1.2.2 Classical diagenesis characterization approaches

The purpose of classical diagenesis characterization for carbonate reservoirs is to describe and explain specific diagenetic processes in a relative time frame by integrating a variety of analytical techniques. In general, the following results should be obtained by diagenesis characterization: 1) identifying and defining the various diagenetic facies (processes) based on the features and distributions of diagenetic products; 2) organizing the various diagenetic processes in chronological order and trying to reconstruct a complete diagenetic sequence; 3) inferring about the origins and chemical properties of multi-types of fluid that are responsible for the diagenetic processes; 4) clarifying the physico-chemical conditions and their evolution at different diagenetic stages. Ultimately, based on the above results, a conceptual geological model can be established to explain the environmental conditions of various fluid-rock

interactions and the co-evolution of diagenesis and reservoir properties. Several classical approaches are commonly used for carbonate diagenesis characterization, and are briefly presented below.

(1) Petrography and mineralogy

Petrographic observation is a basic work for diagenesis study and can be carried out at different scales such as outcrops, drilled cores and microscopic thin sections. Descriptions based on petrographic observation are mostly qualitative and are made on rock textures, features and distribution of the various diagenetic products (e.g., dissociated carbonate fragments, cements and replacive minerals), and the types and amount of pores and fractures (often combined with porosity-permeability measurement). Particularly, the different diagenetic facies (processes) should be placed in chronological order based on cross-cutting relationship of the diagenetic products. As such, a preliminary diagenetic sequence is established, waiting to be further verified by mineralogical and geochemical analyses. For microscopic petrology, in addition to the common light microscope, several strengthening methods, such as scanning electron microscope (SEM), cathode-luminescence and fluorescence microscopes, are also occasionally used, which help to obtain a higher magnification (10–100,000 times) and to better identify the diagenetic sequence (i.e., multi-stage cementation) and the hydrocarbon-bearing character of reservoir rocks, respectively.

Mineralogical analysis is usually done by means of X-ray diffraction and electron probe microanalysis (EPMA) techniques. In general, mineralogical analysis in diagenesis study aims to: 1) identify some unknown and clay minerals that are difficulty to recognize from thin section observations; 2) determine the absolute content (or mineral-distribution map) of diagenetic minerals (e.g., replacement dolomite, calcite and gypsum/anhydrite cements); 3) assess dolomite stoichiometry and crystal ordering that are potentially related to the degree of dolomitization. Compared with petrographic observation, mineralogical analysis provides more lithology- and diagenesis-dependent quantitative data to assess the relative strength of diagenetic alteration and the distribution of diagenetic products at micro-scales (core samples and thin section).

(2) Geochemistry and fluid inclusions

Diagenetic products-based geochemical and fluid inclusions analyses are effective and have been widely applied to determine the diagenetic environments, trace the origins and chemical properties of diagenetic fluids, and date the diagenetic processes. The methods for geochemical analysis of carbonate samples (powdered bulk samples or in-suit microsamples) are various, mainly including carbon and oxygen stable isotopes, strontium isotope, major and trace elements (including rare earth elements; REE), U-Pb isotopic dating and clumped isotopes.

Isotopic analyses of powdered carbonate samples are usually carried out on a specialized isotope ratio mass spectrometer (e.g., Thermo Scientific 253 Plus MS and Finnigan Triton Plus thermal ionization MS). To be specific, carbon and oxygen isotopes are often used to determine the origin of diagenetic fluids (e.g., normal or modified seawater) and mineral precipitation temperature because they are sensitive to fluid properties and temperature. Other factors involved in diagenetic processes, such as the influence of organic carbon and meteoric water, can also be assessed by comparing isotopic values of different samples (Yang et al., 2001; Xiong et al., 2019). Strontium isotope is often used to roughly estimate the age of some specific diagenetic facies (e.g., replacement dolomite), by comparing the measured isotopic values with the evolution curve of marine Sr isotopic values (Nader, 2017). Diagenetic fluids with different sources also show different isotopic features. For instance, crust-sourced (affected by meteoric water or radiogenic silicate minerals) fluids have relatively higher Sr isotopic values, while the mantle-sourced fluids yield relatively lower Sr isotopic values (Huang, 2010).

Major and trace (including REE) elements analyses are carried out using an Inductively Coupled Plasma Mass Spectrometery (ICP-MS; for whole-rock bulk samples) which can be also coupled to a Laser Ablation device (LA-ICP-MS; for in-situ analysis). In the last decade, major and trace elements, especially the rare earth elements, have been widely applied to trace geochemical properties of fluids (such as seawater and pore water) preserved during carbonate deposition and diagenesis (Tostevin et al., 2016; Li et al., 2019). In addition, other diagenetic processes such as meteoric water leaching, terrigenous (detrital) contamination and deep-sourced hydrothermal alteration can be also identified based on special REE distribution

patterns (Hood et al., 2018; Gong et al., 2021). This is mainly due to that the rare earth elements have similar electron configurations and geochemical properties, and are likely subjected to distinct REE fractionation under different diagenetic environments. Thus, rare earth elements of diagenetic mineral could delicately record the variation of ambient environmental conditions during diagenesis, by forming specific REE distribution patterns.

U-Pb isotopic dating is a mature and commonly used technique in geochronology research. It has been widely used in minerals with high U content, such as zircon, monazite, apatite and garnet. In contrast, the development and application of U-Pb isotope dating technique in diagenetic carbonate minerals lag behind relatively and are limited because of the extremely low U content in carbonate rocks. Nevertheless, Shen et al. (2019) developed a laser ablation in situ U-Pb dating method that is suitable for ancient marine carbonate rocks and effectively applied it in the study of diagenetic sequence and pore evolution. This method holds a great potential for determining the accurate formation time (absolute age) of multi-stage carbonate cements, which helps us better understand the diagenetic sequence and reconstruct porosity evolution history, especially in deep-burial carbonate reservoirs that have experienced complex diagenetic alteration by multiple fluids in multi-cycle superimposed basins.

Clumped oxygen isotopic analysis is an emerging method developed in recent years for carbonate diagenesis research and is regard as a new paleo-thermometer. As mentioned above, although oxygen stable isotopic signal could reflect fluid properties and temperature, the results are hindered by two variables (i.e., original/diagenetic fluids chemistry and precipitation temperature) and thus are highly uncertain (Nader, 2017). In contrast, clumped oxygen isotopic analysis is based on the principle of temperature-dependent formation of an isotoplogue of CO_2 with a mass of 47 within the carbonate minerals ($^{13}C^{18}O^{16}O_2^{2-}$ ionic groups). Thus, the clumped oxygen isotope value ($\Delta 47$) is independent of the fluid $\delta^{18}O$ composition and only reflects temperature (Ghosh et al., 2007). Recently, the clumped isotope paleo-thermometry has been applied to constrain precipitation temperature and to calibrate fluid models with related to dolomite formation (Murray and Swart, 2017; Li et al., 2020).

Analysis of fluid inclusions trapped in diagenetic minerals (e.g., cements) is one of the few

methods that can directly obtain information about the thermal and fluid composition of sedimentary basins in the diagenetic history. Investigation of fluid inclusions comprises microthermometry and composition analysis. Specifically, microthermometric analysis is performed on double-polished sections using a Cooling-Heating Stage (e.g., Linkam THMSG 600), and two temperature date, i.e., the homogenization temperature (T_h) and the final melting temperature of ice (T_m) are recorded for each valid liquid-vapor inclusions. The T_h value represents the lowest temperature of formation of the mineral that host the primary fluid inclusions, and the T_m values can be used to estimate the salinity of the fluid itself. Moreover, the T_h values are also frequently employed together with $\delta^{18}O$ isotopic data to determine the source and $\delta^{18}O$ composition of the diagenetic fluid that is responsible for the mineral precipitation (Huang, 2010; Jiang et al., 2016). Composition analysis of fluid inclusions can be achieved by laser Raman spectroscopy analysis or crush-leach Analyses using ICP-MS (see above). Determination of fluid inclusions composition is important for subsequent numerical modeling of diagenesis because the chemical composition and ion concentrations obtained from fluid inclusions can be directly used to deploy the chemical properties of fluid (initial water or boundary water) in a particular hydrogeochemical system.

(3) Laboratory experiments

Laboratory experiment is an effective method to quantitatively investigate water-rock reaction process and its products under specific environmental conditions. For decades, through artificially simulating the different diagenetic conditions (e.g., temperature, pressure and fluid properties), laboratory experiments of water-rock interactions have been widely employed in the study of carbonate diagenesis mainly including dolomitization (dolomite precipitation), dissolution (karstification) and cementation. It is worth noting that due to the differences in systematic errors of laboratories and selection of controlling parameters and the complexity of rock samples, the results of different researchers differ greatly and some are even contradictory.

One of the most famous and important diagenesis experiments is the dolomite precipitation experiment (began from 1968) conducted by Land L.S. who attempted to directly precipitate dolomite at low temperature conditions (25°C) from dilute solution that is thermodynamically

supersaturated with respect to dolomite. However, after 32 years of laboratory experiment, no dolomite precipitation was observed, even though the solution is 1000-fold oversaturation with respect to dolomite (Land, 1998). The result suggests that the formation on dolostone in geological records was likely controlled by kinetics rather than thermodynamics, which also explain why primary dolomite rarely precipitates in modern seawater environments despite the seawater is thermodynamically supersaturated with respect to dolomite. Nevertheless, with the participation of microorganisms (represented by sulfate-reducing bacteria), Vasconcelos et al. (1995) successfully precipitated dolomite that shows the similar characteristics of natural dolomite in modern high-salinity lagoons environment. This experiment has given rise to a new mechanism of dolomitization with related to microbial mediation, namely the microbial dolomite model.

Laboratory experiment of carbonate dissolution provides a forward approach to understand the formation process of paleokarst reservoirs. Typically, Liu et al. (2005) carried out a dissolution experiment to explore the rate-determining mechanisms of limestone and dolostone, and emphasized the importance of the conversion rate of carbon dioxide to bicarbonate in solution for carbonate dissolution. The dolostone is also found to have much lower dissolution rate than that of limestone due to its more complicated surface reaction controlling mechanism. Fan et al. (2007) investigated the dissolution capacity of CO_2-containing aqueous solutions at different temperatures, and the results show a dynamic variation in carbonate dissolution that increases first and then decrease with gradually increasing temperature from 25°C to 200°C, and the dissolution capacity was the strongest at the temperature range of 60–90°C. She et al. (2016) explored the pore evolution in the process of carbonate dissolution, and suggested that the formation of dissolved pore-vugs was collectively controlled by rock textures and diagenetic environments. To be specific, under the same conditions, porous-type reservoir is likely to yield higher amount of dissolution than fracture-type reservoir, and their newly added reservoir spaces are homogeneous intergranular/intercrystalline pores in rock matrix and lumped dissolution vugs/fractures in local areas, respectively. This is due to the different fluid-mineral reactive surface areas determined by initial pore structures and the different fluid flow paths (i.e., diffuse intergranular flow in matrix pores and preferential/conduit flow in fractures).

Meanwhile, the meteoric and telogenetic diagenetic environments (with stable and sufficient supply of CO_2-containing solutions) are supposed to be more favorable for the development of large-scale paleokarst reservoirs than burial diagenetic environment.

Cementation with its thermodynamic/kinetic controls in carbonate rocks has been extensively studied, and the chemical properties and evolution of diagenetic fluids are considered to be the major factors that control the type of cement and the cementation/dissolution balance (Whitaker and Smart, 2007; Xiao et al., 2018). Stack et al. (2014) carried out a mineral precipitation experiment in artificial porous media under laboratory conditions, and found that the relatively large pores (micron-sized) are preferentially filled with calcite that precipitate from $CaCO_3$-supersaturated pore fluids compared to the relatively small pores (nano-sized). The results confirm the effect of pore-size controlled solubility (Lasaga, 1998), and also indicate that the cementation is controlled not only by the diagenetic fluids, but also the heterogeneity of initial reservoir pore structures that may result in differences in the degree of cementation and effectiveness of pore preservation (Ehrenberg and Walderhaug, 2015; Varzina et al., 2020). Subsurface fluid-mineral reaction controlled by pore structure and size is currently an ongoing research because this phenomenon hold important application value in other field besides hydrocarbon reservoir quality evaluation, such as geothermal exploitation (anhydrite cementation and occluding flow pathway; Borgia et al., 2012) and carbon dioxide geological sequestration (self-sealing effect; Wang et al., 2021).

According to the above case examples, laboratory experiments provide a quantitative approach to constrain the process of diagenetic fluid-rock interactions (e.g., reaction rate and priority) with their diagenetic products (e.g., mineral content, distribution and pore changes). However, the greatest and inherent challenge of laboratory experiments is the spatial-temporal restriction of experimental subject and observation of the result. As such, the current laboratory experiments are mostly limited to theoretical and mechanism analyses of a certain fluid-rock interaction based on short-term (at most several decades) observation at the core or thin section scale, and cannot truly replicate the diagenetic process with its spatial-temporal evolution in the prolonged geological history. Therefore, up-scaling these quantitative date obtained from

laboratory experiments for reservoir-scale diagenesis characterization remains a persistent challenge.

In summary, the various diagenesis characterization approaches have their own specialty, and are of great significance for describing reservoir properties, and determining the type, environmental condition and sequence of diagenesis in a relatively chronological order. Although some classical methods (e.g., geochemistry and fluid inclusions) provide quantitative data, most of these data can only be used to analyze the physical and chemical environmental conditions of a particular diagenesis. The reservoir-scale conceptual models of diagenesis and pore evolution are still qualitative. Besides, these approaches are limited more or less by the spatial-temporal restriction of sampling and laboratory observation, and thus the obtained results can only be used for mechanism analysis at the core or microscopic scale, and cannot be directly used for reservoir-scale reservoir quality prediction.

1.2.3 Numerical approach for reservoir diagenesis

With the development of petroleum industry, reservoir diagenesis has made great progress in the past few decades in theory, experimental technique development and field exploration. Meanwhile, the strong heterogeneity of carbonate reservoirs results in gradually increasing difficulty of hydrocarbon exploration, and the demand for precisely characterizing diagenetic geo-bodies is urgent. Under such background, “quantifying diagenesis” is currently a rising field of research and is attracting an increasing attention. As an effective and economical technique, numerical modeling has become an important technique for quantifying diagenesis and reservoir characterization in the past two decades and remains under development (Fig. 1.2). At present, there are three types of numerical simulation technique related to hydrocarbon reservoir diagenesis, including geometry-based modeling, geostatistical modeling and geochemical modeling (Nader, 2017). Both geometry-based modeling and geostatistical modeling are static models based on calculations using existing geometric data (e.g., object-distance) and geological parameters (e.g., mineral contend, porosity and permeability). They are not predictive techniques, rather ways to meaningfully distribute diagenetic features and to improve the static distribution of geological properties based on probability, respectively. In

contrast, geochemical modeling is more significant for reservoir quality prediction in areas that are poorly explored or lack of sufficient basic geological information because it provides a predictive forward modeling approach based on thermodynamic and kinetic rules to simulate the fluid-rock interactions during diagenesis.

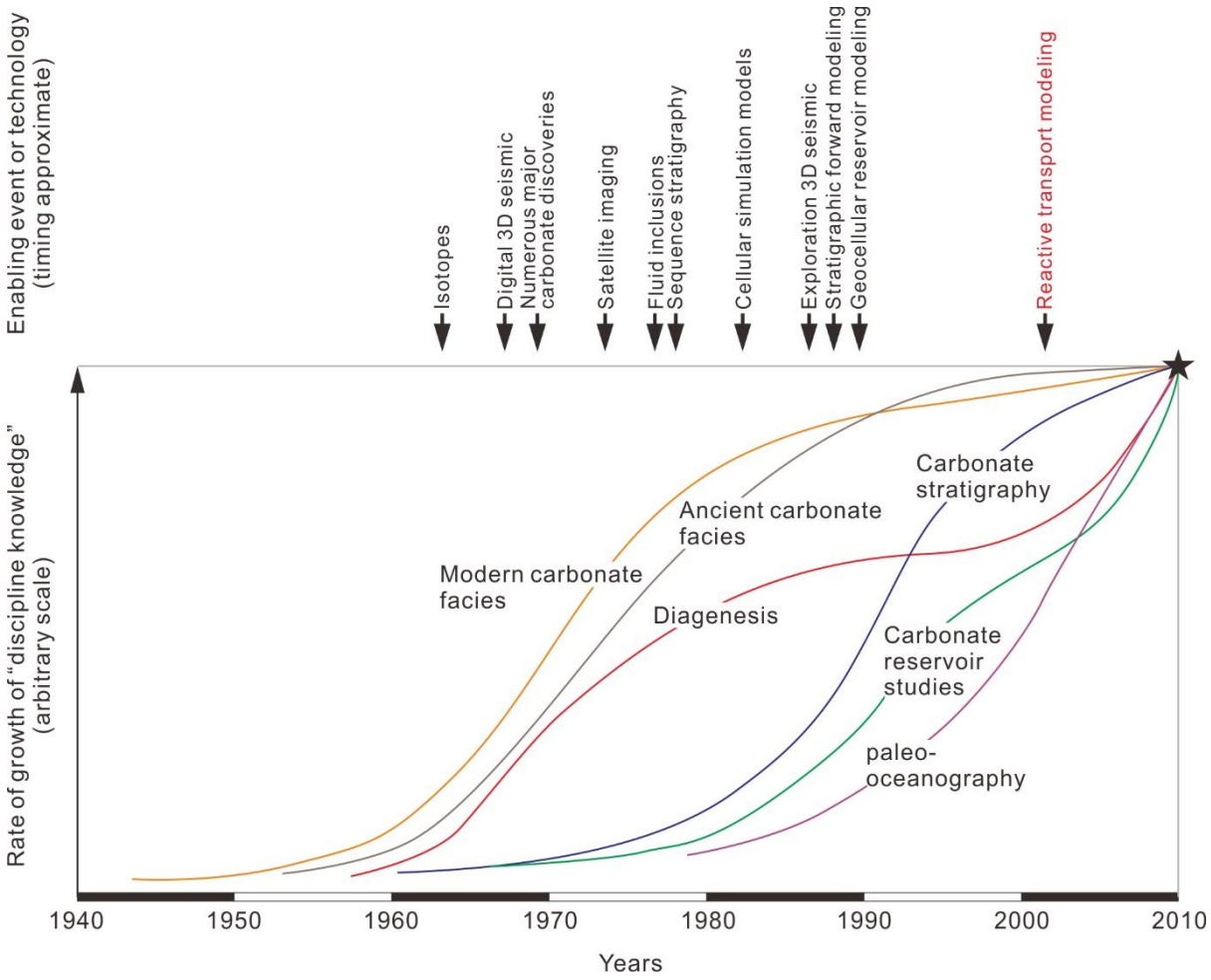

Figure 1.2 The growth of subdiscipline knowledge within carbonate geology and time sequence of some key enabling events and research methods. The star represents out current state of knowledge (modified after Burchette, 2012).

Numerical modeling of diagenesis should be performed integrated with classical reservoir characterization methods (experimental and observational data). Firstly, based on petrographic observation and mineralogical analysis, the types, features and relative importance of diagenesis are identified and a preliminary diagenetic sequence can be established. Subsequently, the various geochemical and fluid inclusions analyses are needed to reveal the diagenetic environments and fluid properties of different diagenetic processes, contributing to

a conceptual diagenetic evolution model. On the basis of these essential geological knowledge, the generic geological model (or specific model for a particular area) is built and the suitable numerical software/code is selected or further developed to simulate each important diagenetic process. In particular, the spatial-temporal evolution of diagenetic geo-bodies and the distribution of physical reservoir properties should be clarified, which are needed to establish a quantitative or semi-quantitative diagenesis and porosity co-evolution model.

The most frequently used and acceptable method for geochemical modeling of diagenesis is reactive transport modeling (RTM) that couples the thermo-hydro-chemical processes in porous media. Compared with classical reservoir characterization methods that focus on the diagenetic products preserved in rock record, RTM approach provides a possibility to forward simulate the diagenetic fluids-rock interactions and their impacts on reservoir properties at both geological and production timescales. Together with sensitivity analysis, quantitative or semi-quantitative constraint can be made on the influence of some key geological factors on diagenetic process. Parametric uncertainty and the relative importance of the various factors can be also assessed. Moreover, the RTM method is more flexible in terms of spatial resolution, and is applicable in different spatial scales from basin to borehole and cores (Fig. 1.3).

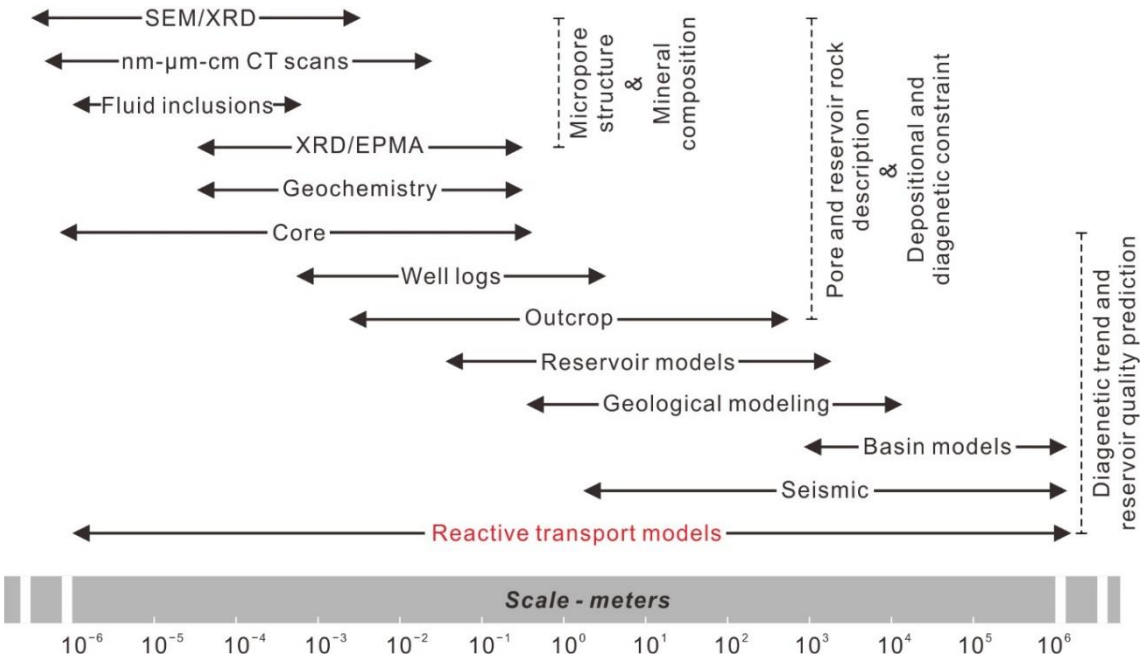

Figure 1.3 Schematic diagram showing the spatial scales and main objectives of various diagenesis characterization approaches (modified after Xiao et al., 2018).

In the past two decades, the RTM approach has been used to simulate multiple hydrocarbon reservoir diagenesis (both natural and artificial) in carbonate rocks, especially the reflux dolomitization and paleo-karstification. For instance, Jones and Xiao (2005) simulated the mineral and porosity evolution during brine reflux dolomitization based on a 2D generic model, and found that: anhydrite precipitation occurs with the replacement reaction and distribute in the dolomite front area; initial rock property heterogeneity results in dolomite fingers extending several hundreds of meters ahead of the dolomite front; dolomite replacement enhances porosity whereas anhydrite cementation occludes porosity. Integrating RTM simulations with borehole and outcrop studies, Gabellone et al. (2016) and Lu and Cantrell (2016) confirmed the conclusions of Jones and Xiao (2005) through two case studies on epeiric ramp (Mississippian Madison Formation, USA) and carbonate platform (Ghawar field, Arad-D reservoir, Saudi Arabia) environments, respectively. They further suggested that: non-stratigraphic dolomite (generally considered as the products of buried brines- or hydrothermal-related dolomitization) can also be generated by reflux dolomitization in areas of strong depositional heterogeneity (i.e., rock permeability and reactivity); fluctuations of sea level result in migration of brine source and the large-scale pervasive dolomite in the formation is likely the result of superposition of multi-stage relatively short-term reflux dolomitization events. Through RTM simulation, Wilson et al. (2001) proposed that the geothermal convection within carbonate platform is an effective dolomitization mechanism, while its dolomite replacement rate is significant lower than that of reflux dolomitization. This model is further supported by Whitaker and Xiao (2010) and Al-Helal et al. (2012), in which the various hydrogeological factors that control the geothermal heat flux and dolomitization process are quantitatively evaluated through sensitivity analysis. Gomez-Rivas et al. (2014) simulated the fault-controlled hydrothermal dolomitization in the Maestrat Basin, Spain, and found that: the overpressured hot ascending brines released in the syn-rift tectonic period has large lateral flow rates, resulting in a wide range of dolomitization of the wall-rocks; in later sag phase of rifting, the hydrothermal fluid and replacement reaction are mostly confined to the dominant channel within the faults.

In comparison with dolomitization, RTM simulations of paleo-karstification associated with

hydrocarbon carbonate reservoirs in different diagenetic environments have been relatively less reported. Xiao and Jones (2006) simulated the fluid flow and styles of diagenesis within the four different hydrological zones (i.e., vadose, meteoric phreatic, mixing and marine) in meteoric diagenetic environment based on a 2D generic model. Their result confirms the valid mechanism of rapid dissolution and porosity increase in the seawater-meteoric water mixing zone (up to 1 km from the coast) and also suggested that the fractures in the vadose and mixing zones are favorable for the gathering of fluid, enhanced dissolution and ultimately forming a karst network. Yang et al. (2020) further simulated the alteration process of the Ordovician carbonate reservoir (Tarim Basin, China) via meteoric water leaching under near-surface low temperature and low pressure conditions during early diagenesis, focusing on the influence of leaching speed, duration and mineral components (relative content of limestone/dolostone) on the depth and extend of dissolution. Wei et al. (2017) applied integrated geological and RTM studies on fault-channeled hydrothermal dissolution of the deep-buried Cambrian dolostone reservoir in Tarim Basin, China, and found that the vertical permeability of wall-rocks significantly affect the fluid and temperature patterns of the fault system and ultimately control the spatial distribution of dissolving-originated porosity.

In summary, RTM is an emerging technique for diagenesis characterization and the practical application of RTM in hydrocarbon reservoir prediction is still in its infancy. In the above case studies, although some models are burdened with parametric uncertainties or cannot give absolute results in terms of quantitative distribution of diagenetic geo-bodies, the diagenetic trends revealed by RTM have well explained the reservoir heterogeneity observed in classical petrographic studies. In general, through RTM approach, and together with experimental and observational data, an improved capability in diagenesis characterization and reservoir prediction can be expected, as shown by: 1) simplifying the complex natural geological processes into conceptual hydrological and geochemical models that are easily understood; 2) providing quantitative or semi-quantitative estimates of the rate and distribution of diagenesis; 3) helping to better describe the diagenetic trends and geo-bodies, and to reduce the uncertainty of reservoir quality prediction.

1.2.4 Challenges in reservoir quality prediction

Due to the fact that we cannot directly observe the diagenetic process of ancient sedimentary rocks, the study of diagenesis is much more difficult than sedimentation that can be largely reproduced and observed in modern sedimentary environments. Although we can simulate the temperature, pressure and even diagenetic fluids of multiple diagenetic processes, the prolonged burial time and reservoir/basin-scale geological environment cannot be simulated or reconstructed in modern laboratories. It is thus very difficult for us to imagine the influence of the complex and integrated physical and chemical effects on diagenetic processes at a time scale of thousands years (ka), millions years (ma) or even longer. Hence, there remains some controversial and unsolved issues regarding carbonate diagenesis, which introduce great uncertainties and limit the accuracy for reservoir quality prediction.

As the formation and distribution of carbonate reservoirs are significantly controlled by diagenesis, the spatial continuity and extension of diagenetic geo-bodies (e.g., dolomite and karst zones) are uncertain, displaying strong reservoir heterogeneity. It is difficult to precisely characterize the spatial distribution of diagenetic geo-bodies and the physical properties of reservoirs between wells or away from well control through classical approaches. For instance, in areas with strong depositional heterogeneity (e.g., high frequency lithofacies variations), the dolomite reservoirs tend to be thin-bedded and have complex dolomite fronts that can be characterized neither by petrographic, geochemical nor seismic approaches because these meter-scale dolomite layer cycles are often below seismic detection. In terms of karst reservoir characterization, although the types of diagenesis and the longitudinal intervals of favorable reservoir in different meteoric diagenetic sub-environments can be determined by existing hydrogeological conceptual model, the degree and lateral extension of karstification, and the porosity change of karst reservoir cannot be quantitatively evaluated.

Moreover, there are still some controversies that cannot be well explained or verified by classical characterization approaches in current studies of carbonate diagenesis. For intense, reflux dolomitization in evaporative environment is often accompanied by gypsum/anhydrite precipitation, and the causality of dolomitization and gypsum/anhydrite precipitation remains

debatable. Meanwhile, it is not very clear whether dolomitization directly produces porosity and what the controlling factors of porosity evolution are. In addition, the control mechanism of different dissolution behaviors between limestone and dolostone in karst process remains controversial. The coupling of geochemical reactions with rock structure changes (e.g., karst collapse and brecciation) in RTM simulation of karstification still needs further exploration.

The inherent defect of using numerical simulations to quantitatively characterize diagenesis is that this approach is still immature and will face many challenges before it can be widely accepted and applied in petroleum industry. Particularly, most of the current simulations are based on simplified generic models, and the reservoir-scale models or results cannot be verified by laboratory experiments. As a result, there are to date few researchers using this approach and they are not confident enough to apply it into practical reservoir prediction. Although the requisite computational power to undertake simulations of complex geo-processes is becoming less of a limitation, the development of simulators for specific geological settings and diagenetic processes (with different hydrological and geochemical mechanisms) remains a challenge. Therefore, it is necessary to continuously try to apply RTM method into more case studies with different geological settings, so as to enrich the theory of fluid-rock interactions associated with diagenesis and to improve the effectiveness of the numerical approach.

1.3 Thesis outline

This thesis focuses on “quantifying carbonate diagenesis” using reactive transport modeling approach. The coupled thermo-hydro-chemical processes of fluid-rock interactions and their impacts on reservoir properties are investigated based on TOUGHREACT simulator. First the two major diagenetic processes, i.e., dolomitization and karstification, were studied using two generic models in which the spatial-temporal variations of mineral and rock porosity during diagenesis are determined. Through sensitivity analyses, key hydrogeological controlling parameters of these two processes were quantitatively evaluated. Following the generic models, a case study was conducted on the hydrocarbon reservoir in the Ordos Basin, China, based on integrated observational data and RTM simulated results. Particularly, the distribution and evolution of carbonate rock porosity under the influences of multistage reflux dolomitization

and facies-controlled eogenetic karst are revealed. The formation mechanisms and potential controlling factors of the dolomite- and karst-reservoirs were also analyzed. Finally, a semi-quantitative diagenesis-porosity evolution was built, which provided valuable clues for further reservoir quality prediction. The flowchart of this thesis is shown in Fig. 1.4 and the following contents have been integrated in this thesis.

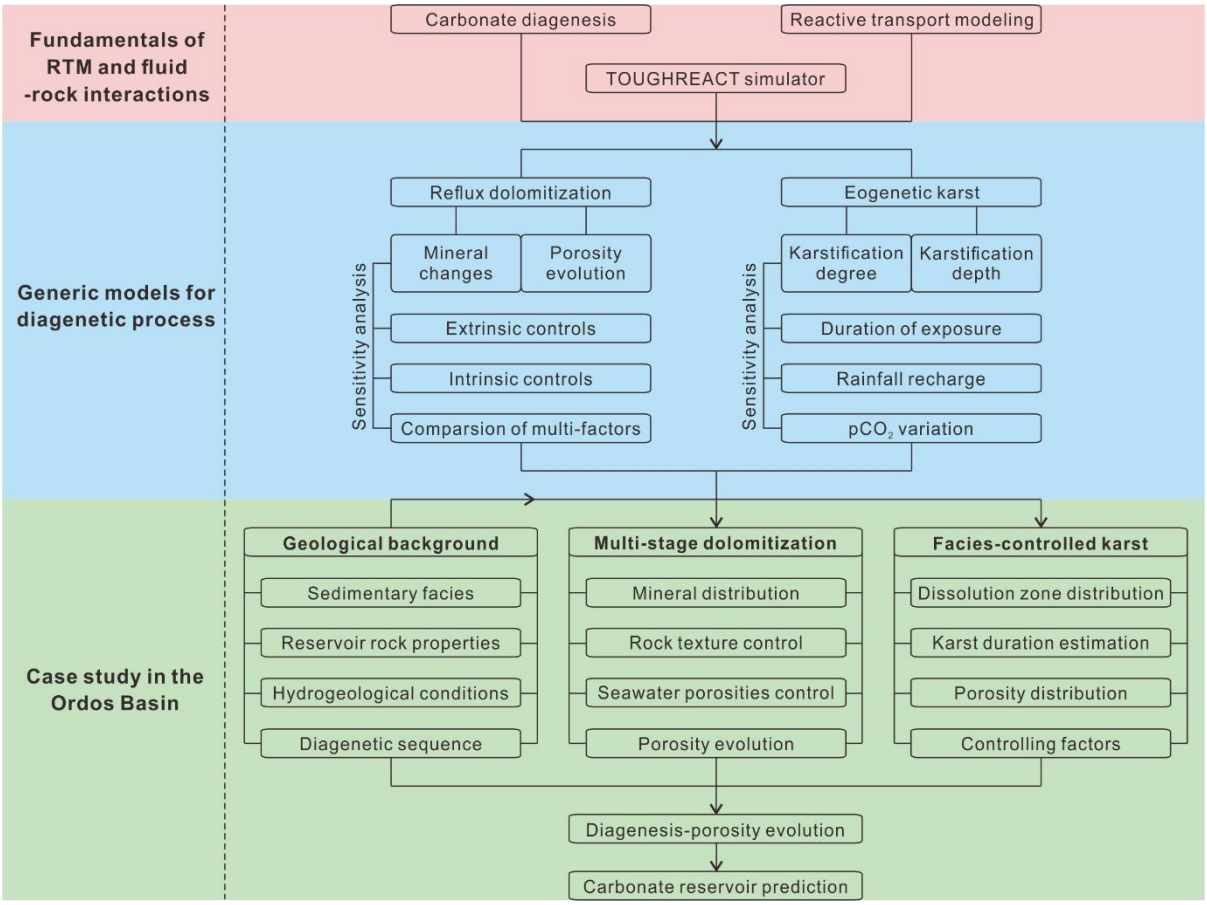

Figure 1.4 Main research contents and flowchart.

Chapter 2 gives the fundamentals of geo-processes associate with carbonate diagenesis. Firstly, the thermodynamic/kinetic mechanisms of the three major digenetic fluid-rock interactions, i.e., carbonate dissolution, replacive dolomitization and gypsum/anhydrite cementation are introduced. Then the methodology and some representative mathematical/numerical models used for the RTM studies in geological porous media are summarized, including chemical reactions, fluid flow and solute transport, and reaction-induced porosity and permeability changes. The coupling of thermo-hydro-chemical domains (T-H-C) in TOUGHREACT with its solution method of are also explained.

Chapter 3 simulates the reflux dolomitization process in evaporated seawater environment. The kinetic process of dolomitization is introduced first. Based on a simplified one-dimensional column model, the spatial-temporal evolution of minerals (i.e., dolomite, calcite and concomitant gypsum cement) and rock properties (porosity and permeability) during dolomitization are investigated. Individual evaluation and contrastive analysis of the control of various extrinsic (brine salinity, temperature and injection rate) and intrinsic factors (reactive surface area and rock fabric) on the replacement reaction rate and dolomitization degree are also conducted through sensitivity analyses.

Chapter 4 simulates the eogenetic karst process in meteoric diagenetic environment. The applicability of the model and selection of porosity-permeability relationship are explained first. Then, using a generic one-dimensional vadose meteoric water-rock system, the carbonate (limestone and dolostone) dissolution processes are systematically simulated under different conditions of the duration of subaerial exposure, climate-related rainfall recharge and atmospheric carbon dioxide concentration, respectively. Following simulation results, the impacts of the above three key geological factors on the karst/dissolution process and their relative importance are discussed in terms of the karst depth penetration and porosity increment. The control mechanism of different dissolution behaviors between limestone and dolostone is also discussed.

Chapter 5 presents an integrated geological and RTM study of the hydrocarbon reservoir in the Ordos Basin, China. The two major diagenetic processes of the studied Ordovician Majiagou Formation reservoir, i.e., multistage reflux dolomitization and facies-controlled eogenetic karst, are simulated on specific two-dimensional models. Based on integrated observational data (i.e., petrographic and reservoir properties analyses, diagenetic sequence and basin burial history) and simulated results, the spatial-temporal distribution and evolution of diagenetic geo-bodies (e.g., dolomite body, gypsum cementation and karst zone) and reservoir porosity are investigated. The formation mechanisms and potential controlling factors of the dolomite- and karst-reservoirs are also discussed through sensitivity analysis and parametric uncertainty analysis. Finally, the diagenesis-porosity evolution of lagoon-facies micrite and shoal-facies

grainstone are reconstructed, and the favorable targets for further exploration of high quality carbonate reservoirs in the Majiagou Formation are also pointed out.

2 Fundamentals of coupled thermo-hydro-chemical geo-processes

2.1 Major fluid-rock interactions in carbonate rocks

The concept of Water-Rock Interaction (WRI) was firstly proposed by A.M. Ovchinnikov in the 1950s. The water-rock interaction system consists of two parts, i.e., the “water” and the “rock”. Specifically, the “water” refers to various fluids and the “rock” refers to various solid phase substances including minerals and rocks. Obviously, plenty of geochemical processes occurring on the surface and subsurface conditions belong to the water-rock interaction. In the last few decades, the study of water-rock interaction has experienced three main periods (Shen and Wang, 2002): 1) an initial period in the 1950s to 1970s with research focuses of various hydrochemical processes under natural conditions and shallow groundwater assessment; 2) a formative period of research framework of water-rock interaction in the 1970s to 1980s with focuses on environmental concerns such as water contamination, geological waste disposal and global changing, and resource exploration such as basin fluids distribution and ore-forming regularity. Geochemical analyses, such as isotopes and trace elements are widely used in this period; 3) a rapid development period from the 1980s to date with continuous focuses on various environmental problems (including WRI with related to biogeochemistry and organic geochemistry) and numerical modeling of coupled thermo-hydro-mechanical-chemical (THMC) processes.

From a perspective of petroleum geology, the study of water-rock interaction in sedimentary basins mainly includes the genesis and evolution of formation water, and the geological fluids-rock interactions during diagenesis with their impacts on reservoir properties. Particularly, the complex fluid-rock interactions in diagenetic process has become a focus of research for hydrocarbon exploration. This is because the diagenetic fluids-induced mineral reactions (dissolution and precipitation) have directly determine the formation mechanism and evolution of reservoir porosity-permeability (mostly secondary pores) after sedimentation. However, the diagenetic process of sedimentary rocks is prolonged, with complex fluid-rock interactions controlled by initial rock fabrics (textures and mineral composition) and diverse diagenetic

environments (temperature, pressure, fluid property, tectonic activity, etc.). Therefore, in order to provide valuable basic data for reservoir quality evaluation and prediction, it is necessary to precisely characterizing the fluid-rock interactions and resulting porosity-permeability evolution during the prolonged diagenetic process using both qualitative classical methods and quantitative numerical approaches. Yang et al. (2015, 2017) carried out a comprehensive study of fluid-rock interactions during diagenesis of clastic rocks (sandstone reservoir) using reactive transport modeling, such as feldspar dissolution, calcite cementation and organic acid intrusion. Herein, this study focuses on several major fluid-rock interactions associated with diagenesis in carbonate rocks (limestone and dolostone) that are crucial for the development and preservation of reservoir porosity, including carbonate dissolution, replacive dolomitization and gypsum/anhydrite cementation.

2.1.1 Carbonate dissolution

(1) Source of hydrogen ions

Mineral dissolution (karstification) is a major formation mechanism of carbonate reservoir spaces and could occur in both near-surface conditions with normal temperature and pressure and burial conditions with high temperature and pressure. The near-surface dissolution is typically represented by meteoric freshwater leaching of exposed carbonate sediments (i.e., H_2O(l)-CO_2(g) system) during eogenetic or telogenetic stage. The burial dissolution is mostly induced by organic acid and hydrogen sulfide in the pores (i.e., H_2O(l)-H_2S(g) system) and is usually associated with degradation of organic matter and sulfate reduction reaction under burial reducing environment.

In meteoric diagenetic environment, CO_2(g) in the atmosphere can be partly dissolved and held in rainwater and ultimately forms H^+, HCO_3^- and CO_3^{2-} in the solution. This ionization process directly controls the pH value of the seepage water and the dissolution/precipitation trend of carbonate minerals, which can be described through the following four steps.

Equilibrium reaction between gaseous CO_2(g) and aqueous CO_2(ag):

$$CO_2(\mathrm{g}) \Leftrightarrow CO_2(\mathrm{aq}); \quad K = 5.155 \times 10^{-2} \tag{2.1}$$

Equilibrium reaction between aqueous CO_2(ag) and carbonic acid:

$$CO_2(\text{aq}) + H_2O \Leftrightarrow H_2CO_3; \quad K = 6.718 \times 10^{-1} \tag{2.2}$$

The first-order ionization reaction of carbonic acid:

$$H_2CO_3 \Leftrightarrow H^+ + HCO_3^-; \quad K = 4.287 \times 10^{-7} \tag{2.3}$$

The second-order ionization reaction of carbonic acid:

$$HCO_3^- \Leftrightarrow H^+ + CO_3^{2-}; \quad K = 4.585 \times 10^{-11} \tag{2.4}$$

Where *K* are the equilibrium constants of the four reactions at standard temperature and pressure (STP) conditions.

Based on Arrhenius equation, Huang (2010) further calculated a set of equilibrium constant data at the temperature range (from 25°C to 250°C) of sedimentary rocks. In general, the equilibrium constants for CO_2 dissolving processes (Eq. 2.1 and Eq. 2.2) show a decreasing trend with increasing temperature, while the equilibrium constants for carbonic acid ionization reactions (Eq. 2.3 and Eq. 2.4) increase with temperature. Although these reactions exhibit different variations of equilibrium constant with temperature, one thing in common is that the equilibrium constant of Eq. 2.4 is extremely lower (by 3–4 magnitudes) than that of the first three reactions, and thus the hydrion (H^+) provided by the second-order ionization reaction of carbonic acid can be ignored. By summing the first three equations, a new Eq. 2.5 is obtained:

$$CO_2(\text{g}) + H_2O \Leftrightarrow H^+ + HCO_3^- \tag{2.5}$$

Equation (2.5) describes the chemical equilibrium process of H_2O(l)-CO_2(g) system related to meteoric diagenesis. Meanwhile, the equilibrium constant of this equation (Eq. 2.5) shows a decreasing trend with increasing temperature (Fig. 2.1a).

In H_2O(l)-H_2S(g) systems, H_2S(g) can be also slightly dissolved in the pore water and forms H^+, HS^- and S^{2-}, which affected the pH value of the pore water and the dissolution/precipitation of carbonate minerals. This process usually occurs during mesogenesis under burial conditions and can be described through the following three steps.

Equilibrium reaction between gaseous H_2S(g) and aqueous H_2S(ag):

$$H_2S(\text{g}) \Leftrightarrow H_2S(\text{aq}); \quad K = 9.245 \times 10^{-2} \tag{2.6}$$

The first-order ionization reaction of hydrosulphuric acid:

$$H_2S(\text{aq}) \Leftrightarrow H^+ + HS^-; \quad K = 9.013 \times 10^{-8} \tag{2.7}$$

The second-order ionization reaction of hydrosulphuric acid:

$$HS^- \Leftrightarrow H^+ + S^{2-}; \quad K = 1.509 \times 10^{-13} \tag{2.8}$$

Similar with H_2O(l)-CO_2(g) system, the equilibrium constant of the second-order ionization (Eq. 2.8) is extremely lower (by ~5 magnitudes) than that of its first-order ionization (Eq. 2.7), indicating that the hydrion (H^+) is mainly provided through the first-order ionization of hydrosulphuric acid. By summing the first two equations, the chemical equilibrium process of H_2O(l)-H_2S(g) system related to burial dissolution can be expressed by:

$$H_2S(\mathrm{g}) \Leftrightarrow H^+ + HS^- \tag{2.9}$$

Where the equilibrium constant shows an increasing trend with temperature (Fig. 2.1b).

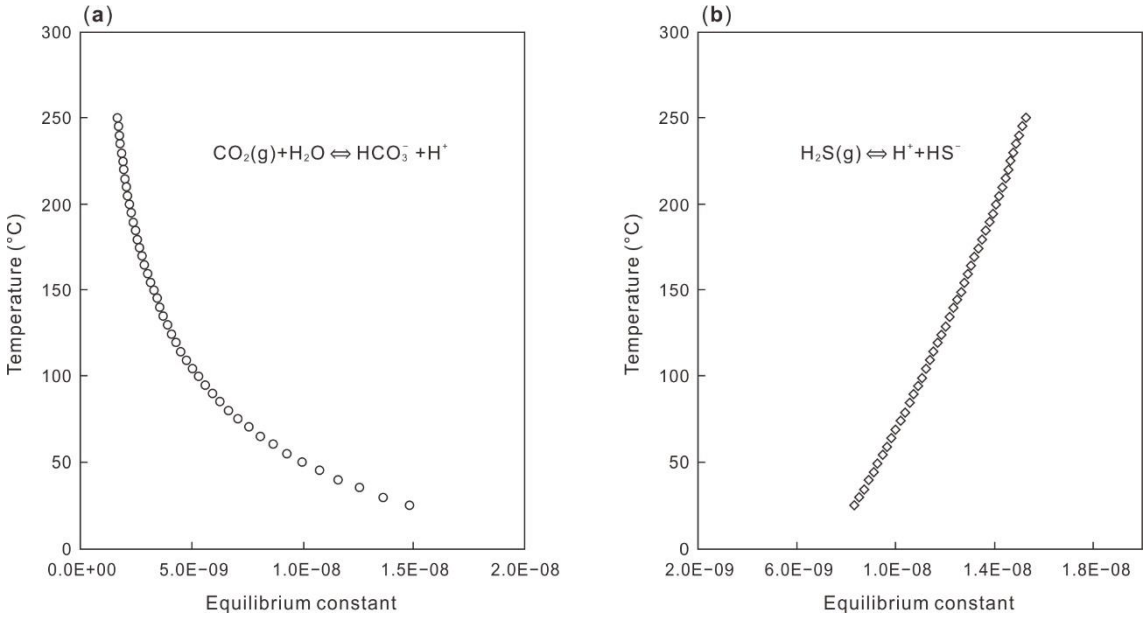

Figure 2.1 Variation in ionization constant with temperature for (a) CO_2(g) and (b) H_2S(g) in water (Huang, 2010).

In addition, according to specific geothermal and pressure gradients (herein use 3°C/100 m and 1 MPa/100 m, respectively), the variation in equilibrium constant with temperature can be further transformed into the variation in equilibrium constant with burial depth (Fig. 2.2). It should be noted that at shallow burial condition (ca. <1000 m), the ionization constant of hydrosulphuric acid is lower than that of carbonic acid. Thus, in the case of co-existence of CO_2 and H_2S, the ionization of hydrosulphuric acid (Eq. 2.7) would be inhibited and most of the hydrion (H^+) in solution are provided by carbonic acid (Eq. 2.3). In contrast, at deep burial

condition (ca. >1000 m), the ionization constant of hydrosulphuric acid is higher than that of carbonic acid, and hydrosulphuric acid play a more important role for providing hydrion (H^+).

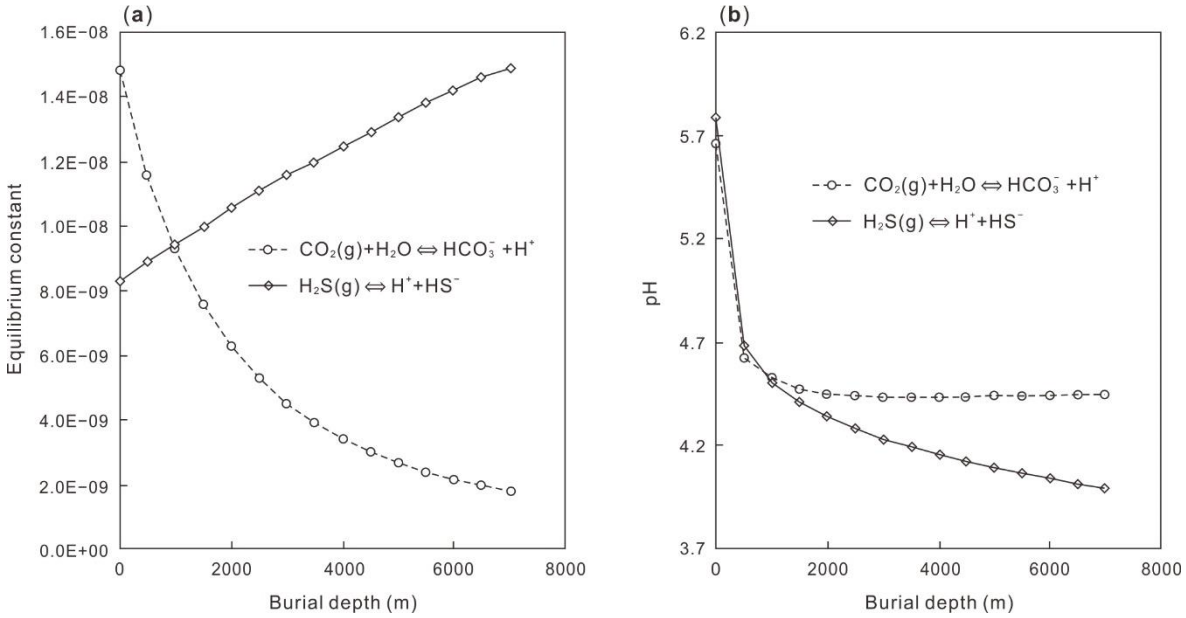

Figure 2.2 Variations in (a) ionization constant and (b) pH value of solution with burial depth for H_2O(l)-CO_2(g) and H_2O(l)-H_2S(g) systems (Huang, 2010).

(2) Carbonate mineral dissolution

The dissolution of calcite and dolomite under acidic conditions are written as:

$$CaCO_3(\text{Calcite}) + H^+ \Leftrightarrow Ca^{2+} + HCO_3^- \tag{2.10}$$

$$CaMg(CO_3)_2(\text{dolomite}) + 2H^+ \Leftrightarrow Ca^{2+} + Mg^{2+} + 2HCO_3^- \tag{2.11}$$

In the equilibrium cases, the dissolution reactions of calcite and dolomite are both exothermic, and a lower temperature condition is conducive to the dissolution of these two major carbonate rocks. The equilibrium constant of these two reactions exhibit apparent decreasing trend with increasing temperature and burial depth (Fig. 2.3). This variation in equilibrium constant with temperature is important to explain the formation mechanism of hydrothermal reservoirs. In late diagenesis, the deep-sourced hydrothermal fluids, which migrate upwards (driven by magmatic activities or tectonic uplifting), could result in intense dissolution of carbonates and porosity increment because the fluids became unsaturated with regard to calcite/dolomite as gradual decreases in temperature and burial depth (Huang, 2010). On the other hand, the mechanism of dolomite precipitation is much more complicated than calcite because it is

sometimes controlled by various kinetic factors (discussed in Chapter 3).

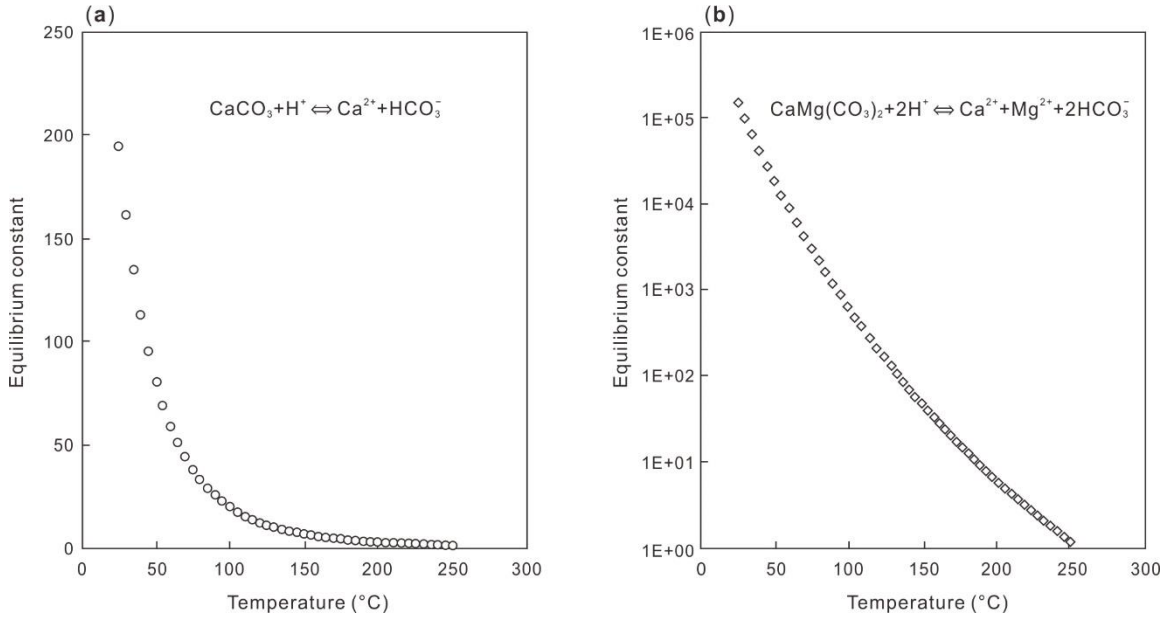

Figure 2.3 Variation in equilibrium constant with temperature for the dissolution reaction of (a) calcite and (b) dolomite (Huang, 2010).

2.1.2 Replacive dolomitization

Dolostone is one of the important hydrocarbon reservoir rocks. Statistically, the dolostone accounts for ca. 80% of the carbonate reservoir found in North America; more than half of the carbonate reservoir in the world (Zengler et al., 1980). Its original mineral, namely dolomite has a relatively simple crystal structure with the chemical composition of $CaMg(CO_3)_2$ for an ideal stoichiometric dolomite. Typically, the ideal dolomite lattice is composed of alternating layers of Ca^{2+} and Mg^{2+} that are separated by CO_3^{2-} layers (Fig. 2.4). Although the dolomite has a relatively simple crystal lattice than aluminosilicate minerals, its genesis are much more complex and there are still some controversies and unknowns regarding the formation mechanism and distribution of dolomite.

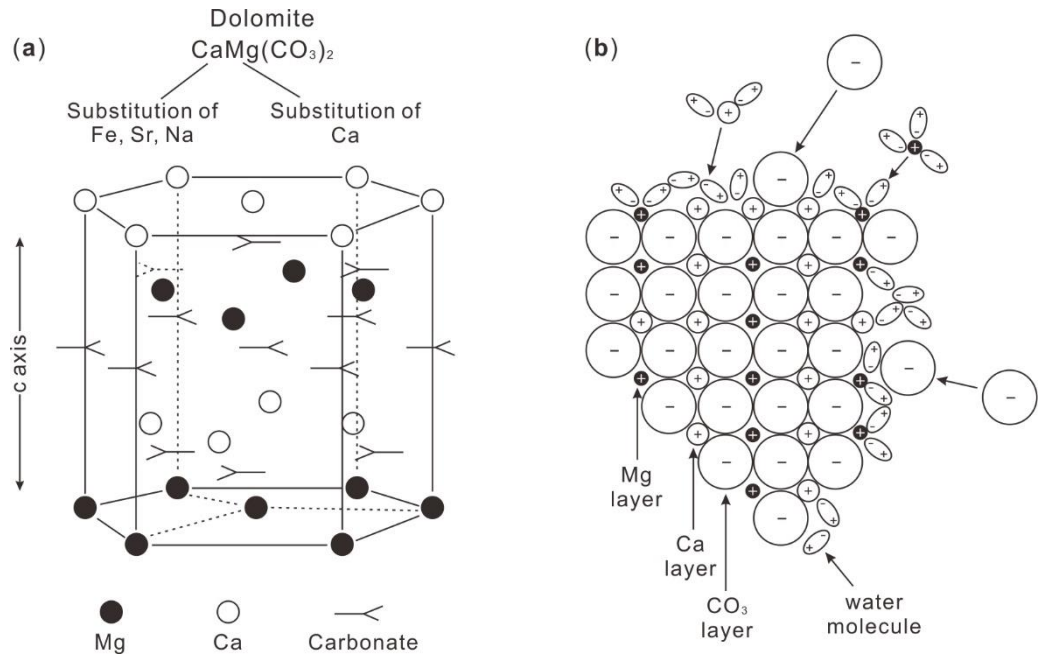

Figure 2.4 Lattice structure of dolomite (Warren, 2000). (a) Ideal structure of stoichiometric dolomite consisting of alternating layers of Ca^{2+} and Mg^{2+} separated by CO_3^{2-} layers. (b) Schematic of non-ideal lattice structure showing how the hydration of cations on the surface of growing crystallite. Mg ions are more hydrated than Ca ions, and the carbonate ions need sufficient energy to displace water molecules adjacent to the cation layer.

One of the interesting and puzzling phenomena is that people cannot manage to grow dolomite directly from solution under near-surface conditions at normal temperature and pressure. However, dolomite is a widespread mineral in nature settings (near-surface conditions of sedimentary rocks). Moreover, dolomite is abundant in ancient strata from the Precambrian, Paleozoic to Mesozoic, whereas it is a rare precipitate in modern seawater although the modern seawater is supersaturated by one to two orders of magnitude with respect to dolomite. These puzzles have constituted the so called “the dolomite problem”. Considering these geological facts, researchers gradually recognized that the marine dolomites, which were widely distributed in geological history, might not be directed precipitated from seawater. Instead, they were likely the products of replacement reaction of calcium carbonate (calcite or aragonite) by dolomite (Fig. 2.5; replacive dolomitization). Accordingly, numerous dolomitization models, such as reflux model, mixing zone model, geothermal convection model and burial model, have been employed to explain the genesis and distribution of dolomite (Machel, 2004).

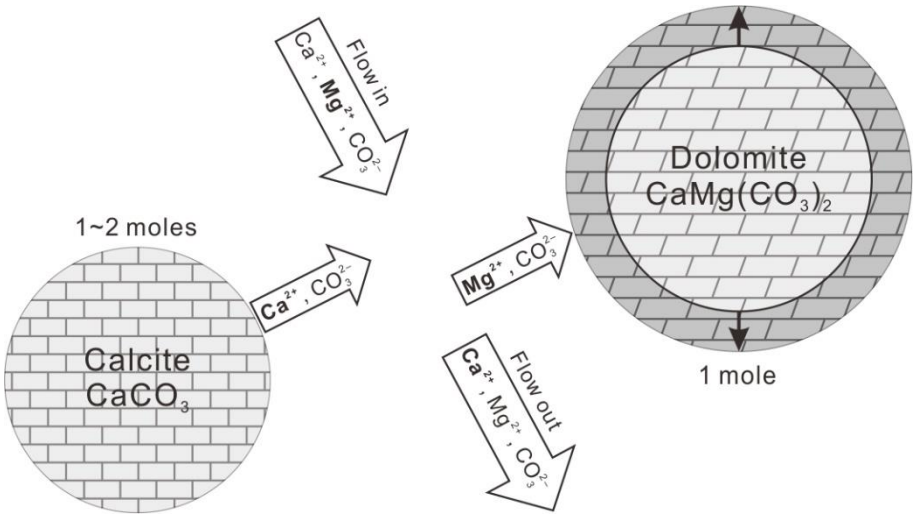

Figure 2.5 Schematic of the replacement reaction of calcite by dolomite (modified from Budd and Park, 2018). The variation in main ions during the dolomitization process are shown in bold within open arrows. The black arrow indicates the change in mineral radius.

According to petrogenesis, the dolomite in geological strata can be simply divided into two types: primary dolomite and replacement dolomite. The primary dolomite is represented by the dolomite directly precipitation from seawater (e.g., under microbial mediation mechanism), and mostly the dolomite cement formed from pore fluids during diagenesis. The formation of dolomite cement can be regarded as a reverse process of dolomite dissolution reaction (Eq. 2.11). The replacement dolomite is more pervasive in geological strata, and the replacement of calcite (or aragonite) by dolomite can be expressed by a generic equation:

$$(2-\mathrm{x})CaCO_3 + \ Mg^{2+} + \mathrm{x}CO_3^{2-} \rightarrow CaMg(CO_3)_2 + (1-\mathrm{x})Ca^{2+} \qquad (2.12)$$

Where x indicates the amount of exogenous CO_3^{2-} involved in the dolomitization reaction with a value range of zero to one.

Machel (2004) summarized the thermodynamic and kinetic factors of dolomite formation. According to the bivariate thermodynamic stability and trivariate kinetic stability diagrams for the calcite-dolomite-water system (Fig. 2.6), favorable chemical conditions of dolomite formation can be speculate: 1) settings with high Mg^{2+}/Ca^{2+} ratios and CO_3^{2-}/Ca^{2+} ratios (i.e., high carbonate alkalinity) such seawater environment and seawater-sourced pore fluid; 2) settings with abundant limestone precursor and a long-lasting and efficient delivery system for the supply of Mg^{2+} or CO_3^{2-} and export of replaced Ca^{2+}; 3) settings with abnormal high

temperatures such as early burial conditions of carbonate platform affected by geothermal convection and deep burial fault system influenced by hydrothermal fluids; 4) settings with proper fluid salinity (lower or higher than seawater) and corresponding Mg^{2+}/Ca^{2+} ratios; 5) settings with sudden release of CO_2 from the fluids such as upwelling hydrothermal solutions along the fault system.

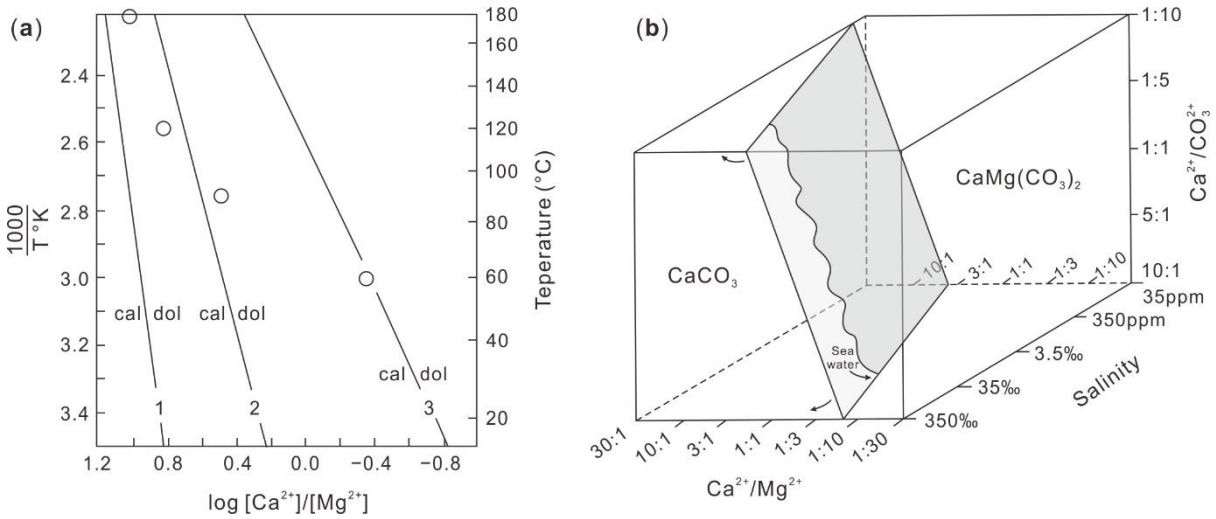

Figure 2.6 Thermodynamic and kinetic stability diagrams for the calcite-dolomite-water system (Machel, 2004). (a) Bivariate thermodynamic stability diagram. Square brackets denote activities. Lines 1, 2, 3 are dividing lines for calcite-dolomite calculated from experimental data, which indicate ideal, fully ordered dolomite, ordered dolomite with slight Ca-surplus, and fully disordered protodolomite, respectively. The four open circles label the results of 7 year-long experimental dolomite formation by Usdowski (1994). (b) Trivariate kinetic stability diagram. The ionic ratios are mole ratios. The stippled field boundary is bent towards higher Ca^{2+}/Mg^{2+} ratios at salinities greater than 35‰.

The above paragraph lists several favorable geochemical conditions of dolomite formation, which cover most of the near-surface and subsurface diagenetic environments. However, in these environments, there are still many undolomitized limestone. These phenomena arouse discussions about potential thermodynamic and kinetic constrains that have inhibited the dolomite formation: 1) The first and most important factor is the presence of kinetic barrier caused by Mg^{2+}-water complexes. Due to a relatively greater strength of electrostatic bond of the Mg^{2+} for water than that for Ca^{2+} or for CO_3^{2-} (Fig. 2.4b), it is very difficult for carbonate

ions to overcome the hydration shell and to bond with Mg^{2+} at normal conditions (Warren, 2000). This could also explain the failure to precipitate dolomite at laboratory conditions by Land (1998) even though the solution is theoretically saturated (25°C, 1000-fold oversaturation, 32 years). As such, the dolomitization process is generally regarded as a kinetic reaction (the treatment of this reaction for RTM study are presented in Chapter 3), and modified seawater, such as being concentrated, heated, cooled, diluted, and with lowed sulfate levels or enhanced CO_3^{2-} activity, are needed to overcome the hydration barrier (Warren, 2000). 2) a lack of efficient supply of Mg^{2+} or CO_3^{2-} due to a relatively closed hydrological system, too small a hydrological head or insufficient diffusion; 3) the presence of low permeable limestone (due to strong cementation) or interlayers (e.g., mudstone and anhydrite rock) that limit the flow of Mg^{2+}-bearing fluids; 4) other kinetic inhibitors such as a short duration of water-rock interaction or a low temperature (<50°C) that might reduce the likelihood of overcoming the hydration barrier and inhibit the nucleation and growth of dolomite (Machel, 2004).

2.1.3 Gypsum/anhydrite cementation

Gypsum/anhydrite is a common sulfate mineral (occurs as cement) in carbonate reservoir pore spaces, and can be formed at various stages (from shallow-medium to deep burial stages) of burial diagenesis. A large number of case study have suggested that an evaporative sedimentary environment and the interbedded carbonate-gypsum strata are favorable conditions for gypsum/anhydrite cementation in the pores (Liu et al., 2020; Xiong et al., 2021b). This is because that a strong evaporation during the sedimentary stage was conducive to the formation of high-saline concentrated seawater that can be sealed in the porous initial sediments. Subsequently, these sediments were subjected to burial environment. Forced by continuous accretion and compaction of the overlying sediments, the Ca^{2+}- and SO_4^{2-}-rich pore fluids sealed in the gypsum/salt-bearing layers would be gradually released and migrate into the adjacent carbonate rocks with higher porosity and permeability. With the increases in burial depth, temperature and pressure, gypsum/anhydrite precipitates from the pore fluids and fills some reservoir pores. It should be noted that anhydrite precipitation normally occurs at a temperature greater than 42°C (Azimi and Papangelakis, 2010). As such, gypsum cementation

is preferred to anhydrite cementation at a relatively lower temperature condition in shallow-medium burial diagenetic environment, with a typical chemical reaction formula as:

$$Ca^{2+} + SO_4^{2-} + 2H_2O \Leftrightarrow CaSO_4 \cdot 2H_2O(\text{Gypsum}) \tag{2.13}$$

In deep burial environment, the flow of diagenetic fluids is tending towards stability and there is a lack of ions supply from exogenous fluids. Thus, the deep burial diagenetic environment is generally characterized by relatively closed hydrogeochemical conditions. Affected by the continuously increasing temperature, the gypsum cements, which formed in the shallow-medium burial stage, would be gradually dehydrated and eventually converted to anhydrite as expressed by:

$$CaSO_4 \cdot 2H_2O(\text{Gypsum}) \Leftrightarrow CaSO_4(\text{Anhydrite}) + 2H_2O \tag{2.14}$$

Equation (2.14) explains why almost all the sulfate cement found in ancient carbonate strata is anhydrite rather than gypsum. Under the influences of tectonic uplift-subsidence and fluctuations of water table (phreatic surface) in some special regions, the transformation between gypsum and anhydrite may occur repeatedly.

2.2 Theoretical background of reactive transport modeling

Reactive transport modeling (RTM) is a multidisciplinary and comprehensive research field that is rapidly evolving with computing power. Due to a wide range of applicability in spatial-temporal scale and flexible resolution, the RTM approach has been extensively used in the study of hydrology, geology, engineering and environmental science in the past two decades (e.g., Whitaker and Smart, 2007; Kaufmann et al., 2010; Yang et al., 2020). For instance, in the field of petroleum geology, the RTM approach has the unique advantage of forward modeling and reconstructing the complicated fluid-rock interactions at multiple temporal and spatial scales, from borehole-scale oil and gas production to basin-scale reservoir properties evolution in geological history (Xiao et al., 2018). In addition, over the past decades, a large number of thermodynamic and kinetic data related to the fluid-rock reactions have been obtained through sustained field and laboratory work (e.g., Lasaga et al., 1994; Morse and Arvidson, 2002; Kaufmann and Dreybrodt, 2007), which provides the theoretical basis for subsequent numerical simulation and quantitative study of geological issues.

In contrast to the classical reservoir characterization methods that usually focus on the geological products, the RTM approach is believed to be able to better predict the spatial-temporal distribution and evolution of geological bodies (such as dolomite body and karst zone) and reservoir properties (porosity and permeability). Through mathematical formulation, the key to a reactive transport model is coupling the fluid (both aqueous and gaseous phases) flow, heat transfer, chemical transport and reactions in geological porous media. Meanwhile, the flexible use of RTM method also requires a comprehensive knowledge of earth science, physical chemistry and computer programming skills. Typically, Xiao and Jones (2007) proposed a general governing equation to describe the coupled transport and geochemical processes related to the pore fluid-rock interactions as follow:

$$\frac{\partial}{\partial t}(\phi C_i) = \frac{\partial}{\partial x}\left(\phi D \frac{\partial C_i}{\partial x}\right) - \phi v \frac{\partial C_i}{\partial x} + \phi \sum_k (\frac{\partial C_i}{\partial t})_k \tag{2.15}$$

Where C_i is the concentration of a specific species in pore fluid, D labels the coefficient term that combines diffusion and dispersion, v is the linear fluid flow rate, ϕ is the porosity and k is the index of other species associated with chemical reactions of species i. Notably, the first two terms on the right-hand side describe the solute transport including diffusion, dispersion and advection. The last term describe the effect of chemical reactions.

Due to the complex boundary conditions of the model and also the complex coupling procedure of flow and transport equations and thermodynamic/kinetic reactions, it is impossible to provide analytical solutions to the equation and thus numerical solutions are required (Xiao et al., 2018). The following section summarizes some representative mathematical and numerical formulations usually used for RTM study in geological porous media.

2.2.1 Chemical reactions

For most of the reactive transport simulators, the chemical reactions in subsurface porous media may comprise a series of thermodynamically or kinetically controlled processes such as gas-aqueous phase exchange, aqueous complexation, ion exchange, mineral dissolution and precipitation.

(1) Gas-aqueous phase exchange

Reactions involving the gas-aqueous phase exchange are often assumed to be at equilibrium (kinetic treatment is considered only in very rare cases). According to the mass action law, the dissolution/exsolution behavior of a gas species can be described using the fugacity as shown in Eq. 2.16 (Steefel et al., 2015).

$$f_l = K_l^{-1} \prod_{j=1}^{N_c} (\gamma_j C_j)^{\upsilon_{lj}} \tag{2.16}$$

Where l is the index of gas species, f_l is the fugacity of the l-th gas, K_l is the equilibrium constant of the reaction, j is the index of aqueous species, N_c is the number is aqueous species, γ_j is the thermodynamic activity coefficient of aqueous species j, C_j is the concentration of aqueous species j with units of mole per kilogram water, υ_{lj} is the number of moles of aqueous species j in one mole of gas species l. The fugacity of a gas species can be related to its partial pressure P_l by means of the fugacity coefficient φ_l (Eq. 2.17).

$$P_l = \frac{f_l}{\varphi_l} \tag{2.17}$$

Commonly, the fugacity coefficient of gas can be assumed to be one at low pressure conditions (close to atmospheric pressure). At high temperature and pressure conditions such as boiling condition and deep aquifers, however, the fugacity coefficient needs to be corrected using the Eq. 2.18 given by Spycher and Reed (1988):

$$\ln \varphi = \left(\frac{a}{T^2} + \frac{b}{T} + c\right) P + \left(\frac{d}{T^2} + \frac{e}{T} + f\right) \frac{P^2}{2} \tag{2.18}$$

Where P is the total gas pressure, T is the absolute temperature, and alphabets a, b, c, d, e and f are all correction coefficients fitted from specific experimental data. In some cases, the gas in the system is assumed to be an idea gas, and the concentration of the gas species can be directly calculated according to the ideal gas law:

$$\frac{n_l}{V} = \frac{P_l}{RT} \tag{2.19}$$

Where n_l and P_l are the number of moles and partial pressure of the gas species l, respectively.

(2) Aqueous complexation

The formation/dissociation of aqueous complexes in solution is also assumed to be at local equilibrium and has a similar mathematical formulation to the gas-aqueous phase exchange

reaction. Following Xu et al. (2004), the concentration of aqueous complexes can be expressed as functions of the concentrations of basis species:

$$C_i = K_i^{-1}\gamma_i^{-1}\prod_{j=1}^{N_c}(\gamma_j C_j)^{v_{ij}} \tag{2.20}$$

Where i is the index of aqueous complex, C_i is the concentration of the i-th aqueous complex, j is the index of basis species, C_j is the concentration of the j-th basis species, N_c is the number of basis species, γ_i and γ_j are the activity coefficients, K_i is the equilibrium constant and v_{ij} is the number of moles of basis species j in one mole of aqueous complex i. With this formulation, a total concentration term can be defined:

$$\Psi_j = C_j + \sum_{i=1}^{N_x} v_{ij}C_i \tag{2.21}$$

Where Ψ_j, denotes the total concentration, comprising the primary species j and the secondary aqueous complexes i, and N_x is the number of secondary aqueous complexes.

In addition to aqueous complexation, surface complexation are also frequently considered in the study of groundwater geochemistry because the sorbing sediment surfaces are regarded to possess functional groups that can form complexes (Davis et al., 2004). This reaction process, which is generally associated with the enrichment behavior of metallic elements in solution via proton exchange and ligand exchange, can be treated similarly with the formation of aqueous complexes in solution (Steefel et al., 2015). Typically, the sorption of a metal via ligand exchange at surface hydroxyl sites can be expressed as:

$$\mathrm{X\cdot OH + M^{z+} \Leftrightarrow X\cdot OM^{z+-1} + H^{+}} \tag{2.22}$$

Where superscript z+ is the valence of the metal. In the equilibrium case, the mass action equation can be written as:

$$K_{eq} = \frac{[\mathrm{X\cdot OM^{z+-1}}][\mathrm{H^{+}}]}{[\mathrm{X\cdot OH}][\mathrm{M^{z+}}]} \tag{2.23}$$

Where the square brackets, [], denote activity and K_{eq} is the equilibrium constant of the reaction (Eq. 2.22) and is affected by the degree (free energy) of surface ionization.

(3) Ion exchange

For reversible geochemical processes, thermodynamic treatment is commonly used and valid. Thus, the ion exchange reaction can be also described by the mass action law, yielding a generic form (Xu et al., 2004) as follow:

$$\frac{1}{v_i}S_i + \frac{1}{v_j}\left(X_{v_j} - S_j\right) \Leftrightarrow \frac{1}{v_i}\left(X_{v_i} - S_i\right) + \frac{1}{v_j}S_j \tag{2.24}$$

In the equation, the subscripts i and j label the dissolved (free) cation in solution and the interlayer cation, respectively; v_i and v_j are the stoichiometric coefficients (equal to their charges) of the two kinds of cation. Notably, the given reaction expression indicates the exchange process of the dissolved cationic species S_i in solution with the S_j in the exchange sites ($Xv_j{-}S_j$), as well as the formation of the new interlayer cation ($Xv_i{-}S_i$). Accordingly, the equilibrium constant (or exchange coefficient) K_{ij}^* of this reaction can be expressed by:

$$K_{ij}^* = \frac{w_i^{1/v_i} \cdot a_j^{1/v_j}}{w_j^{1/v_j} \cdot a_i^{1/v_i}} \tag{2.25}$$

Where a_i and a_j are the activity of the dissolved species Si and S_j, w_i and w_j are the activity of the interlayer cations ($Xv_i{-}S_i$) and ($Xv_j{-}S_j$), respectively.

(4) Mineral dissolution and precipitation

Mineral dissolution and precipitation processes involved in the fluid-rock interactions can be treated thermodynamically or kinetically. In the equilibrium case, the mineral reaction can be regarded as a similar fashion to the formation/dissociation of aqueous complexes. On the basis of Eq. 2.21, the total component concentration (Steefel et al., 2015) now is given by:

$$\Psi_j = C_j + \sum_{i=1}^{N_x} v_{ij} C_i + \sum_{k=1}^{N_m} v_{kj} C_m \tag{2.26}$$

Where Ψ_j is the total concentration of component j, C_j, C_i and C_m are the concentration of the j-th aqueous species, i-th aqueous complex and m-th mineral, respectively; N_x and N_m are the number of aqueous complex and mineral, respectively; v_{ij} and v_{kj} are the number of moles of basis species j in one mole of i-th aqueous complex and one mole of m-th mineral, respectively.

Although thermodynamic treatment of mineral reaction can deal with problems at (near) equilibrium and reversible processes, for most of the geochemical conditions, the mineral reactions are usually irreversible and are difficult to reach equilibrium due to an extremely slow

reaction rate. As such, these processes should be considered kinetically if the reaction system is far from equilibrium. Particularly, Steefel et al. (2015) further divided the treatment methods of mineral reactions into three types as follows (without microbially mediated mechanism), depending on whether the reaction is reversible and whether it includes a dependence on Gibbs energy or saturation state.

For TST (transition state theory) type reactions, the mineral reactions are treated as reversible, with a continuous rate between dissolution and precipitation at equilibrium. A dependence on Gibbs energy or saturation state is explicitly included (Lasaga, 1984). The reaction rate R_m is expressed by:

$$\begin{aligned} R_m &= sgn[\Omega] A_m k_m \left(\prod a^n\right) \left|\exp\left(\frac{\eta \Delta G}{RT}\right) - 1\right|^m \\ &= sgn[\Omega] A_m k_m \left(\prod a^n\right) \left|(\frac{Q_m}{K_{eq}})^\eta - 1\right|^m \end{aligned} \tag{2.27}$$

Where sgn[Ω] = sgn[log(Q_m/K_m)] gives the sign of the reaction term, negative for dissolution and positive for precipitation, A_m is the reactive surface area of the mineral, k_m is the rate constant. The term $\prod a^n$ is the product of all the far from equilibrium effects (catalytic or inhibitory) and the last term on the right hand side is referred to as the "affinity term" that shows the dependence of the rate on Gibbs energy or saturation state. Q_m is the ion activity product and K_{eq} is the equilibrium constant. The superscript η and m are exponential fitting parameters determined experimentally or theoretically.

For irreversible reactions that include a dependence on Gibbs energy or saturation state, the reaction rate is given by Steefel et al. (2015) as follow:

$$R_m = \begin{cases} sgn[\Omega] A_m k_m \left(\prod a^n\right) \left|\exp\left(\frac{\eta \Delta G}{RT}\right) - 1\right|^m, & \Delta G < 0 \\ 0, & \Delta G > 0 \end{cases} \tag{2.28}$$

This equation can be applied to describe mineral reaction with only dissolution (or precipitation) and the reaction process in which the dissolution and precipitation rate laws are different.

For irreversible reactions without ΔG dependence, the reaction rate is expressed by:

$$R_m = A_m k_m \left(\prod a^n\right) \tag{2.29}$$

In addition to the above pore fluid-mineral reactions, microbially mediated mechanisms (mostly biological redox reactions) might be also included in some special cases such as bioremediation and underground hydrogen storage. The relevant numerical formulations can be found in Maggi et al. (2008) and Hagemann (2018).

2.2.2 Fluid flow and solute transport

(1) Multiphase flow

Variably saturated flow can be described using the full set of multiphase flow and conservation equations. For each component j in phase α, the component conservation equation (Steefel et al., 2015) can be expressed by:

$$\frac{\partial[\phi \sum_\alpha \rho_\alpha S_\alpha Y_{j\alpha}]}{\partial t} = \nabla \cdot \left[-\sum_\alpha \rho_\alpha Y_{j\alpha} \frac{k_{ra} k_{sat}}{\mu} (\nabla P - \rho_\alpha \mathrm{g} e_z) \right] + \rho_\alpha Q_j \tag{2.30}$$

Where ϕ is the porosity, ρ_α is the density of phase α, S_α is the phase saturation, $Y_{j\alpha}$ is the mass fraction of component j in phase α, t is time, $\nabla\cdot$ is the divergence operator, k_{ra} is the relative permeability, k_{sat} is the permeability for fully saturated conditions, μ is the dynamic viscosity, ∇P is the fluid pressure gradient, g is the acceleration of gravity, e_z is a unit vector in the vertical direction and Q_j is the volumetric source term.

Alternatively, if hysteresis is not taken into account, the variably saturated flow can be also described via Richards equation (Panday et al., 1993). In this case, the assumption of a passive air phase is valid, and the equation is given by:

$$S_a S_s \frac{\partial h}{\partial t} + \phi \frac{\partial S_a}{\partial t} = \nabla \cdot [k_{ra} \mathrm{K} \nabla h] + Q_a \tag{2.31}$$

Where S_a is the saturation of aqueous phase, S_s is the specific storage coefficient and h is the hydraulic head calculated by:

$$h = z + \frac{P}{\rho_f \mathrm{g}} \tag{2.32}$$

Where z is the depth and ρ_f is the fluid density. Another variable K in Eq. 2.31 is defined as hydraulic conductivity tensor and can be calculated by:

$$\mathrm{K} = \frac{k_{sat} \rho_f \mathrm{g}}{\mu} \tag{2.33}$$

On the other hand, for a single-phase flow that can be regarded as a special case of multiphase flow, the equation for fluid continuity (Steefel et al., 2015) is written as:

$$\frac{\partial[\phi\rho_f]}{\partial t} = \nabla \cdot \left[\rho_f q\right] + \rho_f Q_a \tag{2.34}$$

Where q is the volumetric flux (or Darcy flux) of water and is defined in terms of the fluid pressure gradient:

$$q = \phi v = -\frac{k_{sat}}{\mu}[\nabla P - \rho_f g e_z] \tag{2.35}$$

Where v is the pore velocity with common units of meter per second, and other variables are as defined above.

In addition to the above typical component conservation equations, relative permeability and saturation formulations are also essential to fully describe the flow system. The hydraulic functions, which involve the relative permeability, capillary pressure and aqueous phase saturation, in modern reactive transport simulators are mostly standard, and can be further found in Xu et al. (2004) and Steefel et al. (2015).

(2) Molecular diffusion

In addition to Darcy flow, chemical solutes in porous media can be also transported through diffusion and dispersion. Molecular diffusion refers to the thermal motion of all (liquid or gas) particles at temperatures above absolute zero. According to the Fick's first law, the diffusion flux of a chemical species in solution is proportional to the concentration gradient:

$$J_j = -D_j \nabla C_j \tag{2.36}$$

Where J_j is the diffusive flux of the j-th species, D_j is the diffusion coefficient and C_j is the concentration. For the case of a certain volume, this relationship can be expressed by the Fick's second law derived through integrating the diffusive fluxes over a control volume:

$$\frac{\partial C_j}{\partial t} = -\nabla \cdot \left[J_j\right] = \nabla \cdot [D_j \nabla C_j] \tag{2.37}$$

Which provides an expression for the change in concentration in terms of the divergence of the diffusive flux.

In porous media, the above relationships expressed by Fick's law should be corrected by considering the tortuosity in porous media. The tortuosity (Bear, 1972) is defined by:

$$T_L = (\frac{L}{L_e})^2 \tag{2.38}$$

Where the T_L is the tortuosity, L and L_e are the path lengths the solute would follow in water alone and in actual porous media, respectively. With this, the diffusion coefficient in porous media is corrected as:

$$D_i^* = T_L D_i \tag{2.39}$$

And the diffusive flux can be written as:

$$J_i^{diff} = -\phi D_i T_L \nabla C_i = -\phi D_i^* \nabla C_i \tag{2.40}$$

Where D_i^* and J_j^{diff} are the diffusion coefficient and the diffusive flux for species i in porous media, respectively.

It's worth noting that the Fick's law is the simplest way to treat molecular diffusion and is a strictly phenomenological relationship. By combining with the Nernest-Planck equation, Steefel et al. (2015) given a more rigorous formulation that considers the gradient in chemical potential as the driving force for diffusion:

$$J_j = -D_j \nabla C_j - \frac{z_i F}{RT} D_i C_i \nabla \psi - D_j C_j \ln \gamma_j \tag{2.41}$$

Where z_i is the species charge, F is the Faraday's constant, T is the temperature in Kelvin, ψ is the electrical potential and γ_j is the activity coefficient. Specifically, on the right hand side, the first term is the Fickian diffusion term as defined in Eq. 2.36; the second term denotes the gradient in electrostatic potential that commonly result from the diffusion of charged species at different rates, and the last term indicates the contribution from gradients in activity coefficients (Steefel et al., 2015).

(3) Mechanical dispersion

Mechanical dispersion (also called hydraulic dispersion) refers to the process whereby solutes are mechanically mixed by velocity variations at the microscopic level during advective transport. Mathematically, mechanical dispersion is defined as the product of the fluid velocity and dispersivity (Bear, 1972):

$$\begin{aligned} D_L &= \alpha_L V_i \\ D_T &= \alpha_T V_i \end{aligned} \tag{2.42}$$

Where D denotes the mechanical dispersion, α is the dispersivity, V_i is the average velocity in

the principal direction of flow, subscripts L (longitudinal) and T (transverse) label the dispersion parallel and perpendicular to the principal direction of flow, respectively. Further, the dispersion tensor can be also expressed using tensorial index notation, as follow (Steefel et al., 2015):

$$D_{ij} = \alpha_T \bar{V} \delta_{ij} + (\alpha_L - \alpha_T) \overline{V_i V_j} \Big/ \bar{V} \tag{2.43}$$

Where $\bar{V}$ is the average velocity magnitude, δ_{ij} is the Kronecker delta, and $\overline{V_i}$ and $\overline{V_j}$ are the velocity magnitudes in the I and J coordinate directions, respectively.

(4) Reactive transport equation

By combining the transport and chemical reaction network terms, Steefel et al. (2015) provided a general form of reactive transport equation that is applicable for most of the geochemical reactions in porous media:

$$\frac{\partial(\phi S_L C_i)}{\partial t} = \nabla \cdot (\phi S_L D_i^* \nabla C_i) - \nabla \cdot (q C_i) - \sum_{r=1}^{N_r} \upsilon_{ir} R_r - \sum_{m=1}^{N_m} \upsilon_{im} R_m - \sum_{l=1}^{N_g} \upsilon_{il} R_l \tag{2.44}$$

Where the accumulation term (on the left hand side of the equation) is expressed as the product of the porosity ϕ, liquid saturation S_L and species concentration C_i. On the right hand side of the equation, the first and the second terms describe the solute transport via diffusion and Darcy flow, respectively. The last three terms are reaction terms, representing the aqueous reactions R_r, mineral reactions R_m and gas reactions R_l, respectively.

Given the possibility of equilibrium aqueous complexation reactions, it is sometimes necessary to use a total concentration Ψ_i (Eq. 2.21) instead of aqueous concentration C_i for the Eq. 2.44. Moreover, the treatment of diffusion using Nernst-Planck equation might be also selected, and in this case the Fickian treatment of diffusion (the first term on the right hand side) in Eq. 2.44 can be replaced by the Nernst-Planck equation (Eq. 2.41).

2.2.3 Reaction-induced porosity and permeability changes

(1) Porosity changes

The feedback of geochemical reactions (particularly mineral dissolution and precipitation) on the fluid flow and solute transport processes in porous media is considered in most modern

reactive transport simulators. This feedback is normally achieved by recalculating the porosity and permeability at each time step as the porosity of the medium is directed associated with the mineral volume changes during dissolution-precipitation processes. Usually, the rock porosity ϕ is calculated by:

$$\phi = 1 - \sum_{m=1}^{N_m} \phi_m \tag{2.45}$$

Where N_m is the number of minerals and ϕ_m is the volume fraction of m-th mineral in the rock.

(2) Fracture permeability changes

Porosity-permeability co-evolution due to mineral reactions is an ongoing research so as to be applicable for various complicated natural geo-systems (e.g., Kaufmann, 2016; Worthington et al., 2016; Menke et al., 2021). Generally, the porosity-permeability relationship can be treated differentially in terms of fracture and matrix permeability changes.

The simplest treatment of fracture permeability changes as a result of mineral reactions is the cubic law (Steefel and Lasaga, 1994), which depends solely on porosity changes:

$$k = k_i(\frac{\phi}{\phi_i})^3 \tag{2.46}$$

Where k is the modified permeability, k_i and ϕ_i are the initial permeability and porosity, respectively. This cubic law is proposed based on an assumption of plane parallel fractures of uniform aperture and yields zero permeability only under the condition of zero fracture porosity.

However, in some natural geo-systems, preferential precipitation of minerals in micropores or narrower interconnecting apertures (i.e., pore-size dependent precipitation; Stack, 2015) would result in extremely low permeability values (near zero) whereas the porosity is rarely decreased (obvious greater than zero). In this case, the cubic law (Eq. 2.46) is not applicable. To address this, an improved porosity-permeability relationship, which considers the effect of fracture aperture changes, was developed (Xu et al., 2004):

$$k' = \frac{(b_{0,h} + \Delta b)^3}{12s} \tag{2.47}$$

Where k' is the permeability resulted from a change of hydraulic aperture, Δb is the aperture change as a result of mineral dissolution/precipitation, and $b_{0,h}$ is the initial hydraulic aperture

that can be approximated by:

$$b_{0,h} = [12k_0 s]^{1/3} \tag{2.48}$$

Where k_0 and s are the initial fracture permeability and spacing, respectively, and can be determined by air-permeability measurements.

(3) Matrix permeability changes

In reactive transport simulators, the porosity-permeability relationship for the rock matrix is commonly described using the Kozeny-Carman equation (Bear, 1972):

$$k = k_i \frac{(1-\phi_i)^2}{(1-\phi)^2}\left(\frac{\phi}{\phi_i}\right)^3 \tag{2.49}$$

Where the variables are as defined in the above Eq. 2.46.

Although the Kozeny-Carman relation has been effectively employed in some homogeneous and simplified geological media, laboratory and field studies have gradually suggested that there are some major limitations with respect to the this equation since it fails to reflect the potential influences of pore space geometry, connectivity, and the distribution of precipitates, etc. To accurately evaluate the matrix permeability changes with variation of porosity in more complex geological media, Verma and Pruess (1988) introduced three additional parameters and provided an improved porosity-permeability relationship as follow:

$$\frac{k-k_c}{k_i-k_c} = \left(\frac{\phi-\phi_c}{\phi_i-\phi_c}\right)^\tau \tag{2.50}$$

Where k_c and ϕ_c represent the asymptotic values of permeability and porosity, which are the lowest values to which these parameters can be reduced by increasing the confining pressure (Verma and Pruess, 1988). For example, when the permeability reduces to zero due to full occlusion by precipitates in pore throats, the ϕ_c is the critical value of porosity (disconnected pore spaces) at which permeability goes to zero (Xu et al., 2004). The superscript τ is a power law exponent. Generally, parameters k_c, ϕ_c and τ are geological media-dependent and can be determined experimentally.

2.3 TOUGHREACT simulator

In this study, modeling of fluid-rock interactions associated with carbonate diagenesis was

performed using the reactive transport computer code TOUGHREACT_V1.2 (Xu et al., 2004). It was developed on the basis of the existing multiphase fluid and heat flow code TOUGH2 by introducing a reactive geochemistry module and coupling thermo-hydro-chemical processes. The TOUGHREACT was developed by the Earth Sciences Division, Lawrence Berkeley National Laboratory, and the primary code was released by the Energy Science and Technology Software Center (ESTSC) of U.S. Department of Energy (DOE) in 2004. In general, the TOUGHREACT is a comprehensive non-isothermal multi-component reactive fluid flow and geochemical transport simulator, and can be applied to one-, two- or three-dimensional porous and fractured media with physical and chemical heterogeneity.

Four major processes are involved in the multiphase fluid flow and heat transfer, including: (1) pressure-, viscosity- and gravity-driven fluid flow in liquid or gas phases; (2) interactions between different flowing phases that are expressed by relative permeability and capillary pressure curves; (3) heat transfer by conduction and convection and (4) diffusion of water vapor and air. For thermophysical and geochemical properties calculation, the density and viscosity of the fluid (both liquid and gas phases) and the thermodynamic and kinetic data controlling mineral-water-gas reactions are regarded as functions of temperature. Advection-molecular diffusion transport of the aqueous ions and gaseous components are also considered in the multiphase flow. In terms of the chemical process, a variety of reactions, which include aqueous complexation, acid-base, redox, gas dissolution/exsolution, and cation exchange are involved at local equilibrium state. Notably, either thermodynamically or kinetically controlled reaction can be selected to perform mineral dissolution and precipitation. Linear adsorption and decay of chemical species can be also included.

Due to a wide temperature range (typical 0 to 300 °C) in the thermodynamic database and the flexibility of thermodynamic data expansion without code modification, the model can deal with a variety of subsurface geo-processes that proceed under conditions of wide ranges of temperature, pressure, water saturation and ionic strengths. To date, the TOUGHREACT has been successfully employed to investigate numerous reactive fluid and geochemical issues including carbon dioxide geological sequestration (Xu et al., 2006; Liu et al., 2015), nuclear

waste disposal (Xu et al., 2003; Sonnenthal et al., 2005), geothermal energy development (Seol and Lee, 2007; Taron et al., 2009), diagenesis in sedimentary rocks (Whitaker and Xiao, 2010; Yang et al., 2017), contaminant transport and remediation (Arora et al., 2015), groundwater quality assessment (Schwartz, 2012, 2015), biogeochemistry (Maggi et al., 2008; Ajami and Gu, 2010) and petroleum development (Zhang et al., 2019; Lu et al., 2020).

2.3.1 Governing equations

Based on the user's guide of this reactive geochemical transport code provided by Xu and Pruess (1998) and Xu et al. (2004), the main numerical models and governing equations associated with dolomitization and karstification of carbonate rocks are summarized as follows, which couple the fluid-heat flow, solute transport, chemical reactions and porosity-permeability changes processes.

(1) Fluid-heat flow and chemical transport

In TOUGHREACT, the governing equations of fluid-heat flow and chemical transport are generally derived from the principles of mass conservation and energy conservation and thus have similar structures. In a flow system, the changes in the basic mass (i.e., water, air and chemical components) and energy (i.e., heat) of an arbitrary domain equals the sum of the flux from connecting domains and the external injection (or withdrawal) source:

$$\frac{d}{dt}\int_{V_n} M^{\kappa} dV_n = \int_{\Gamma_n} F^{\kappa} \cdot n d\,\Gamma_n + \int_{V_n} q^{\kappa} dV_n \tag{2.51}$$

Where V_n [m^3] is the control volume for an arbitrary domain, κ is the basic mass/heat component, M^{κ} is the mass or heat accumulation, F^{κ} is the mass or heat flux, Γn [m^2] is the closed surface of Vn and q^{κ} is the source or sink term.

This model has been discussed in detail by Pruess et al. (1999) to describe the multiphase fluid and heat flow within porous media in reservoirs. In the case of fluid flow, assuming that the basic mass components are uniformly distributed in all phases, the mass accumulation of component κ is the sum of the masses of this component in each phase:

$$M^{k} = \phi \sum_{\beta} S_{\beta} \rho_{\beta} X_{\beta}^{\kappa} \tag{2.52}$$

Where M^{κ} [kg/m^3] is the mass accumulation, ϕ [-] is the porosity, β is the phase index, S_{β} [-] is the saturation of phase β, ρ_{β} [kg/m^3] is the density of phase β and X_{β}^{κ} [-] is the mass fraction of component κ in phase β.

According to the Darcy's law, assuming that the various components in a specific phase are completely mixed and have the same velocity, the mass flux of phase β can be described as follows:

$$F_{\beta} = \rho_{\beta} u_{\beta} = -k \frac{k_{r\beta} \rho_{\beta}}{\mu_{\beta}} \left(\nabla P_{\beta} - \rho_{\beta} \mathrm{g} \right) \tag{2.53}$$

Where u_{β} [m/s] is the Darcy velocity of phase β, k and $k_{r\beta}$ [m^2] are the absolute permeability and relative permeability of phase β, respectively, μ_{β} [kg/(m·s)] is the viscosity of phase β, P_{β} [Pa] is the fluid pressure of phase β and g [m/s^2] is the gravitational acceleration.

Hence, the total mass flux F^{κ} [kg/(m^2·s)] of component κ can be calculated by summation of the individual mass fluxes in various phases based on the mass fraction of component κ in each phase:

$$F^{\kappa} = \sum_{\beta} X_{\beta}^{\kappa} F_{\beta} \tag{2.54}$$

In terms of chemical solute transport, the transport equation is expressed using the total dissolved concentrations of chemical components that are concentrations of their basis species plus their associated aqueous secondary species (Walter et al., 1994; Xu et al., 2004), as follows:

$$\mathrm{M}_j = \phi S_l C_{jl} \tag{2.55}$$

Where j is the aqueous chemical component, M_j [mol/L] is the total dissolved concentration of j, S_l [-] is the saturation of liquid and C_{jl} [mol/L] is the component concentration of j in the liquid phase.

In the liquid phase, advection and diffusion of aqueous species are the major processes involved in chemical transport. Assuming that the diffusion coefficient of a specific liquid phase is identical for all aqueous species, the flux of component concentration for an arbitrary domain can be expressed as follows:

$$F_j = u_l C_{jl} - (\tau \phi S_l D_l) \nabla C_{jl} \tag{2.56}$$

Where F_j [mol/(m^2·s)] is the flux of concentration for component j, u_l [m/s] is the Darcy velocity of the liquid phase, D_l [m^2/s] is the diffusion coefficient of the liquid phase and τ is a tortuosity factor accounting for the complex geometry of the flow through the pores. Generally, the medium tortuosity is relevant to the porosity and saturation of the phase and has been empirically given by Millington and Quirk (1961):

$$\tau_\beta = \phi^{1/3} {S_\beta}^{7/3} \tag{2.57}$$

Where τ_β is the medium tortuosity of phase β, ϕ [-] is the porosity and S_β [-] is the saturation of phase β.

(2) Dissolution-precipitation of equilibrium/kinetic minerals

Both equilibrium and kinetic reactions are involved in the modeling of pore fluid-rock interactions. For equilibrium minerals, the mineral saturation index SI is generally used to describe the current state and trend of mineral dissolution/precipitation, with a positive value indicating precipitation and a negative value indicating dissolution. At equilibrium, this mineral saturation index equals zero:

$$SI_m = log_{10}\Omega_m = 0 \tag{2.58}$$

Where m is the equilibrium mineral index, SI_m is the mineral saturation index of mineral m and Ω_m is the equilibrium mineral saturation ratio, which can be expressed as follows:

$$\Omega_m = K_m^{-1} \prod_{j=1}^{N_C} c_j^{v_{mj}} \gamma_j^{v_{mj}} \qquad m = 1 \dots N_P \tag{2.59}$$

Where K_m is the equilibrium constant of mineral m, which is temperature-dependent, j is the aqueous basis species, N_c is the number of aqueous species as basis species (or component), c_j is the concentration of component j, superscript v_{mj} is the number of aqueous j components participating in the dissolution equilibrium equation of mineral m, γ is the thermodynamic activity coefficient and N_p is the number of equilibrium minerals.

In terms of kinetic minerals, the reaction rate is commonly calculated based on the kinetic work on water-rock interactions from Lasaga et al. (1994):

$$r_n = f\left(c_1, c_2, \dots, c_{N_C}\right) = \pm \overline{k_n} A_n \left|1 - \Omega_n^\theta\right|^\eta \qquad n = 1 \dots N_q \tag{2.60}$$

Where n is the mineral index for kinetic rate condition, r_n [mol/(m^2·s)] is the dissolution/precipitation rate of mineral n, which indicates dissolution when r_n>0 and precipitation when r_n<0, k_n [mol/(m^2·s)] is the rate constant of kinetic mineral n, A_n [m^2/kg H_2O] is the specific reactive surface area of mineral n per kg H_2O, and Ω_n is the kinetic mineral saturation ratio, which is defined the same way as Ω_m in (Eq. 2.59). Fitting parameters θ and η are empirically obtained from dissolution/precipitation experiments for specific kinetic minerals.

Given that abundant experimental data regarding the dissolution/precipitation of different minerals have been recorded at 25 °C, the temperature-dependent rate constant k can be generally approximated by the Arrhenius equation (Steefel and Lasaga, 1994):

$$k = k_{25}\exp\left[\frac{-E_a}{R}\left(\frac{1}{T}-\frac{1}{298.15}\right)\right] \tag{2.61}$$

Where k_{25} [mol/(m^2·s)] is the rate constant at 25 °C, E_a [J/mol] is the activation energy, R is the gas constant and T is the absolute temperature (in Kelvin).

However, given that this general form of the kinetic rate constant in (Eq. 2.61) is only well suited in pure water at neutral pH, dissolution/precipitation processes of different minerals might be affected by different reaction mechanisms (i.e., H^+-acid mechanism and OH^--base mechanism) (Lasaga et al., 1994; Palandri and Kharaka, 2004). Therefore, a modified kinetic rate constant $\bar{k}$ is involved in TOUGHTREACT, which considers three reaction mechanisms under neutral, acid and base conditions:

$$\begin{aligned}\bar{k} = {} & k_{25}^{\mathrm{nu}}\exp\left[\frac{-E_a^{\mathrm{nu}}}{R}\left(\frac{1}{T}-\frac{1}{298.15}\right)\right] + k_{25}^{\mathrm{H}}\exp\left[\frac{-E_a^{\mathrm{H}}}{R}\left(\frac{1}{T}-\frac{1}{298.15}\right)\right] a_{\mathrm{H}}^{n\mathrm{H}} \\ & + k_{25}^{\mathrm{OH}}\exp\left[\frac{-E_a^{\mathrm{OH}}}{R}\left(\frac{1}{T}-\frac{1}{298.15}\right)\right] a_{\mathrm{OH}}^{n\mathrm{OH}}\end{aligned} \tag{2.62}$$

Where superscripts or subscripts nu, H, and OH denote the reaction under neutral, acid and base mechanisms, respectively, a [mol/m^3] is the activity of the species and n is the power term (constant). Specifically, neutral and acid mechanisms are considered in the dissolution of dolomite in this study, and the parameters for calculating kinetic rate constants were taken from the EQ3/6 database (Wolery, 1992), which is concomitant with the simulation code.

(3) Porosity and permeability changes

Constraining porosity-permeability changes is a major focus of research on fluid-rock interactions during carbonate diagenesis. The dissolution and precipitation of minerals directly determine the variation in porosity-permeability and the reservoir quality. Meanwhile, this variation in rock permeability would provide prompt feedback on the pore fluids, resulting in heterogeneous flow pathways and progressively complicated fluid-rock interactions. In TOUGHREACT, the porosity evolution is calculated according to the sum of changes in the volume fraction of each reactive mineral:

$$\phi = 1 - \sum_{m=1}^{nm} fr_m - fr_u \tag{2.63}$$

Where ϕ [-] is the porosity, nm is the number of minerals, fr_m [-] is the volume fraction of mineral m in the rock and fr_u [-] is the volume fraction of nonreactive rock.

Under natural geological conditions, the relationship between the porosity and permeability of reservoir rocks is complex and generally controlled by numerous factors, such as the pore distribution and the size, shape and connectivity of pore throats. Fortunately, a variety of numerical models have been proposed to describe the permeability evolution in karst aquifers using different matrix- or fracture-flow contributions (Kaufmann et al., 2010; Kaufmann, 2016; Gong et al., 2019). In this study, a classical porosity-permeability equation is adopted to estimate the change in permeability with porosity variation based on the Kozeny-Carman relation:

$$k = k_i \frac{(1-\phi_i)^2}{(1-\phi)^2}\left(\frac{\phi}{\phi_i}\right)^3 \tag{2.64}$$

Where k [m^2] is the permeability over time, k_i [m^2] is the initial permeability and ϕ_i [-] is the initial porosity.

2.3.2 Solution method

Referring to Xu et al. (2004), the calculation flow chart of coupled processes of non-isothermal multiphase fluid flow, solute transport and chemical reactions in TOUGHREACT is illustrated in Figure 2.7. Specifically, the computational processes for numerical solution of multiphase

flow and heat transfer are the same as in TOUGH2, with space discretization method of integral finite difference (IFD). Figure 2.8 shows the space discretization and geometric parameters for the IFD method. This approach has the major advantage to deal with systems with irregular grids, and is suitable to proceed fluid-heat flow and chemical transport processes within heterogeneous porous or fracture media at multiple dimensions (Pruess et al., 1999).

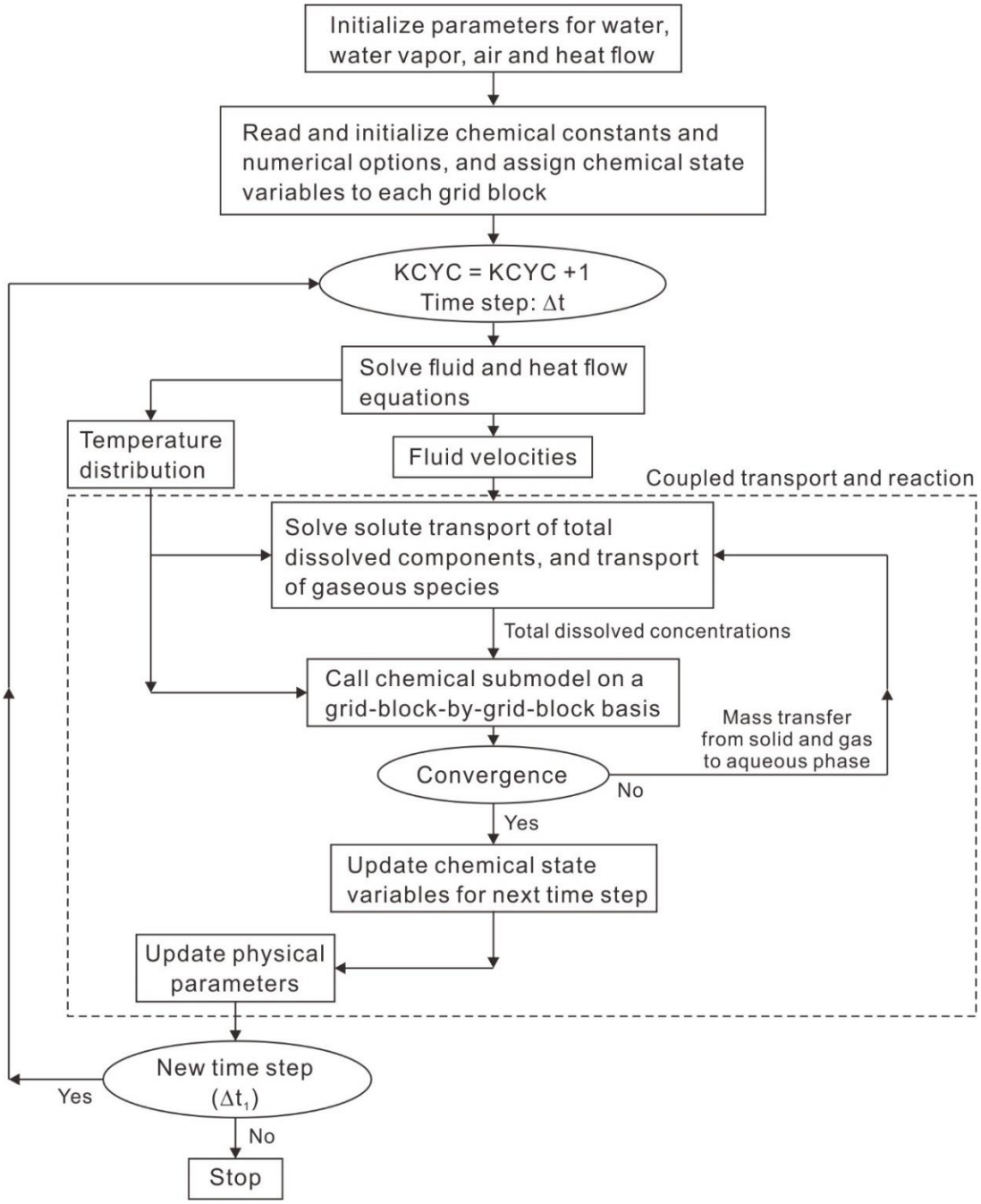

Figure 2.7 Flow chart of the TOUGHREACT program (Xu et al., 2004).

As mentioned above, the governing equations for fluid-heat flow and chemical transport have similar structures (derived from the principles of mass conservation and energy conservation),

and thus both of them can be solved by the same numerical method. For IFD method, the mass and energy conservation equations for an arbitrary domain can be written in an integral form as follow:

$$V_n \frac{\Delta M_n}{\Delta t} = \sum_m A_{nm} F_{nm} + V_n q_n \tag{2.65}$$

Where subscript n labels an arbitrary grid block in the system, subscript m labels an arbitrary grid block connected with grid block n, Vn is the volume of grid block n, M_n is the mass (for water, air and chemical components) or energy (for heat) density of grid block n, Δt is the time step, A_{nm} is the contact surface area between grid blocks n and m, F_{nm} is the mass and energy flux over surface segments A_{nm} and q_n is the average source/sink rate in grid block n per unit volume (Fig. 2.8).

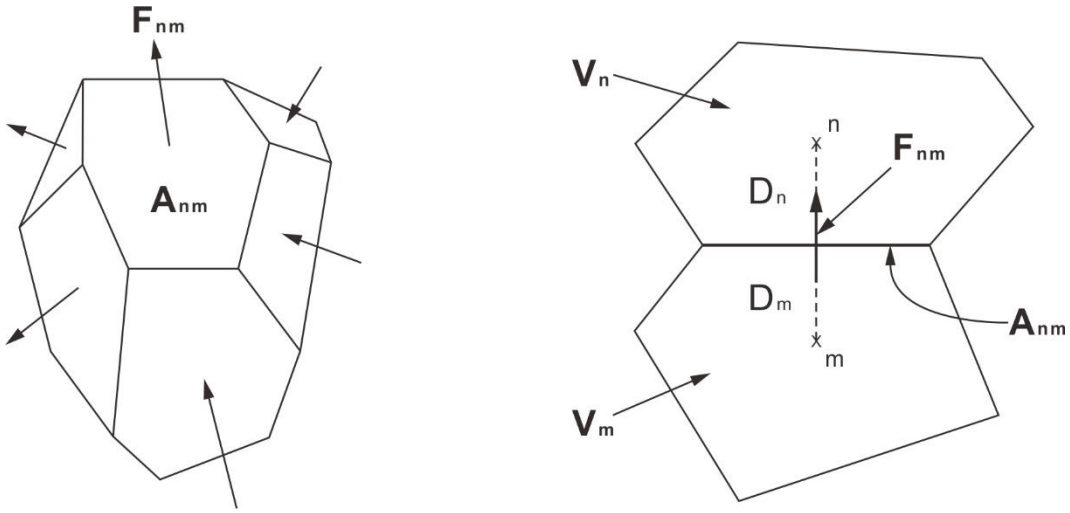

Figure 2.8 Space discretization and geometric data for the integral finite difference method (Xu et al., 2004).

For numerical solution of the coupled thermo-hydro-chemical processes, the thermodynamic and hydrodynamic calculations are fully coupled, while the chemical calculation are partially coupled. During simulation, time discretization is achieved by first-order fully implicit finite difference method, which helps to avoid unreasonable time step limit during multiple phases flow and to achieve unconditional stability (Pruess et al., 1999). The multiphase fluid flow and heat transfer are solved in the original TOUGH2 simulator using Newton-Raphson iteration. The chemical calculations, which comprises solution transport and geochemical reaction, are

implemented in TOUGHREACT simulator using a sequential iteration approach (SIA) or a sequential non-iterative approach (SNIA) (Xu et al., 2004).

To be specific, within a time step, the multiple phases fluid flow and heat transfer processes are firstly calculated according to the thermo-hydro fully coupled flow equations. Subsequently, the obtained results (i.e., fluid velocities and phase saturations) are employed for solving chemical transport process component-by-component including solute transport of total dissolved components and transport of gaseous species. After solution of the transport equations, the dissolved concentrations of aqueous species are obtained and then substituted into the chemical reaction submodel to solve the equilibrium/kinetic reaction equations on a grid block-by-grid block basis. The chemical transport and reactions are solved iteratively until convergence. Ultimately, the changes of physical parameters, such as the concentrations of aqueous and gaseous species and the porosity-permeability of geological media, will provide feedback to the fluid flow and heat transfer processes for the next time step. As such, the coupling process of thermo-hydro-chemical domains (THC) is achieved. To avoid duplication, detailed numerical procedures on the space/time discretization and iteration approach are not elaborated in the present dissertation as they have been discussed in detail by Pruess et al. (1999) and Xu et al. (2004).

3 Reflux dolomitization in evaporated seawater environment

3.1 Basic idea

Dolomitization is a geological process by which the carbonate mineral dolomite ($MgCa(CO_3)_2$) is formed when magnesium ions replace calcium ions in another carbonate mineral, calcite ($CaCO_3$) (Hardie, 1987). It is common for this mineral alteration into dolomite to take place due to evaporation of water in various geological environment (e.g., the sabkha area, salt lake and high-salinity seawater). The dolomite problem, as mentioned in Section 2.1.2, has been a long-standing enigma and intensively debated focus in sedimentology and petroleum geology. Over the past two centuries, continuous progress has been made to enrich the research methods of dolomite from petrography, geochemistry, microthermometry, laboratory experiments to numerical modelling. Accordingly, significant theoretical progress has been made regarding the genetic models of dolomite in geological formations, the nature of dolomitization fluids and its favorable developmental conditions (e.g., Badiozamani, 1973; Arvidson and Mackenzie, 1999; Warren, 2000; Wang et al., 2014; Budd and Park, 2018). Besides, the dolomitization process itself is also of great significance in the field of petroleum geology (carbonate reservoir exploration). Due to the fact that the radius of Mg^{2+} is smaller than that of Ca^{2+}, the process of calcite ($CaCO_3$) replaced by dolomite ($MgCa(CO_3)_2$) can be volume-decreased under specific hydrogeochemical conditions (Huang et al., 2017). As such, a number of intercrystalline micropores can be generated in the newly formed dolostone, serving as favorable hydrocarbon reservoir spaces (Fig. 3.1). According to global statistics, dolostone reservoir accounts for more than half of the carbonate reservoirs in the world.

Nevertheless, a few controversies and uncertainties still remain to date, such as the contribution of mixed-water dolomitization and microbial dolomitization (Gregg et al, 2015; Kaczmarek et al., 2017), the various porosity evolution during dolomitization under different hydrogeochemical systems (Schmoker and Halley, 1982; Cantrel et al., 2004; Jiang et al., 2016) and quantitatively constraining the spatial and temporal distribution of dolomite and concomitant gypsum/anhydrite (Gabellone et al., 2016; Yang et al., 2020).

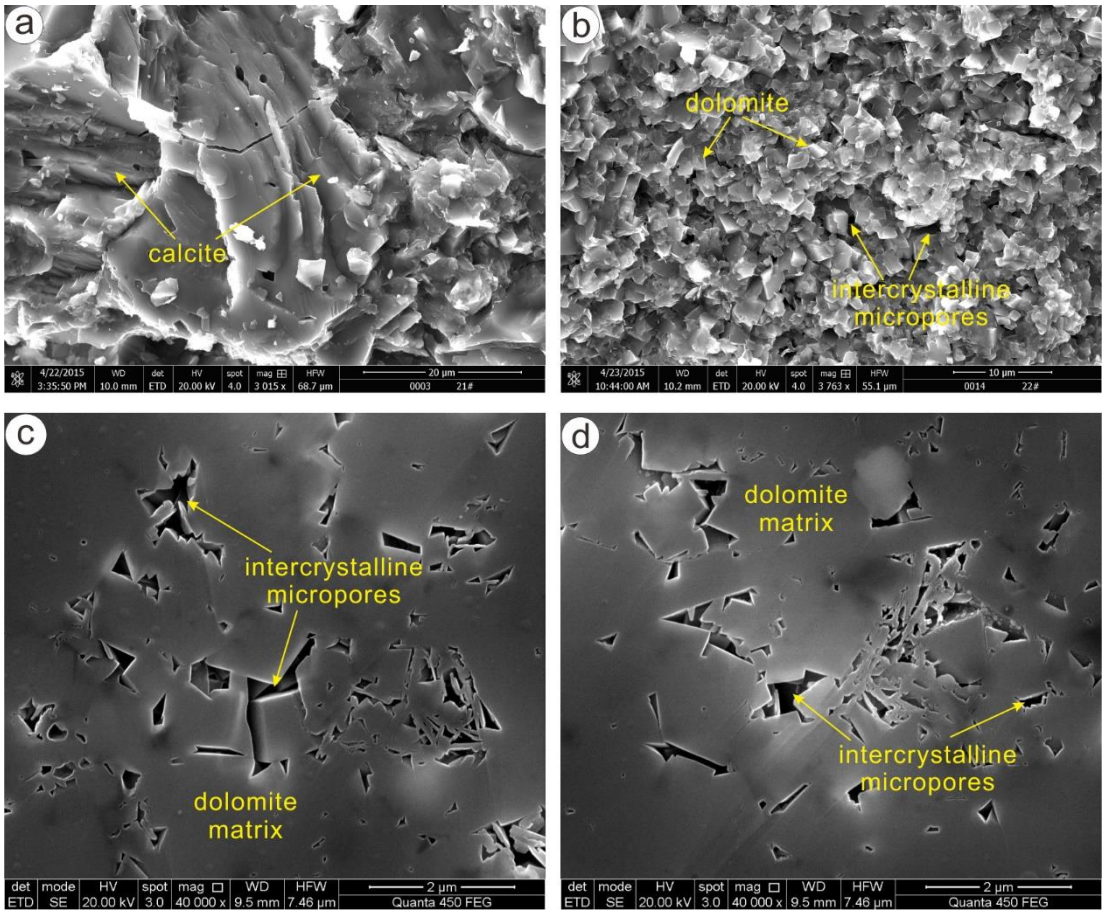

Figure 3.1 SEM photographs showing the micro-characteristics of (a) calcite, (b) dolomite and (c–d) intercrystalline micropores formed during seepage reflux dolomitization (argon ion-beam polishing of the surface). The samples are from the Paleogene lacustrine dolomite reservoir, Qaidam Basin, China, provided by PetroChina Qinghai Oil Field Company.

As an emerging method for reservoir diagenesis study, reactive transport modelling (RTM) has been proved to be effective for assessing the impact of fluid-rock interactions on reservoir quality at multiple spatial and temporal scales (Yang et al., 2015, 2017). The application of RTM in dolomitization almost covers all the genetic models, including reflux model (Jones and Xiao, 2005), geothermal convection model (Whitaker and Xiao et al., 2010), mixed-water model (Cooper et al., 2014) and fracture-controlled hydrothermal model (Gomez-Rivas et al., 2014). Generally, different sedimentary environments have diverse hydrogeological conditions and fluid circulation regimes, which ultimately result in complicated distributions and geometries of the diagenetic bodies. The water properties and atmospheric environment also vary with geological times. Thus, a persistent challenge for RTM simulation of reservoir diagenesis is the contradiction between the complexity of rock texture and solute transport in

natural systems with the simplification of generic models.

Although multiple dolomitization models have been investigated by RTM simulations, the reflux model has attracted special attention since its extensive forming environments and accounting for the majority of the widespread dolomite in geological history. Previous studies have mainly focused on relatively large-scale environments such as epeiric ramp and platform margin (Jones et al., 2004; Al-Helal et al., 2012; Gabellone et al., 2016). Less attention has been paid to the reflux system of alternating shoal-lagoon facies within an evaporative intra-platform basin. Affected by regional climatic and sea level fluctuations, the intra-platform basin could be sensitive to high-frequency transgression-regressions (Mitchum and Wagoner, 1991; Xiong et al., 2019, 2022), which resulted in cyclic superposition of deposition sequences with various lithology and rock textures. In this case, the reflux of brines (i.e., concentrated seawater) would be easily affected by the meter-scale depositional sequences and potential impermeable layers (e.g., mudstone and gypsum rocks). In a few seminal numerical studies, the brine was usually specified as of single-source with a constant position and injection rate, which failed to reflect the migration and evolution of brine source caused by sea level fluctuations and sediment aggradation in natural systems. Besides, the dolomite produced by reflux model was generally thought to be continuous and stratigraphically accordant. Simulation results of Lu and Cantrell (2016), however, suggested the heterogeneous occurrence of non-stratigraphic dolostone in reflux model due to progressive migration of evaporation pond towards deeper intra-shelf basin.

Obviously, the dolomitization process is complicated and the influencing mechanisms of diverse geological factors still need further exploration. Therefore, to lay a foundation for further elaborate RTM simulations within specific geological sittings, a simplified column model is necessary as a basis for evaluating the impacts of diverse extrinsic/intrinsic geological factors on the dolomitization process. The results would help to understand the relationships between sedimentology, hydro-geochemistry and dolomitization.

3.2 Model setup and parameters

3.2.1 Kinetic process of dolomitization

According to thermodynamic theories, the precipitation/dissolution of dolomite ($CaMg(CO_3)_2$) can be discriminated by comparing its ion activity product ($Q = [Ca^{2+}][Mg^{2+}][CO_3^{2-}]^2$) with solubility product constant (K_{sp}), and the dolomite tends to precipitate when $Q > K_{sp}$ while to be dissolved when $Q < K_{sp}$. To be specific, Hsu (1962) and Hardie (1987) gave the estimated K_{sp} values for stoichiometric dolomite and disordered dolomite of about 10^{-17} and $10^{-16.5}$, respectively. The steady-state dolomite ion activity product (Q) of modern seawater is approximately$10^{-15.01}$. Obviously, the modern seawater is thermodynamically supersaturated with respect to dolomite (the ion activity product is one to two orders of magnitude larger than solubility product constant) and dolomite should spontaneously precipitate from the seawater. However, dolomite is rarely found in modern seawater except in some extremely saline environments with the participation of microbial induced mineralization (Dupraz et al., 2009). Moreover, Land (1998) conducted a bench-scale synthesis experiment of dolomite under low-temperature conditions (25°C, 1 atm), but failed to precipitate dolomite from dilute solution despite 1000-fold oversaturation after 32 years. These facts have dramatically improved our understanding of the formation of dolomite and have indicated that the dolomitization process is largely kinetically controlled.

Sustained works on the dolomitization mechanism have further suggested that the dolomite precipitation is strongly coupled with calcite dissolution. Machel (2004) speculated that the dolomitization occurs via calcite dissolution followed by dolomite precipitation. This is further evidenced by dolomite crystals growing on the edges and corners of dissolved calcite substrates (dissolution etch pits) observed in high-temperature synthesis experiment of dolomite (Kaczmarek and Sibley, 2007). Hence, the dolomitization process is usually treated as a reaction network in the RTM simulations with a pair of reactions (Whitaker and Xiao, 2010; Lu and Cantrell, 2016):

$$CaCO_3(Calcite) \Leftrightarrow Ca^{2+} + CO_3^{2-} \tag{3.1}$$

$$Ca^{2+} + Mg^{2+} + 2CO_3^{2-} \Leftrightarrow CaMg(CO_3)_2(Dolomite) \quad (3.2)$$

Given that the reflux dolomitization mostly occurs in saline seawater environments such as evaporative lagoon and salt-bearing basins, this process is usually accompanied by gypsum ($CaSO_4 \cdot 2H_2O$) precipitation and dissolution. Thus the sulfate cementation is also considered in the simulation, which occurs due to the combination of released Ca^{2+} from calcite dissolution and SO_4^{2-} in the solution:

$$Ca^{2+} + SO_4^{2-} + 2H_2O \Leftrightarrow CaSO_4 \cdot 2H_2O(Gypsum) \quad (3.3)$$

Consistent with previous RTM simulations of reflux dolomitization (Jones and Xiao, 2005; Gabellone and Whitaker, 2016), the dissolution and precipitation of calcite and gypsum are modeled as thermodynamic processes which are controlled by the saturation state of the dolomitizing fluid and the fluid-rock system equilibrates within an individual model timestep (Xu et al., 2004; Whitaker and Xiao, 2010). In contrast, given the relative abundance of dolomite (with regard to limestone) in geological history and the failure of bench-scale synthesis experiment of dolomite, the presence of kinetic barrier (Mg^{2+}-water complexes) have been recognized to be the primary cause that inhibits dolomite precipitation (Hardie, 1987; Warren, 2000; Zhang et al., 2012). Therefore, the precipitation of dolomite is generally modeled as a kinetic process and can be described using the general kinetic reaction rate law that is consistent with the rate expression proposed by Lasaga et al. (1994):

$$r = k_d A_s \left(1 - \frac{Q}{K_{eq}}\right)^q \quad (3.4)$$

Where r [mol/s] is the reaction rate, with positive values indicating mineral dissolution and negative values indicating precipitation; A_s [m^2/g] is the specific reactive surface area that depends on the different sizes and shapes of the mineral particle; Q is the ion activity quotient in the fluids and K_{eq} is the equilibrium constant of mineral and q is the reaction order generally determined by specific laboratory experiment; k_d [mol/(m^2·s)] is the rate constant that is temperature-dependent and can be expressed by the Arrhenius function:

$$k_d = Ae^{\frac{-E_a}{RT}} \tag{3.5}$$

Thus, the kinetic process for dolomite precipitation can be written as:

$$r_{dol} = A_s Ae^{-\left(\frac{E_a}{RT}\right)}\left(1 - \frac{Q}{K_{eq}}\right)^q \tag{3.6}$$

Where r_{dol} is the reaction rate of dolomite; A_s is the specific reactive surface area of dolomite; A is the pre-exponential factor and 11.2 mol cm^{-2} sec^{-1} is used here for dolomite according to previous RTM simulations (Gabellone and Whitaker, 2016); E_a is the activation energy (1.335 $\times 10^5$ J/mol); R is the universal gas constant; T is the temperature (in Kelvin); Q is the activity quotient in the fluids; K_{eq} is the equilibrium constant of dolomite and a value of 2.26 is used for the reaction order (q) of dolomite according to the dolomite precipitation experiment by Arvidson & MacKenzie (1999). Detailed thermodynamic data for aqueous species and minerals were taken from the EQ3/6 geochemical database (Wolery, 1992) which is concomitant with the simulation code (Xu et al., 2004).

3.2.2 Generic column model and rock properties

The reflux dolomitization was simulated in a simplified 1D grid system that represents the replacement of limestone by dolostone within a vertical column of porous carbonate sediments (Fig. 3.2). Specifically, in some evaporative environments such as restricted-evaporated lagoons and salt-bearing basins, intense evaporation and concentration of seawater would result in an increase in salinity and the formation of brine. The concentrated seawater (brine), which has relatively high density and Mg/Ca ratios, tend to migrate towards the deep basin and simultaneously seep into the initial limestone sediments, leading to reflux dolomitization (Warren, 2000). The 50-m-long vertical column, which comprises initial porous limestone sediments, is evenly discretized into 50 grid cells. Given that the reflux dolomitization might occur in diverse sedimentary microfacies, three types of lithofacies (i.e., grainstone, grain-dominated packstone and micrite), which has different rock-fabrics and initial porosities-permeabilities, were involved in the simulation. Nevertheless, the initial mineralogy of different rock types are the same, including 95% calcite ($CaCO_3$), 4% gypsum ($CaSO_4 \cdot 2H_2O$)

and 1% "seed" dolomite ($CaMg(CO_3)_2$) which provides primary nucleation sites for dolomite precipitation simulation.

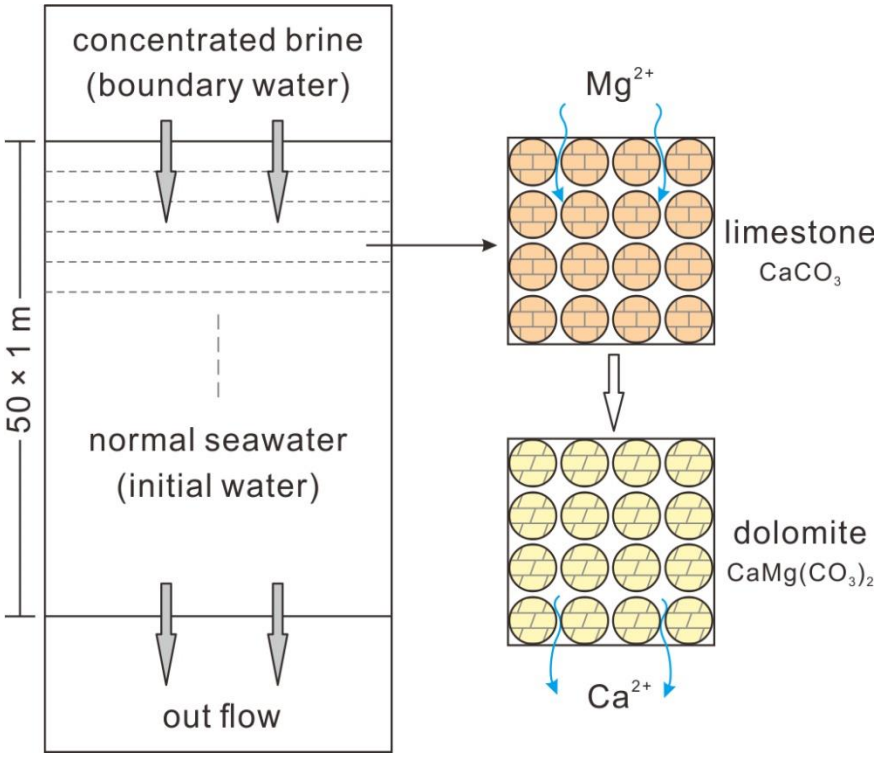

Figure 3.2 Schematic illustration of the 1D vertical column model showing the initial and boundary conditions of the grid system and the replacement of limestone by dolostone during dolomitization.

Although the current rock properties can be obtained by lab-measurement, the initial porosity and permeability of early sediments are significantly different from their current values due to a long period of compaction and diagenetic alteration. For RTM study of early dolomitization, the initial porosity-permeability data of the grid cells were generally specified as depositional porosity-permeability depending on various rock-fabrics (or textures) of the primary carbonate sediments (Al-Helal et al., 2012). To be specific, according to the rock-fabric petrophysical relationships (Lucia, 1995) and porosity-depth models (Ehrenberg and Nadeau, 2005; Al-Helal et al., 2012) for carbonate rocks (Fig. 3.3), an initial 47% porosity and 1.00×10^{-9} m^2 permeability were specified for grainstone; an initial 30% porosity and 3.85×10^{-12} m^2 permeability were specified for grain-dominated packstone; an initial 18% porosity and 1.00×10^{-13} m^2 permeability were specified for micrite (Table 3.1).

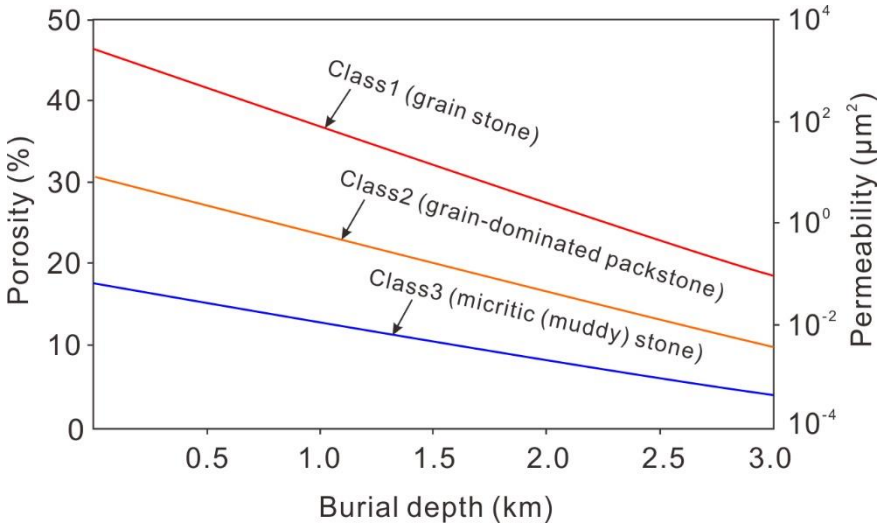

Figure 3.3 Depth-dependent initial porosity and permeability for different lithofacies and rock-fabrics (modified after Al-Helal et al., 2012).

Reactive surface area (RSA) is used in the code to initialize nucleation of kinetic minerals. Although there is currently no convincing data to precisely constrain the RSA of geological porous media, the RSA is generally assumed to be proportional to the average percentage of fines (fine fraction). Thus, the particle size and morphology of mineral can be used to estimate specific RSA in different rock textures (German and Park, 2009). In the simulation, the RSA of grainstone, grain-dominated packstone and micrite are assumed to be 100 $cm^2 g^{-1}$, 1000 $cm^2 g^{-1}$ (base case scenario) and 10000 $cm^2 g^{-1}$ (Table 3.1), which are representative of 250 μm, 25 μm and 2.5 μm-diameter dolomite rhombs, respectively (Gabellone and Whitaker, 2016).

Table 3.1 Initial porosity-permeability and reactive surface area of three types of lithofacies involved in the 1D simulation of reflux dolomitization.

Lithofacies & rock fabrics	Porosity (%)	Permeability (m^2)	Rock-fabric petrophysical relationship	RSA ($cm^2 g^{-1}$)
Grainstone	47.0	1.00×10^{-9}	Class 1	100
Grain-dominated packstone	30.0	3.85×10^{-12}	Class 2	1000
Micrite	18.0	1.00×10^{-13}	Class 3	10000

Note: the rock-fabric petrophysical relationship for carbonate rocks refers to Lucia (1995).

3.2.3 Hydrogeological conditions

Given that the reflux dolomitization mostly occurs in near-surface to shallow burial conditions, the initial temperature of the grid system can be assumed as sea surface temperature. An initial

30°C was specified for base case scenario and a few temperatures, i.e., 20, 40 and 50°C, were considered for sensitivity analysis. Meanwhile, similar with previous RTM studies (e.g., Al-Helal et al., 2012; Gabellone and Whitaker, 2016), the grid system was assumed to be initial saturated with modern seawater (initial water; salinity of 35‰), representative of the primary pore fluid sealed in carbonate sediments. The boundary water were specified as four types of modern brine sampled from surface water in several modern saline environments (Table 3.2). Specifically, chemical composition of the Ralph Sink brine (salinity of 186‰) was used for the base case scenario, and other brines (salinity range of 48–249‰) were involved in sensitivity analysis, representative of different evaporation intensities that affect the dolomitization process. The saturation indices (Log *Q/K*) with regard to the major carbonate and evaporite minerals in different brines are also documented in Table 3.2, obtained from the calculation by Bethke (1998); Jones and Xiao (2005) and Al-Helal et al. (2012).

Table 3.2 Chemical compositions and mineral saturation indices of initial and boundary water used for 1D dolomitization simulation.

Component (mol L^{-1})	Initial water	Boundary water I	Boundary water II	Boundary water III	Boundary water IV
Sources	Modern seawater	Cygnet Pond	Ibis Pond	Ralph Sink	Phreatic Majanna
Na^+	$4.85e^{-1}$	$6.74e^{-1}$	$1.26e^{0}$	$3.18e^{0}$	$4.45e^{0}$
Cl^-	$5.66e^{-1}$	$8.03e^{-1}$	$1.46e^{0}$	$3.70e^{0}$	$5.35e^{0}$
K^+	$1.06e^{-2}$	$1.28e^{-2}$	$2.56e^{-2}$	$6.56e^{-2}$	$1.04e^{-1}$
Ca^{2+}	$1.07e^{-2}$	$1.22e^{-2}$	$2.44e^{-2}$	$2.22e^{-2}$	$1.22e^{-2}$
Mg^{2+}	$5.51e^{-2}$	$8.06e^{-2}$	$1.37e^{-1}$	$3.39e^{-1}$	$5.98e^{-1}$
HCO_3^-	$2.13e^{-3}$	$1.62e^{-3}$	$1.54e^{-3}$	$1.67e^{-3}$	$1.65e^{-3}$
SO_4^{2-}	$2.93e^{-2}$	$4.18e^{-2}$	$7.78e^{-2}$	$1.37e^{-1}$	$2.11e^{-1}$
Mg/Ca molar	5.1	6.6	5.6	15.3	48.9
pH	8.2	8.0	7.7	7.1	6.7
Salinity (‰)	35	48	85	186	249
Saturation index of minerals					
Calcite	0.78	0.26	0.32	-0.07	-0.49
Dolomite	3.51	2.48	1.74	1.46	1.22
Gypsum	-0.77	-0.92	-0.19	-0.08	-0.03

Data from Logan (1987), Bethke (1998), Jones and Xiao (2005) and Al-Helal et al. (2012).

In general, nine primary aqueous species (H_2O, H^+, Ca^{2+}, Mg^{2+}, Na^+, K^+, HCO_3^-, SO_4^{2-} and Cl^-) and eleven secondary aqueous species ($CaCO_3(aq)$, $CaHCO_3^+$, $CaOH^+$, $CaSO_4(aq)$, $CO_2(aq)$, CO_3^{2-}, HSO_4^-, $MgCO_3(aq)$, $MgHCO_3^+$, $MgOH^+$ and OH^-) were incorporated into the geochemical calculations. Moreover, different brine injection rates, which includes 0.2 m yr^{-1}, 0.5 m yr^{-1}, 0.8 m yr^{-1} (base case scenario) and 2.0 m yr^{-1}, were considered in the simulation to evaluate the influence of recharge capacity of brine on the dolomitization process. Detailed controlling parameters used for base case simulation and sensitivity analyses are summarized in Table 3.3 and Table 3.4, respectively.

Table 3.3 Controlling parameters used for base case simulation of 1D reflux dolomitization.

Parameters	Values (Source)
Initial porosity	30%
Initial permeability	3.85×10^{-12} m^2
Initial mineralogy	95% calcite; 4% gypsum and 1% dolomite (70% of rock volume)
Thermodynamics and kinetics	Thermodynamics for calcite and gypsum; kinetics for dolomite
Dolomite precipitation rate constant	$4.58e^{-19}$ mol m^{-2} sec^{-1} (Gabellone and Whitaker, 2016)
Reactive surface area	1000 cm^2 g^{-1} for dolomite
Temperature	30 °C
Initial water	Modern seawater (Nordstrom et al., 1979)
Boundary water	Ralph Sink brine (salinity of 186‰) (Jones and Xiao, 2005)
Brine injection rate	0.8 m yr^{-1}

3.3 Base case simulation

3.3.1 Volume change of major minerals

(1) Volume change of dolomite

Simulation result of base case scenario shows that within the vertical column of limestone sediments, the initial calcite are gradually dolomitized from top to bottom as the continuous injection of high salinity (with high Mg/Ca ratio) brine (Fig. 3.4). To be specific, during initial dolomitization, the replacement reaction (calcite replaced by dolomite) can be only observable in a very shallow depth. The depths of dolomitization zone are approximately 3 m and 12 m, with the dolomite volume changes of only 2.1% and 37.8% after 0.1 ka (expressed as thousand

years) and 1 ka simulation, respectively. With time, the dolomitization process in the upper part of the column tends to reach chemical equilibrium at a simulation time of about 5 ka, yielding a maximum volume increase in dolomite of 50.01% (i.e., 75.2% of the initial calcite was replaced by dolomite). Eventually, the dolomitizing fluid (brine) could seep throughout the column and give rise to a pervasive replacement reaction after a simulation time of approximately 20 ka.

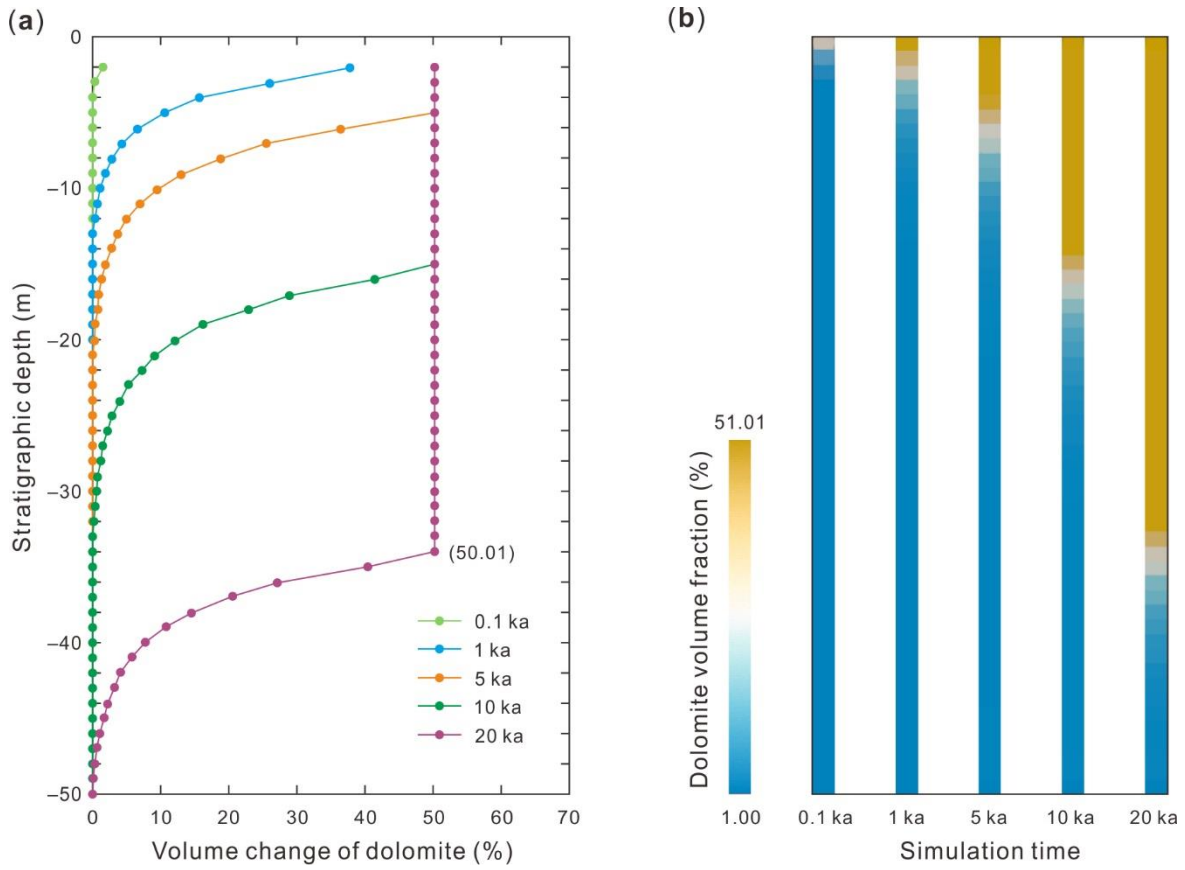

Figure 3.4 Simulation results showing the (a) volume change of dolomite and (b) total dolomite volume fraction in the rock with variation in simulation time.

(2) Volume change of calcite

The mineralogical evolution of calcite is closely associated with the gradual precipitation of dolomite. In general, the volume fraction of calcite shows a decreasing trend in contrast to the increasing dolomite (Fig. 3.5a). Due to the co-evolutionary relationship between these two carbonate minerals, the vertical depth of calcite decrease is nearly the same with that of dolomite increase. In addition, the volume fraction of calcite also remains unchanged after a simulation time of about 5 ka, with a maximum volume decrease in calcite of -54.71% at

equilibrium. It should be noted that the amount of calcite decrease is slightly higher than that of dolomite increase (50.01%). This is mainly because that the injected brine (boundary water) has a negative value (*SI* = -0.07) of saturation indices with regard to calcite (Table 3.2). Hence, a small amount of extra calcite in the rock (4.7%) tends to be dissolved in the brine even though the replacement reaction (dolomitization process) has reached equilibrium.

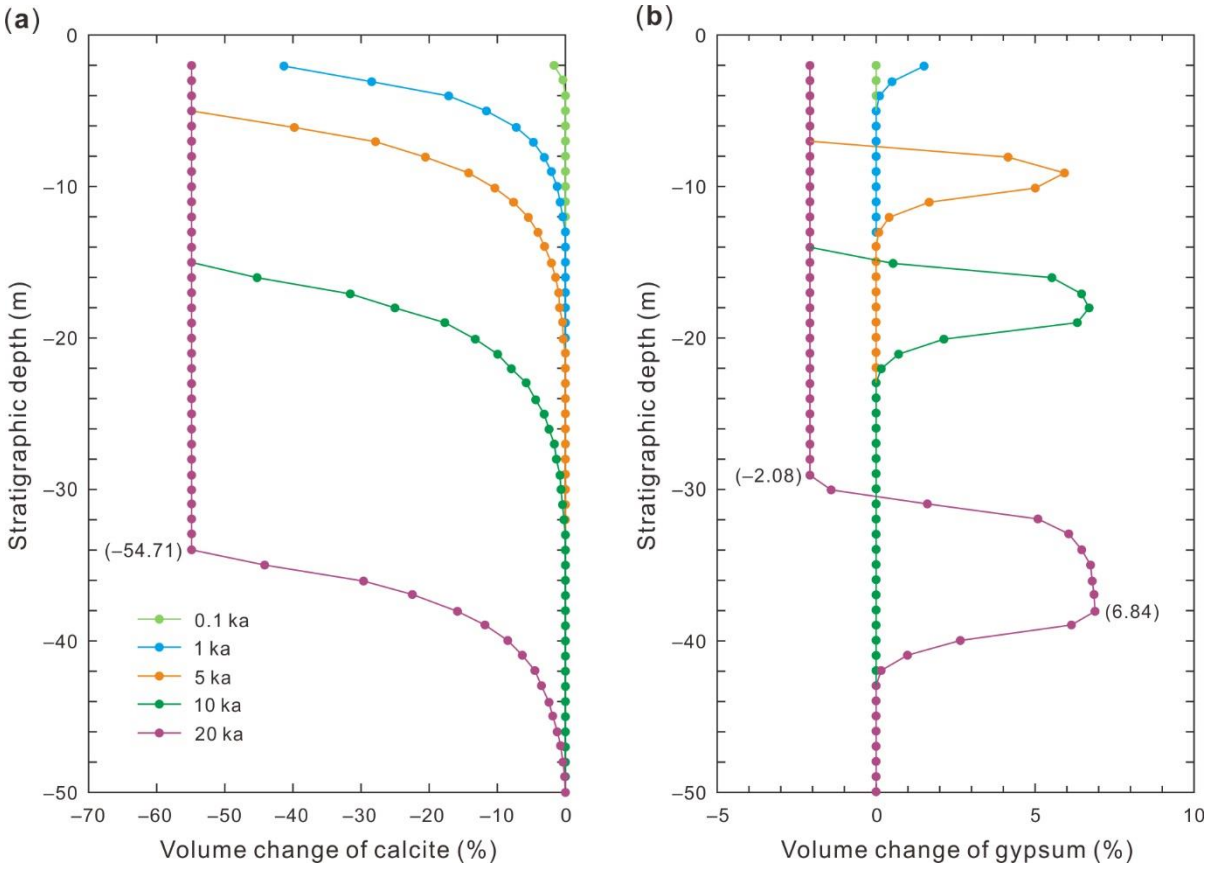

Figure 3.5 Simulation results showing the volume changes of (a) calcite and (b) gypsum with variation in simulation time.

(3) Volume change of gypsum

In comparison with the above mineralogical evolution of dolomite and calcite, the volume change of gypsum is relative complicated. In general, the gypsum shows a typical characteristic of dynamic variation during dolomitization, as featured by gypsum precipitation in the early stage but subsequently being dissolved in the late stage (Fig. 3.5b). A careful comparison of the mineralogical distribution of gypsum with dolomite indicates that the dynamic processes of gypsum precipitation/dissolution are also significantly controlled by the dolomitization process. Particularly, in the vertical, the location of gypsum cementation is highly consistent

with the dolomite front zone where the replacement reaction just reach equilibrium. Thus, the gypsum precipitation was likely a result of the combination of Ca^{2+} released from replacement reaction ($MgCa(CO_3)_2$ replaced by $CaCO_3$) and SO_4^{2-} supplied by the injected brine. The maximum volume increase of gypsum is 6.84% at a stratigraphic depth of -34 m after 20 ka simulation. Furthermore, after equilibrium of dolomitization process, the porous media tends to be dominated by injected brine (boundary water), and the early-formed gypsum tends to be dissolved since the brine are unsaturated with regard to gypsum (*SI* = -0.08; Table 3.2). The maximum volume decrease in gypsum is -2.08%.

3.3.2 Porosity and permeability evolution

Due to the fact that magnesium has a relatively smaller ionic radius than that of calcium (Weyl, 1960), the replacement of two moles calcite ($CaCO_3$) by one mole dolomite ($MgCa(CO_3)_2$) during dolomitization is generally regarded as a volume-decreased process and reservoir pores can be generated. In general, our simulation result is consistent with previous theoretical analysis that replacive dolomitization contributes to the formation of new porosity for dolostone reservoirs (e.g., Zhang et al., 2010; Huang et al., 2017). Nevertheless, the simulation result has indicated that the rock porosity of dolomitized carbonate reservoir is not always proportional to the degree of dolomitization (dolomite abundance). Potential influence of secondary minerals (herein the dynamic processes of gypsum precipitation/dissolution) might introduce great complexities to the diagenesis-rock property evolution during dolomitization. Specifically, the rock porosity-permeability evolution during our simulation also displays a characteristic of dynamic variation (Fig. 3.6), which is mainly determined by the relative dominance of the two distinct controlling factors, i.e., pore-infill by gypsum precipitation and pore-increment via volume-decreased dolomitization. For example, at a simulation time of 20 ka, the gypsum cementation is relatively dominant at the stratigraphic depth range of -34 m to -39 m in which the enrichment of Ca^{2+} released from replacement reaction could lead to abundant gypsum precipitation. Thus, in this dolomite front zone, there is a slight decreases in rock porosity and permeability of -1.86% and -0.64 μm^2, respectively. However, the rock porosity-permeability would rapidly be reinstated following the subsequent gypsum

dissolution in the injected brine (Fig. 3.6). At equilibrium, the maximum porosity and permeability increment is 7.48% and 4.57 μm^2, respectively, in comparison with its original limestone precursor.

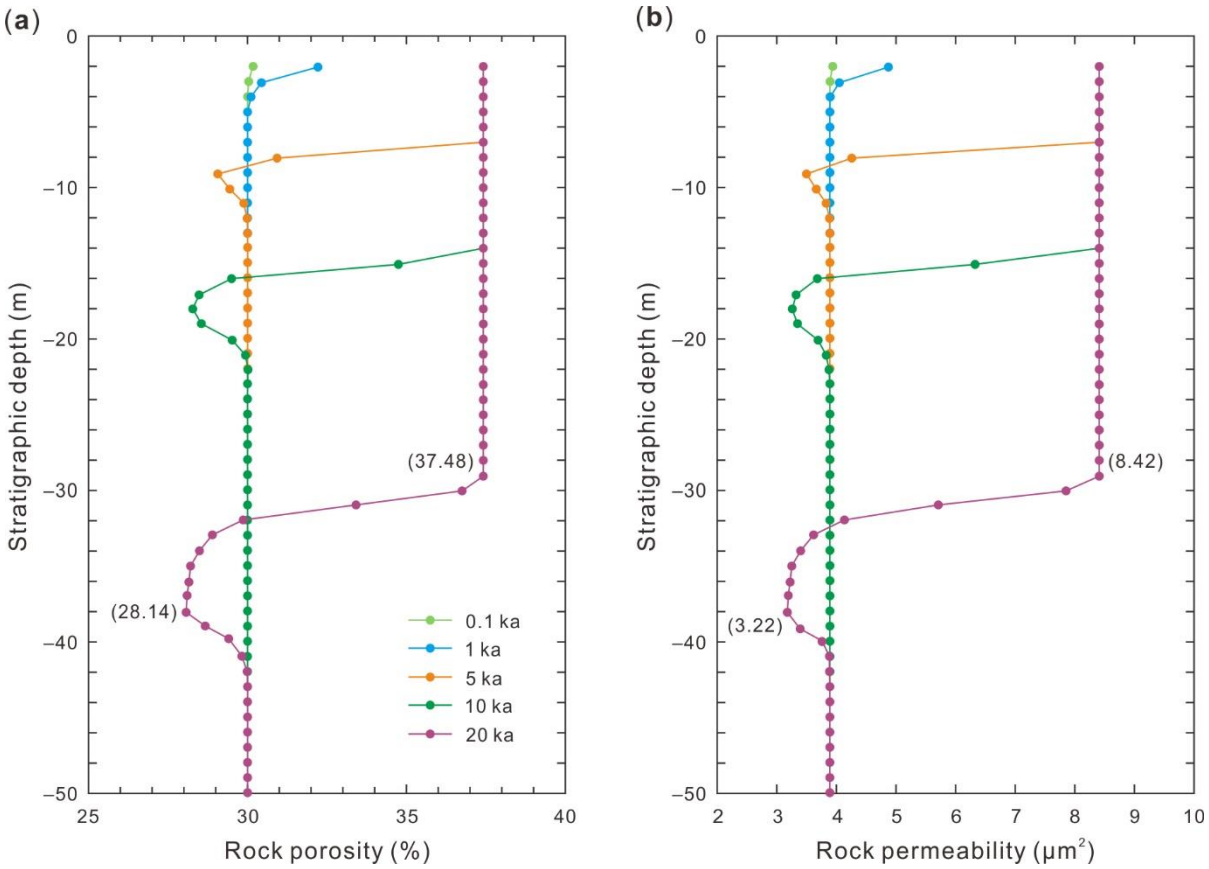

Figure 3.6 Simulation results showing the distribution of (a) rock porosity and (b) permeability with variation in simulation time.

3.4 Sensitivity analysis

In a natural geological system, the reflux dolomitization event can be affected by numerous hydrogeochemical factors associated with dynamic evolution of the complicated geological conditions (Warren, 2000). To reveal the influencing mechanisms and potential parameter uncertainties of these controlling factors on the dolomitization process, sensitivity analyses were conducted in the following part with regard to several key extrinsic and intrinsic parameters including the brine salinity, temperature, recharge capacity of brine, reactive surface area of dolomite crystal and rock fabric (Table 3.4). The data were extracted at a depth = -30 m of the column.

Table 3.4 Controlling parameters used for sensitivity analyses of 1D reflux dolomitization.

Parameters	Base case scenario	Values (Range)	Figure
Extrinsic controls			
Brine salinity	186‰	48‰, 85‰ and 249‰	Fig. 3.7
Temperature	30°C	20 °C, 40 °C and 50 °C	Fig. 3.8
Brine injection rate	0.8 m yr^{-1}	0.2, 0.5 and 2.0 m yr^{-1}	Fig. 3.9
Intrinsic controls			
Reactive surface area	1000 cm^2 g^{-1}	100 and 10000 cm^2 g^{-1}	Fig. 3.10
Rock fabric	grain-dominated packstone	grainstone, micrite	Fig. 3.11

3.4.1 Extrinsic controls

(1) Brine salinity

For sensitivity analysis, three types of brine were involved in the simulation, with salinities of 48‰, 85‰ and 249‰ representing an increase in evaporation capacity. In general, the ion concentration of the brine plays an important role in the dolomitization process because it directly affects the reaction rate of dolomite precipitation in the solution. Meanwhile, higher salinity would also result in higher fluid density, which promotes the downward flow of the brine. Influenced by these two effects, the reaction rate and degree of dolomitization display an increasing trend with elevated brine salinity. To be specific, the dolomitization process could reach equilibrium in a relatively short period under high brine salinity condition. The degree of replacement reaction (calcite replaced by dolomite) also shows a positive correlation with brine salinity, as evidenced by the gradually increasing dolomite abundances (volume fractions of the total rock) of 46.34%, 50.01% and 51.83% at equilibrium under salinity conditions of 85‰, 186‰ (base case scenario) and 249‰, respectively (Fig. 3.7a). Under condition of a low brine salinity (48‰), the dolomitization process exhibits an extremely low reaction rate, with a dolomite volume fraction less than 15% after a simulation time of 50 ka.

In contrast to the dolomite evolution, the calcite volume fraction shows a decreasing trend with time. Under salinity conditions of 85‰, 186‰ and 249‰, the calcite volume fraction are 15.90%, 11.79% and 9.74% at equilibrium, respectively (Fig. 3.7b). Notably, the gypsum volume fraction shows a dynamic evolution of gradual increase in the early stage followed by

rapid decrease in the late stage (Fig. 3.7c), which is consistent with the result of base case simulation. Specifically, the maximum gypsum volume fractions during dolomitization process are 5.17%, 9.64% and 9.11% under salinity conditions of 85‰, 186‰ and 249‰, respectively. At equilibrium, the gypsum volume fraction is uniformly 0.72% and is lower than its initial volume fraction (2.8%) because a part of initial gypsum has been dissolved in the brine.

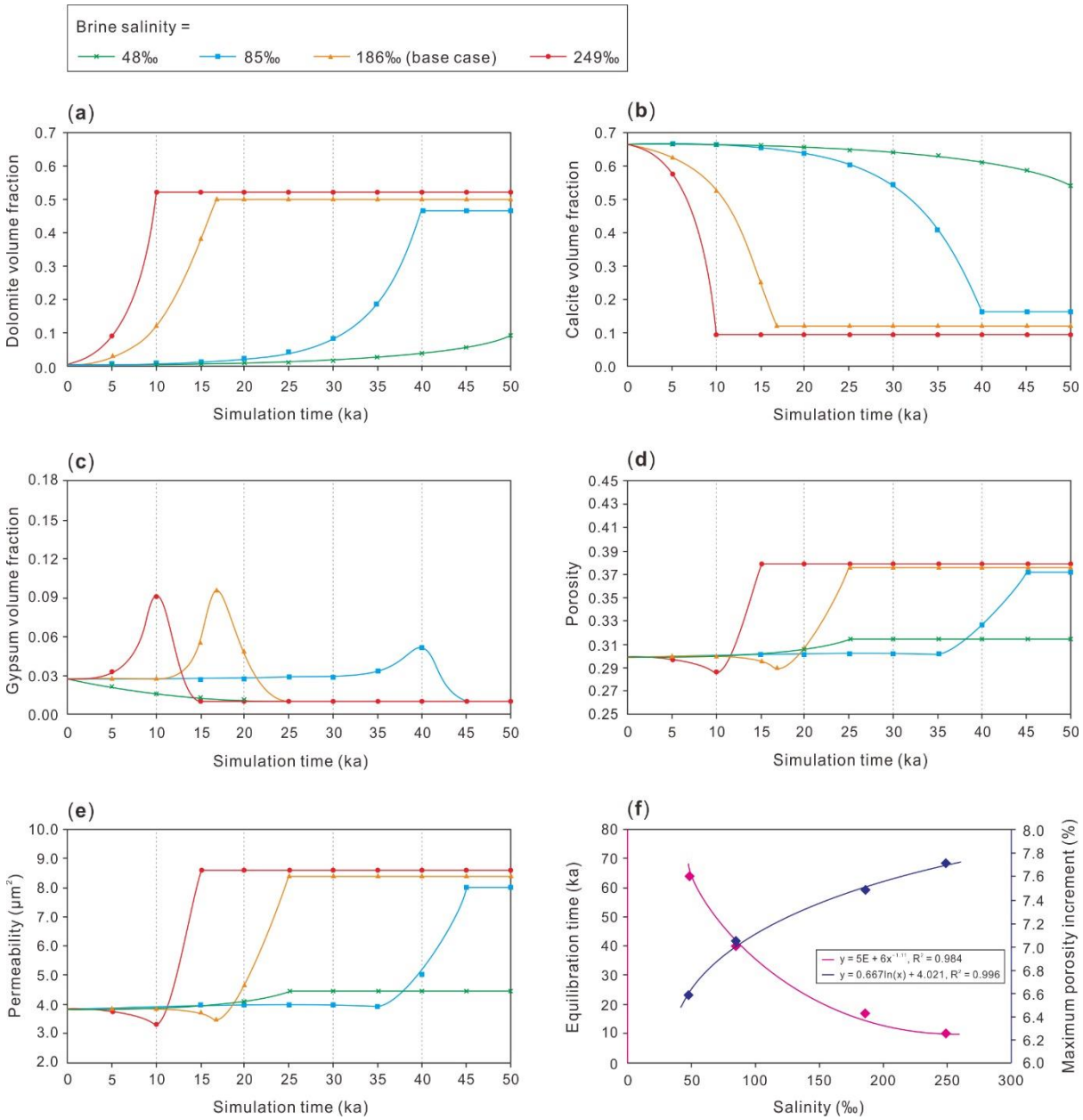

Figure 3.7 Sensitivity analysis of brine salinity. Mineralogical volume fraction of (a) dolomite, (b) calcite and (c) gypsum. (d) & (e) Rock porosity and permeability. (f) Simulation time needed for dolomitization equilibrium and maximum porosity increment at different salinity conditions.

In addition, the rock porosity and permeability have the similar evolution patterns, also

displaying a dynamic evolution of slight decrease during the stage of gypsum precipitation followed by a substantial increase due to subsequent gypsum dissolution (Fig. 3.7d and e). As discussed in the base case simulation, the rock porosity-permeability evolution during dolomitization process is mainly influenced by the pore increment process via dolomitization and the pore infill process by secondary gypsum cementation. Superposed on that, the results of sensitivity analysis further suggest a positive impact of elevated brine salinity on the dolomite reservoir properties, as shown by a gradual increase in the maximum porosity increment of 7.03%, 7.48% and 7.71% under brine salinity conditions of 85‰, 186‰ and 249‰, respectively (Fig. 3.7f).

(2) Temperature

The global sea surface temperature varies intensively in the geological history, and three temperatures, i.e., 20°C, 40°C and 50°C, were considered here for sensitivity analysis. According to the Arrhenius function (Eq. (3.5)), the rate constant (k_d) of dolomite precipitation is closely related to the temperature and relatively higher temperature could promote the replacement reaction to reach equilibrium in a shorter time (Fig. 3.8a). Meanwhile, the degree of dolomitization also has a positive correlation with temperature, as shown by the elevated dolomite volume fraction with increasing temperature (Fig. 3.8a). At equilibrium, the dolomite volume fractions under temperature conditions of 20°C, 30°C (base case scenario), 40°C and 50°C are 40.85%, 50.01%, 51.47% and 52.58%, respectively.

During dolomitization, the calcite volume fraction shows a decreasing trend with simulation time, yielding values of 22.07%, 11.79%, 10.15% and 8.91% under temperature conditions of 20°C, 30°C, 40°C and 50°C, respectively (Fig. 3.8b). Moreover, the gypsum precipitation in the dolomite front zone can also be influenced by the reaction temperature. The maximum gypsum volume fractions during dolomitization process are 9.74%, 9.64%, 8.31% and 6.50% with gradual increasing temperatures from 20°C to 30°C to 40°C and to 50°C (Fig. 3.8c). As a result, the rock porosity (a minimum value of 27.34% at 20°C) and permeability (a minimum value of 3.01 μm^2 at 20°C) exhibit slightly decreasing trends with gypsum precipitation in the early stage of dolomitization (Fig. 3.8d and e). Subsequently, the porosity and permeability

increase significantly with the dissolution of early-formed gypsum cement. In addition, the maximum porosity increment at equilibrium is also proportional to the temperature, yielding values of 6.35%, 7.48%, 7.64% and 7.73% with a gradual increase in temperature from 20°C to 50°C (Fig. 3.8f).

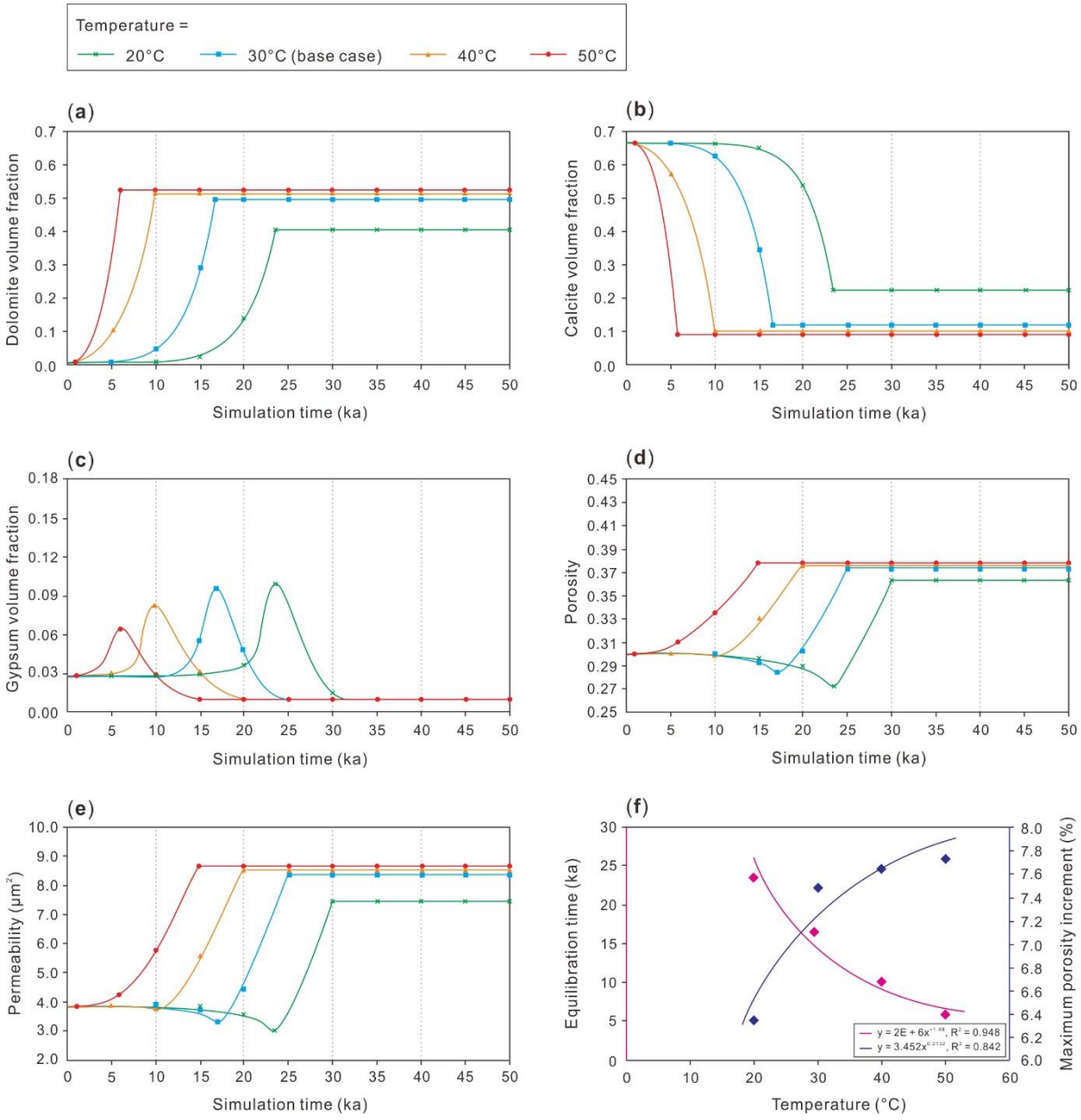

Figure 3.8 Sensitivity analysis of temperature. Mineralogical volume fraction of (a) dolomite, (b) calcite and (c) gypsum. (d) & (e) Rock porosity and permeability. (f) Simulation time needed for dolomitization equilibrium and maximum porosity increment at different temperature conditions.

(3) Brine injection rate

The injection rate in the simulation reflects the recharge capacity of brine (evaporated seawater) into the initial limestone sediments. Previous geological studies have shown that the brine recharge can be influenced by multiple hydrogeological factors such as the evaporation intensity (climatic conditions), phreatic surface fluctuations and geomorphic characteristics of the restricted-evaporative environment associated with reflux dolomitization (Warren, 2000; Gabellone et al., 2016). In the current study, three different brine injection rates, i.e., 0.2, 0.5 and 2.0 m yr^{-1} were involved for sensitivity analysis. In general, higher injection rates result in higher fluid flux and replacement reaction rate, as shown by a gradual decrease in the simulation time needed to reach equilibrium with increasing brine injection rate (Fig. 3.9a). Approximately, the dolomitization process can reach equilibrium at simulation times of 26.7, 16.8 and 6.8 ka under brine injection rate conditions of 0.5, 0.8 (base case scenario) and 2.0 m yr^{-1}, respectively. However, the dolomite volume fraction remains unchanged, with a uniformly value of 50.01% at equilibrium even under different conditions of brine injection rates (Fig. 3.9a). This suggests that the dolomitizing fluid flux in the initial sediments has a minor influence on the degree of dolomitization, although it affects the replacement rate of calcite by dolomite.

Moreover, the calcite volume fraction decreases with simulation time and reaches a unified value of 11.79% at equilibrium (Fig. 3.9b). The maximum gypsum volume fractions during dolomitization process are 10.17% and 9.64% under brine injection rate conditions of 0.5 and 0.8 m yr^{-1}, respectively (Fig. 3.9c). Notably, the gypsum precipitation was not observed at a brine injection rate of 2.0 m yr^{-1}. This is probably because this extremely high injection rate has resulted in high fluid flux and replacement reaction rate, and the process of gypsum precipitation took place too fast to be captured in the discrete points in time (a gap of ca. 5 ka) during simulation. The minimum rock porosity and permeability during dolomitization process are 28.03% and 3.19 μm^2 at a brine injection rate of 0.5 yr^{-1}, respectively, corresponding to the point-in-time of maximum gypsum precipitation (Fig. 3.9d and e). Furthermore, due to a unified degree of dolomitization (dolomite volume fraction), the rock porosity and permeability also remain consistent values of 37.48% (a porosity increment of 7.48%) and 8.42 μm^2 at equilibrium, respectively, even under different conditions of brine injection rates (Fig.

3.9f).

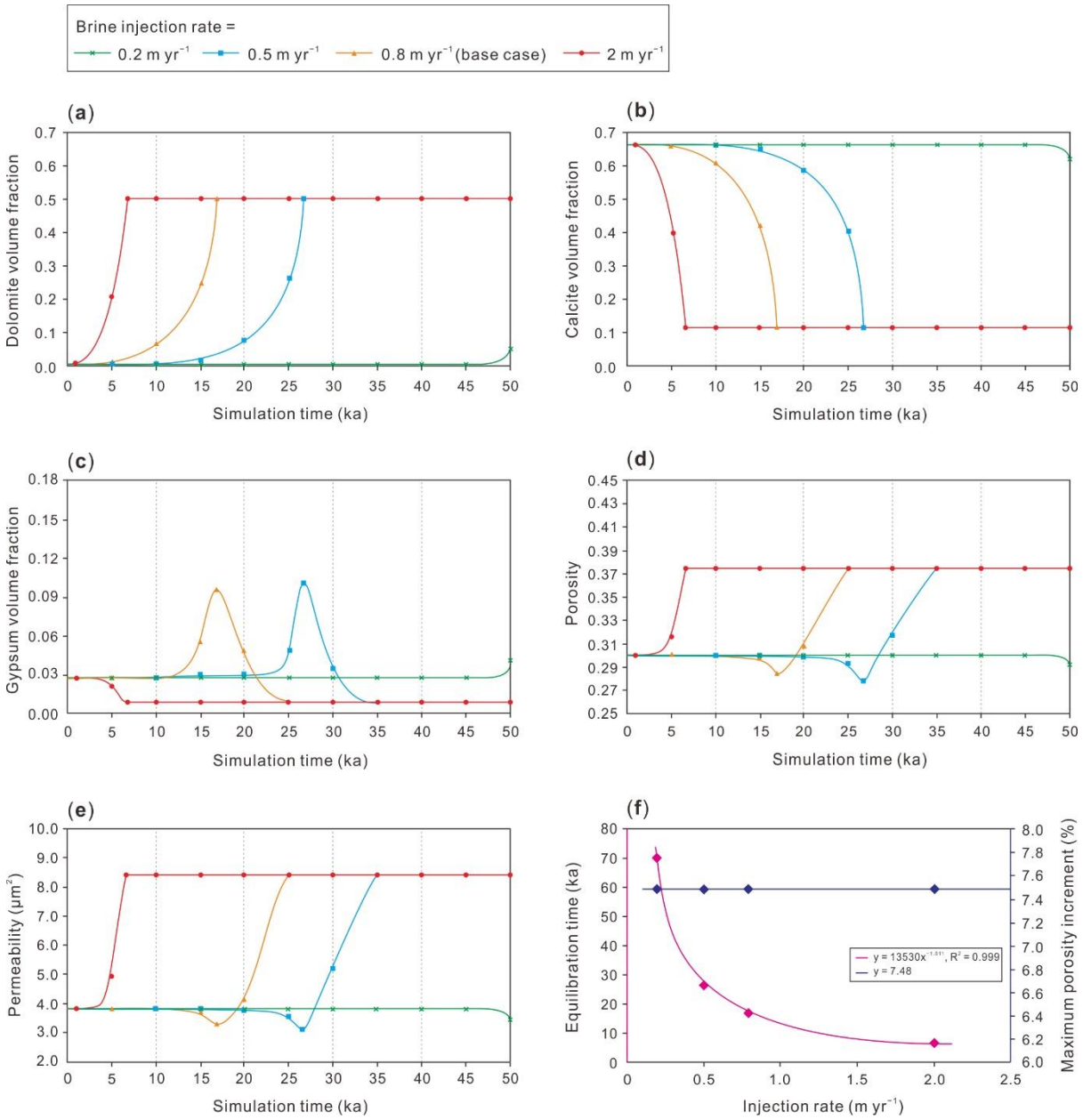

Figure 3.9 Sensitivity analysis of brine injection rate. Mineralogical volume fraction of (a) dolomite, (b) calcite and (c) gypsum. (d) & (e) Rock porosity and permeability. (f) Simulation time needed for dolomitization equilibrium and maximum porosity increment at different injection rate conditions.

3.4.2 Intrinsic controls

(1) Reactive surface area (RSA)

The reactive surface area is a key intrinsic parameter describing the microscopic properties of

the rock particles, which reflects the reactivity of the porous media. For sensitivity analysis, two different RSA values, i.e., 10^2 and 10^4 cm^2 g^{-1}, were involved, representing an increase in particle size of dolomite crystal but a decrease in its reactivity. According to the kinetic reaction rate law for dolomite precipitation (Eq. (3.6)), the reaction rate is directly proportional to the reactive surface area of dolomite crystals. Thus, relatively large RSA should accelerate the reaction rate and the replacement of calcite by dolomite. This is consistent with the simulation result. Approximately, the dolomitization process can reach equilibrium at simulation times of 50.0, 16.8 and 5.7 ka, corresponding to RSA values of 10^2, 10^3 (base case scenario) and 10^4 cm^2 g^{-1}, respectively (Fig. 3.10a). The degree of dolomitization, however, seems to be unaffected by the variation in RSA, as indicated by unified dolomite volume fraction of 50.01% at equilibrium.

The calcite volume fraction shows an opposite evolution to the dolomite, and reaches a value of 11.79% at equilibrium (Fig. 3.10b). Dynamic processes of gypsum precipitation and dissolution have been also observed during dolomitization, and the maximum gypsum volume fraction are 11.20%, 9.64% and 2.85% under RSA conditions of 10^2, 10^3 and 10^4 cm^2 g^{-1}, respectively (Fig. 3.10c). In addition, the rock porosity and permeability are 37.48% and 8.42 μm^2 at equilibrium, respectively (Fig. 3.10d–f), which are consistent with the result of base case simulation. Notably, the temporary process of porosity-permeability decrease were not observed in the simulation with RSA value of 10^4 cm^2 g^{-1}. This is likely because in such condition of a high RSA value (rock reactivity), the pore infill process in the early-stage via gypsum precipitation has been entirely overprinted by the stronger pore increment process due to the high dolomitization rate.

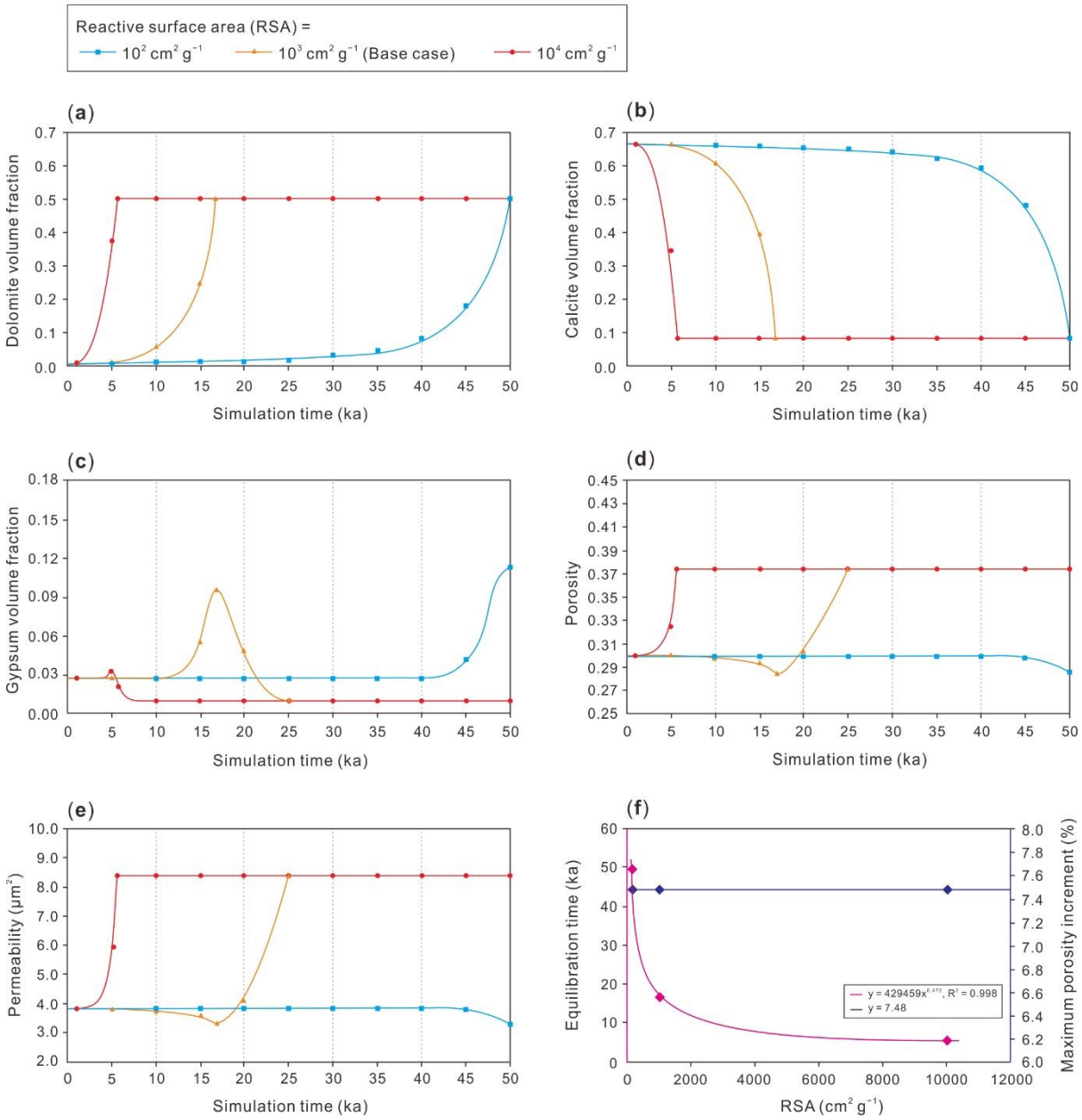

Figure 3.10 Sensitivity analysis of reactive surface area. Mineralogical volume fraction of (a) dolomite, (b) calcite and (c) gypsum. (d) & (e) Rock porosity and permeability. (f) Simulation time needed for dolomitization equilibrium and maximum porosity increment at different reactive surface area conditions.

(2) RSA coupled with porosity-permeability (Rock fabrics)

In addition to the sediment reactivity (RSA) that has been discussed in the above paragraphs, different rocks types (or fabrics) also lead to different fluid mobility (initial porosity-permeability). Herein, three types of rock fabrics, which reflect the coordinated variation of particle size and initial porosity-permeability (Table 3.1), were considered in the base case

simulation and sensitivity analysis, including grainstone (RSA = 10^2 cm^2 g^{-1}; porosity = 47% and permeability = 1.00×10^{-9} m^2), grain-dominated packstone (base case scenario; RSA = 10^3 cm^2 g^{-1}; porosity = 30% and permeability = 3.85×10^{-12} m^2) and micrite (RSA = 10^4 cm^2 g^{-1}; porosity = 18% and permeability = 1.00×10^{-13} m^2).

According to the simulation results, the micritic stone has the highest degree of dolomitization, yielding a dolomite volume fraction of 58.48% at equilibrium that is apparently higher than that of packstone (50.01%) and grainstone (38.01%) (Fig. 3.11a). However, the grainstone, which has the lowest RSA but highest initial porosity-permeability, reaches equilibrium (at approximately 12.7 ka) prior to packstone (at ca. 16.8 ka) and micrite (at ca. 18.9 ka) (Fig. 3.11a). Given that higher RSA could accelerate the reaction rate as suggested by the above sensitivity analysis of RSA, a relatively high porosity-permeability and resulting high fluid flux seems to have played a more important role in accelerating the dolomitization rate. This suggests that the promotional effect of dolomitization rate from increasing dolomitizing fluid mobility (flux) would be more significant than increasing sediment reactivity (i.e., higher reactive surface area).

During dolomitization, the calcite volume fraction (relative to total rock volume) has declined by 42.15% (from 50.35 to 8.20%), 54.71% (from 66.5% to 11.79%) and 63.7% (from 77.9% to 14.20%) for grainstone, packstone and micritic stone, respectively (Fig. 3.11b). Gypsum precipitation and dissolution were observed in all types of rocks, with the maximum gypsum volume fraction of 8.07%, 9.64% and 11.39% for grainstone, packstone and micritic stone, respectively (Fig. 3.11c). Moreover, due to the different degrees of dolomitization and initial rock properties, the porosity-permeability evolution of three types of rock are distinct from each other (Fig. 3.11d and e). Particularly, the minimum rock porosities for grainstone, packstone and micrite are 45.73%, 28.14% and 15.82%, respectively, corresponding to the point-in-time of maximum gypsum precipitation (Fig. 3.11c and d). With subsequently gypsum dissolution, these rock porosities increase to 52.66%, 37.48% and 26.76% after equilibrium, yielding porosity increments of 5.66%, 7.48% and 8.76% for grainstone, packstone and micrite, respectively (Fig. 3.11f).

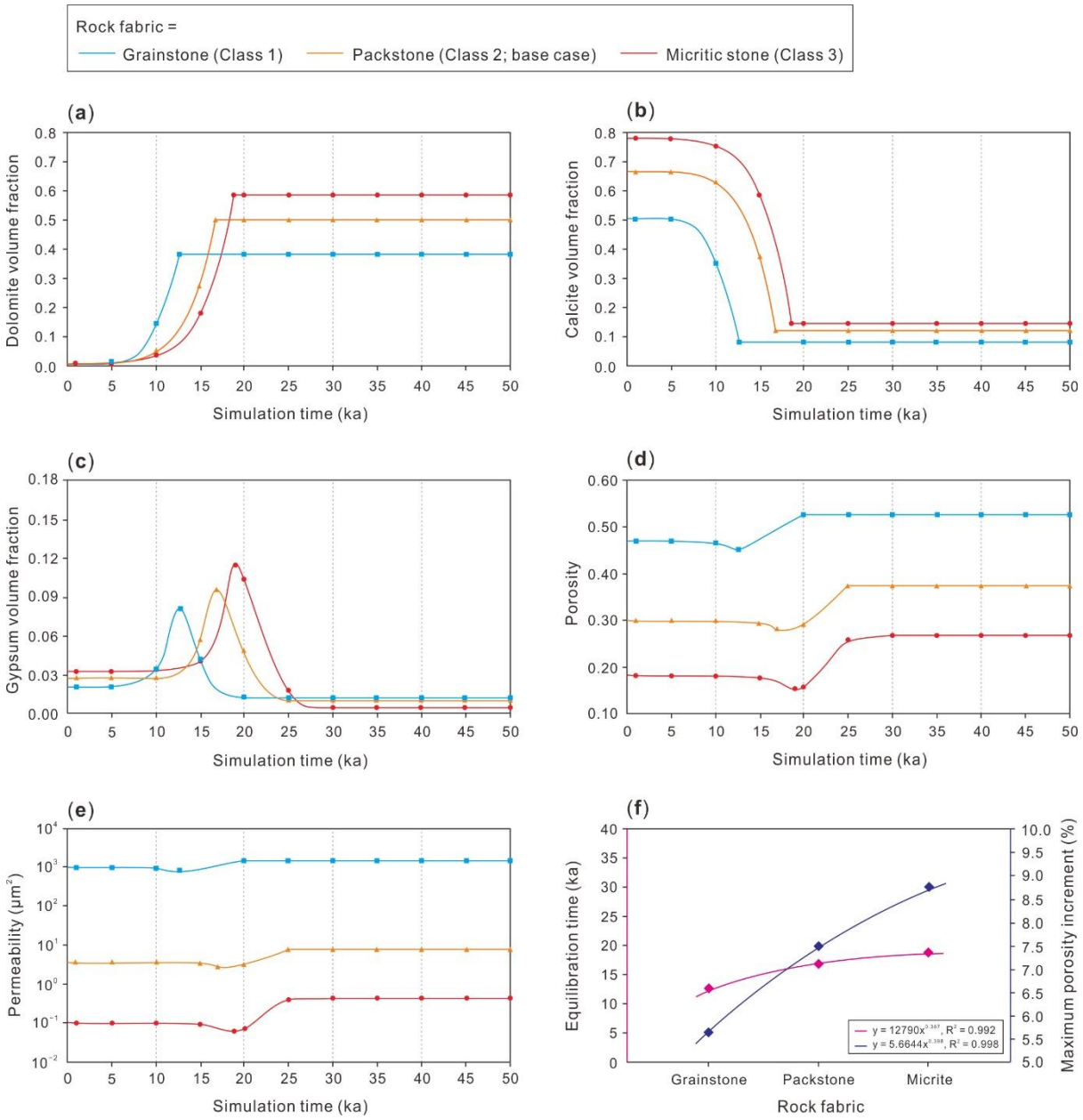

Figure 3.11 Sensitivity analysis of rock fabric. Mineralogical volume fraction of (a) dolomite, (b) calcite and (c) gypsum. (d) & (e) Rock porosity and permeability. (f) Simulation time needed for dolomitization equilibrium and maximum porosity increment at different rock fabric conditions.

3.4.3 Comparison of different controlling parameters

According to the above sensitivity analyses of individual parameters, these hydrogeochemical factors have different influences on the dolomitization process with regard to reaction rate and mineralogical (i.e., dolomite, calcite and gypsum) evolution. In order to evaluate the relative importance of these extrinsic/intrinsic controls in promoting high quality dolomitized

carbonate reservoirs, herein we compare the different simulation results in terms of the time needed for dolomitization equilibrium (dolomitization rate) and the porosity increment after equilibrium (degree of dolomitization), rather than the maximum mineral reaction rate as used by Jones and Xiao (2005) or the dolomite cement volume fraction as used by Gabellone and Whitaker (2016). A clear comparison of various controlling parameters and relevant data are illustrated in Fig. 3.12.

In general, all the five investigated factors have impacts on the dolomitization rate. The brine salinity, temperature, RSA and injection rate are inversely proportional to the simulation time needed for dolomitization equilibrium (Fig. 3.12a). Particularly, the increases in brine salinity (from 48‰ to 249‰) and injection rate (from 0.2 to 2.0 m yr^{-1}) could significant accelerate the reaction rate and reduce equilibration time. The influence of rock fabric on dolomitization rate is relatively complicated, reflecting a combined effect of sediment reactivity and fluid mobility. For instance, although the micrite has the highest RSA that should give rise to a rapid reaction, the dolomitization rate has been limited by its relatively low rock permeability and fluid flux (Fig. 3.12a). This result might have suggested that in relatively impermeable system the fluid mobility should be more important than sediment reactivity, while in pore permeable system, the dolomitization rate is more affected by sediment reactivity.

Moreover, the degree of dolomitization varies with brine salinity, temperature and rock fabrics, as shown by their different porosity increments after dolomitization equilibrium (Fig. 3.12b). The RSA and brine injection rate, however, seem to have no impact on the degree of dolomitization, with a unified porosity increment of 7.48% consistent with base case simulation. Specifically, the porosity increment increases with elevated brine salinity and temperature, as well as the transformation of rock fabrics from grainstone to packstone to micritic stone. With increasing brine salinity from 48‰ to 249‰ and temperature from 20°C to 50°C, the porosity increment increase from 6.58% to 7.71% and from 6.35% to 7.73%, respectively. Notably, although the micrite has relatively low dolomitization rate compared with two other types of rock fabric due to the limitation of low fluid mobility, the micrite has yielded a higher porosity increment of 8.76% because of more pervasive dolomitization (i.e.,

a higher dolomitization degree).

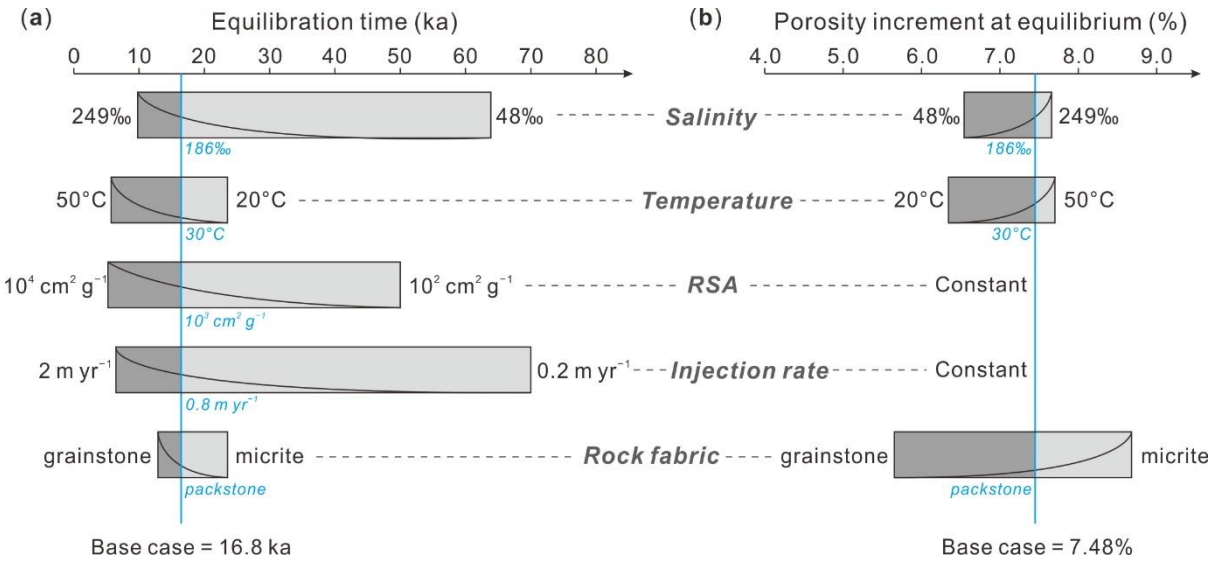

Figure 3.12 Tornado diagram summarizing the results of sensitivity analyses and showing the comparisons of various controlling parameters in terms of (a) the time needed for dolomitization equilibrium (dolomitization rate) and (b) the porosity increment after equilibrium (degree of dolomitization).

3.5 Summary

In this chapter, the kinetic process of dolomitization was presented, and the temporal and spatial evolution of minerals and rock properties during dolomitization were investigated using RTM simulations in a simplified one-dimensional column model. Based on sensitivity analysis, several key controlling parameters were evaluated individually, shedding lights on the influence mechanisms of these extrinsic and intrinsic factors on the dolomitization process. Results from this generic model study suggest that:

The kinetic process of dolomitization is modeled as a reaction network that comprises calcite dissolution followed by dolomite precipitation. Increasing dolomite, decreasing calcite and dynamic evolution (precipitation followed by dissolution) of gypsum were observed during simulation. The gypsum precipitation, which distributed in the dolomitization front zone, was likely related to the combination of released Ca^{2+} during dolomitization (2 mole $CaCO_3$ replaced by 1 mole $MgCa(CO_3)_2$) and SO_4^{2-} in the solution.

Collectively influenced by pore-increment via dolomitization and pore-infill by gypsum precipitation, the rock porosity-permeability display a dynamic evolution of slight decrease followed by substantial increase.

Multiple factors, which includes hydrogeochemical conditions and rock fabrics (sediment reactivity and fluid mobility), determine the reaction rate and degree of dolomitization. Specifically, higher brine salinity, temperature, RSA and injection rate accelerate the dolomitization rate, while the degree of dolomitization can be only enhanced under conditions of higher brine salinity and temperature, as well as fine-grained rock fabric such as micrite.

4 Eogenetic karst in meteoric water-rock system

4.1 Basic idea

Karstification usually refers to the processes of chemical dissolution and associated modification of soluble rocks (mostly carbonates and evaporites), occurring in a wide variety of climatic and tectonic settings (e.g., meteoric diagenetic environment for subaerially exposed rock strata; James and Choquette, 1988). The term “eogenetic” is applied to karst (Vacher and Mylroie, 2002) to characterize the karst process that affects newly formed deposited sediments when these sediments are exposed to subaerial weathering and meteoric water prior to deep burial. This eogenetic karst (or soft-rock karst), which is hydrodynamically controlled by an intergranular pore system in the matrix (Fig. 4.1a), is distinguished from the telogenetic karst (or hard-rock karst) that develop mostly along fracture systems within ancient rocks that have been re-exposed after the porosity reduction of burial diagenesis (Grimes, 2006; Florea and Vacher, 2007; Tan et al., 2015).

In recent years, the eogenetic karst, which is one important type of paleokarst (or ancient karst) developed in geological history and preserved within the rock strata, has received increasing attention since it provides crucial information on hydrocarbon reservoir genesis and prediction. A number of high-quality carbonate reservoirs have been revealed to be associated with eogenetic karst, especially in the sedimentary facies of intraplatform shoals and microbial mounds that formed in the paleotopographic highs of the carbonate platform and were sensitive to the leaching of meteoric water during sea level regressions (e.g., Mehrabi et al., 2015; Xiao et al., 2019; Zhong et al., 2019). This karst process played a major role in the expansion of primary pores and the production of new reservoir space (Fig. 4.1b-d). Moreover, these karst systems formed in the early stage significantly control burial diagenesis and porosity evolution since they determine the flow path and priorities of reservoir optimization for basinal fluids (Rahimpour-Bonab et al., 2012; Zhao et al., 2014; Xiong et al., 2020b). Hence, eogenetic karst is of great significance for understanding the distribution and heterogeneity of carbonate reservoirs in marine petroliferous basins.

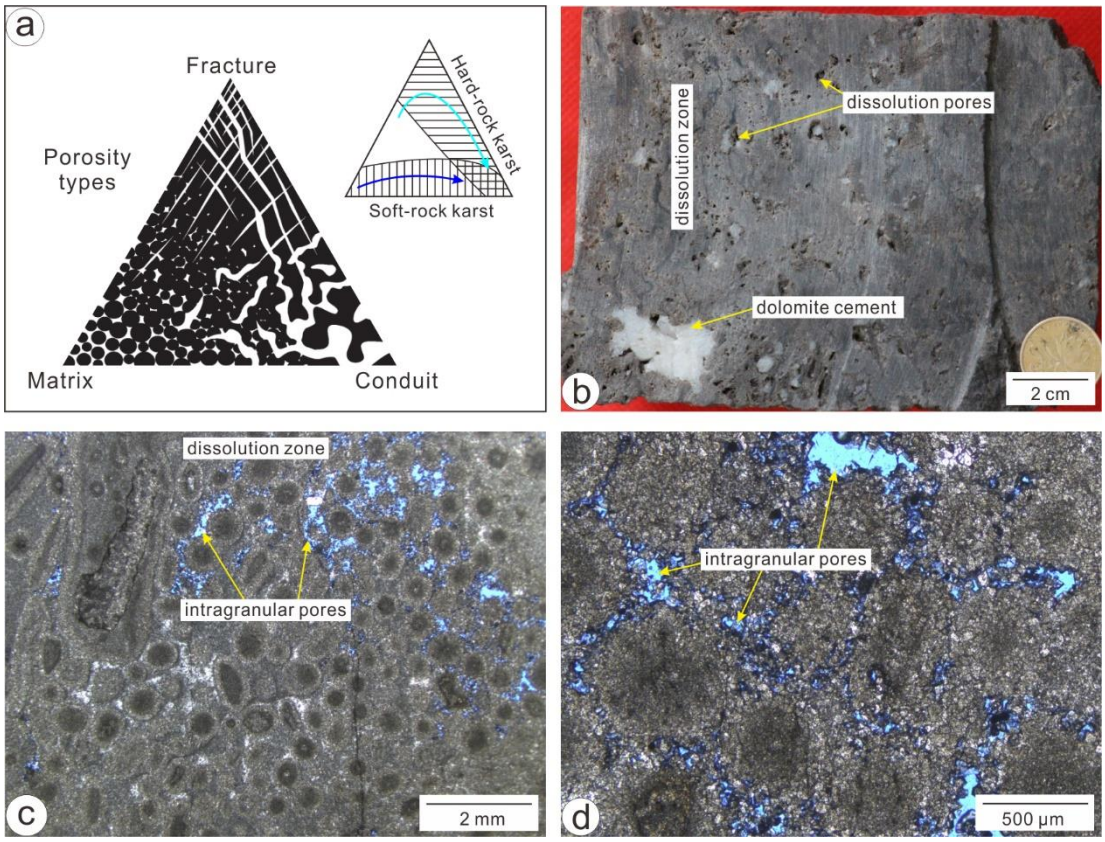

Figure 4.1 (a) Schematic illustration of the different dissolution mechanisms of soft-rock karst (or eogenetic karst) and hard-rock karst (modified after Grimes, 2006). (b–d) Core and thin section photographs showing the macro-micro characteristics of eogenetic karst (samples form the Ordovician karst reservoir, Ordos Basin, China).

Although the petrographic features of eogenetic karst have been well studied, quantifying karst process with its impact on porosity evolution remains a persistent challenge in the field of petroleum geology that limits the accuracy of reservoir quality predictions at multiple temporal and spatial scales. For instance, most of the previous studies, which were based on petrographic analyses of outcrops and cores and geochemical constraints of diagenetic fluids, have provided a basis for identifying meteoric diagenesis and multilevel exposure surfaces (Mehrabi et al., 2018; Liu et al., 2019; Xiong et al., 2019; Xie et al., 2020). Nevertheless, these studies failed to reveal a quantitative relationship between the exposure time and the extent and intensity of dissolution, and thus introduced uncertainties into the prediction of such meter-scale cyclical carbonate reservoirs. Yang (2001) proposed an isotopic approach to estimate the duration of subaerial exposure based on the whole-rock $\delta^{13}C$ depletion in vadose meteorically altered

limestone. This iterative model, however, simply considers the carbon isotope exchange during water-rock interactions from a static perspective and ignores the dynamic variation in the isotopic signals of meteoric water during the seepage process. The carbon isotope values of seawater vary significantly with geological time and specific environmental conditions (Veizer et al., 1999); this variation also raises doubts about the universality of this method. Moreover, a number of lab experiments have been conducted to model the karst process of carbonate reservoirs with respect to meteoric and burial diagenetic environments (e.g., Arvidson et al., 2003; Stack et al., 2014; Keshavarz et al., 2019). These experiments provided quantitative evaluations of the influence of various physicochemical conditions on the fluid-rock interactions and resulting porosity changes at the core scale. However, their results are vastly different and even challenge each other due to differences in the experimental conditions, control parameters and rock textures (e.g., She et al., 2016; Bouissonnié et al., 2018; Poonoosamy et al., 2020). Given the limitations of experiments and observation times, artificial diagenesis under laboratory conditions usually cannot reflect realistic diagenetic processes over geological timescales. As such, it is difficult to precisely characterize the distribution of geological bodies and to practically promote reservoir predictions using the results of laboratory experiments.

Reactive transport modeling (RTM) is an effective research method for geological issues that couples multiphase flow, solute transport and chemical reaction processes (Xu et al., 2006; Whitaker and Xiao, 2010; Charlton and Parkhurst, 2011; Garcia-Fresca et al., 2012). To date, this approach has been widely employed in simulations of fluid-rock interactions within porous media during multiple diageneses, such as dolomitization, illitization, mineral dissolution and precipitation, and carbon dioxide sequestration by mineralization (e.g., Al-Helal et al., 2012; Liu et al., 2015; Islam et al., 2016; Gabellone et al., 2016; Xiao et al., 2018). Although the karst system has been frequently investigated using RTM, these studies mostly focus on the modern karstology with applications in groundwater resources management and ecological assessment (e.g., Kaufmann et al., 2010; Hao et al., 2013; Worthington et al., 2016). Less attention has been paid to the paleokarst systems (Yang et al., 2020a), especially the meteoric water-rock interactions and resulting porosity evolution under the influence of various extrinsic/intrinsic

hydrogeological factors from a hydrocarbon geological perspective. Compared with traditional reservoir characterization approaches that focus on karst products preserved in rock records, RTM has flexible spatial and temporal resolutions to reconstruct the co-evolution of mineral reactions with porosity changes at both geological and production timescales, which helps to reduce the prediction uncertainty of paleokarst-related hydrocarbon reservoirs. Particularly, this chapter aims to: (1) determine the mineral and porosity distributions in a one-dimensional eogenetic karst system; (2) quantitatively evaluate the impacts of key geological factors on the karst process and their relative importance in promoting high-quality carbonate reservoirs.

4.2 Model setup and parameters

4.2.1 Applicability of the model

Fluid-rock interactions during the karst process of carbonate rocks are mainly controlled by the flow of unsaturated fluids, chemical transport and reactions, and porosity-permeability changes (Whitaker and Smart, 2007; Worthington et al., 2016). To reveal the fluid-rocks interactions during eogenetic karst and their impacts on carbonate reservoirs, simulations of carbonates dissolution process in a meteoric water-rock system were also performed using the reactive transport computer code TOUGHREACT (Xu et al., 2004). Further details on the numerical models and governing equations of the flow, transport, chemical reactions and porosity-permeability changes are introduced in chapter 2.

Notably, constraining porosity-permeability changes is a major focus of research on fluid-rock interactions during carbonate diagenesis. Temporal variations in rock porosity-permeability can modify fluid flow and result in progressively complicated fluid-rock interactions (Xu et al., 2006). Hence, the feedback between flow and chemistry is considered in the code and the Kozeny-Carman porosity-permeability equation is used for matrix permeability changes in the present simulations. It should be noted that although various matrix- and fracture-flow models have been developed to investigate the porosity-permeability coevolution during karstification (e.g., Kaufmann et al., 2010; Worthington et al., 2016; Gong et al., 2019), these studied are mostly based on telogenetic karst (or hard-rock karst) in which the fracture porosity and conduit

flow significantly affect the flow and mineral dissolution processes (Fig. 4.1a). The eogenetic karst, which is discussed in the present study, is distinct from the telogenetic karst. Firstly, a major characteristic of eogenetic karst is that the rock comprises early sediments (e.g., arenite and oolitic limestone) that have barely been affected by compaction (i.e., soft-rock karst). In these porous grain-supported carbonate rocks, laboratory experiments have shown that the flow path of meteoric water is mainly provided by intergranular pores, characterized by random and diffuse flow (i.e., diffuse intergranular flow; Fig. 4.1a) (She et al., 2016; Maddah et al., 2020). Secondly, the duration of leaching by meteoric water for eogenetic karst (generally less than 1 Ma (million years)) is apparently shorter than that for telogenetic karst (up to hundreds of Ma) (Xiao et al., 2016). According to abundant petrological analyses, the eogenetic karst is featured by relatively homogeneous enlargement of intergranular pores, and the initial granular structure of the rock has not been significantly altered (Saller et al., 1999). In this case, the conduit flow and fracture porosity should have a minor impact on the eogenetic karst system. Therefore, the studied eogenetic karst system is comparable to other early diagenetic porous systems (e.g., dolomitization) that have been extensively simulated using TOUGHREACT (Whitaker and Xiao, 2010), and the Kozeny-Carman model is also applicable for this unique karst system. Similar RTMs of karstification using TOUGHREACT have been also documented by Xiao et al. (2018) and Yang et al. (2020).

4.2.2 Generic column model and rock properties

The eogenetic karst in a vadose meteoric water-rock system was simulated in a simplified 1D single-mineral system that represents a vertical column of porous carbonate sediments (Fig. 4.2a). During sea level falls, the carbonate platforms are likely exposed and subjected to a meteoric diagenetic environment (Grimes, 2006; Dyer et al., 2017). The 25-m-long column, which represents the exposed carbonate sediments in a vadose meteoric environment, is evenly discretized into 25 grid cells. Given that eogenetic karst was mostly developed in the shoal-facies environment in the palaeo-highs of carbonate platforms (Xiong et al., 2019; Zhong et al., 2019), porous grainstone was thus adopted to specify the initial rock properties in this study (Fig. 4.2b). As also mentioned in the rock property setting for 1D simulation of reflux

dolomitization (Section 3.2.2), the new carbonate sediments during eogenetic period were weakly affected by cementation, compaction or burial diagenesis and thus had relatively high porosity-permeability (Lucia et al., 1995). According to the rock-fabric petrophysical relationships and porosity-depth models for carbonate reservoirs (Ehrenberg and Nadeau, 2005; Perrin et al., 2020), an initial homogeneous 30% porosity and 3.85 × 10^{-12} m^2 permeability were specified throughout the column.

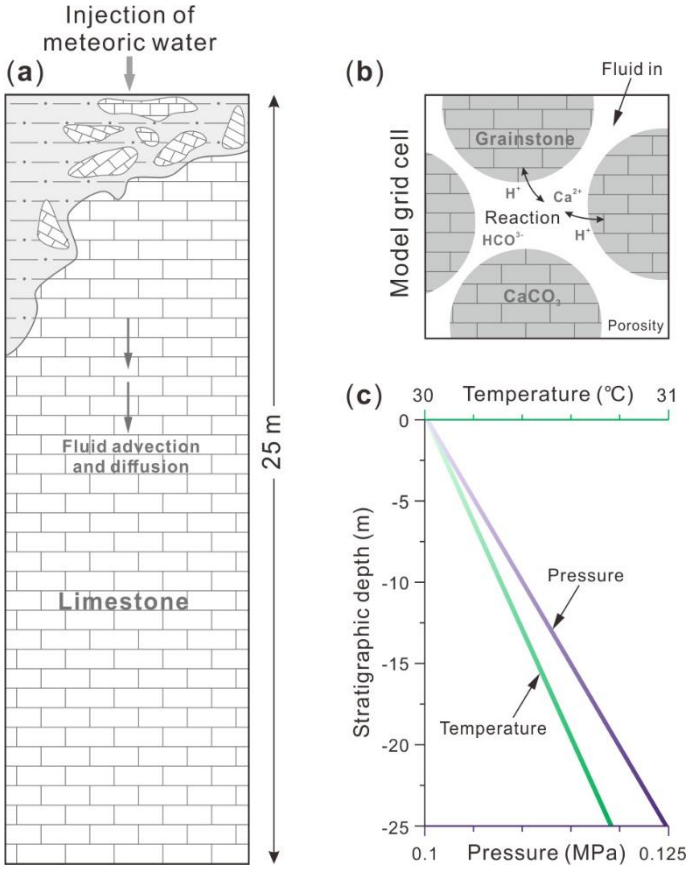

Figure 4.2 (a) Schematic illustration of the 1D vertical column showing the karst features and fluid flow during eogenetic karst. (b) Schematic of a single model grid cell showing the major fluid-rock interactions in the pore space (modified after Dyer et al., 2017). (c) Stratigraphic depth profile showing the initial temperature and pressure of the column.

Moreover, given the possibility that in some evaporitic environments, granular limestone sediments have undergone dolomitization prior to subaerial exposure, there is a motivation to explore the difference between limestone and dolostone during the eogenetic karst process. Specifically, for the single-mineral system in the present study, one type of mineral, i.e., pure calcite or pure dolomite is involved in each simulation. Although dolostone was specified to

have the same initial porosity-permeability as limestone, their rate-determining mechanisms are different. Due to the existence of Mg^{2+}-water complexes that inhibit nucleation of dolomite, dolomite is generally regarded as a kinetic mineral, as supported by extensive work on its geochemical mechanism and lab experiments (e.g., Land, 1998; Arvidson and MacKenzie, 1999; Warren, 2000). In the simulation, the kinetic rate constants (k_{25}) for dolomite dissolution are 2.951E-8 mol m^{-2} sec^{-1} with activation energy (Ea) of 52.2 kJ mol^{-1} and 6.457E-4 mol m^{-2} sec^{-1} with activation energy (E_a) of 36.1 kJ mol^{-1} under neutral and acid mechanisms, respectively. They are taken from Xu et al. (2007). The dissolution of calcite, however, is generally modeled as a thermodynamic process controlled by the saturation and equilibrium state of the fluid-rock system (Xiao et al., 2018; Yang et al., 2020b). Detailed thermodynamic data for aqueous species and minerals are given in the EQ3/6 geochemical database (Wolery, 1992) which is concomitant with the simulation code (Xu et al., 2004).

4.2.3 Hydrogeological conditions

An initial 30 °C temperature and 0.1 MPa pressure are specified in the upper boundary of the column, representing a common global mean temperature in geological history (e.g., the Middle Ordovician, Trotter et al., 2008) and the normal atmosphere in a subaerial setting, respectively. The following cells are calculated based on the geothermal gradient (3 °C/100 m) and formation pressure gradient (0.98 MPa/100 m) (Fig. 4.2c). Given that the chemical composition of seawater varies intensively in geological history and a lack of complete hydrochemical data, the column is assumed to be initially saturated with modern seawater determined according to Nordstrom et al. (1979), representative of the initial pore fluid. The chemical composition of meteoric water is adopted from the ion concentration of modern atmospheric precipitation near the equator (Fattore et al., 2014; Yang et al., 2020a) (Table 4.1). In each simulation, the meteoric water is recharged from the top of the column with a constant rate calculated according to annual rainfall data. Meteoric water then seeps into the deeper column and react with the rock matrix, representing the processes in which the shoal-facies grainstone was exposed and meteoric water infiltrated the pore space during sea-level lowstands. The petrological and hydrogeochemical parameters for base case simulation are

summarized in Table 4.2.

Table 4.1 Hydrochemical features of the fluids used for simulation.

Component (mol L^{-1})	Na^+	Cl^-	K^+	Ca^{2+}	Mg^{2+}	HCO_3^-	SO_4^{2-}	pH
Pore fluid (initial water)	$4.85e^{-1}$	$5.66e^{-1}$	$1.06e^{-2}$	$1.07e^{-2}$	$5.51e^{-2}$	$2.13e^{-3}$	$2.93e^{-2}$	8.22
Meteoric freshwater (boundary water)	$2.32e^{-4}$	$2.28e^{-4}$	$2.53e^{-5}$	$4.28e^{-5}$	$2.47e^{-5}$	$5.08e^{-5}$	$2.82e^{-5}$	5.66

Table 4.2 Controlling parameters used for base case simulation.

Parameters	Values (Source)
Calcite dissolution	$CaCO_3 + H^+ = Ca^{2+} + HCO_3^-$
Dolomite dissolution	$MgCa(CO_3)_2 + 2H^+ = Mg^{2+} + Ca^{2+} + 2HCO_3^-$
Initial porosity	30%
Initial permeability	3.85×10^{-12} m^2
Thermodynamics and kinetics	Thermodynamics for calcite; kinetics for dolomite
Dolomite dissolution rate constants	$2.951e^{-8}$ mol m^{-2} sec^{-1} (neutral); $6.457e^{-4}$ mol m^{-2} sec^{-1} (acid)
Reactive surface area	500 cm^2 g^{-1} for dolomite
Surface temperature	30 °C
Initial water	Modern seawater (Nordstrom et al., 1979)
Boundary water	Modern atmospheric precipitation (Yang et al., 2020a)
Duration of subaerial exposure	5 ka–1 Ma (time range of eogenetic karst)
Rainfall recharge	628 mm/a (average annual rainfall in China)
pCO_2	320 ppm (post-industrial value in the 1970s)

Hydrogeochemical conditions in a vadose meteoric water-rock system can be affected by various factors, such as the geographical location, sea surface temperature, atmospheric CO_2 concentration, seawater chemical composition, initial porosity-permeability heterogeneity and even the root respiration and bacterial decomposition of organic matter in the soil (White, 1988; Whitaker and Smart, 2007). For petroleum geologists, however, a few of these factors are of the greatest concern since they determine the extent and intensity of the palaeokarst, which is critical for reservoir prediction on a regional scale (Zhang and Liu, 2009). Therefore, this paper focuses on the duration of subaerial exposure, climate-related rainfall recharge and atmospheric pCO_2 variation over geological time. Sensitivity analyses (Table 4.3) were performed to reveal

the impacts of these key hydrogeological factors on the eogenetic karst process.

Table 4.3 Summary of the key hydrogeological parameters used for sensitivity analyses.

Simulation number	Lithology	Duration of exposure (ka)	Rainfall (mm/a)	Atmospheric CO_2 concentration (ppm)	Model purpose
1	Limestone	5–1000	628	320	Base case (limestone)
2		5–1000	200	320	Sensitive to rainfall
3		5–1000	400	320	
4		5–1000	800	320	
5		5–1000	628	200	Sensitive to pCO_2
6		5–1000	628	500	
7		5–1000	628	1000	
8		5–1000	628	2000	
9		5–1000	628	3000	
10		5–1000	628	4000	
11		5–1000	628	5000	
12	Dolostone	5–1000	628	320	Base case (dolostone)
13		5–1000	200	320	Sensitive to rainfall
14		5–1000	400	320	
15		5–1000	800	320	

Specifically, evaluating the impact of exposure time on the palaeokarst was mostly based on the classification of subaerial exposure by Saller et al. (1999) in the previous studies (Rameil et al., 2012; Xiong et al., 2019; Xie et al., 2020). However, this classification is only a discrete result (i.e., 5, 50 and 130 ka) of a rough estimate according to pore changes. Numerical simulations in the present study would contribute to establish a continuous quantitative relationship between the exposure time and reservoir porosity changes. The simulation time is 1 Ma, corresponding to the maximum dissolution time of eogenetic karst. The rainfall recharge for the base case simulation is specified as 628 mm/a (expressed as millimeter per year), according to the current average annual rainfall in China. Given the climate variation in different regions, sensitivity analyses are also performed using the other three different rainfall data: 200, 400 and 800 mm/a, representative of a gradual increase in climatic wetness (Yin et al., 2016). The atmospheric pCO_2 for the base case simulation is specified as 320 ppm that

represents a post-industrial value in the 1970s (Cramer, 1993). Moreover, a series of discrete data are adopted in the sensitivity analyses, ranging from 200 to 5000 ppm that represent the low- and high-levels of atmospheric pCO_2 in the geological history (Berner, 1997).

4.3 Simulation results

4.3.1 Duration of subaerial exposure

Eogenetic karst generally occurs in the relatively high positions within a carbonate platform and is controlled by periodic sea-level fluctuations (Xiao et al., 2019; Xiong et al., 2019). Compared with telogenetic karst, which is commonly associated with tectonic uplift, eogenetic karst is characterized by an apparently short period of subaerial exposure. Saller et al. (1999) classified the karst process into four types according to the progressive exposure times and features of dissolved pores: very brief or no subaerial exposure (<5 ka), brief to moderate subaerial exposure (5–50 ka), moderately long subaerial exposure (50–130 ka) and prolonged subaerial exposure (>130 ka). The simulation result of the base case (simulation No. 1) (rainfall = 628 mm/a, pCO_2 = 320 ppm) shows that there is a decreasing trend in the amount of calcite dissolution with increasing distance from the recharging cell of meteoric water on the top of the column (Fig. 4.3a). Both the karst depth penetration and the amount of dissolution gradually increase with increasing exposure time and recharge of seepage water. The amounts of calcite dissolution over the periods of 5 ka, 50 ka and 130 ka are 0.57%, 5.87% and 15.31%, respectively. Moreover, the evolution of rock porosity is highly consistent with the calcite dissolution trend during the simulation in both the depth and time domains (Fig. 4.3b).

4.3.2 Climate-related rainfall recharge

Climate conditions also impact karst mainly by determining the amount of meteoric water recharged into the formation. Generally, the climatic zone can be divided into four types according to the average annual rainfall of a specific area: arid zone (<200 mm/a), semi-arid (200–400 mm/a), semi-humid (400–800 mm/a) and humid (>800 mm/a) (Yin et al., 2016). In the simulation, sensitivity analysis of rainfall recharge is implemented by changing the injection rate of meteoric water from the top of the column. The results (simulations No. 2–4)

show that the burial depth affected by karst, the amount of calcite dissolution (Fig. 4.4a) and rock porosity (Fig. 4.4b) would all increase to a large extent under higher rainfall recharge and relatively humid conditions. At an exposure time of 130 ka, the amounts of calcite dissolution under rainfall conditions of 200 mm/a, 400 mm/a and 800 mm/a are 4.99%, 10.35%, and 18.46%, respectively.

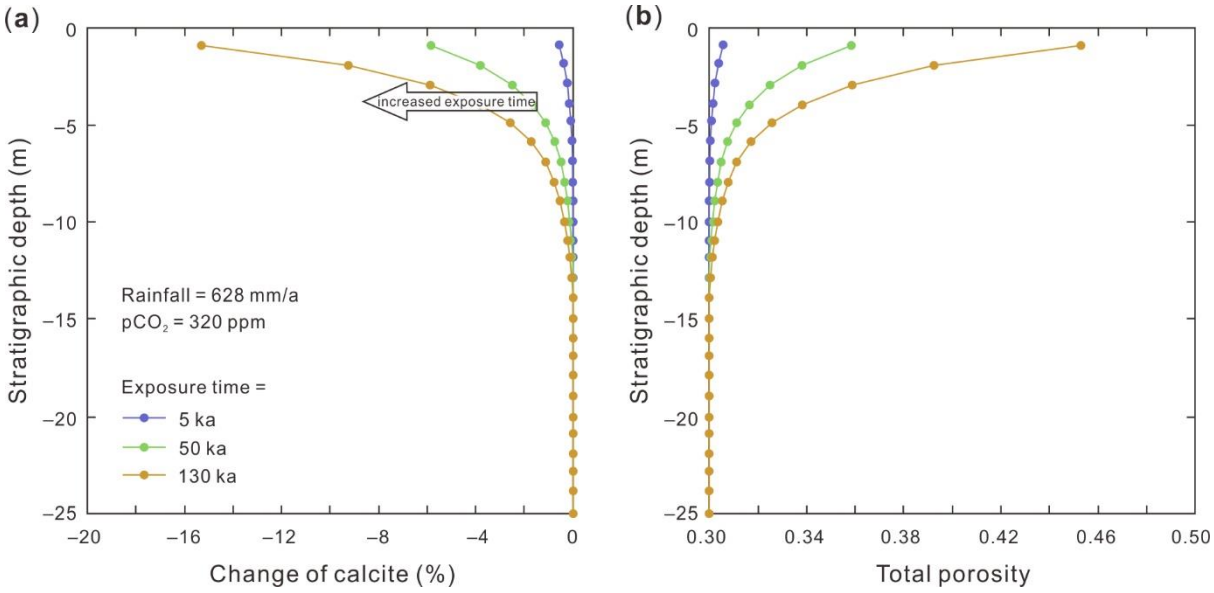

Figure 4.3 Simulation results showing the amount of (a) calcite dissolution and (b) porosity evolution with variation in exposure time.

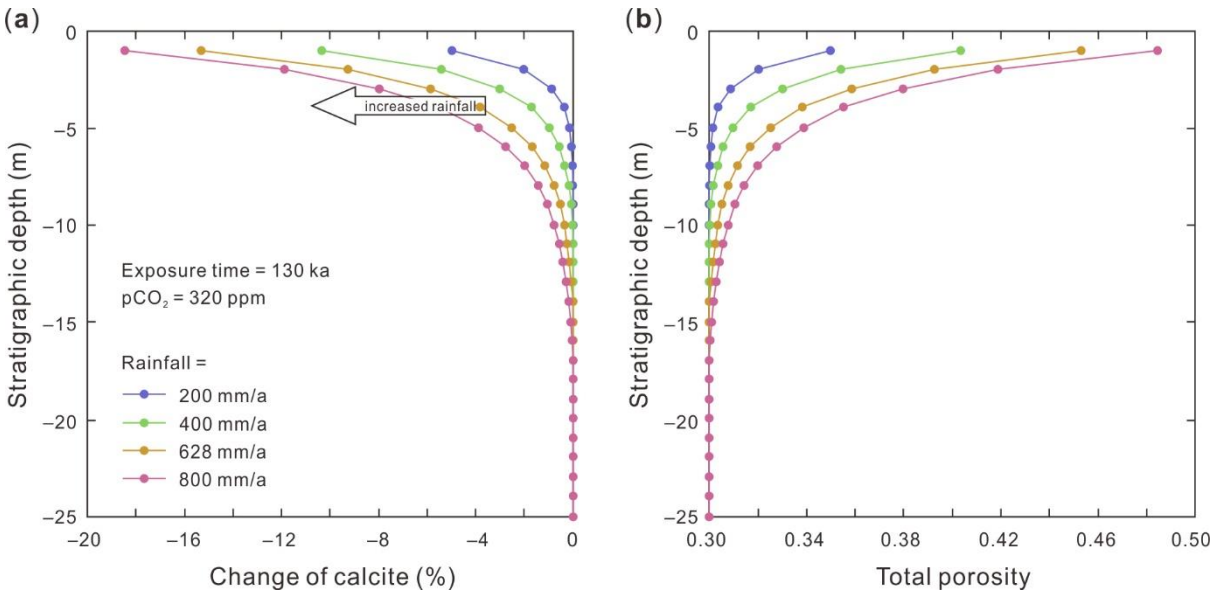

Figure 4.4 Simulation results showing the amount of (a) calcite dissolution and (b) porosity evolution with variation in rainfall recharge.

4.3.3 Atmospheric carbon dioxide concentration over geological history

The atmospheric carbon dioxide concentration (pCO_2) varies intensively during geological history due to the varying intensities of volcanic activity at different geological periods. It affects carbonate dissolution by changing the partial pressure of carbon dioxide and the hydrion (H^+) concentration in meteoric/rain water. This relationship between atmospheric pCO_2 and pH value of rainwater has been approximated by Bogan et al. (2009) and Kong and Long (2014) based on equilibrium calculations of aqueous carbonate systems with regard to rainwater pH values (Fig. 4.5). Simulations (No. 5–11) under different pCO_2 conditions show that the burial depth affected by karst remains almost unchanged (Fig. 4.6). However, there are increasing trends in the amount of calcite dissolution and rock porosity with increasing pCO_2 (Fig. 4.6). For instance, at an exposure time of 130 ka, the amounts of calcite dissolution under pCO_2 conditions of 200 ppm, 500 ppm, 2000 ppm and 5000 ppm are 14.52%, 15.56%, 16.89% and 17.67%, respectively. Generally, an increase in atmospheric CO_2 concentration has a minor impact on the stratigraphic depth affected by karst, while it could promote the dissolution rate of calcite and the increase of porosity.

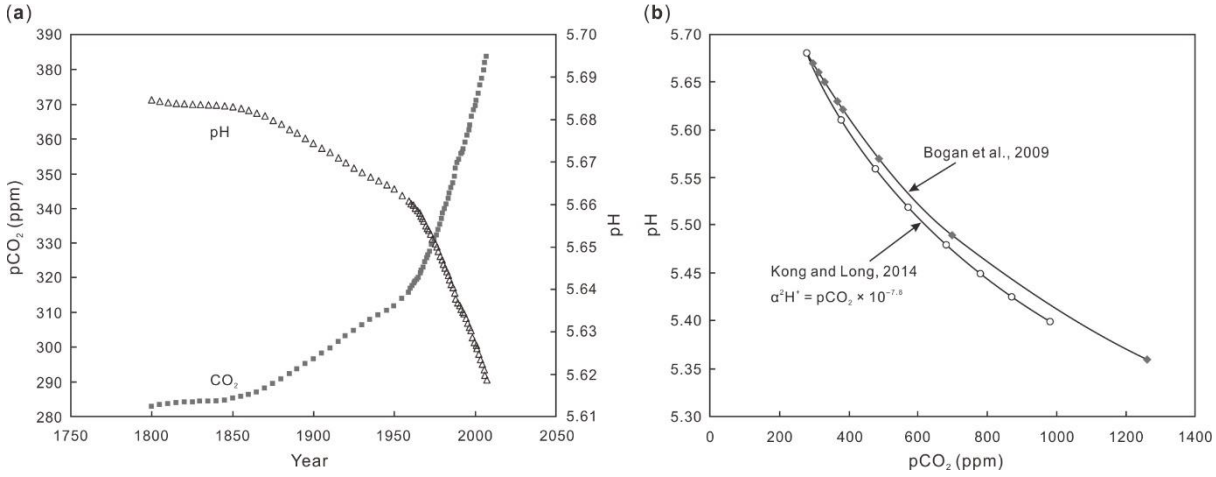

Figure 4.5 The relationship between atmospheric pCO_2 and pH value of rainwater. (a) The historical change in atmospheric pCO_2 and calculated rainwater pH at 25°C and 1 atm (Bogan et al., 2009). (b) Approximate quantitative relationships between atmospheric pCO_2 and rainwater pH (data from Bogan et al., 2009 and Kong and Long, 2014, respectively).

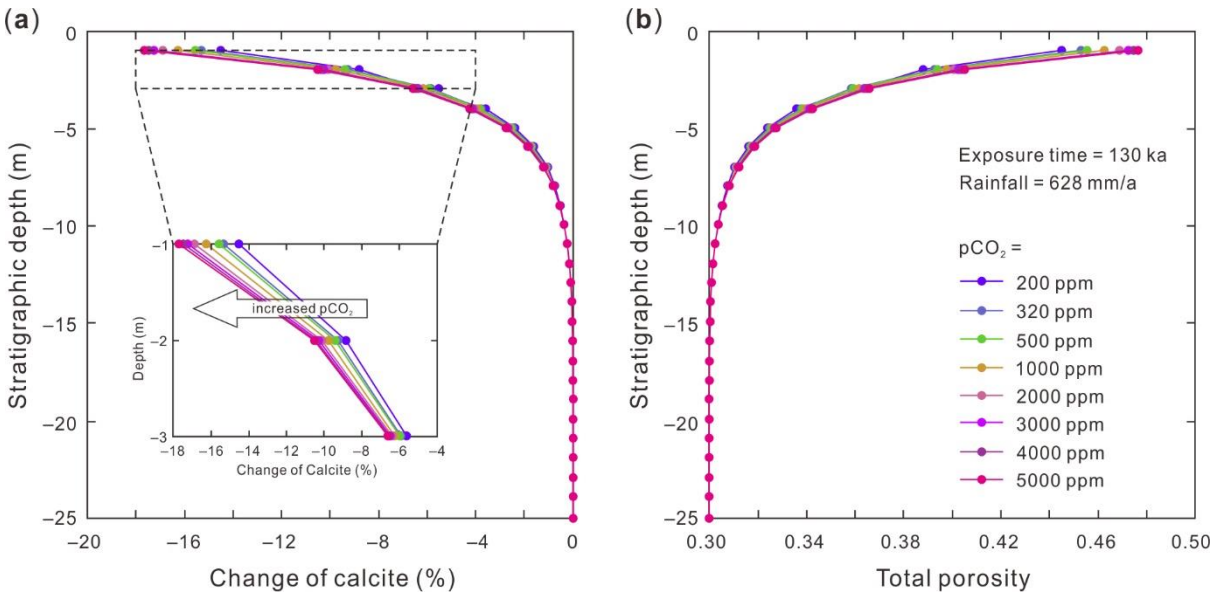

Figure 4.6 Simulation results showing the amount of (a) calcite dissolution and (b) porosity evolution with variation in atmospheric CO_2 concentrations.

4.4 Interpretation and discussion

4.4.1 Vertical extent of karst and porosity increment

Simulation results of the base case and sensitivity analyses have shown that the three extrinsic factors have different influences on karst. To reveal the quantitative relationships between these factors and the vertical extent and intensity of karst, herein we define the karst-affected depth (karsted depth) as the vertical extent in which the amount of calcite dissolution exceeds 1%, and the porosity increment indicates the extracted data at a stratigraphic depth of -1 m.

(1) Exposure time and climatic control of karsted depth

Both exposure time and rainfall recharge impact the karst-affected depth, amount of calcite dissolution and porosity increment (Fig. 4.7). Particularly, in semi-humid to humid areas, an increasing exposure time would significantly enlarge the karst-affected depth, as shown by a depth increased by at least 12.2 m during 1 Ma simulation (Fig. 4.7a). In relatively arid areas, however, the enlargement of karst-affected depth (up to 4.0 m) caused by increases in exposure time (1 Ma) is apparently smaller than that in humid areas. Generally, under the same condition of exposure time, a humid climate (rainfall ≥ 800 mm/a) would lead to a large vertical extent of karst that is greater than three times that in an arid climate (rainfall ≤ 200 mm/a) (Fig. 4.7a,

b). This indicates that a relatively humid climate would contribute to a deeper meteoric diagenetic environment and the formation of thick-bedded reservoirs. Our data interpretation is comparable to previous field studies and hydrogeochemical modeling of karst on modern carbonate islands (Whitaker and Smart, 2007; Paterson et al., 2008; de Periere et al., 2017), which highlight the climate control (rainwater fluid flux) on karst and as shown by apparently greater vadose zone depths and higher dissolution rates on wet islands than on dry islands.

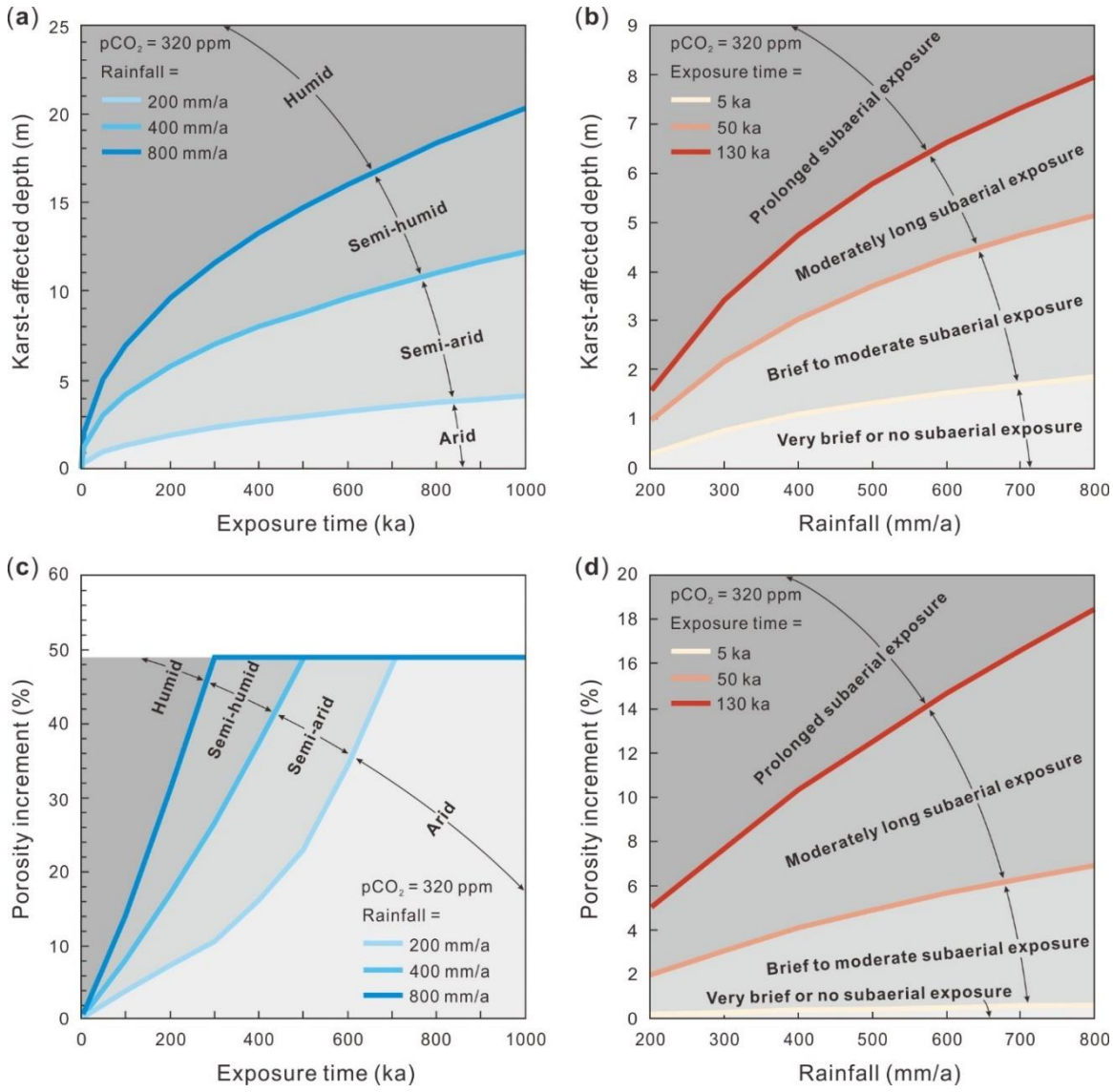

Figure 4.7 Calcite dissolution collectively controlled by exposure time and climate-related rainfall recharge. (a) Karst-affected depth as a function of exposure time under different climate conditions. (b) Karst-affected depth as a function of rainfall during different stages of subaerial exposure. (c) Porosity increment (at stratigraphic depth = -1 m) as a function of exposure time under different climate conditions. (d) Porosity increment as a function of rainfall during different stages of subaerial exposure.

Furthermore, during the simulation, there is an increase trend in porosity-permeability due to successive calcite dissolution (Fig. 4.8a–c). Although the positive feedback between increasing dissolution and flow would theoretically accelerate rainwater flow to greater depths (Kaufmann, 2016), the simulation results show that the increase in karsted depth gradually slows with time (Fig. 4.7a). This is likely related to an elevated calcite saturation index in the lower part of the column because of Ca^{2+} and HCO_3^- released during calcite dissolution and then enriched in the front of the flow path (Fig. 4.8e, f). Meanwhile, the ambient geothermal gradient has been revealed to be an important factor affecting the calcite dissolution/precipitation processes in vadose systems because a downward increase in the temperature can result in a concomitant decrease in calcite solubility (Whelan et al., 2002). Moreover, the downward seepage of rainwater might have been limited by the gradually increasing strata pressure, and thus the decreasing amount of calcite dissolution in the lower column may also be a result of lateral flow that is not captured in the one-dimensional simulations in the present study. Generally, the simulation results are consistent with extensive geological observations from outcrops and boreholes in which the eogenetic karst-controlled reservoirs developed mostly in relatively thin diagenetic lenses just several meters below the exposure surfaces (Shen et al., 2015).

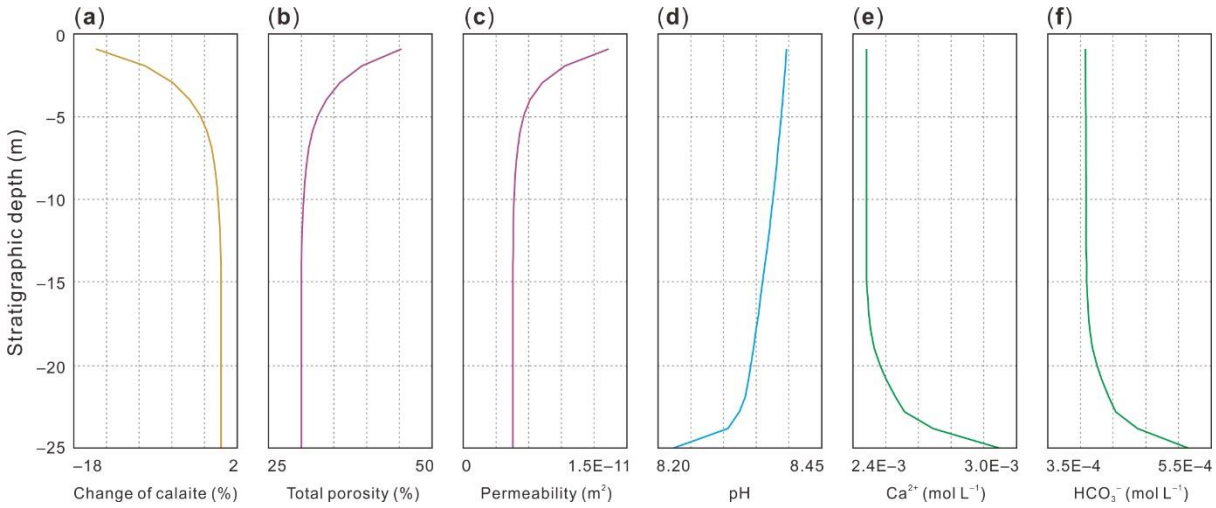

Figure 4.8 Depth profiles showing the distribution of (a) the amount of calcite dissolution; (b) rock porosity; (c) rock permeability; (d) pH value of pore fluid; (e) Ca^{2+} concentration and (f) HCO_3^- concentration of the base case simulation (rainfall = 628 mm/a, pCO_2 = 320 ppm) at an exposure time of 130 ka.

(2) Porosity changes with varying pCO_2 in geological history

Atmospheric carbon dioxide concentration controls the dissolution rate of calcite in CO_2-containing aqueous solutions mainly by changing the chemical composition of the $CaCO_3$(s)-H_2O(l)-CO_2(g) system at the water-mineral interface (Kaufmann and Dreybrodt, 2007; Bogan et al., 2009). Generally, higher pCO_2 is conducive to the conversion of CO_2 into H^+ and HCO_3^- in the solution and thus facilitates carbonate minerals (e.g., calcite and dolomite) dissolution (Eq. 2.5; Fig. 4.6). Nevertheless, the vertical fluid flow in the vadose meteoric water-rock system is nearly unaffected by the variation in pCO_2, as indicated by the similar karst-affected depths under various atmospheric pCO_2 conditions (Fig. 4.6a). Our simulation results are consistent in an overall trend with previous numerical models and core experiments (Buhmann and Dreybrodt, 1985; Maddah et al., 2020) and have shown that pCO_2 is a major rate-determining factor of meteoric water-rock interactions in carbonate rocks. Furthermore, to quantitatively evaluate/reconstruct the impact of atmospheric pCO_2 variation over the prolonged geological periods on the eogenetic karst process and resulting reservoir porosity evolution, discrete data obtained from the simulations based on sensitivity analysis were first plotted and fitted in Fig. 4.9a. According to the logarithmic function describing the relationship between pCO_2 and the porosity increment (at stratigraphic depth = -1 m), the variation in atmospheric pCO_2 over geological time (Fig. 4.9b) (Berner, 1997) can then be transferred into the evolution of the porosity increment with geological time under specific hydrogeological conditions (herein illustrated by the base case scenario with exposure time = 130 ka and rainfall = 628 mm/a; Fig. 4.9c).

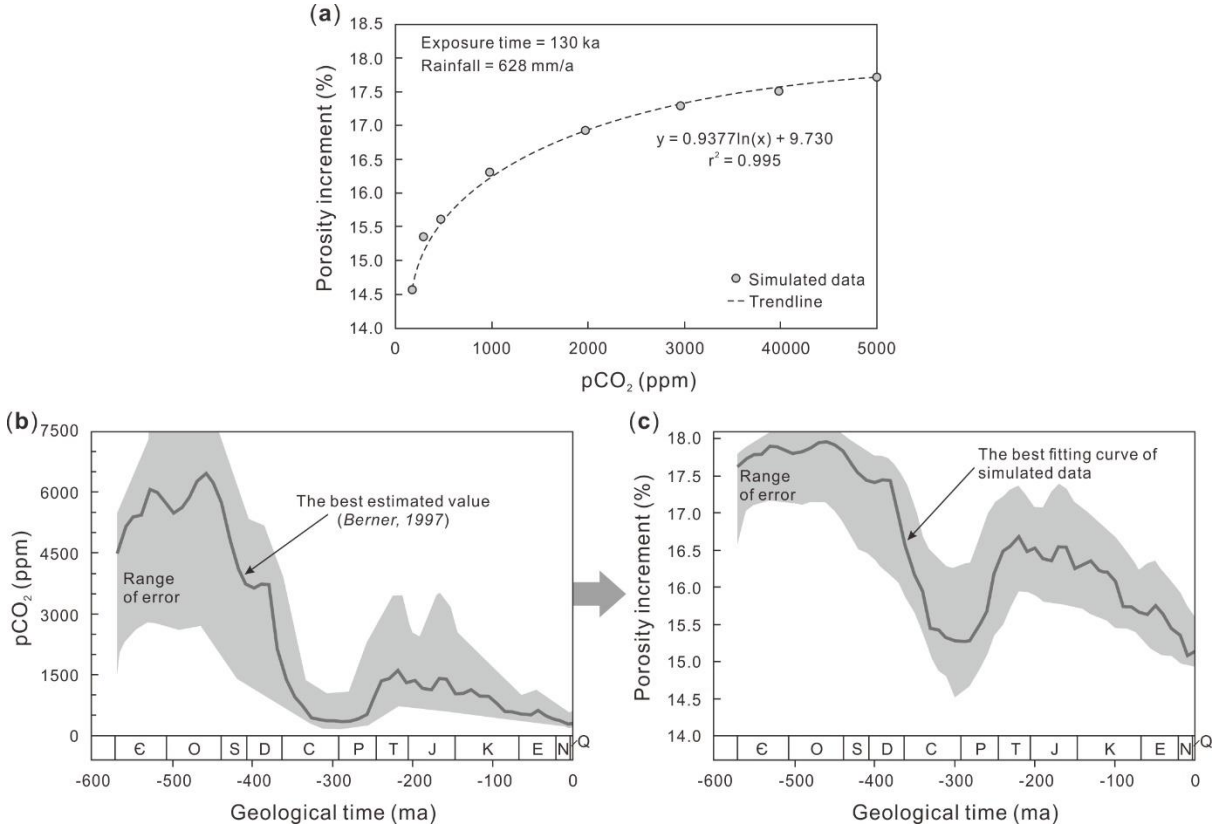

Figure 4.9 (a) Results of sensitivity analysis of atmospheric CO_2 concentrations showing the logarithmic relationship between pCO_2 and the porosity increment (at stratigraphic depth = -1m). (b) Variation in the atmospheric CO_2 concentrations over geological time (modified from Berner, 1997). (c) Estimated variation in the porosity increment over geological time based on the logarithmic function in (a).

4.4.2 Calcite vs. dolomite

Apart from the above extrinsic factors (i.e., duration of exposure, rainfall and pCO_2), intrinsic factors, especially the rock types (lithofacies), might also have significant influences on the development and porosity evolution of carbonate reservoirs. Sustained lab experiments on the dissolution of carbonate rocks have shown that limestone is preferentially dissolved over dolostone, especially under shallow-burial environments (e.g., Liu et al., 2005; Genty et al., 2012; She et al., 2016; Maddah et al., 2020). In the present study, comparative simulations of limestone and dolostone were performed under the same hydrogeological conditions (base case scenario), showing that the amount of dolomite dissolution and its porosity increment are apparently lower than that of calcite (Fig. 4.10). These numerical results are comparable to

experimental data of previous laboratory studies and have indicated that limestone sediments, without experiencing early dolomitization, tend to have a higher vertical extent of karst zone and porosity increment during eogenetic diagenesis under near-surface environment. Similar phenomena have been widely documented in hydrocarbon carbonate reservoirs, such as the Cretaceous Mishrif Formation in the Halfaya oilfield, Middle East, the Cambrian Longwangmiao Formation and the Permian Changxing Formation in the Sichuan Basin, China, where eogenetic karst features and high-porosity zones mostly occur within limestone (Lu et al., 2019; Zhong et al., 2019; Li et al., 2020).

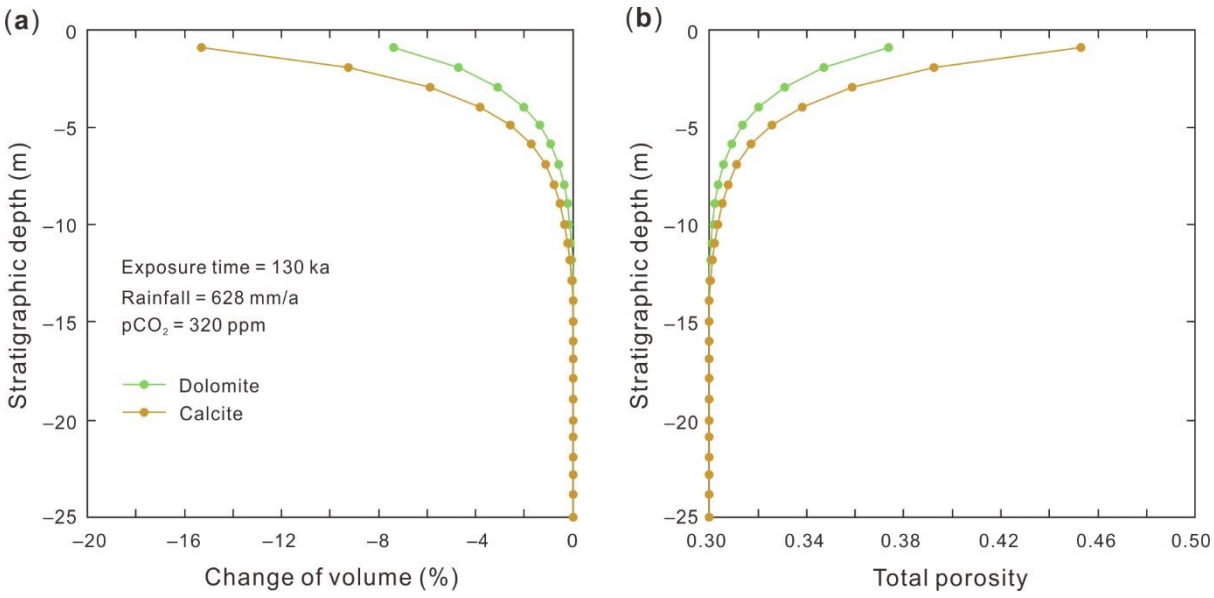

Figure 4.10 Comparative simulations of calcite and dolomite showing that (a) the amount of dissolution and (b) the porosity increment of dolomite are lower than that of calcite.

Although there has been extensive work documenting the difference in dissolution between limestone and dolostone, the causes remain controversial. Some researchers suggest that this difference is mainly due to the relatively higher influence of varying temperature and pressure on the dissolution of dolomite than calcite, and the difference between these two minerals tends to be reduced under deep-burial conditions (Yang et al., 1995; Tan et al., 2017). Other studies, however, tend to believe that the relatively lower reactivity of dolostone is mainly caused by its complicated dolomite surface speciation in aqueous systems, which inhibits the mass transport of ions (i.e., Mg^{2+}) into solution from rock surfaces via diffusion (Liu et al., 2005; Pokrovsky et al., 2005, 2009; Perez-Fernandez et al., 2017). In particular, dolomite is rarely

generated in modern seawater environments or laboratory conditions (25°C, 1 atm), although modern seawater is thermodynamically supersaturated with respected to dolomite (Lippmann, 1982; Land, 1998). These studies have dramatically improved our understanding of the mechanism that the dissolution/precipitation of dolomite is generally kinetically controlled while that of calcite is thermodynamically controlled (Palandri and Kharaka, 2004; Xu et al., 2004). This difference in rate-determining reaction mechanisms has been adopted in the reactive transport simulations in the present study, which provides a new clue in interpreting the difference in dissolution and porosity evolution between limestone and dolostone during eogenetic diagenesis.

In comparison with telogenetic karst, eogenetic karst has a relatively short duration of subaerial exposure, generally less than 1 Ma (Xiao et al., 2016; Yang et al., 2020a). In this case, a short period of time has become a crucial factor limiting the degree of kinetic reaction (i.e., dissolution/precipitation processes of dolomite). A statistical truism that the dolomite abundance (relative to limestone) progressively increases with stratigraphic age has also highlighted the importance of time accumulation for dolomite precipitation occurring very slowly at geological timescales (Given and Wilkinson, 1987; Warren, 2000; Ning et al., 2020). For equilibrium minerals (e.g., calcite), however, the reaction will reach thermodynamic equilibrium in a relatively short period depending on the mineral saturation state. Moreover, eogenetic karst generally occurs in near-surface to very shallow-burial environments, with a relatively low temperature. According to the Arrhenius equation describing the temperature-dependent rate constant (Steefel and Lasaga, 1994; Xu et al., 2004), the reaction rate of kinetic minerals is proportional to temperature, and thus, a low temperature in a subaerial environment would lead to a low dissolution rate of dolomite. In contrast, the solubility of calcite is inversely proportional to temperature (Whelan et al., 2002), and this low-temperature condition contributes to a higher calcite solubility and eventually an enhanced dissolution and reservoir porosity (Morse and Arvidson, 2002). Hence, the smaller karst-affected depth of dolostone (e.g., 12.59 m at 1 Ma) than that of limestone (e.g., 20.37 m at 1 Ma) is likely the result of the lower dissolution rate of dolomite (Figs. 4.7a, b and 4.11a, b), although the flow paths and diffusion depths of meteoric water in these two rock matrices are highly similar. At equilibrium,

the maximum porosity increments of dolostone and limestone are the same (Figs. 4.7c, d and 4.11c, d) and are mainly determined by the chemical composition of the meteoric water. Even so, the time required for dolostone to reach equilibrium is larger than that for limestone, which also reflects the importance of time accumulation to the kinetic reaction.

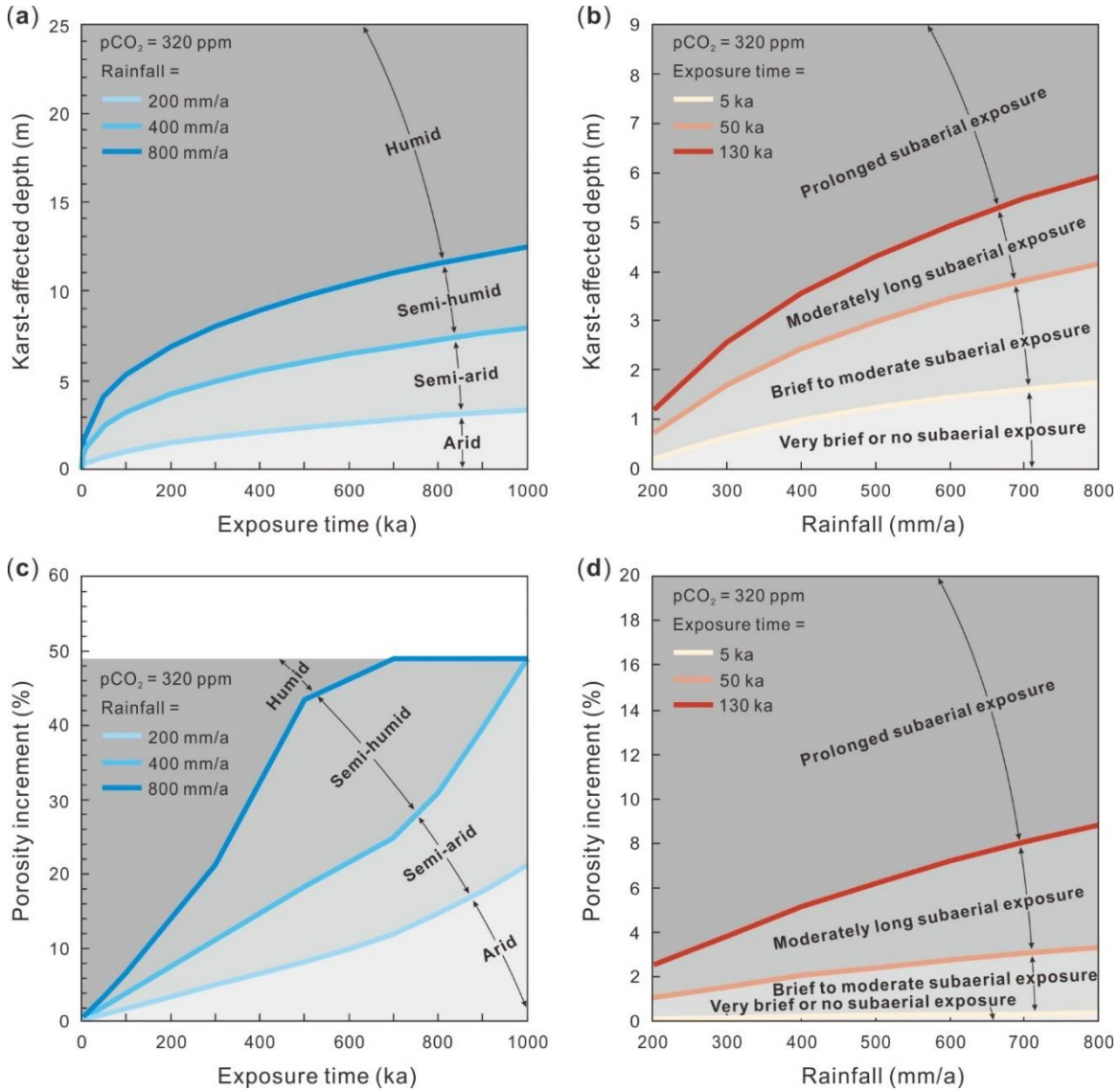

Figure 4.11 Dolomite dissolution collectively controlled by exposure time and climate-related rainfall recharge. (a) Karst-affected depth as a function of exposure time under different climate conditions. (b) Karst-affected depth as a function of rainfall during different stages of subaerial exposure. (c) Porosity increment (at stratigraphic depth = -1 m) as a function of exposure time under different climate conditions. (d) Porosity increment as a function of rainfall during different stages of subaerial exposure.

Furthermore, to determine the relative importance of different controlling factors, the karst-

affected depth was plotted versus exposure time and rainfall; this plot shows that the promotion effect of calcite dissolution resulting from increasing rainfall would be more significant than an increasing exposure time (Fig. 4.12a). For dolomite, however, the relative importance of increasing rainfall has been weakened (Fig. 4.12b), which exhibits the restriction of a relatively low kinetic rate on dolomite dissolution even under high fluid flux conditions.

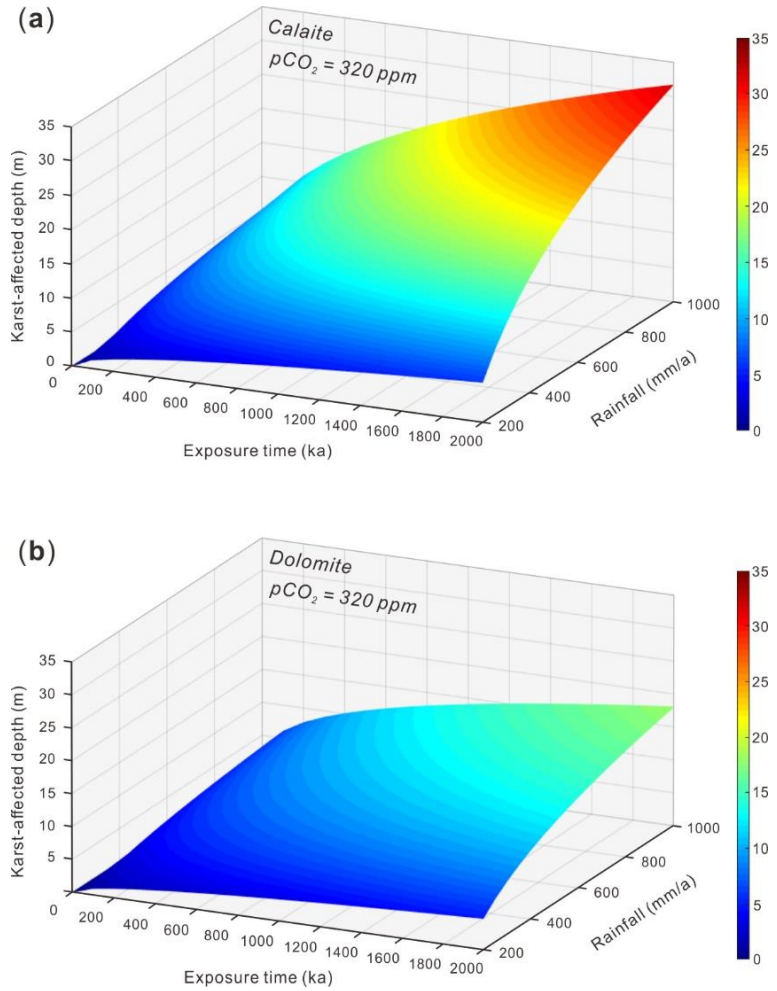

Figure 4.12 Three-dimensional surface diagrams showing the karst-affected depth versus exposure time and rainfall recharge for (a) calcite and (b) dolomite.

It should also be noted that the carbonate dissolution and porosity changes could not directly represent the present pore characteristics since no burial diagenesis was taken into account in the current simulations and some simplifications are necessary in all modeling approaches. Nevertheless, the karst-affected depth during eogenetic diagenesis generally determines the vertical extent of karst systems and the preferential zones for burial diagenetic alteration, thus providing potential predictions of paleokarst-related carbonate reservoirs, especially for intra-

platform thin-bedded shoal reservoirs controlled by periodic sea-level fluctuations. This chapter simulates the coupled flow and geochemical processes of eogenetic fluid-rock interactions in a generic column model and provides a semi-quantitative evaluation of the impacts of key geological parameters on the paleokarst process as well as a new clue for carbonate reservoir quality prediction.

4.4.3 Limitations of the continuum model

From the perspective of petroleum geology, a fundamental challenge in palaeokarst-related reservoir characterization and prediction is the accurate constraint of diagenetic alteration with porosity distribution via leaching by meteoric water at multiple spatial and temporal scales. In the present study, although semi-quantitative evaluations of the controls on eogenetic karst have been carried out on three extrinsic factors (i.e., duration of exposure, rainfall and pCO_2) and one intrinsic factor (i.e., rock types), there are still some limitations since the current model fails to replicate features such as the heterogeneity in diagenetic alteration and the changes in rock structures. Specifically, an assumption for the continuum-scale system is that the chemical species in each phase are completely mixed, leading to a uniform distribution of species concentrations and reaction progression. However, in a natural marine carbonate platform, the complexity of petrofabrics and sedimentary structures (e.g., gypsum nodules, insoluble organic-rich bio-framework in microbialites) could result in strong heterogeneity in rock reactivity, i.e., fabric-selective dissolution (Stoffers and Müller, 1979). The frequent sea level fluctuations also lead to the superposition of karstification in multiple periods and ultimately an extremely complicated process of porosity evolution (Xiong et al., 2019, 2021c).

Meanwhile, although the classical Kozeny-Carman relation, as discussed earlier in this chapter, is regarded to be applicable for this unique eogenetic karst system (soft-rock karst), the use of this porosity-permeability relation and a Darcy flow approximation may not be adequate to describe the flow, transport and porosity-permeability changes within other types of karst system, e.g., the telogenetic karst system (hard-rock karst). This is mainly because the mobility and reactivity of the meteoric water in a telogenetic karst system are largely controlled by the fracture porosity and conduit flow in which the fluid concentration gradients from the center

of the channel to the walls may develop (Hao et al., 2013; Kaufmann, 2016). Moreover, strong karstification is usually accompanied by collapse of overlying strata and numerous weathering product such as weathering crusts, palaeosols, caliche and bauxite (James and Choquette, 1987; MacLean et al., 1997; Tan et al., 2015), leading to the formation of irregular collapse breccias and mixed infills of dissociated carbonate fragments (i.e., chaotic clasts-supported structures) in the early-formed dissolved pores (Xiao et al., 2016; Xie et al., 2020). These uncertainties have all introduced great difficulties in description of mineral reaction and porosity-permeability relation in a complicated karst system. Hence, the coupling of sedimentary heterogeneity, diagenetic geochemical reactions and changes in rock structures needs further exploration in the reactive transport modeling of paleokarst and associated hydrocarbon reservoirs evolution.

4.5 Summary

In this chapter, the RTM method was employed to investigate the distribution and evolution of minerals (i.e., calcite and dolomite) and rock porosity in a one-dimensional vadose meteoric water-rock system. Based on sensitivity analysis, the impacts of several key extrinsic (hydrogeological parameters) and intrinsic (limestone/dolostone) factors on the fluid-rock interactions and reservoir porosity evolution during eogenetic karst were quantitatively evaluated. From a hydrocarbon geological perspective, the relative importance of these factors in promoting high-quality carbonate reservoirs was also discussed. The present chapter was published in a similar form in the *Applied Geochemistry* (Xiong et al., 2021a) and the main conclusion are as follows.

In a vadose eogenetic karst system, there is a downward decreasing trend in carbonate dissolution and rock porosity. The exposure time and rainfall recharge significantly determine the karst-affected depth and porosity increment. The amount of calcite dissolution is also affected by a downward decrease in calcite solubility (temperature-dependent) and the enrichment of Ca^{2+} and HCO_3^- in the lower part. The promotional effect of calcite dissolution from increasing rainfall is more significant than an increasing exposure time.

The atmospheric carbon dioxide concentration is a major rate-determining factor of meteoric water-rock interactions in carbonate rocks. Although the pCO_2 has a minor impact on the extent of karst, it facilitate the dissolution rate of carbonate rocks under high pCO_2 conditions. The influence of atmospheric pCO_2 variation over geological time on the porosity increment during eogenetic karst was reconstructed under conditions of a base case scenario.

In a near-surface low-temperature environment, limestone tends to have higher dissolution rate and karst-affected depth than dolostone during eogenetic karst process due to their different rate-determining reaction mechanisms, i.e., thermodynamically controlled calcite and kinetically controlled dolomite.

5 Case study of hydrocarbon reservoir in the Ordos Basin, China

5.1 Geological background

5.1.1 Tectonic and sedimentary characteristics

The Ordos Basin is a large, superimposed basin located in the western North China Block (Fig. 5.1a), with an area of ~250 × 10^3 km^2 (Feng et al., 1998). During deposition of the Middle Ordovician Majiagou Formation, the Ordos Basin was structurally affected by a paleo-uplift (namely the Central Uplift), which resulted in significant changes to the paleogeography and depositional environment (Fig. 5.1b). West of the paleo-uplift was an epicontinental sea, where tidal flat, carbonate platform and shelf deposits developed (Chen et al., 2019). To the north and east of the paleo-uplift, a semi-closed, intracratonic epeiric sea dominated the area, and two secondary tectonic units (i.e., the Yishan Slope and Shanbei Depression) can be recognized according to geomorphic changes from west to east (Fu et al., 2017; Chen et al., 2018; Galamay et al., 2019). In particular, the subsalt Majiagou Formation (i.e., $Ma5_7$ to $Ma5_{10}$) in the Yishan Slope was dominated by shallow-marine carbonates deposited in the facies of tidal flat, intra-platform shoals, dolomite platform flat and lagoons (Fig. 5.1c). These carbonate intervals form potential source rocks and hydrocarbon reservoirs (Wang and Al-Aasm, 2002). Specifically, The eighth ($Ma5_8$) and tenth ($Ma5_{10}$) submembers mostly comprise gypsiferous and argillaceous rocks interpreted to have been deposited under conditions of a dry and hot climate as well as high salinity. The seventh ($Ma5_7$) and ninth ($Ma5_9$) submembers mostly consist of carbonate rocks deposited during intermittent marine transgression. Intra-platform shoal-facies dolomite can be found within these latter submembers, and forms as the major hydrocarbon reservoir rock (Fig. 5.2b) (Fu et al., 2019). The Shanbei Depression was characterized by a high-salinity evaporative lagoon environment during sea level regressions, where massive deposits of gypsum and halite formed ($Ma5_6$) and served as favorable regional cap rocks in the Ordos Basin. Alternatively, during sea level transgressions (i.e., $Ma5_7$ and $Ma5_9$ periods), the Shanbei Depression was characterized by low salinity and well seawater exchange, in which limestone sediments are dominant (Fig. 5.1c).

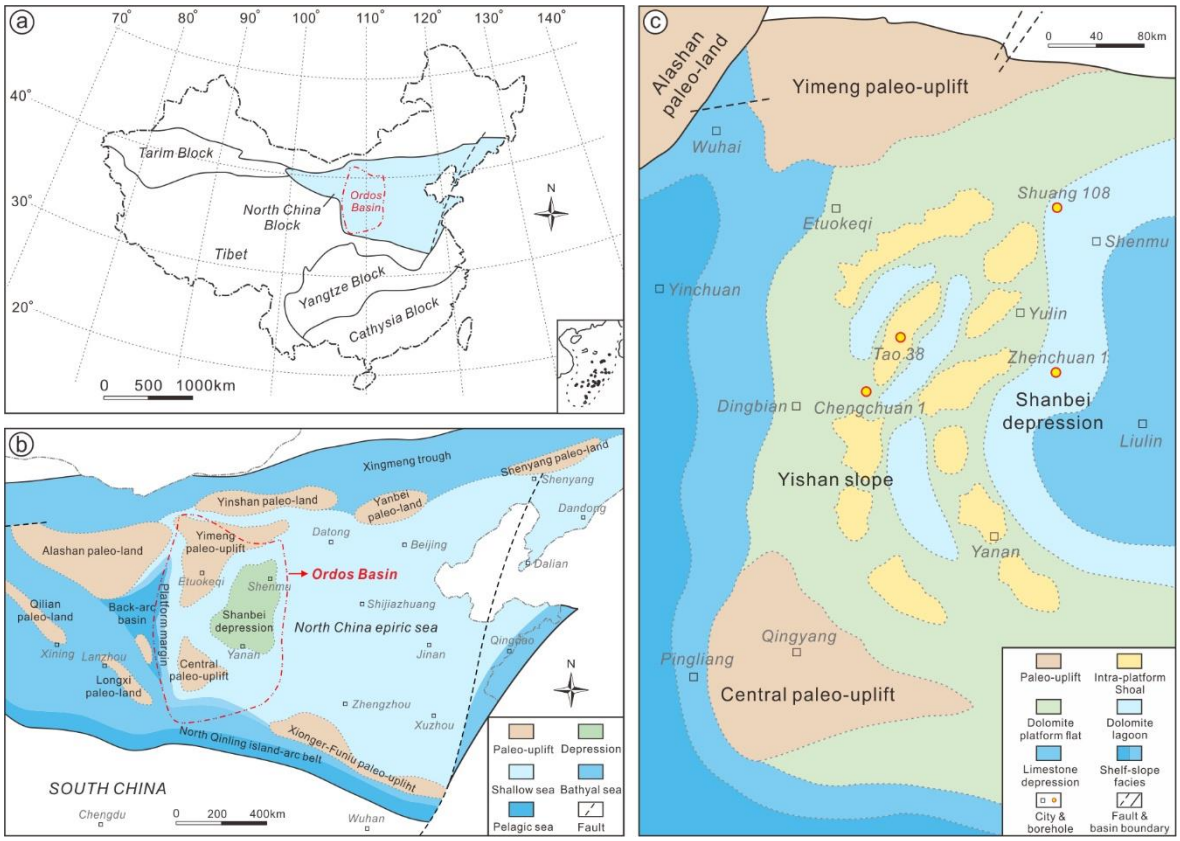

Figure 5.1 Geological setting of the Middle Ordovician Ordos Basin. (a) Simplified sketch map showing the position of the North China Block and the Ordos Basin. (b) Paleogeographic map of the North China Block during the Middle Ordovician showing major structural units and the location of the Ordos Basin (modified after Chen et al., 2018). (c) Larger-scale map of the Ordos Basin, outlined in (b), which shows the distribution of sedimentary facies during sea level transgressions of the Majiagou stage (i.e., the $Ma5_7$ and $Ma5_9$ periods; modified after Fu et al., 2017).

Due to compressional tectonic events at the periphery of the North China Block, the Ordos Basin records periodic sea level regressions and evaporatic environments during the Middle Ordovician (Chen et al., 2019; Liu et al., 2019). As such, the Majiagou Formation is made up of multisets of carbonate-evaporite successions (Fig. 5.2b). Meanwhile, multi-stage hiatuses in deposition and eogenetic karst have also been identified in the core records of carbonate intervals (Fu et al., 2019; Xiong et al., 2019; Xie et al., 2020). These short-term periods of penecontemporaneous karstification, which stack vertically, have been shown to be associated with Middle Ordovician high-frequency sea level fluctuations and intermittent subaerial

exposure of local paleo-highs (Xiong et al., 2019; Liu et al., 2020). After deposition of the Majiagou Formation, the North China Block was greatly uplifted due to the Caledonian orogeny from the Late Ordovician to the Early Carboniferous (Wang and Al-Aasm, 2002; Meng et al., 2019). The Ordos Basin was thus subjected to prolonged weathering and leaching by meteoric water over a period of about 130 Ma (Fig. 5.2a) (He et al., 2013; Xiao et al., 2019), which ultimately gave rise to the formation of the large-scale weathering crust at the top of the Majiagou Formation and the superimposition of eogenetic and telogenetic karst.

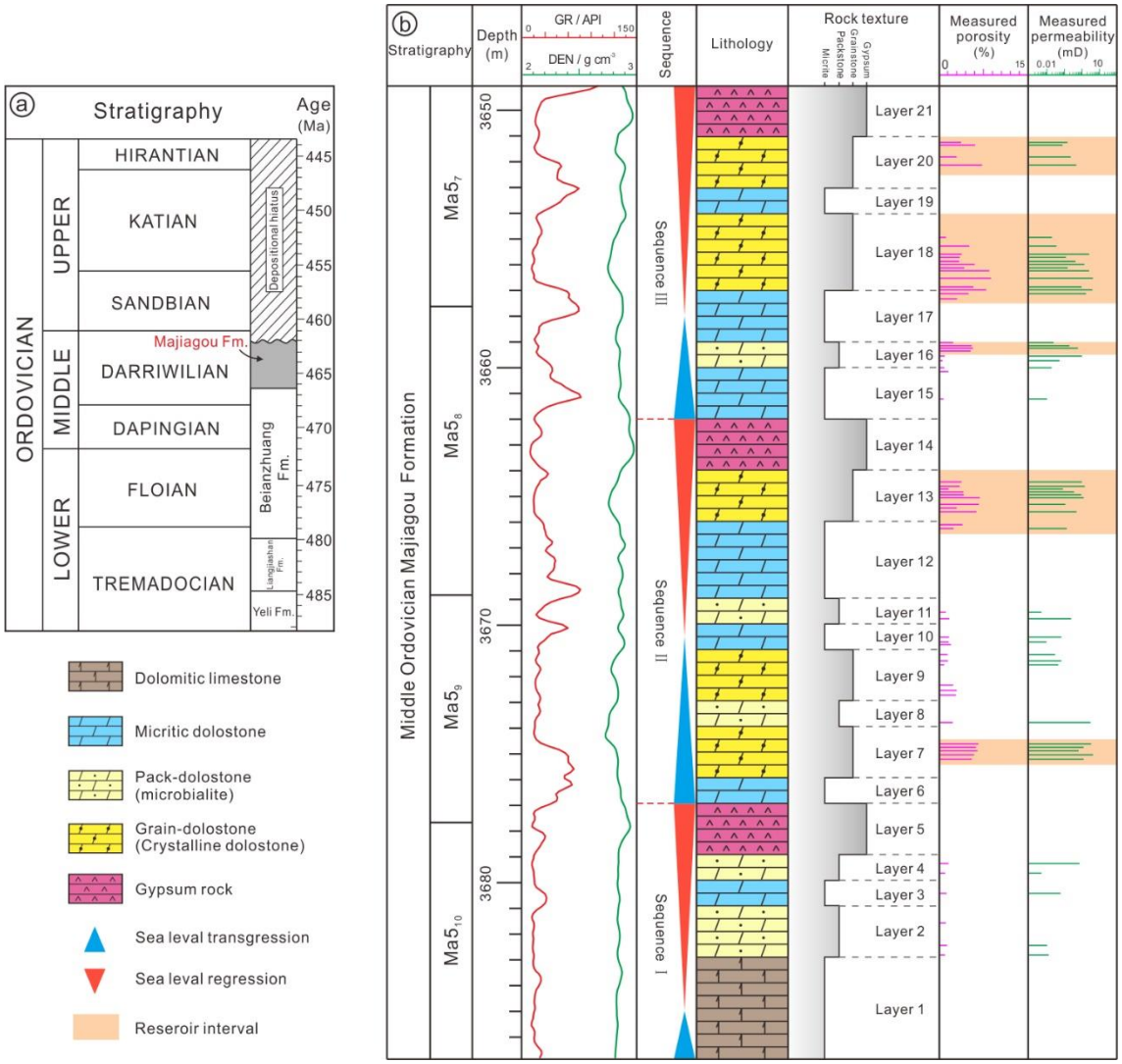

Figure 5.2 Stratigraphy and lithology of the sub-salt Majiagou Formation (i.e., Ma5$_{5–10}$). (a) Ordovician time scale (after Haq and Schutter, 2008) and simplified chronostratigraphic framework for the Ordos Basin (absolute ages after Zhang et al., 2019). (b) Comprehensive stratigraphic column of Well Jintan1 showing the lithology, rock textures, depositional sequences, measured porosity-permeability and distribution of reservoir rocks.

5.1.2 Characteristics of reservoir rocks

Based on detailed macro and micro petrographic observations of drill cores and thin sections in the Ordos Basin, two major types of reservoir pore were identified in the sub-salt Majiagou Formation (Fig. 5.3), including the dissolved pores (and vugs) in granular dolostone and the intercrystalline pores in crystalline dolostone (although fenestral pores in microbialites have also been found occasionally, they were not discussed in the present study due to a very small proportion). The dissolved pores- and intercrystalline pores-dominated reservoir spaces distribute mostly in the carbonate intervals of $Ma5_7$ and $Ma5_9$ sub-members and form the major hydrocarbon reservoir rocks in this area. In terms of porosity genesis, they have been revealed to be closely related to the eogenetic karst and dolomitization (superimposed by burial recrystallization), respectively (Fu et al., 2019; Xiong et al., 2020a).

To be specific, the dissolved pores (and vugs) developed mainly in the shoal-facies grainstone such as dolarenite and oolitic dolostone (Fig. 5.3a). They are the results of dissolution and expansion of primary intergranular or intragranular pores. Exposure and erosion surfaces can be frequently found at the top of karst-affected grainstone. These pores (and vugs), generally 0.05–0.3 mm in size, exhibit irregular shapes under the microscope (Fig. 5.3b–c). Occasionally, the pores (and vugs) can be half-infilled by dissociated carbonate fragments from the ambient rock matrix and pore cements including gypsum and coarse-grained calcite and dolomite, forming the geopetal structure.

Intercrystalline pores are widely observed in the finely to medium crystalline dolostone (Fig. 5.3d–f). The dolomite crystals are 50–200 μm in size, euhedral to subhedral, and poikilotopic. The formation of these pores are related to early-stage reflux dolomitization and intense burial recrystallization (Xiong et al., 2020b). Under the microscope, the intercrystalline pores are generally polygonal and 0.1–2.0 mm in size and have angular shapes. Besides, the distribution of intercrystalline pores is sometimes controlled by the primary granular structure, as shown by relict textures of precursor grains in the crystalline dolostone (Fig. 5.3e). This indicates that this type of reservoir is also associated with shoal-facies grainstone.

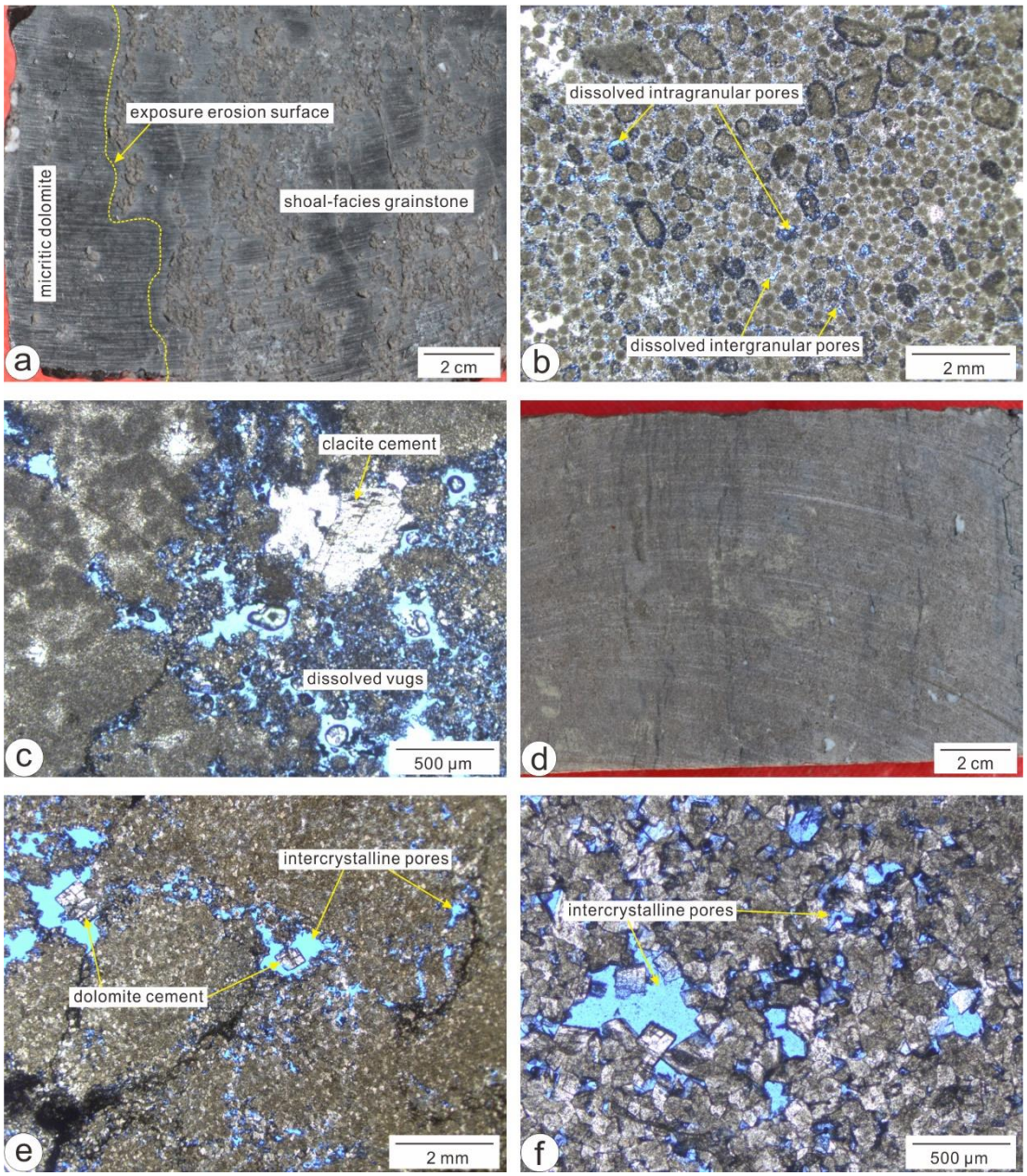

Figure 5.3 Reservoir rocks and pore characteristics of the sub-salt Majiagou Formation in the Ordos Basin. (a) Core photograph of shoal-facies grainstone with obvious karst features. Erosion surface (yellow line) can be found at the top of grainstone, overlaid by micritic dolostone. Well Jin4, 3,670.89 m. (b) Photomicrograph of grainstone (oolitic dolostone) with abundant intergranular and intragranular pores. Well Jin2, 3,587.83 m, blue casted thin section. (c) Photomicrograph of grainstone (dolarenite) with abundant dissolved pores and vugs. Well Jin4, 3,671.42 m. (d) Core photograph of crystalline dolostone with numerous tiny pores homogeneously distributed in core. Well Tao17, 3,782.39 m. (e) Photomicrograph of crystalline dolostone with well-preserved intercrystalline pores and only a few coarse dolomite cement. Note the distribution of intercrystalline pores are still controlled by residual granular

structures. Well Tao38, 3,631.33 m. (f) Photomicrograph of crystalline dolostone with well-preserved intercrystalline pores. Well Tao38, 3,630.56 m.

In comparison with other old, superimposed basins, numerous studies have shown that the sub-salt Majiagou Formation in the Ordos Basin underwent relatively weak diagenetic alteration during the prolonged burial process (Fu et al., 2019; Liu et al., 2020). Except for the inevitable compaction of ancient strata, the studied rocks was relatively less affected by burial diagenesis because the interbedded gypsum layers strongly impeded the diffusion and superimposition of burial fluids such as basinal brines and magmatic hydrothermal fluids. Consequently, abundant petrological and reservoir features related to the reflux dolomitization and eogenetic karst have been well-preserved in the carbonate intervals, providing a valuable case study to investigate the dolomitization and paleokarst processes, as well as their impacts on hydrocarbon reservoir properties. Combining the abundant geological data and the RTM approach as discussed in the previous two chapters, the follow part investigate the two key types of carbonate diagenesis in the sub-salt Majiagou Formation in the Ordos Basin, i.e., multistage reflux dolomitization and facies-controlled eogenetic karst.

5.2 Multistage reflux dolomitization of carbonate-evaporite successions

5.2.1 Conceptual geological model and grid system

The model design of reflux dolomitization simulation is based on regional geology and drilling data (particularly petrographic analysis) from the Middle Ordovician Majiagou Formation in the Ordos Basin, North China. In generally, the Majiagou Formation is characterized by multi-sets of carbonate-evaporite successions, with favorable hydrocarbon exploration target of granular and crystalline dolomites (Fu et al., 2019; Xiong et al., 2020a). The periodic fluctuations of sea level and water properties during the depositional stage have led to diverse changes in lithology, mineralogy as well as rock textures (Chen et al., 2019), which provide an excellent material to investigate the impact of high-frequency depositional sequences on reflux dolomitization. To be specific, during the Middle Ordovician, the study area was a restricted-evaporative carbonate platform, in which the circulation of seawater was greatly restricted by

several paleo-uplifts on the periphery of the basin (Chen et al., 2018; Liu et al., 2019). In such a geographic setting, a warm, semi-arid to arid climate could have enhanced evaporation and resulted in elevated salinity and Mg/Ca ratio of the seawater. Hence, the primary limestone sediments in the lagoon and shoal facies were likely to subject to replacement dolomitization when highly saline seawater infiltrated and migrated downslope (Fig. 5.4). Moreover, high-frequency sea level fluctuations during this stage have controlled the depositional sequence of lagoon-shoal facies and water exchange between the platform interior and the open marine environment (Bai et al., 2016; Xiong et al., 2021c). As a result, the cyclic transgressions-regression (evaporation) processes resulted in periodic dolomitization events. In general, a multistage reflux dolomitization model could explain the initial replacement of the underlying limestone sediments by dolomites.

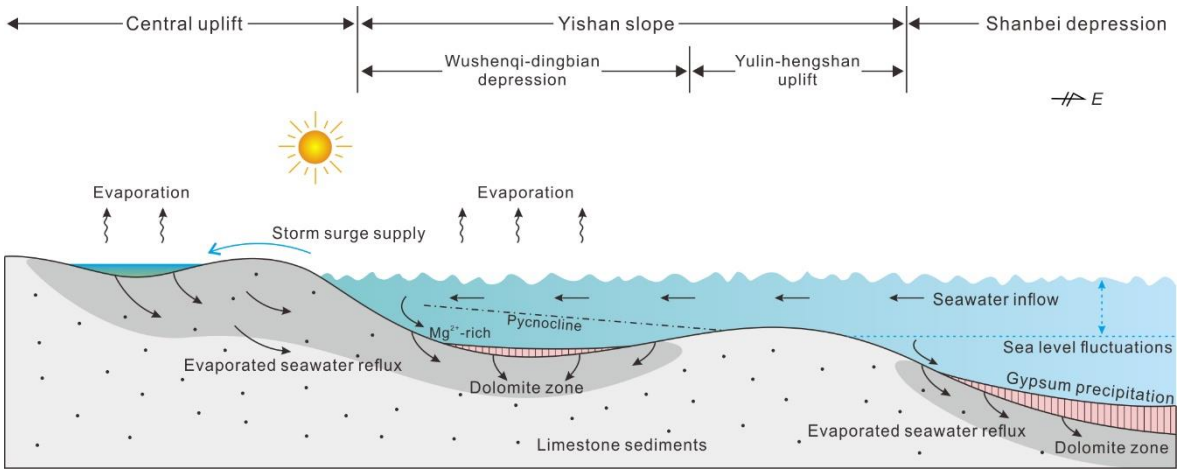

Figure 5.4 Conceptual geological model of reflux dolomitization within one depositional sequence in the Ordovician Majiagou Formation.

The reflux dolomitization was simulated in a two-dimensional inter-well scale rectangular domain that is 500 m wide and 38 m thick (Fig. 5.5a). This grid system has a total of 1,900 cells and the node spacing is uniformly specified as 10 m in the horizontal direction and 1 m in the vertical direction. The hydrological boundary conditions are similar with previous simulation of reflux dolomitization performed by Lu and Cantrell (2016). The left and lower boundaries are specified as no flow, and the right boundary (basinward) is open to flow. The upper boundary, successively varying with superimposed depositional sequences, has a specified constant temperature and pressure, representing an intra-platform near-surface

environment where the brines formed (Fig. 5.5b).

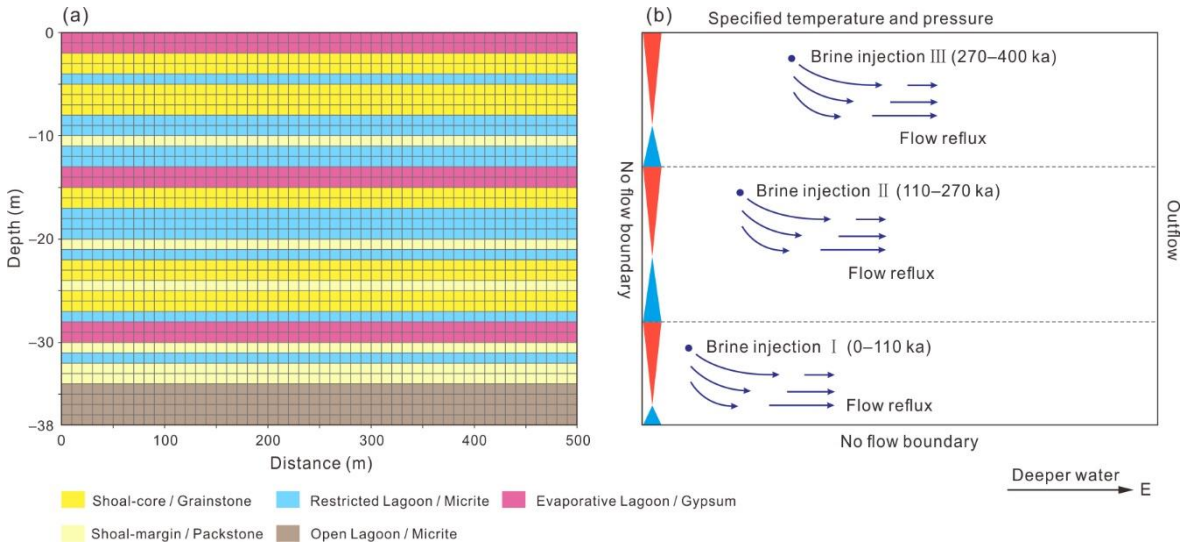

Figure 5.5 (a) 2D grid system showing the lithological distribution. (b) Schematic illustration of superimposed depositional sequences showing the variations in the position of brine ponds and hydrological boundary conditions.

5.2.2 Rock properties and hydrogeological conditions

The lithological features were obtained based on core and thin section observations from Well Jintan1 (Fig. 5.2b). Four types of rock textures can be distinguished in the studied Majiagou Formation, namely micrite, packstone, grainstone and gypsum rock. According to that, the simulated stratum is 38 m thick, comprising three depositional sequences in the vertical. These sequences have similar stacking patterns and are generally composed of micrite, packstone, grainstone and gypsum rock from the bottom to the top, representing the deposition process of upward-shallowing sequence. The fine fraction of different rock types, defined as the fraction of granular component <63 μm, is shown in Table 5.1. In order to investigate the impact of gypsum layers on fluid reflux process, additional simulations (sensitivity analysis) were performed with/without the presence gypsum layers. During the simulations, the gypsum were replaced by grainstone or micrite, representing the final sediments in a regression cycle or the initial sediments of the next transgression cycle, respectively.

According to the various classes of rock-fabric petrophysical relationships proposed by Lucia (1995), the depositional porosity of carbonates could exceed 40%. However, in a evaporative

carbonate platform environment, submarine cementation (e.g., fibrous cement) and slight compaction might had occurred during very early period before the dolomitization of limestone sediments, which led to apparent porosity and permeability decrease (Liu et al., 2020). Thus the porosity-permeability data used for reflux simulation should be less than its depositional values. Based on the rock texture-based porosity evolution of the Majiagou Formation carbonate reservoir in this area (Su et al., 2010), different initial porosities were specified for different rock types (Table 5.1; Fig. 5.6), and the permeabilities were still calculated according to the rock-fabric petrophysical relationships from Lucia (1995). Meanwhile, the reactive surface area (RSA) of grainstone, packstone and micrite are assumed to be 100 cm^2g^{-1}, 250 cm^2g^{-1} and 500 cm^2g^{-1} (Table 5.1, Fig. 5.6), representative of 260 μm, 100 μm and 50 μm-diameter dolomite rhombs, respectively (Gabellone and Whitaker, 2016).

In addition, the permeability anisotropy ($k_{horizontal}/k_{vertical}$ ratio) in carbonate rocks was specified as 10 and is comparable with many previous reactive transport simulations of dolomitization (Jones, 2000; Jones and Xiao, 2005). The gypsum rock is generally regarded as good cap rock and thus a relatively low porosity (3%) and permeability (5.50×10^{-16} m^2) was specified. In the simulation, variation in porosity is calculated by the change of mineral volume fraction and is controlled by the dissolution-precipitation of minerals with different densities (Xu et al., 2004). The Carman-Kozeny relation is used to characterize the evolution of permeability with regard to porosity changes.

Table 5.1 Lithology, rock texture, fine fraction, initial porosity-permeability and reactive surface area of four types of rock in the subsalt Majiagou Formation.

Rock texture	Layers	Fine fraction (%)	Porosity (%)	Permeability (m^2)	RSA (cm^2g^{-1})
Grainstone	7, 9, 13, 18, 20	0.05	30.0	3.85×10^{-12}	100
Packstone	2, 4, 8, 11, 16	0.45	22.5	4.50×10^{-13}	250
Micrite	3, 6, 10, 12, 15, 17, 19	0.95	10.0	3.50×10^{-15}	500
Evaporite	5, 14, 21	0.95	3.0	5.50×10^{-16}	500

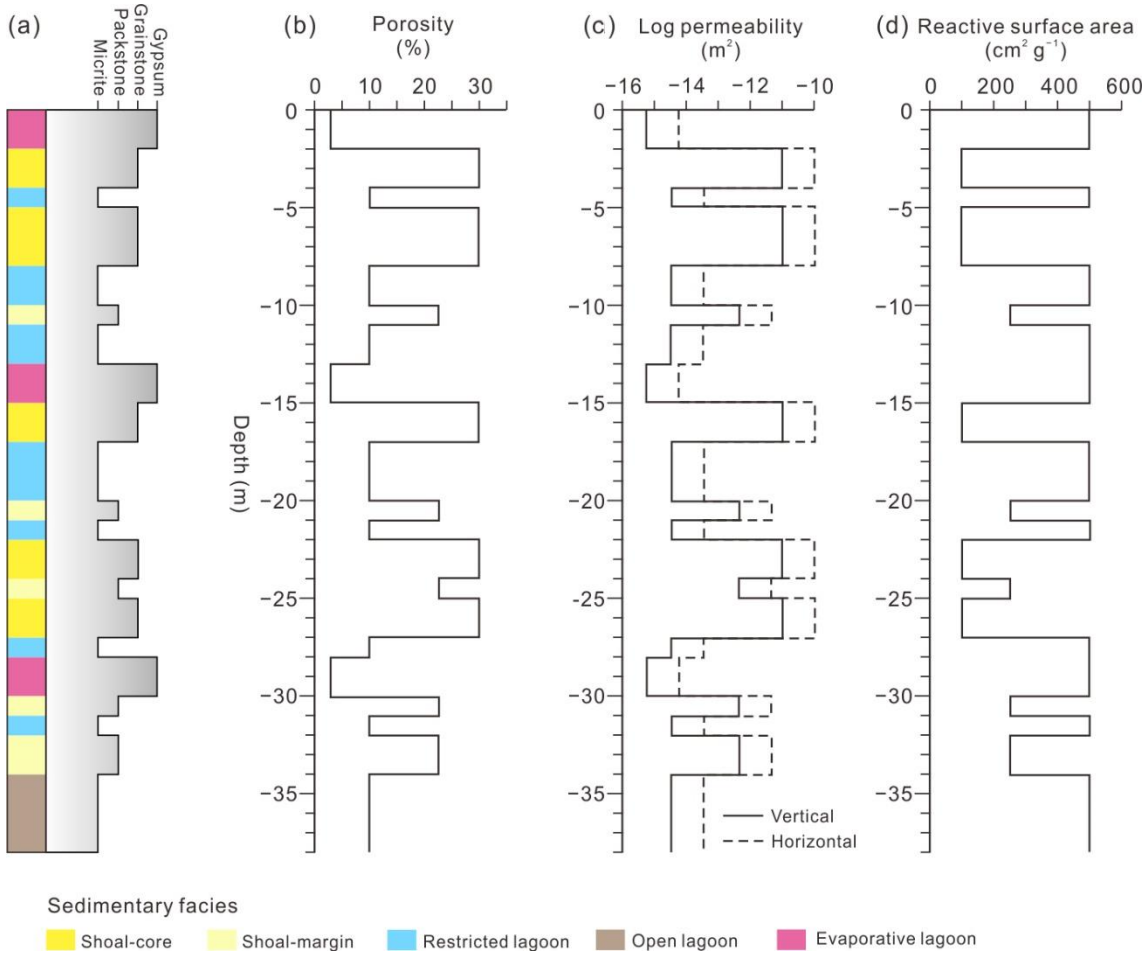

Figure 5.6 Simplified lithological column and depth profiles showing the initial rock properties (porosity, permeability and reactive surface area) of the sub-salt Majiagou Formation.

In order to reconstruct cyclic depositional evolution and dolomitization events, the simulation was divided into three stage, representing three progressive depositional sequences with the duration of 110 ka, 160 ka and 130 ka, respectively. The duration of these sequences were estimated based on the ICS (International Commission on Stratigraphy) international chronostratigraphic chart (Gradstein et al., 2012) and the proportion of each sequence to the Majiagou Formation. The calculated average deposition rate is 8.5 cm ka^{-1}, which falls within the statistical results of long-term accumulation rate of ancient carbonate platforms (commonly 1.3 cm ka^{-1} to 36.35 cm ka^{-1}; Sarg, 1988).

Similar with many previous generic simulations in the literature, the model is assumed to be initially saturated with modern seawater. It should be noted that although the paleo-oceanic properties have been frequently studied and the composition of seawater during the Ordovician

can be measured based on primary fluid inclusions of marine halite, concentrations of only four major ions have been obtained so far, i.e., Ca^{2+} = 72 mmol L^{-1}, Mg^{2+} = 91 mmol L^{-1}, K^{2+} = 31 mmol L^{-1} and SO_4^{2-} = 50 mmol L^{-1} in average (Hardie, 1996). Unfortunately, this is not enough for our simulation because the lack of several other key ion concentrations (i.e., Na^{2+}, HCO_3^-, Cl^-) and the uncertain of pH value (or charge balance) of the Ordovician seawater. Moreover, these obtained ion concentrations can only reflect the chemical composition of concentrated seawater (brine) in which the evaporites (i.e., halite) precipitated (Kovalevych et al., 2006; Meng et al., 2018), and should be much higher than that of the normal seawater in which carbonate deposits dominated. Therefore, the chemical composition of well-constrained modern seawater (Table 3.2) is still adopted in the case study.

Based on the thermodynamic calculation, modern seawater is supersaturated for dolomite (Hsu, 1967). However, dolomite is rarely generated in modern seawater environment or standard laboratory conditions (25°C, 1 atm), which indicate that the precipitation of dolomite is significantly controlled by kinetic process (Lippmann, 1982; Land, 1998). The brine pond position was situated in the upper left corner of each depositional sequence beneath the evaporites, reflecting the occurrence of dolomitization driven by salinity increase before evaporites precipitation. Due to great uncertainties of the evaporation intensity and seawater composition, chemical properties of the brines that formed the Majiagou dolomites is not well constrained. As such, three types of brine, which have been discussed in the RTM simulation of 1D dolomitization (Chapter 3), are also used here for base case simulation and sensitivity analysis. The chemical composition of these brines were derived from the surface water in some modern saline environments (Table 3.2), including Ibis Pond (Brine 1; salinity of 85‰), Ralph Sink (Brine 2; salinity of 186‰) and Phreatic Majanna (Brine 3; salinity of 249‰). In each simulation one type of dolomitization fluid with specified chemical composition was injected at a constant rate of 0.8 m yr^{-1} in the brine pond cell. Given the near-surface to very shallow depth setting of reflux dolomitization, geothermal heating is regarded to have less impact on the entire reflux system. Thus our simulations are isothermal, with a temperature specified as 30°C that is representative of a global mean sea surface temperature in the Middle Ordovician (Trotter et al., 2008).

5.2.3 Temporal and spatial distributions of mineralogy and porosity

Simulation result of the base case scenario shows the spatial distribution and temporal evolution of minerals and porosity in the superimposed depositional sequences (Fig. 5.7). In general, three dolomite bodies were successively formed during a total of 400 ka simulation. Within an individual sequence, dolomitization occurred beneath the brine pond, progressively forming a tabular dolomite body with a width of ca. 300 m. In the front area of dolomite body, there is a steady decline in dolomite abundance with increasing depth and distance away from the brine source. Meanwhile, the extension of dolomite body in grainstone and packstone is apparently wider than that in micrite. Moreover, the degree of dolomitization in different rock textures are diverse, showing a gradual increase in maximum dolomite abundance from grainstone (57.92%) to packstone (64.13%) to micrite (74.48%). With superimposition of depositional sequences in the vertical, dolomitization process in the previous sequence would gradually stop due to a lack of further brine injection. As a result, the morphology and extent of the dolomite body tend to be stable, with only minor flow and reaction in its dolomite front zone probably caused by slight fluid diffusion.

During the dolomitization, gypsum precipitation was observed in the dolomite front zone and the maximum volume of gypsum cement is 5.80%. However, these early-precipitated gypsum cement and even initial gypsum (rock composition) tended be gradually dissolved in the late stage of dolomitization, with a maximum variation of gypsum abundance being -3.6%. This is consistent with the dynamic process of gypsum precipitation/dissolution observed in 1D dolomitization in chapter 3. The distribution and evolution of rock porosity are highly relevant to the dolomite body, as shown by a gradual increase in porosity-permeability with a higher degree of dolomitization. In general, the porosity achieves the maximum in the core part of dolomite body while the porosity increments in the areas of gypsum-cementation are relatively small. The variation in porosity of different types of rock are also various, with the maximum porosity increments of grainstone, packstone and micrite being 5.68%、6.29% and 7.31%, respectively.

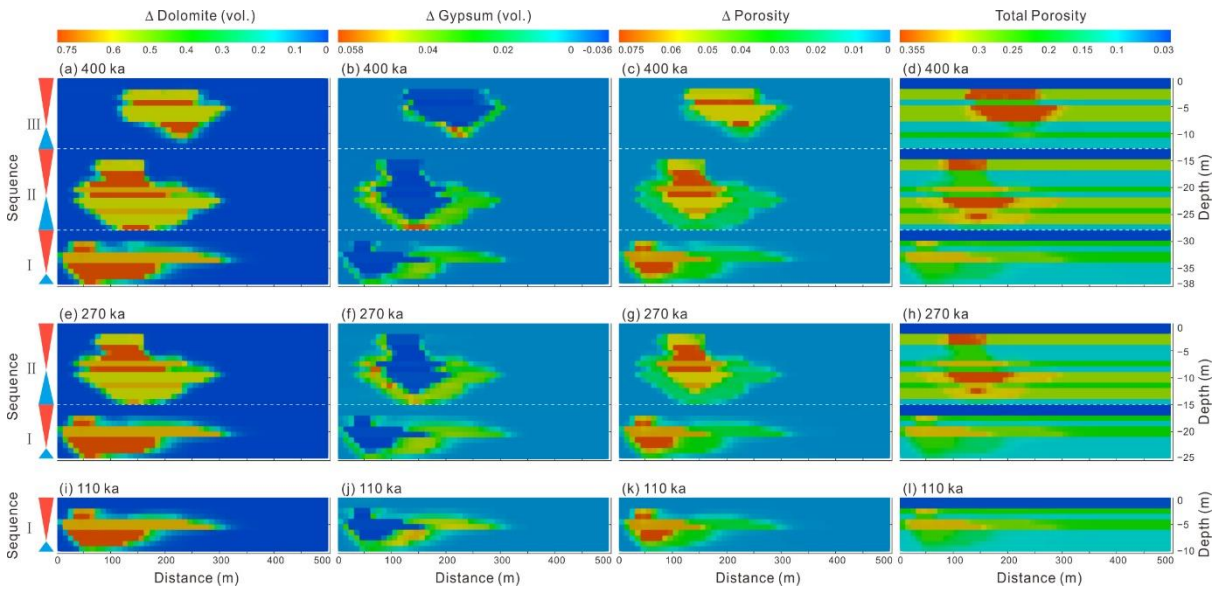

Figure 5.7 Temporal and spatial distribution of mineralogy (volume changes of dolomite and gypsum) and porosity (porosity change and total rock porosity) for base case simulation with superimposition of depositional sequences. (a–d) Sequence III, at 400 ka; (e–h) Sequence II, at 270 ka; (i–l) Sequence I, at 110 ka.

5.2.4 Rock texture control on dolomitization

Within a deposition sequence, the dolomite abundance is relatively higher in the middle-upper parts of the dolomite body, and gradually declines with increasing depth and lateral distance due to consumption of Mg^{2+} in the brine. Meanwhile, the gypsum precipitation, especially those in the lower part of the dolomite body, could fill in pores and reduce the downward flow of the brine. Thus the fluid flux is preferentially concentrated on the lateral orientation, progressively forming a tabular dolomite body (Fig. 5.8a, c).

Simulation results also suggest that the rock texture is a critical control of dolomitization process since it determines permeability and reactivity of the initial sediments. The Damköhler number, which is defined as the ratio of the chemical reaction rate to the mass transfer rate, can describe the relative importance of these two intrinsic controls (Whitaker et al., 2012). Generally, in a flow system, the degree of diagenesis is mostly limited by the reaction rate, thus the micrite with larger RSA will be dolomitized more rapidly. On the contrary, if fluid flux is insufficient and flow rate is the major limiting factor, dolomitization will be focused rapidly

on the more permeable, though less reactive grainstone. Due to the combined effect of these two competing factors (i.e., flow rate and sediments reactivity), Lu and Cantrell (2016) suggest that the reflux dolomitization can produce stratigraphically discordant dolomite (a complex dolomite body with heterogeneous 'fingers') that was previously thought to be of hydrothermal origin. In our simulations, relatively open hydrogeological conditions allow continuous replenishment of Mg^{2+} and carrying away Ca^{2+}, and thus can be regarded as a flow system (Fig. 5.8b). Therefore, the highest RSA and reactivity of micrite give rise to a maximum reaction rate and dolomite abundance. The grainstone with the smallest RSA, on the contrary, has the lowest reaction rate and dolomite abundance, while the lateral extension of dolomite in grainstone is widest because of its highest porosity-permeability and flow rate. The packstone, which has a medium RSA and permeability, shows intermediate values of reaction rate, dolomite abundance and lateral extension between the micrite and grainstone (Fig. 5.8b).

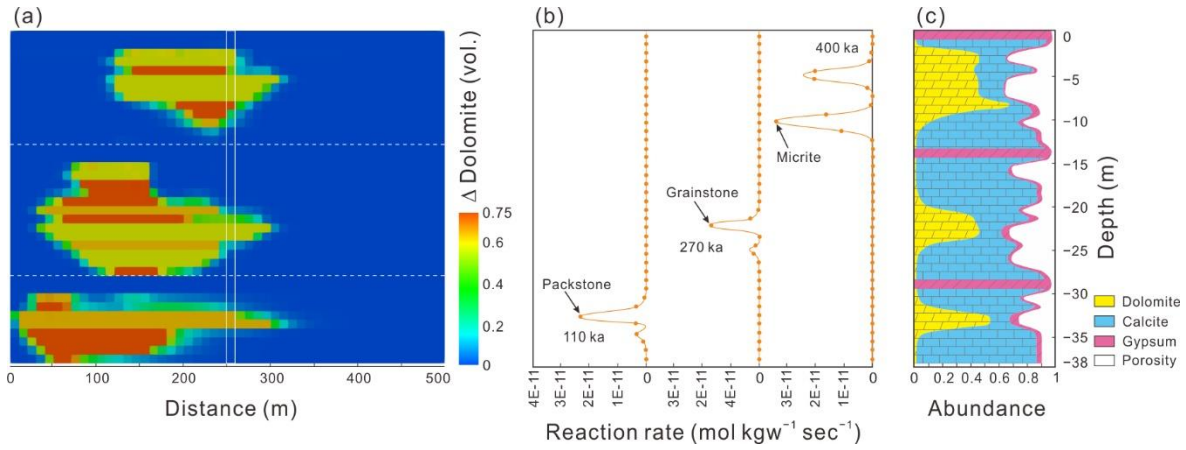

Figure 5.8 (a) Result of base case simulation showing the spatial distribution of dolomite changes at 400 ka. The solid white box indicates the location for extraction of 1D data. (b) Extracted 1D data at x = 260 m showing the reaction rate of packstone, grainstone and micrite at 110 ka, 270 ka, and 400 ka, respectively. (c) Extracted 1D data at x = 260 m showing the minerals abundance and rock porosity at 400 ka.

5.2.5 Effects of seawater compositions and gypsum layers

Reflux dolomitization can be affected by a series of key geological parameters, including extrinsic controls (e.g., brine composition, flow rate, temperature and evaporating intensity) and intrinsic controls (e.g., RSA, rock texture, dolomite rate constant and porosity-permeability

feedback). Given that the sensitivity analysis of reflux dolomitization has been investigated intensively for some generic models in the literature (Al-Helal et al., 2012; Gabellone and Whitaker, 2016), the accuracy and uncertainty of various input parameters involved in the simulation can be quantitatively evaluated. Nevertheless, for a specific geological setting in the Ordos Basin, herein we focus on the impacts of brine salinity and gypsum layer on the reflux dolomitization in the cyclic carbonate-evaporite successions. The range of values of the major controlling parameters are listed in Table 5.2.

Table 5.2 Controlling parameters used for base case simulation and sensitivity analysis.

Parameters	Values (Range)
Extrinsic controls	
Temperature	35°C
Brine salinity	186‰ for base case; 85‰ and 249‰ for sensitivity analysis
Initial flow rate	0.8 m yr^{-1} for base case scenario; 1.2 m $yr^{-1}$for sensitivity analysis
Boundary conditions	See Fig. 5.5
Brine pond evolution	110 ka, 160 ka and 130 ka for three depositional sequences, respectively
Intrinsic controls	
Rock fabrics	Micrite, packstone, grainstone and gypsum rocks; gypsum replaced by micrite and grainstone for sensitivity analysis
Initial water	Modern seawater equilibrated with calcite and pCO_2
Initial porosity	3 to 30%
Initial permeability	5.50×10^{-16} to 9.85×10^{-12} m^2
Permeability anisotropy	10 for carbonates
Reactive surface area	100 to 500 cm^2 g^{-1}
Thermodynamics and kinetics	Thermodynamics for calcite and gypsum; kinetics for dolomite
Dolomite precipitation rate law	Arvidson & MacKenzie (1999)

(1) Sensitivity to different brines

In addition to the base case simulation (brine 2, salinity = 186‰), another two simulations representing different evaporation intensities and water properties (brine 1, salinity = 85‰; brine 3, salinity = 249‰) were conducted (Fig. 5.9). In general, there are obvious increases in the rate and extent of dolomitization with increasing brine salinities. Gypsum cement can be observed in all the simulations and higher brine salinity (close to gypsum saturation) leads to

more extensive precipitation of gypsum in the flow path. Particularly, in the simulation of brine 1, relatively low dolomitization rate but high gypsum cementation in the dolomite front even result in a slight decrease in total porosity (approximately -3%).

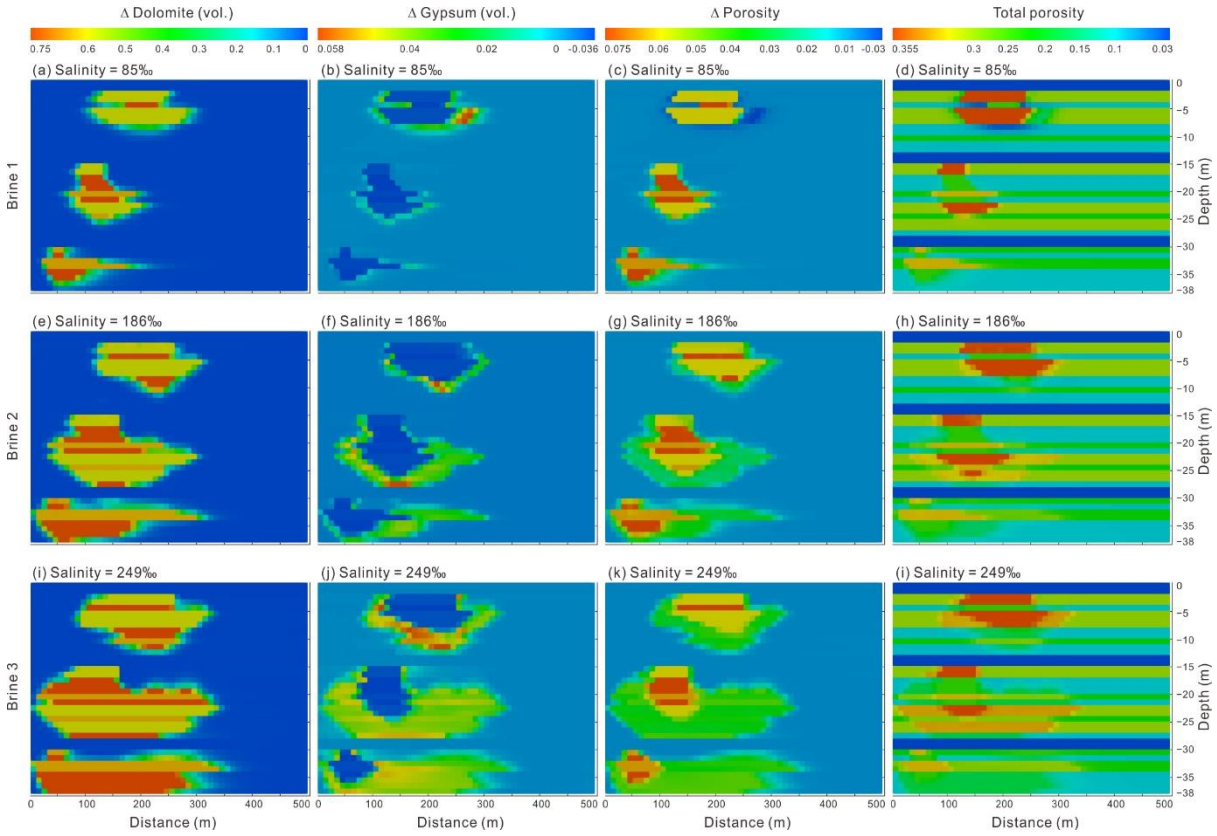

Figure 5.9 Effect of different brine salinities on the distribution of dolomite, gypsum and porosity at 400 ka. (a–d) Salinity = 85‰. (e–h) Salinity = 186‰ (base case). (i–l) Salinity = 249‰.

Given that the evaporation intensity and salinity of seawater in the geological history changed frequently with seasons and climatic variations (Warren, 2010), three types of brines were involved in the simulations to evaluate the dolomitization process under conditions of different seawater properties. Generally, an increase in brine salinity would resulted in higher density of water, fluid flux and reaction rate, and ultimately an enlargement of dolomite body (Fig. 5.9a, e, i). Although a larger dolomite body was generated, relatively high salinity (brine 3, close to gypsum saturation) would have also led to more gypsum precipitation. Thus the porosity increment of the simulation of brine 3 is relatively less than that of brine 2 (Fig. 5.9g, k). This indicates that the porosity increase during dolomitization is not always proportional to the

dolomitization rate or brine salinity, but is simultaneously and significantly affected by gypsum precipitation. In the simulation of brine 1, a slight decline of total porosity (ca. -3%) was observed in the dolomite front. This was likely related to a relatively low dolomitization rate under this low brine salinity condition because the increase of pores by dolomitization is less than the pores cement-filled by gypsum precipitation.

(2) With/without the presence of gypsum layers

To reveal the impact of cyclic gypsum layers on the dolomitization process, simulations were also performed under the assumption of gypsum rock replaced by grainstone or micrite, as well as a variation in brine injection rate (0.8 m yr^{-1} and 1.2 m yr^{-1}) (Fig. 5.10).

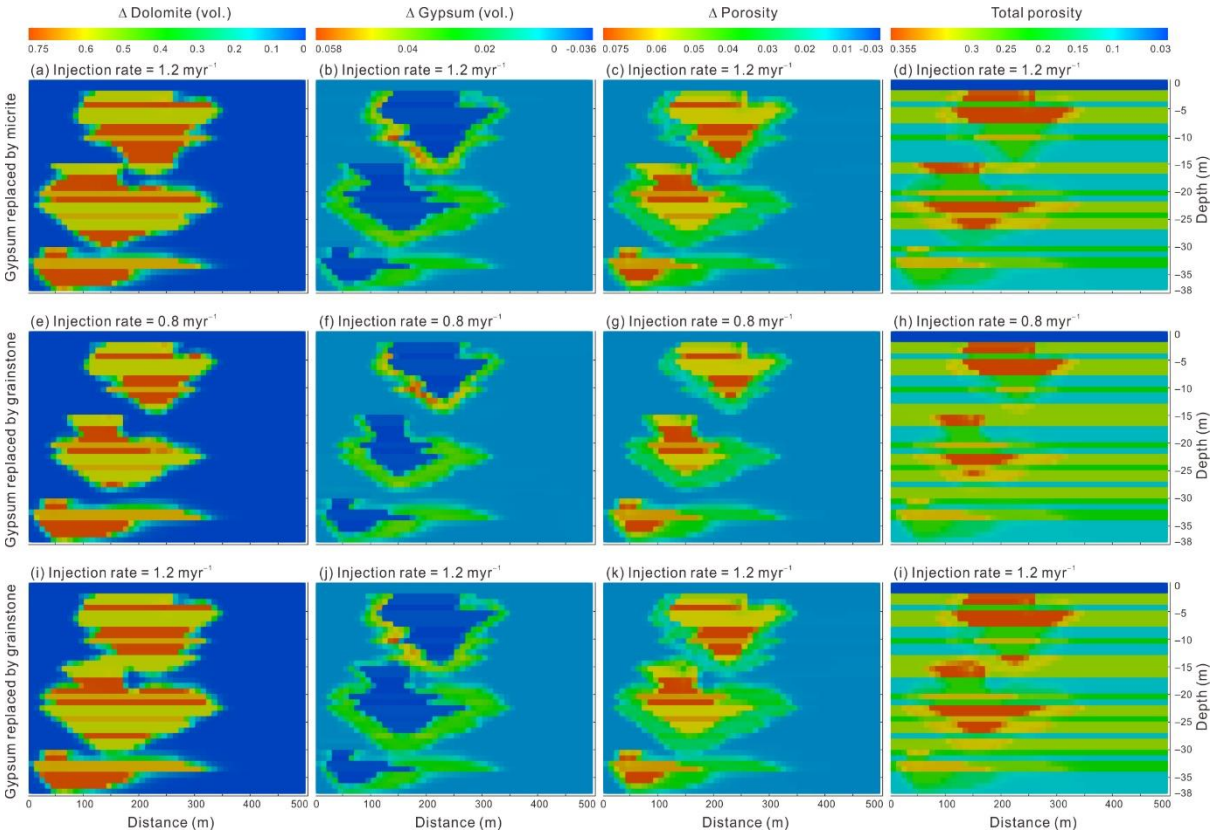

Figure 5.10 Effect of gypsum layers and brine injection rate on the distribution of dolomite, gypsum and porosity at 400 ka. (a–d) Gypsum rock replaced by micrite, injection rate = 1.2 m yr^{-1}. (e–h) Gypsum rock replaced by grainstone, injection rate = 0.8 m yr^{-1}. (i–l) Gypsum rock replaced by grainstone, injection rate = 1.2 m yr^{-1}.

To be specific, the grainstone represents high-energy shoal-facies sediments developed in the upper part of a regression semi-cycle, while the micrite represents low-energy lagoon-facies

sediments at the bottom of the next transgression semi-cycle. In general, the new reflux system, in which the gypsum rock is replaced by carbonates, has little impact on the degree of dolomitization and morphology of an individual dolomite body. However, these three isolated dolomite bodies tend to eventually merge into a large dolomite zone without intercalated gypsum layers. The presence of high-permeable grainstone and an increase in brine injection rate could both accelerate this trend and are conducive to the formation of a large-scale high-porosity zone.

(3) Implications for dolomite distribution

The epeiric intra-platform basin is sensitive to high-frequency sea level and climatic fluctuations (Mitchum and Wagoner, 1991; Xiong et al., 2019), which is typically featured by cyclic carbonate-evaporite successions. In the Ordovician Majiagou Formation, the gypsum rocks developed mainly in the upper part of periodic depositional sequences, corresponding to the late stage of eustatic regressions during which the seawater is highly evaporated and concentrated. Meanwhile, fluctuations of sea level are usually accompanied by lateral migration of brine source and change of hydrogeological conditions, which resulted in successive reflux events. Specifically, a relatively small dolomite body can be formed during each individual sequence and reflux event. The intercalated gypsum layers, however, have impeded the downward seepage of brines and prevented these isolated dolomite bodies from merging into a larger dolomite zone due to its extremely low porosity-permeability. As a result, in the cyclic carbonate-evaporite successions, thin-bedded dolomite interlayers beneath the evaporites (e.g., gypsum rock and halite) constitute the favorable target for hydrocarbon reservoir exploration (Chen et al., 2018; Fu et al., 2019; Xiong et al., 2020b). In contrast, these isolated dolomite bodies, which were formed in different depositional sequences and hydrogeological conditions, tended to merge and interconnect with each other under conditions of the gypsum layers replaced by grainstone or micrite. In this case, a large, continuous dolomite zone with high reservoir properties could eventually develop (Fig. 5.11). Sensitivity analysis of the presence of gypsum layers has indicated that the large-scale stratigraphically accordant dolomite in the Ordos Basin might result from superposition of a series of relatively short-lived reflux dolomitization events, rather than a single long dolomitization event as

proposed previously (He et al., 2014).

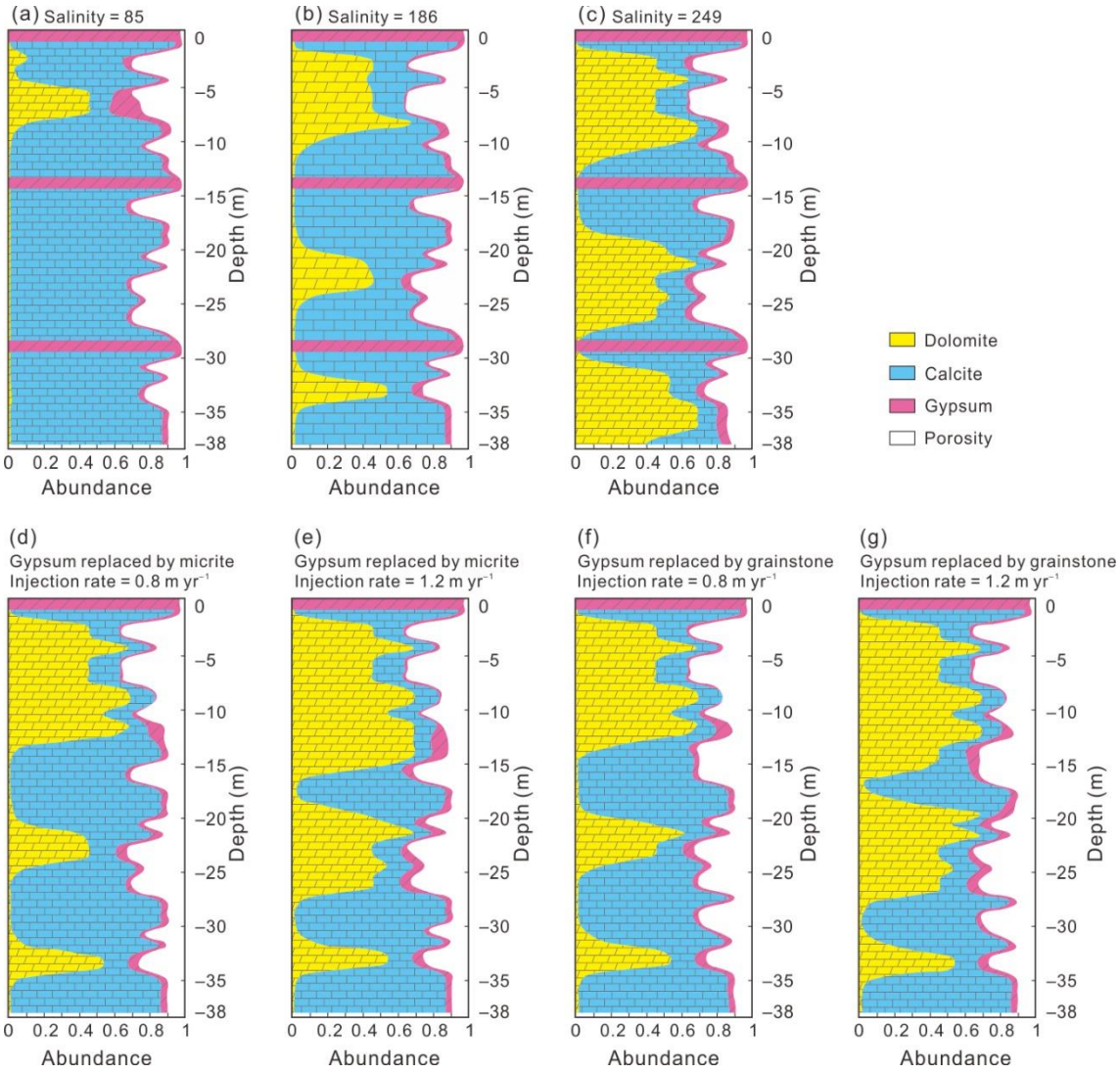

Figure 5.11 Extracted 1D data of simulation results for sensitivity analysis at x = 260 m showing the minerals abundance and rock porosity at 400 ka. (a–c) Sensitivity analysis of different brines salinities with brine injection rate = 0.8 m yr^{-1}. (d–g) Hypothetical simulations of gypsum layers replaced by grainstone and micrite with different brine injection rates.

5.2.6 Porosity evolution during dolomitization

The dolomite is a major target for hydrocarbon exploration in carbonate reservoir. In many petroliferous basins, especially under deep burial conditions, dolomite was found to have better reservoir properties than its limestone precursor and the porosity increases with the dolomite abundance (Schmoker and Halley, 1982; Ehrenberg et al., 2006; Liu et al., 2017). This highlights the importance of constraining dolomite distribution for carbonate reservoir

prediction. Nevertheless, there is a great controversy to date about the relationship between dolomitization and porosity genesis. Intensive debate has been focused on whether dolomitization directly generate pores, and the amount of porosity increment remains poor understood (Cantrel et al., 2004; Lucia et al., 2004; Jiang et al., 2016). Simulation results in this study provide a useful clue in discussing the porosity evolution during dolomitization. In general, the dolomitization process and resulting porosity change can be described by the replacement reaction (Eq. 5.1) proposed by Morrow (1982):

$$(2-\mathrm{x})CaCO_3 + \ Mg^{2+} + \mathrm{x}CO_3^{2-} \rightarrow CaMg(CO_3)_2 + (1-\mathrm{x})Ca^{2+} \quad (5.1)$$

Where x = 0–1, and the porosity change can be calculated based on the difference in molar volume between dolomite and calcite. Particularly, three specific cases can be recognized according the amount of exogenous CO_3^{2-} involved in the dolomitization reaction:

(1) If x = 0, the replacement reaction can be written as:

$$2CaCO_3 + \ Mg^{2+} \rightarrow CaMg(CO_3)_2 + Ca^{2+} \quad (5.2)$$

In this case, dolomitization will take place by mole-for-mole replacement of Ca^{2+} by Mg^{2+} (i.e., mole-for-mole model, Weyl, 1960). Given that the dolomite is smaller in molar volume of crystal (magnesium has a smaller ionic radius than calcium) compared to its calcite precursor, a theoretical increase of porosity 12.96% can be generated by this mole-for-mole volume-decreased dolomitization model (Chen et al., 1985). However, it should be noted that this dolomitization model was assumed to take place only in completely hydrologically-closed systems with no exogenous Mg^{2+} and CO_3^{2-} supply and no overdolomitization.

(2) If x = 0.26, the replacement reaction can be written as:

$$1.74CaCO_3 + \ Mg^{2+} + 0.26CO_3^{2-} \rightarrow CaMg(CO_3)_2 + 0.74Ca^{2+} \quad (5.3)$$

Where a small quantity of exogenous CO_3^{2-} is involved in the reaction, and the pore volume remains unchanged during the dolomitization process.

(3) If x = 1, the replacement reaction can be written as:

$$CaCO_3 + \ Mg^{2+} + CO_3^{2-} \rightarrow CaMg(CO_3)_2 \quad (5.4)$$

In this case, the produced dolomite is generally regarded as primary dolomite (or dolomite cement), rather than replacement dolomite. Half of the CO_3^{2-} in dolomite is of exogenous source and the porosity is reduced.

According to our simulations, there is an apparent increase in porosity during dolomitization, as shown by the maximum increment of 5.68%, 6.29% and 7.31% for grainstone, packstone and micrite, respectively (Fig. 5.12a). The porosity increment for various rock textures are all lower than the estimated 12.96% for ideal mole-for-mole dolomitization. This indicates that a small quantity of exogenous CO_3^{2-} ($x < 0.26$) from injected brine has been involved in the replacement reaction, which is consistent with the open hydrogeological conditions established in this study (Fig. 5.5b). Besides, a slight overdolomitization has been also recorded in micrite and packstone, evidenced by a slight decrease in porosity with increasing dolomite abundance at the late stage of dolomitization (Fig. 5.12a). This was likely resulted from the continuous injection of brine in which a small amount dolomite cement was formed by excess Ca^{2+}, Mg^{2+} and CO_3^{2-} and then infilled in pores.

Gypsum is a common mineral in evaporatic environments and has significant impacts on the reservoir properties. However, the causality of dolomitization and gypsum precipitation has been a long debated issue. Some researchers suggest that the consumption of Ca^{2+} and enhanced Mg/Ca ratio in the brine due to gypsum ($CaSO_4 \cdot 2H_2O$) precipitation have promoted the dolomitization (Feng et al., 1998; Yang et al., 2018). While others believe that the replacement of calcium by magnesium during dolomitization have resulted in Ca^{2+} enrichment of the reflux brine ahead of the dolomite body, which then generated gypsum (Jones and Xiao, 2005; Gabellone and Whitaker, 2016). In our simulations, the injected brines (boundary water) are unsaturated with respect to gypsum and the gypsum precipitation occurred mostly in the dolomite front zone. This is comparable with the results of Jones and Xiao, 2005 and indicates that the gypsum precipitation was likely related to the Ca^{2+} released by dolomitization and then enriched in the dolomite front zone. This interpretation can also be supported by the collaborative evolution of gypsum precipitation and reservoir porosity (Fig. 5.12b). In the early stage, the precipitation rate of gypsum was relatively slow, and the pores cement-filled by

gypsum was less than the pores increment by dolomitization. Thus the total porosity slightly increased with gypsum abundance. Subsequently, the gypsum precipitation was accelerated, and the total porosity tented to decrease when the pores cement-filled by gypsum was greater than the pores increment by dolomitization. With continuous injection of brines, these early-formed gypsum cement would be eventually dissolved since the brines are unsaturated with respect to gypsum. Consequently, there is a steady linear increase in total porosity with gypsum dissolution after pervasive dolomitization.

In summary, the porosity evolution during dolomitization reflect the comprehensive effect of multi-factors including specific hydrogeological condition, initial sediment texture (i.e., permeability and reactivity), degree of dolomitization and dynamic precipitation-dissolution process of the concomitant gypsum. Although the simulation results could not directly represent the current pore characteristics since no burial diagenetic alterations were taken into account, this RTM approach enables a quantitative description and assessment of the impact of high-frequency depositional sequences on early reflux dolomitization, as well as the co-evolution of dolomite, gypsum and reservoir porosity.

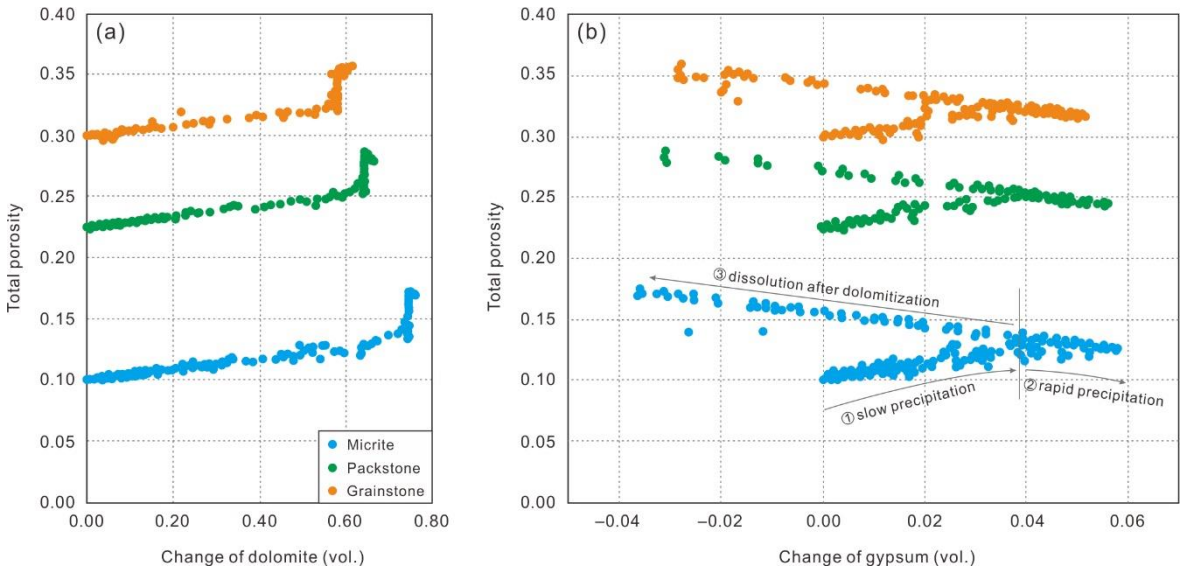

Figure 5.12 Correlation analysis of the changes in mineral abundance with total porosity (data from base case simulation at 400 ka). (a) Cross-plot of dolomite change with porosity. (b) Cross-plot of gypsum change with porosity. Note the three stages showing the different porosity evolution with gypsum precipitation and dissolution.

5.3 Facies-controlled eogenetic karst of shoal deposits

5.3.1 Conceptual geological model and grid system

As noted above, the shoal-facies-related granular dolostone and crystalline dolostone constitute the major reservoir rocks in the sub-salt Majiagou Formation in Ordos Basin. The formation of these high quality carbonate reservoirs were mainly controlled by intermittent subaerial exposure and dissolution processes (i.e., eogenetic karst) due to high-frequency sea level fluctuations during the Middle Ordovician, as evidenced by multistage erosional surfaces recognized in the core samples (Xiong et al., 2019; Xie et al., 2020). These multistage exposure surfaces and their underneath dissolution features were found to be highly consistent. To be specific, in the shallow marine restricted-evaporative environment of the North China platform, the shoal-facies deposits (initially dominated by grainstone) are most likely to be exposed due to their relatively high position and then subject to meteoric diagenetic environment (Fig. 5.13). Due to a lack of compaction, the initial sediments were generally unconsolidated and had relatively high porosities and permeabilities, thus providing effective diffusion paths for the early meteoric water, which was characterized by random and diffuse flow; i.e., diffuse intergranular flow (Saller et al., 1999; Xiao et al., 2016). As such, unsaturated meteoric water can easily seep into the grainstone from the top of the shoals and then spreads along the intergranular pores, leading to the dissolution of carbonate rock matrix (initial limestone sediments) and the expansion of primary intergranular and intragranular pores.

Subsequently, the dissolved shoals were overlain by new sediment during transgression and sea level rise, which preserved the erosion surfaces and brought vadose infills. Due to the high-frequency sea level changes and periodic hydrodynamic variations, these two processes (i.e., karstification during regression and vadose infill during transgression) were repeated until the deposits were buried. This ultimately resulted in the superposition of high-frequency cycles of surface exposure and eogenetic karst system. In general, this eogenetic karst process was collectively controlled by sedimentary paleo-geomorphology, intermittent sea level regressions and grainstone-hosted favorable flow path, thus displaying a typical characteristic of shoal-facies control. During burial, some of the early-formed karst systems were subjected to

diagenetic alterations such as burial dolomitization, recrystallization and slight pores cementation, which ultimately form the present shoal-facies dolostone reservoirs that are characterized by dissolved pores (and vugs) and intercrystalline pores.

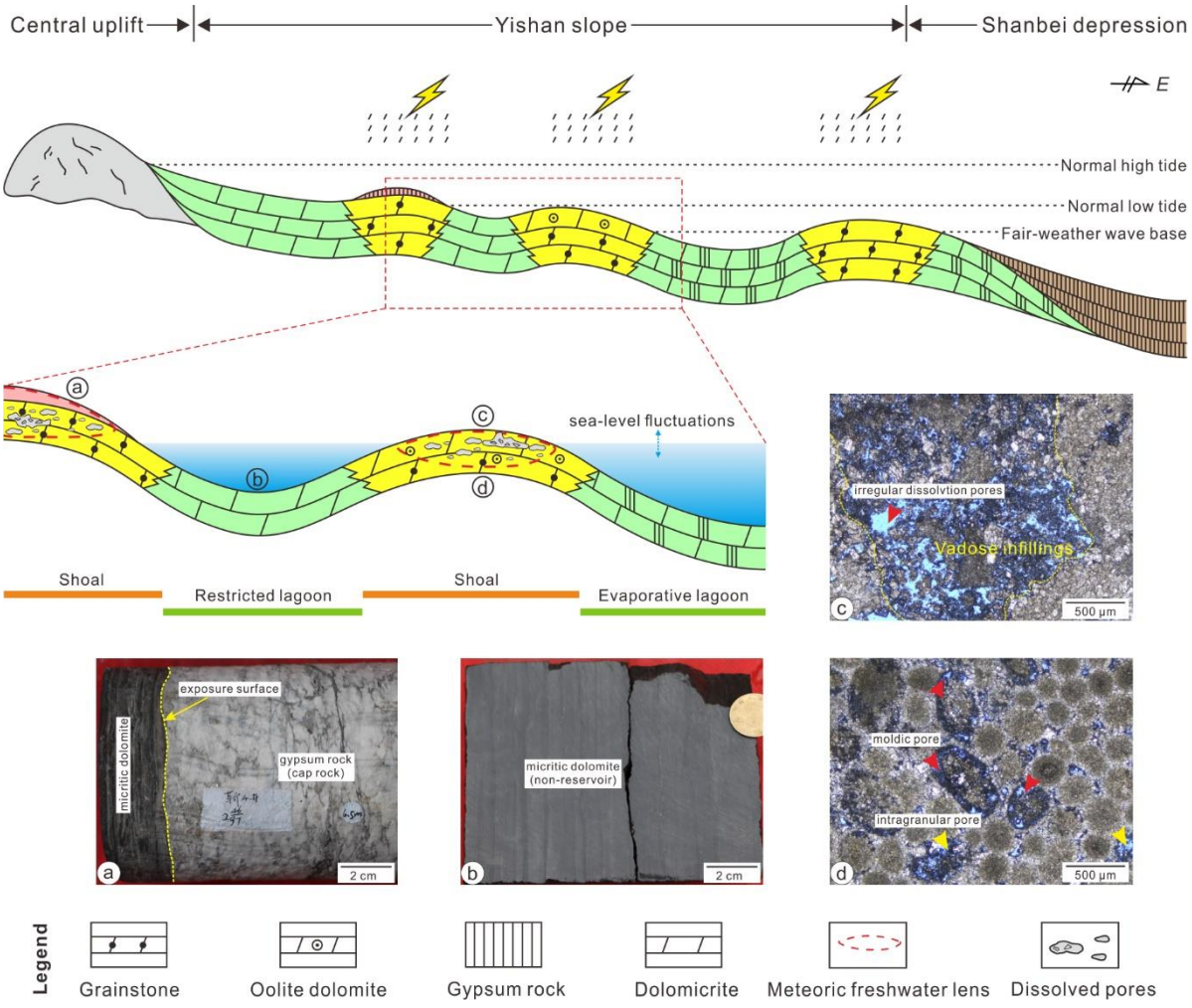

Figure 5.13 Conceptual geological model of eogenetic karst showing the location of meteoric diagenetic environment and typical lithological features of the sub-salt Majiagou Formation in the Ordos Basin.

To reveal the geochemical mechanisms and potential controlling factors of the meteoric water-rock interactions during subaerial exposure and karstification processes, the following part adopts a two dimensional geometric model that represents an individual shoal-facies reservoir in the Middle Ordovician Ordos Basin. Based on the thermo-hydro-chemical coupled model applied in chapter 4, the facies-controlled eogenetic karst process of shoal deposits during an exposure event can be simulated. The mineral-porosity distribution and evolution can also be

reconstructed. In general, this grid system has a total of 2,100 cells, and the width and thickness are 700 m and 20 m, respectively (Fig. 5.14a). Notably, the thickness of the grid system is relatively larger in the middle part, with a maximum of 15.7 m, corresponding to a relatively high sedimentation rate in the shoal cores (Tan et al., 2014). In contrast, the edges of the grid system are thinner, with a minimum of 8.0 m, corresponding to a relatively low sedimentation rate in the shoal margins. The hydrological boundary conditions are similar to the above one-dimensional column model for eogenetic karst simulation. A total of 10 cells at the top of the grid system are configured as the injection cells of meteoric water, and the lower boundary allows the outflow of aqueous species released during carbonate dissolution process.

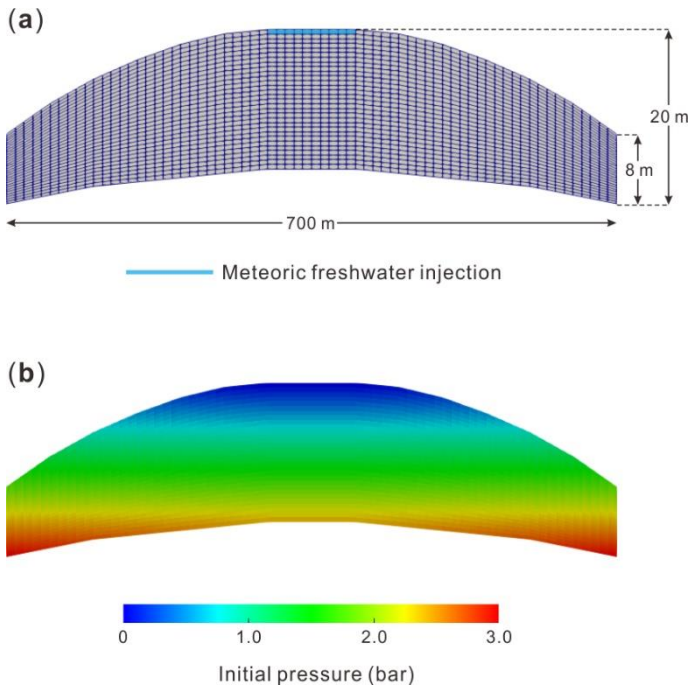

Figure 5.14 (a) 2D grid system an individual shoal facies showing the variation in thickness and the location of meteoric water injection cells. (b) Initial pressure distribution of the grid system.

5.3.2 Rock properties and hydrogeological conditions

A large number of petrographic and reservoir studies in the Ordos Basin have indicated that the eogenetic karst developed mainly in the newly deposited grainstone and thus exhibited a characteristic of shoal-facies control (Xiao et al., 2019; Xiong et al., 2019; Liu et al., 2020). Hence, porous grainstone (i.e., granular limestone) was adopted to specify the initial rock

properties in the simulation, which is consistent with the rock property setting of the previous one-dimensional column model. In general, an initial homogeneous 30% porosity and 3.85×10^{-12} m^2 permeability ($k_{horizontal} = k_{vertical}$) were specified throughout the two-dimensional grid system, based on the porosity evolution reconstruction in the study area (Su et al., 2010) and the rock-fabric petrophysical relationships and porosity-depth models for carbonate reservoirs (Ehrenberg and Nadeau, 2005; Perrin et al., 2020). Given the uncertainties of permeability anisotropy that is an intrinsic factor affecting heterogeneity of the flow caused by some specific sedimentary structures (e.g., laminated texture and normal/reverse vertical grading of particles), four other scenarios, i.e., $k_{horizontal} / k_{vertical} = 0.2$, 0.5, 2.0 and 5.0, were also involved in the simulation for parametric uncertainty analysis.

Similar with the previous column model, an initial 30°C temperature and 0.1 MPa pressure are specified in the upper boundary of the grid system, representing a common global mean temperature in the Middle Ordovician (Trotter et al., 2008) and the normal atmosphere in a subaerial setting, respectively. The following cells are calculated based on the geothermal gradient (3°C/100 m) and formation pressure gradient (0.98 MPa/100 m) (Fig. 5.14b). In the simulation, the grid system was specified to be initially saturated with modern seawater (initial water; Table 4.1), and the meteoric water (boundary water; Table 4.1) was injected from the top boundary (10 cells) of the grid system. For base case scenario, the injected rate was calculated according to the volume of each injection cell and a given annual rainfall recharge datum (628 mm/a). The atmospheric pCO_2 was specified as 5,500 ppm, corresponding to a mean value of atmospheric carbon dioxide concentration during the Ordovician period (Fig. 4.9a). Moreover, given that some key hydrogeological parameters, e.g., sea surface temperature (25–40°C), atmospheric pCO_2 (3,000–7,500 ppm) and climate-related rainfall (200–800 mm/a), were fluctuated during the Ordovician period, sensitivity analyses were thus carried out to evaluate the influence of these parametric uncertainties on the meteoric water-rock interactions as well as the distribution and porosity evolution of karst-related shoal reservoir. Detailed lithological and hydrogeochemical parameters for base case simulation and sensitivity analyses are summarized in Table 5.3.

Table 5.3 Lithological and hydrogeochemical parameters used for 2D simulation of eogenetic karst.

Parameters	Values (Source)
Calcite dissolution	$CaCO_3 + H^+ = Ca^{2+} + HCO_3^-$
Lithology	Shoal-facies grainstone
Initial porosity	30%
Initial permeability	3.85×10^{-12} m^2
Permeability anisotropy	$k_{horizontal}$ / $k_{vertical}$ = 0.2, 1.0 (base case), 0.5, 2.0 and 5.0
Thermodynamics and kinetics	Thermodynamics for calcite dissolution
Initial water	Modern seawater
Boundary water	Modern atmospheric precipitation
Duration of subaerial exposure	5 ka–300 ka
Sea surface temperature	25, 30 (base case), 35 and 40 °C
Rainfall recharge	200, 400, 628 (base case) and 800 mm/a
pCO_2	3,000, 5,500 (base case), 6,500, 7,500 ppm

5.3.3 Simulation results and discussion

According to the result of base case simulation (temperature = 30°C; pCO_2 = 5,500 ppm; rainfall = 628 mm/a), a dissolution zone of calcite formed beneath the meteoric water injection cells and extended downward and laterally with increasing exposure time (Fig. 5.15). This is highly similar with the shape and development of the meteoric freshwater lens observed in many previous studies of modern karst or paleokarst systems (Whitaker and Smart, 2007; Swart and Oehlert, 2018). To quantitatively describe the distribution and evolution of the karstification process, herein we define the dissolution lens as the area in which the amount of calcite dissolution exceeds 1%. In general, in both directions (downward and lateral), the amount of dissolution decreases with the increase in the distance from the meteoric water source. To be specific, at exposure time = 5 ka (Fig. 5.15a), the influence of meteoric water leaching on the shoal deposits is minor, with a maximum amount of dissolution of only 1.76%. During this initial exposure stage, the dissolution lens has not yet formed, with very small karst-affected zone in both vertical (less than 2 m) and lateral (nearly negligible) directions. With time, a half oval-shaped dissolution lens gradually formed, located at the top of the shoal. At exposure time = 50 ka (Fig. 5.15b), a maximum calcite dissolution of 5% can be observed,

and the major part of the lens yields dissolution of 2–4%. The range of dissolution lens is about 6.5 m and 180 m in the vertical and lateral directions, respectively. At exposure time = 130 ka (Fig. 5.15c), the range of dissolution lens expands to 10.5 m and 200 m in the vertical and lateral directions, respectively. Meanwhile, there is also an elevated degree of karstification as shown by a maximum amount of dissolution of 12.2% and a range of 4–8% for the major part of the lens. At exposure time = 300 ka (Fig. 5.15d), the maximum amount of dissolution of those grid cells near the meteoric water source is 34.0%, and the major part of the lens shows a relatively wide range of amount of dissolution from 5% to 20%. During this stage, the meteoric water could permeate the entire shoal deposits in the vertical, and has also a wide range of impact (approximately 240 m) in the lateral.

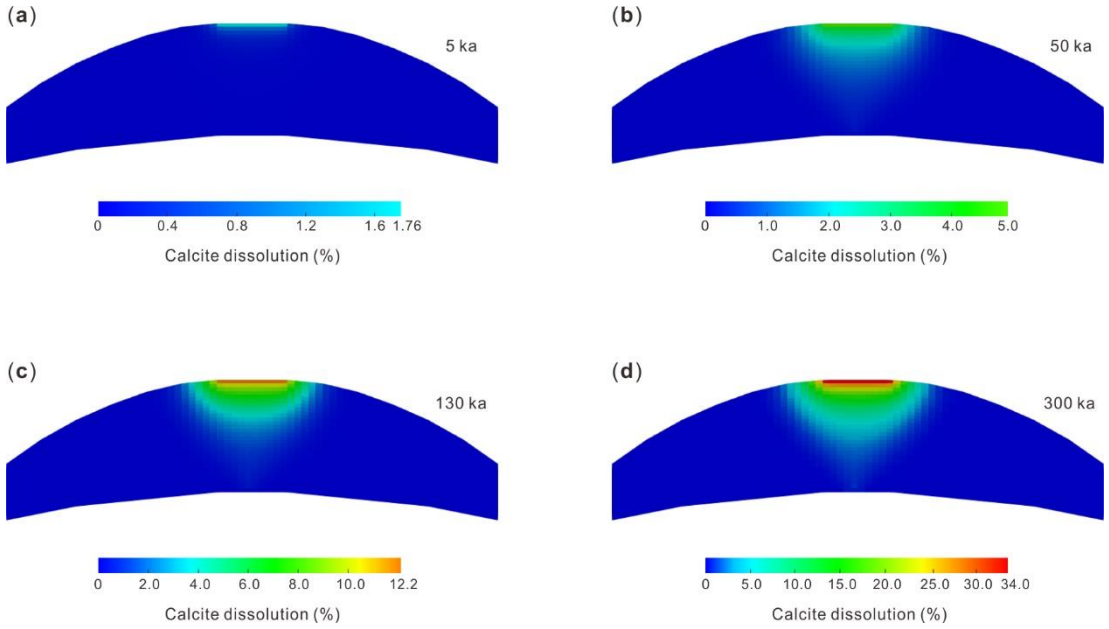

Figure 5.15 Simulation result of base case scenario showing the distribution and amount of calcite dissolution at exposure times of (a) 5ka, (b) 50 ka, (c) 130 ka and (d) 300 ka.

The above simulation has shown the quantitative relationships between exposure time with the amount of calcite dissolution and the range of dissolution lens. Combined with field studies and statistical analyses of the thickness (via core observation) and physical properties (porosity of the core samples with karst features under the microscope) of karst-related reservoirs, the exposure time needed for the formation of each individual shoal-facies reservoir, which cannot be achieved by previous studies of reservoir geology, can be estimated. Using a combination

of water-rock interactions simulation in karst system and traditional reservoir properties data obtained from field study, this study presents the first attempt to quantitatively estimate the duration of subaerial exposure of the carbonate platform. To be specific, based on detailed core observation and statistics of 23 cored wells in the Ordos Basin, the karst-related shoal reservoirs show a wide range of thickness, from 0.3 m to 6.9 m (average 2.4 m). Nevertheless, most of these reservoirs have relatively centralized thickness of 1–3 m, accounting for 60.9% of all the reservoirs (Fig. 5.16a). Meanwhile, measurements of a total of 75 core samples show that the karst-related shoal reservoirs in the Ordos Basin have rock porosities of 1.5–6.7% (average 3.1%), with most of them ranging from 2–4% that accounts for 66.7% (Fig. 5.16b). According to abundant petrographic evidence as previously shown by Liu et al. (2020) and Xiong et al. (2020a), the initial intergranular pores of the grainstone sediments have mostly been occluded due to prolonged burial compaction (the Ordovician Majiagou Formation has a general burial depth of 3,000–4,000 m), whereas the karst-related dissolved pores (and vugs) have been well-preserved. In other words, the measured porosities of core samples could approximately represent the newly produced porosities via karstification. Therefore, it can be inferred that the duration of subaerial exposure and karstification of shoal-facies grainstone in the sub-salt Majiagou Formation ranges mainly between 30–110 ka (Fig. 5.17), This is consistent with the brief to moderately long subaerial exposure (5–130 ka) as classified by Saller et al. (1999) that is characterized by fine matrix pores (molds and intercrystalline pores) and small conduit pores (vugs, fractures and fissures).

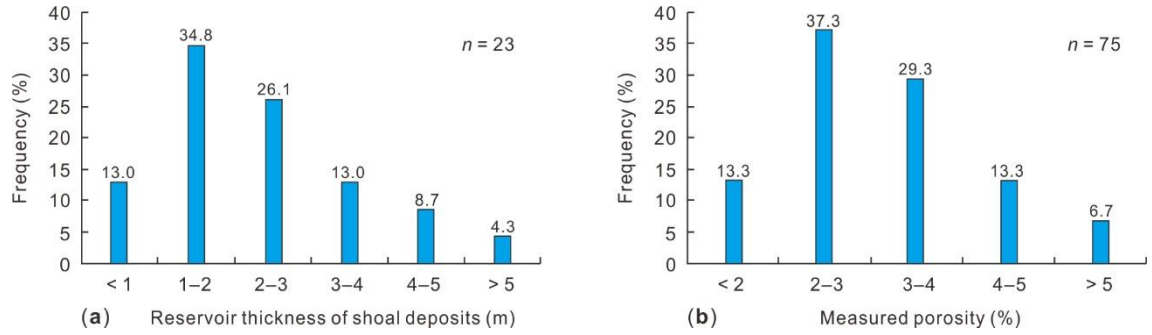

Figure 5.16 Statistical analyses of the physical properties of reservoirs based on field study. (a) Frequency histogram of the thickness of shoal-facies reservoirs obtained from core observation. (b) Frequency histogram of the measured porosity of karst-related core samples.

In addition, physical property analysis of core samples also shows obvious heterogeneity in porosity distribution within an individual shoal. Generally, the rock porosity co-varies with the cyclic depositional sequences (Fig. 5.2b), and reaches a maximum in the upper parts of each individual shoal as shown by a decreasing trend of porosity with increasing distance from the exposure surface (Fig. 5.17). This is highly consistent with the porosity distribution in the simulation, and the measured porosities are all located between the two porosity evolution curves of 30 ka and 110 ka (Fig. 5.17). These features have collectively indicated that the top-down meteoric water leaching during subaerial exposure stage is the major mechanism of shoal-facies reservoir development in the sub-salt Majiagou Formation, Ordos Basin, rather than organic acid-controlled carbonate dissolution during burial as previous proposed because the burial dissolution is normally not depth-dependent within an individual shoal.

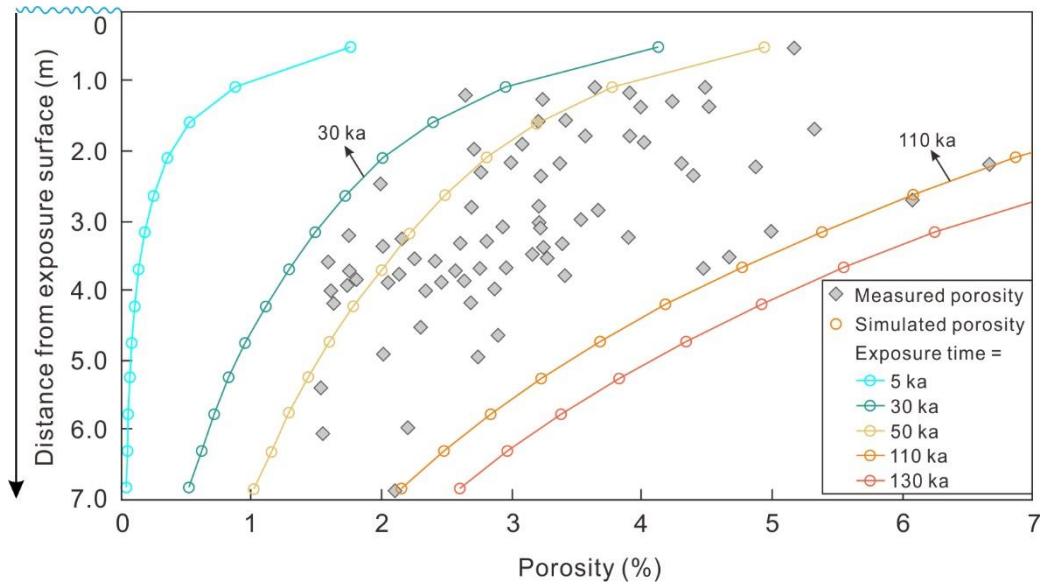

Figure 5.17 Comparison of measured rock porosity with simulated porosity. The measured porosities show a decreasing trend with increasing distance from exposure surface, and are distributed between the simulated porosity curves of 30 ka and 110 ka.

5.3.4 Controlling factors of karst-reservoir development

The controlling factors of paleokarst in the Ordovician Ordos Basin and their impacts on reservoir development have been extensively studied. Nevertheless, the previous studies focus mainly on the petrographic characterization such as reservoir types, accumulative thickness of

shoal-deposits, identification of multi-stage subaerial exposure surfaces and reconstruction of paleokarst model (e.g., Wang and Al-Aasm, 2002; He et al., 2013; Xie et al., 2020), less attention has been paid to the different reservoir properties under influences of various extrinsic hydrogeochemical conditions and intrinsic rock textures. For instance, the potential influences of global sea surface temperature, climate-related rainfall recharge, atmospheric carbon dioxide concentration during the Ordovician and sedimentary permeability anisotropy have been barely discussed in the literature; whereas these factors have been proven to have significant impacts on the formation of carbonate reservoirs according to the simulation study of the column model in the previous chapter 4. As a result, the long-standing paleokarst products-based research methods and the uncertainties of key hydrogeochemical conditions have limited the accuracy of reservoir quality prediction in the Ordos Basin. In this study, the thermo-hydro-chemical coupled RTM simulation has been verified to be an effective method to quantitatively constrain and reconstruct the water-rock interactions and resulting porosity evolution in a meteoric karst system. Therefore, the following part further evaluates the influences of these key parameters on the degree of karstification and the distribution of dissolution lens within an individual shoal-facies reservoir. In the simulation, only one parameter was changed for sensitivity analysis, and the rest remain the same as the base case scenario with an exposure time of 130 ka.

(1) Sea surface temperature

To reveal the impact of temperature variation on the eogenetic karst process, a group of gradually elevated temperatures are specified as the initial temperatures at the top boundary of the grid system, including 25, 30, 35 and 40°C, representing the temperature fluctuation of global sea surface during the Ordovician (age ca. 485.4–443.8 Ma; Trotter et al., 2008). The simulation results show different degrees of karstification and ranges of dissolution lens with temperature variation (Fig. 5.18). Particularly, the range of dissolution lens expands obviously with the increase in temperature, from a limited area close to the meteoric water source at 25°C to a large area that almost covers the entire longitudinal depth of the shoal at 40°C. This indicates that the higher temperature would facilitate the diffusion and downward seepage of meteoric water within the vadose zone of the exposed shoal, and contribute to a deeper meteoric

diagenetic environment and the formation of thick-bedded reservoirs. However, the degree of karstification is inversely proportional to temperature, as shown by a significant decline in the maximum amount of dissolution from 21.2% at 25°C to 4.4% at 40°C. This can be well-explained by the Arrhenius equation (Eq. 3.5) because the calcite solubility is inversely proportional to temperature, and thus an increasing temperature condition contributes to a decreasing calcite solubility and eventually a lower degree of dissolution and rock porosity increment (Morse and Arvidson, 2002).

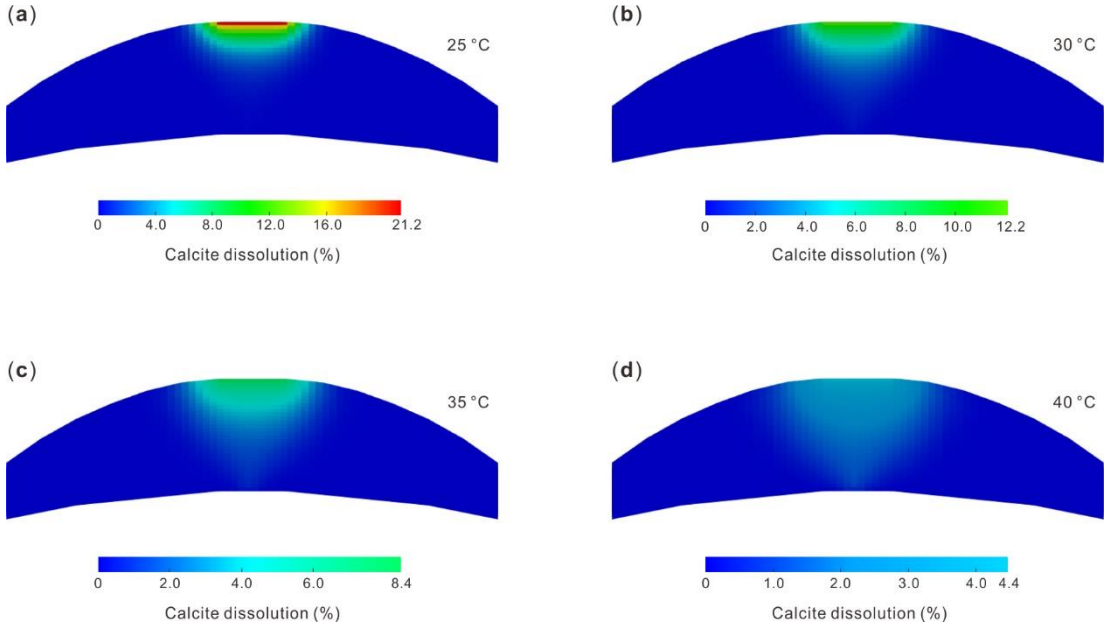

Figure 5.18 Simulation result of sensitivity analysis showing the distribution and amount of calcite dissolution under conditions of different sea surface temperatures.

(2) Climate-related rainfall recharge

The regional rainfall recharge is usually related to the climate condition (Whitaker and Smart, 2007), which largely determine the flux of meteoric water permeating into the geological formation. The simulation results show that the rainfall recharge has significant influences on both the degrees of karstification and the ranges of dissolution lens (Fig. 5.19). For instance, in arid to semi-arid environments (rainfall recharge <400 mm/a), the dissolution lens is limited to a very small area beneath the meteoric water injection cells, with the maximum amount of calcite dissolution of 4.6% and 7.8% under rainfall conditions of 200 mm/a and 400 mm/a, respectively. In humid to semi humid environments (rainfall recharge ≥400 mm/a), however,

the range of dissolution lens is apparently larger than that in arid to semi-arid environments, and the maximum amount of calcite dissolution under rainfall conditions of 628 mm/a and 800 mm/a are 12.2% and 18.6%, respectively. In general, the simulation results have indicated that a relatively humid climate with high rainfall recharge is important for the formation of large-scale high quality carbonate reservoir. This is also consistent with the result of the previous simulation in the column model (Xiong et al., 2021a).

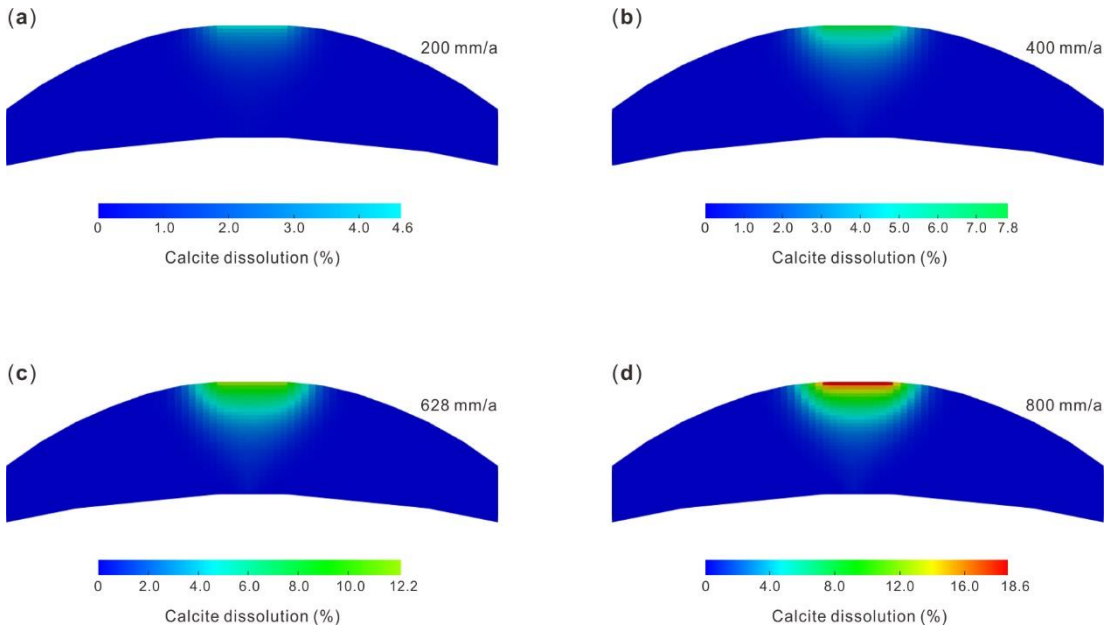

Figure 5.19 Simulation result of sensitivity analysis showing the distribution and amount of calcite dissolution under conditions of different rainfall recharges.

(3) Atmospheric carbon dioxide concentration

Given that the estimated pCO_2 value during the Ordovician by Berner (1997) has a wide range of error (from ca. 2,500 ppm to over 7,500 ppm, with the best value of ca. 5,500 ppm), it is essential to evaluate the impact of great pCO_2 variation on the eogenetic karst process. The impacting mechanism of pCO_2 on the eogenetic karst has been clarified using column model of meteoric water-rock system in the previous chapter 4, which affects carbonate dissolution mainly by changing the partial pressure of carbon dioxide and the conversion of CO_2 into H^+ and $HCO3^-$ in the solution. A comparison of the simulation results under conditions of different pCO_2 (i.e., 3,000, 5,500, 6,500 and 7,500 ppm) shows that the distribution and range of the dissolution lens remain almost unchanged, with an area of 6.5 m and 180 m in the vertical and

lateral directions, respectively (Fig. 5.20). Nevertheless, there is an increasing trend in the degree of karstification with gradual increase in pCO_2, as shown by an elevated maximum amount of dissolution from 10.8% (pCO_2 = 3,000 ppm) to 18.2% (pCO_2 = 7,500 ppm). The result has indicated that the pCO_2 can be an important rate-determining factor and relatively higher pCO_2 is conducive to produce higher rock porosity during eogenetic karst, while the thickness and range of the reservoir are nearly unaffected.

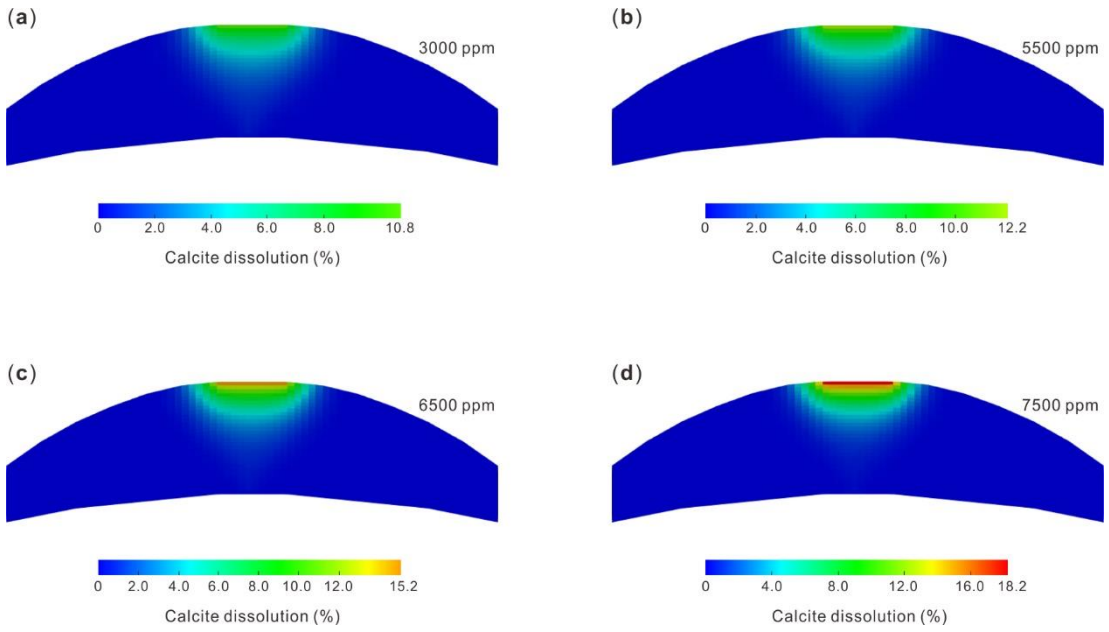

Figure 5.20 Simulation result of sensitivity analysis showing the distribution and amount of calcite dissolution under conditions of different atmospheric carbon dioxide concentrations.

(4) Permeability anisotropy

The permeability anisotropy is a common parameter used to evaluate the physical property of reservoir rocks, which refers to the difference of permeability in different directions. It is usually related to the degree of order (the higher the degree of order, the stronger anisotropy) and the shape of rock particles, as well as some special sedimentary or diagenetic fabrics (Witt and Brauns, 1983; Rasolofosaon and Zinszner, 2002; Armitage et al., 2011). For example, the permeability anisotropy in shale reservoir is mostly controlled by its bed-parallel lamellated fractures (Zeng et al., 2016); the permeability anisotropy of sandstone reservoir can be influenced by various types of bedding structures including vertical, parallel and oblique beddings (Liu et al., 2018); the permeability anisotropy of carbonate reservoirs is generally

associated with some specific sedimentary fabrics such as the microbial laminas and their intervenient primary fenestral pores, the low-permeable argillaceous interlayers and the micro-fractures formed by soft sediment deformation (Sun et al., 2017). The influence of permeability anisotropy on the karst process is mainly determined by the differences in seepage and diffusion rates of meteoric water in different directions, which results in great uncertainties in the range and extending trend of the dissolution lens. To evaluate the difference in calcite dissolution within a shoal reservoir, four types of permeability anisotropy, i.e., $k_{horizontal}/k_{vertical}$ = 0.2, 0.5, 2.0 and 5.0, were involved in the simulation (Fig. 5.21). To be specific, when $k_{horizontal} < k_{vertical}$, the dissolution lens tends to extend vertically, and the meteoric water has greater influence in the vertical direction of the shoal while the lateral expansion of dissolution lens has been limited by relatively low $k_{horizontal}$. In contrast, when $k_{horizontal} > k_{vertical}$, the diffusion of meteoric water is preferential in the lateral direction, thus leading to a relatively small karst depth penetration and eventually a horizontal elliptic dissolution lens located at the top of the shoal. The result has also shown that although the permeability anisotropy has significant influences on the shape and extending trend of the dissolution lens, the degree of karstification has been less affected, as indicated by a minor change in the maximum amount of dissolution (from 10.6% to 13.2%) at different values of permeability anisotropy.

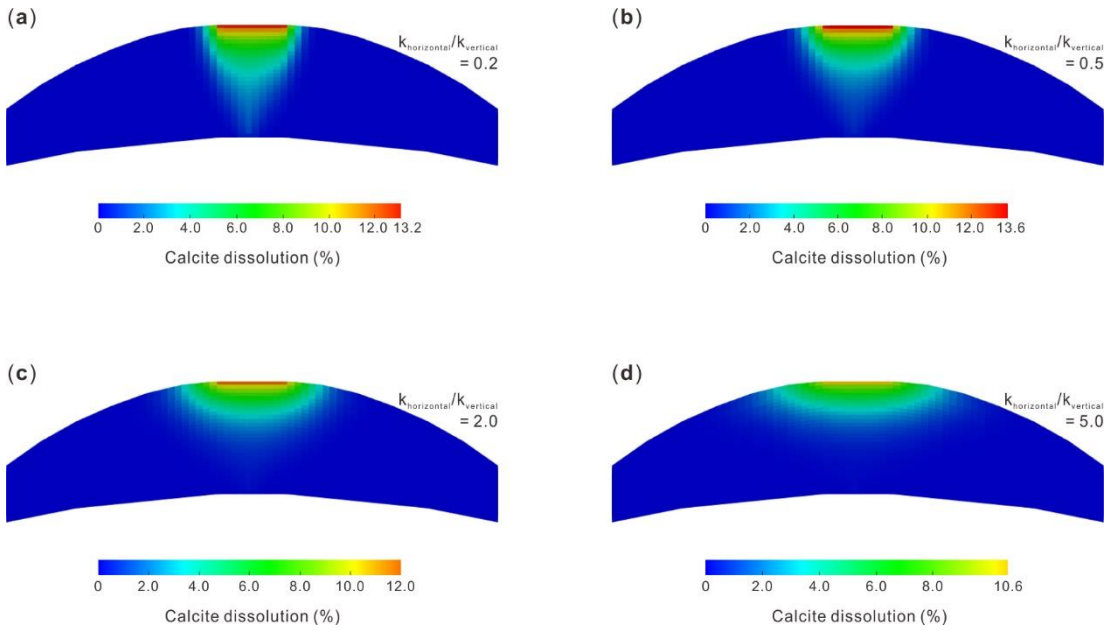

Figure 5.21 Simulation result of sensitivity analysis showing the distribution and amount of calcite dissolution under conditions of different values of permeability anisotropy.

5.4 Diagenesis-porosity evolution and carbonate reservoirs prediction

5.4.1 Diagenetic history and porosity evolution

The Ordos Basin is a polycyclic superposition basin that formed in an earlier geological history and has experienced a long period of evolution. After sedimentation of the Middle Ordovician Majiagou Formation, the sub-salt carbonate strata (i.e., $Ma5_{7–10}$) in the study area underwent the prolonged diagenetic processes from submarine, shallow burial, subaerial exposure to medium-deep burial conditions (Fig. 5.22). The relevant diagenetic environments were also complicated and varied greatly from seawater to meteoric to burial brine environments. As a result, abundant characteristics associated with the prolonged diagenetic alteration have been documented in the rock records (Fig. 5.23). Based on detailed petrographic analysis of drill cores and also the author's previous works on the multiple diagenesis in this area (Xiong et al., 2019, 2020a), this prolonged diagenetic process of the carbonate reservoir in the sub-salt Majiagou Formation can be divided into three main stages, corresponding to the different diagenetic fluids and environmental conditions.

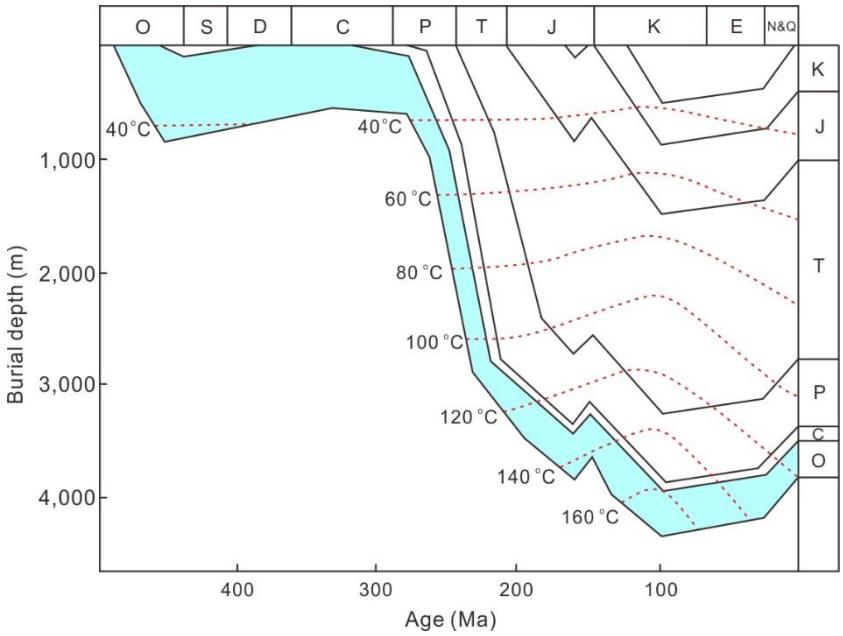

Figure 5.22 Stratigraphic burial and thermal history of the Ordovician strata in the Ordos Basin, based on frilling data from well Tainsheg1 (modified after Wang and Al-Aasm, 2002).

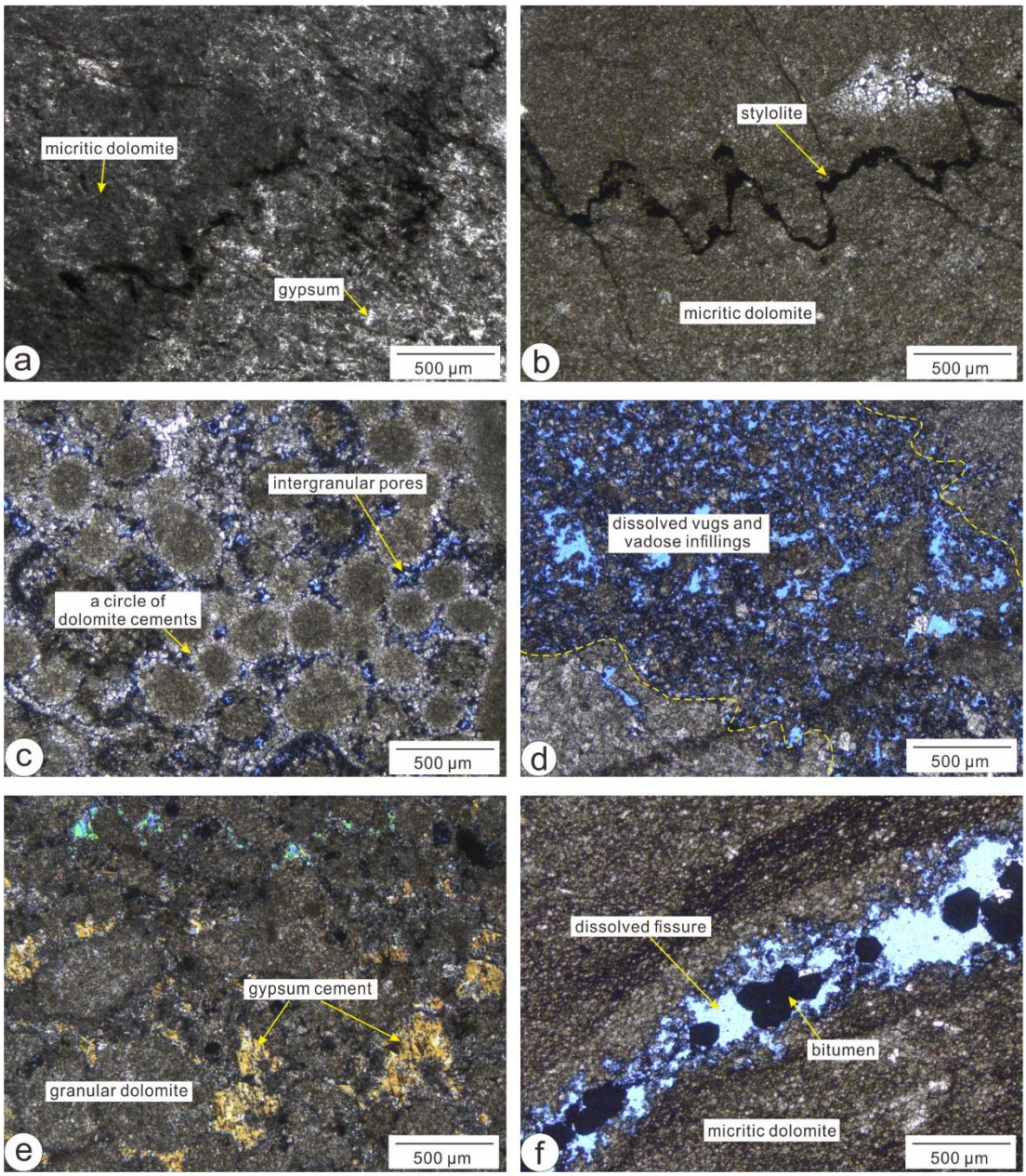

Figure 5.23 Photomicrographs showing the various diagenetic features of the sub-salt Majiagou Formation in the Ordos Basin. (a) The coexistence of micritic dolomite and gypsum in dolomite front zone. Well Jin2, 3,610.50 m. (b) Stylolite in the micritic dolostone, suggesting an intense compaction during medium to deep burial stage. Well Jin2, 3,590.02 m. (c) Oolitic dolostone, note the rim of dolomite isopachous cements enveloping the ooids. Abundant intergranular pores are well-preserved. Well Jin2, 3,587.83 m. (d) Crystalline dolostone with typical paleokarst features. The dissolved vugs are half-infilled by vadose dolomite silts. Well Jin2, 3,591.72 m. (e) Granular dolostone with abundant gypsum cements infilled in the intergranular pores. Well Jin2, 3,586.75 m. (f) Micrite dolomite with open fissure formed by burial dissolution. Note the bitumen floating within the fissure, indicating potential

hydrocarbon degradation during after the formation of dissolved fissure. Well Tong76, 3,725.44 m.

Syngenetic to very early diagenetic stage. This stage is characterized by primary precipitation of primary carbonate and evaporite minerals in the submarine environment. These initial sediments were generally unconsolidated and had relatively high porosities and permeabilities. With the accumulation of sediments, compaction took place and the initial calcareous sediments (calcite muds and particles) were subjected to rapid micritization and lithification processes, forming the widespread micritic and granular limestone. Moreover, during sedimentation of the Ordovician Majiagou Formation, the North China Block was in the low-latitude subtropical zone and the Ordos Basin was characterized by a shallow-marine carbonate platform restricted by ambient paleo-uplifts (Wang et al., 1990; Fu et al., 2017). In such a geographic setting, periodic evaporation of seawater and the increase of salinity contributed to the multistage reflux dolomitization events in the relatively lowlands of the platform (i.e., lagoon). The shoal-facies grainstone, which was located at paleo-highs of the platform due to its relatively rapid sedimentation rate (Tan et al., 2014), was more likely to be exposed and subjected to meteoric water leaching during periodic sea level regressions, leading to the multistage eogenetic karst systems.

Shallow burial stage. After sedimentation of the Ordovician Majiagou Formation, the cyclic carbonate-gypsum deposits, which were weakly consolidated, underwent the shallow burial environment. Due to continuous increase of the overlying sediments and under the influence of increasing compaction, high salinity fluids (i.e., hypersaline seawater sealed in pores) were released from the cyclic gypsum layers and then seeped into the adjacent carbonate rocks, resulting in gypsum cementation in the intergranular pores. Although the inflow of compaction-released hypersaline seawater and gypsum precipitation during this period resulted in significant reservoir degradation, a recent study has shown that this gypsum cementation occurred mainly in the shoal margins, and this densification and relatively poor properties of the shoal margins protected the shoal core from cementation and alteration by hypersaline seawater (Xiong et al., 2020a). Thus, abundant dissolved pores have been well-preserved in

the core part of shoals.

Medium to deep burial stage. Since the late Carboniferous, the North China Block have slowly subsided after a long period of tectonic uplift due to the Caledonian orogeny from the Late Ordovician to the Early Carboniferous (Wang and Al-Aasm, 2002; Meng et al., 2019). Hence, the sub-salt Majiagou Formation underwent a continuous burial environment with a rapid increase in burial depth, and reached the maximum burial depth of more than 4,000 m in the Cretaceous period (Fig. 5.22). In medium to deep burial environment, the diagenetic fluids are mainly hypersaline seawater and basinal brines that were sealed in the in site rock porosity and salt-bearing depression (eastern Ordos Basin), respectively. The grainstone, which developed in shoal facies, preserved abundant dissolved pores and vugs that could provide flow pathways for burial diagenetic fluids. Thus, with gradual increases in formation temperature and pressure, these Mg^{2+}-rich high salinity burial fluids preferentially migrated into the porous grainstone. As a result, burial dolomitization and recrystallization occurred in the shoal-facies grainstone, resulting in transformations of lithology and pore structure from the granular dolomite with intergranular pores into the crystalline dolomite with intercrystalline pores (Xiong et al., 2020a). In addition, hydrocarbon degradation-related organic acids and magmatic activities-related hydrothermal fluids also resulted in slight burial dissolution in local areas. Although the microfractures can be occasionally observed in dolostone, most of them have been full-infilled by medium-coarse calcite cements and thus have poor reservoir capacity.

It should also be noted that although the diagenetic environments and fluid properties of the Majiagou Formation in the Ordos Basin have been revealed generally, the carbonate rocks in different sedimentary facies exhibit different diagenetic pathways, thus resulting in differential evolution of reservoir properties. Based on a combination of the quantitative constraints of dolomitization and karstification during early diagenesis in this study, and the qualitative analysis of burial diagenesis in the previous studies, the diagenesis-porosity evolution of the two main types of carbonate rock in the study area are established (Fig. 5.24).

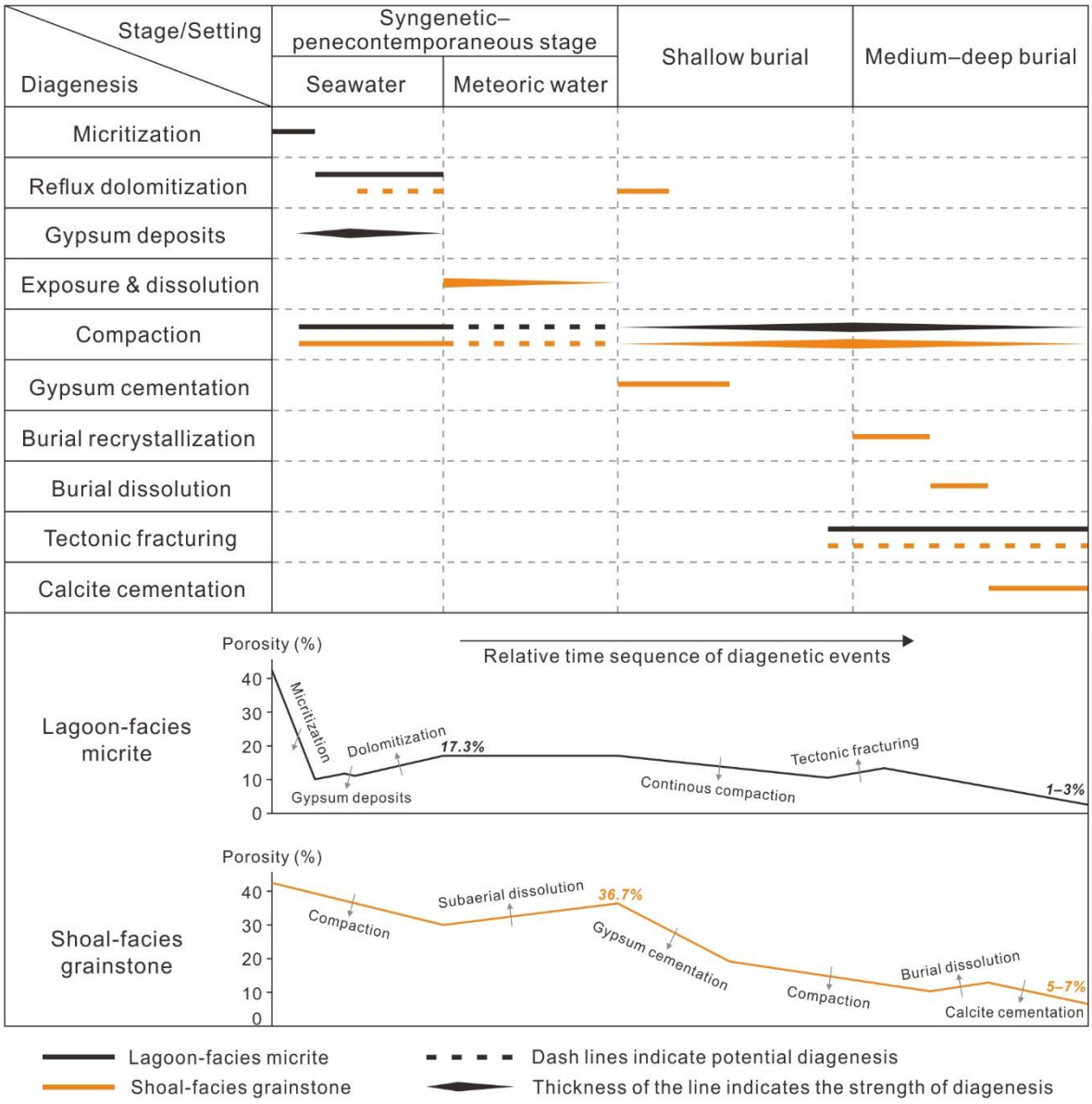

Figure 5.24 Diagenetic pathways and porosity evolution of the two main types of carbonate rock in the sub-salt Majiagou Formation in the Ordos Basin.

(1) Diagenesis-porosity evolution of lagoon-facies micrite

The newly deposited carbonate sediments typically have high porosities of more than 40% (Schmoker and Halley, 1982). However, the primary porosity of these fine-grained deposits in lagoon facies would decline dramatically (to ca. 10%) during very early diagenetic stage as the results of rapid micritization, lithification and compaction. Meanwhile, the relatively arid climate and intense evaporation in the Ordovician Ordos Basin led to the increase in seawater salinity. The high-density concentrated seawater would then seep downward and migrate into the relatively lowlands of the platform, and thus promoted reflux dolomitization of the initial

calcareous fine-grained sediments (micrite) in restricted-evaporative lagoon environment. According to the 2D simulation of multistage reflux dolomitization, the dolomitization process was accompanied by precipitation and dissolution of gypsum (Fig. 5.23a), and the evolution of rock porosity depended on the relative rates of pore-infill by gypsum precipitation and pore-increment via dolomitization. To be specific, in the flow path of dolomitizing fluids (the dolomite front zone), the enrichment of Ca^{2+} that was released during the replacement of calcite by dolomite resulted in relatively high rate of gypsum precipitation ($CaSO_4 \cdot 2H_2O$) and thus a slight decrease in rock porosity. Subsequently, the early-formed gypsum tended to be dissolved since the continuously injected dolomitizing fluid are unsaturated with respect to gypsum, which gave rise to a re-increase of the rock porosity. After pervasive dolomitization, the lagoon-facies micritic dolostone has a general porosity increment of 7.31% compared with its micrite (limestone) precursor (Fig. 5.12). On the other hand, due to a relatively low geomorphic position, the lagoon-facies micritic dolostone was barely affected by subaerial exposure or meteoric water leaching at the penecontemporaneous stage. During burial, the porosity of micritic dolostone exhibited a steady decreasing trend under continuous compaction (Fig. 5.23b). Although a small quantity of microfractures might be produced due to the influence of tectonic compression during the Late Jurassic period (driven by the Yanshanian orogeny), which resulted in a slight increase in porosity, most of these microfractures then were infilled by macrocrystalline calcite cement under deep burial conditions. In general, the lagoon-facies micritic dolostone eventually shows relatively low porosities of 1–3% (Fig. 5.24).

(2) Diagenesis-porosity evolution of shoal-facies grainstone

For the shoal-facies grainstone in the Majiagou Formation, detailed petrographic analysis shows that some of the particles in the dolarenite and oolitic dolostone are enveloped by a rim of dolomite cements (Fig. 5.23c). These isopachous cements, which are fine-grained, typically grown around the outer edges of the particles under submarine to shallow burial environments (Zuo et al., 2019; Liu et al., 2020). Although these cements occupied part of the primary pore space, the residual intergranular pores tended to be isolated and well-preserved since the annular cementation of particles strengthened the granular structures (Tan et al., 2014). Therefore, in the early diagenetic stage, the porosity decline of shoal-facies grainstone under

the influence of compaction should be lower that of lagoon-facies micrite. Moreover, in comparison with lagoon-facies micrite, a major characteristic of shoal-facies grainstone is that it underwent eogenetic karst (Fig. 5.23d) during penecontemporaneous stage due to its relatively high geomorphic position, which resulted in a porosity increment of about 6.7% according to the simulation result (Fig. 5.17). During the subsequent burial diagenetic stage, the porous grainstone was subjected to gypsum cementation (Fig. 5.23e) and recrystallization, leading to a decline of reservoir porosity as well as a transformation of rock structure (i.e., from granular dolomite with intergranular pores into crystalline dolomite with intercrystalline pores). Additionally, burial dissolution associated with organic acids and hydrothermal fluids were observed in local area of the Ordos Basin (Fig. 5.23f), which resulted in a slight short-term increase in porosity superimposed on the long-term decreasing trend. In general, the shoal-facies deposits, which currently includes granular and crystalline dolostone, exhibit good reservoir capacities and have relatively high porosities of 5–7% (Fig. 5.24).

5.4.2 Implications for carbonate reservoirs exploration

Based on the above analyses of diagenetic history and porosity evolution, reflux dolomitization and eogenetic karst during the syngenetic to early diagenetic stage are the two dominant factors that improve the reservoir quality. Although a few other types of constructive diagenesis have also been occasionally observed in the studied area, such as recrystallization and burial dissolution, numerous studies have shown that the occurrence of these burial diageneses were still controlled by the early-form high porosity-permeability zones (Fu et al., 2019; Xiao et al., 2019; Xiong et al., 2021c). Thus, the main contribution of the superimposition of burial diagenesis was to optimize the pore structure of early-formed reservoirs (i.e., transformation from intergranular pores to intercrystalline pores). This is conducive to the preservation of reservoir porosity because the crystallized structure of dolostone are generally thought to be more resistant to compaction (Schmoker and Halley, 1982; Jiang et al., 2016), but which has limited effect on the direct generation of new pore spaces. In general, the dolostone reservoir in the Majiagou Formation (Ordos Basin) display a typical characteristic of control by early diagenesis. Therefore, the predictions of reservoir quality should be traced back to the nature

of the sedimentary environment and paleo-geomorphology that have significantly controlled the occurrence of dolomitization and karstification in the early diagenetic stage.

Simulation results of 2D reflux dolomitization have shown that the widespread dolostone in the carbonate-evaporite successions was likely the result of superposition of a series of relatively short-term dolomitization events. For an individual dolomitization event, a tabular dolomite body was formed beneath the gypsum layer, corresponding to the late stage of the depositional sequence. These dolomite zones have relatively higher porosity-permeability than the limestone precursors. Therefore, in the vertical, the dolomite strata, which are sandwiched in between the cyclic gypsum layers, are likely to be favorable exploration targets (e.g., the $Ma5_9$ and $Ma5_7$ sub-members). Particularly, a recent exploration breakthrough has been made in the thin-bedded dolostone interlayers between the multiple gypsum layers in the $Ma5_6$ sub-member (Huang et al., 2021), which also supports our simulation results. In general, this predictive analysis is based on two reasons. First, in the restricted-evaporative shallow marine environment of the study area, the Middle Ordovician high frequency sea level fluctuations resulted in periodic increase in seawater salinity and the superimposition of multistage depositional sequences. Commonly, a single upward-shallowing sequence ends with the gypsum deposition, which indicates that during the process of gradually increasing seawater salinity, the later stage of carbonate deposition (i.e., prior to the final sulfate precipitation such as gypsum and halite) should be the favorable period for reflux dolomitization. Second, these multiple gypsum layers, which directly overlie the dolostone reservoirs, serve as good cap rocks. The relatively high sedimentation rate of gypsum and subsequent release of free water due to the dehydration during burial (i.e., transformation from gypsum ($CaSO_4 \cdot 2H_2O$) to anhydrite ($CaSO_4$)) could also result in disequilibrium compaction and increase in pore fluid pressure (Tingay et al., 2009; Daigle et al., 2017). Thus, overpressure might be generated within the interbedded carbonate strata, which is conducive to the preservation of dolostone reservoir spaces and the enhancement of oil and gas productivity.

Moreover, the spatial distribution of karst-related reservoir is closely related to the paleo-geomorphology during sedimentation. To be specific, the Middle Ordovician Ordos Basin was

characterized by a general landscape of higher in the west (uplift) and lower in the east (depression), and there was a clear lithofacies transition of limestone (mudstone) to dolostone to gypsum and salt rocks from the west to the east (Fig. 5.1c). Based on the paleo-geomorphic setting and our simulation results characterizing the range and degree of eogenetic karst, herein we propose that the regional paleo-highlands in the middle-eastern parts of Yishan Slope area (i.e., along the Shanbei Depression) should be favorable targets for further exploration of such karst-related reservoir in the sub-salt Majiagou Formation (Fig. 5.25), rather than the Central Uplift and its surrounding areas as previously thought (Wu et al., 2014; Yu et al., 2018). Several main reasons are as follows.

First, the Yishan Slope area was located in the transition zone between the Central Uplift and the salt-dominated Shanbei Depression, with a moderate seawater salinity that is favorable for dolomitization. During syngenetic period, this area was subjected to pervasive reflux dolomitization. Second, this shallow seawater area, which was generally in the high-energy subtidal to intertidal zone (Fu et al., 2017; Chen et al., 2019), contributed to the development of the foundation of the reservoir rocks, i.e., carbonate shoal grainstone in the relative paleo-highlands (Fig. 5.25). Due to periodic sea level fluctuations in the Middle Ordovician Ordos Basin (Xiong et al., 2019), these shoal-facies deposits were susceptible to intermittent subaerial exposure and leaching by meteoric water, leading to facies-controlled dissolution and interconnected pore networks. The adjacent paleo-lowlands, however, were dominated by the organic-rich argillaceous carbonates and laminar gypsum deposits of a restricted-evaporative lagoon environment. As such, multisets of source-reservoir-cap assemblages, which comprise interbedded argillaceous dolostone, granular/crystalline dolostone with pore networks, and gypsum layers, were formed. Moreover, these interbedded carbonate-evaporite successions would have contributed to a relatively closed diagenetic system during burial as the high-density gypsum layers would have significantly impeded the diffusion of burial fluids (e.g., basinal brines and magmatic fluids), thus facilitating the preservation of early-formed pores in the carbonate karst system (Bjørlykke and Jahren, 2012; Liu et al., 2020). In general, based on identification of the multistage subaerial exposures via core and logging data, and together with the above simulation results, we conclude that the exploration for high-quality hydrocarbon

reservoirs (i.e., karst-altered dolostone) in the Majiagou Formation (Ordos Basin) could be concentrated on the core part of carbonate shoals, particularly at locations a few meters (normally less than 3 m) below the multistage subaerial exposure surfaces.

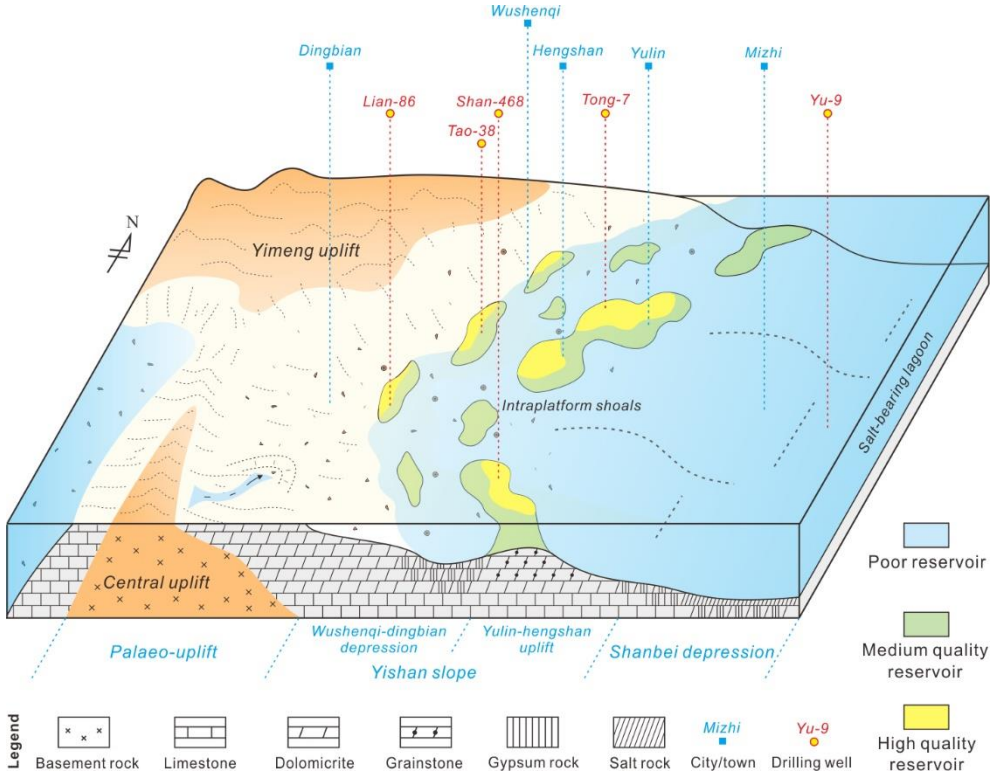

Figure 5.25 Conceptual geological model showing the paleogeomorphic feature, sedimentary environment and distribution of hydrocarbon reservoirs in the sub-salt Majiagou Formation in the Ordos Basin (the locations of shoal deposits refer to Fu et al., 2017).

5.5 Summary

In this chapter, a case study, which combined RTMs method and traditional geological methods (i.e., petrography and physical reservoir properties), was conducted in the Middle Ordovician Majiagou Formation in the Ordos Basin, North China. On the basis of existing geological knowledge and abundant drill data, simulations were performed on the two key types of carbonate diagenesis including multistage reflux dolomitization and facies-controlled eogenetic karst. Particularly, the temporal and spatial evolution of minerals and reservoir porosities were reconstructed. Controlling factors of these two diagenetic processes were also investigated based on sensitivity analysis and evaluation of parametric uncertainty. Finally, a new diagenesis-porosity evolution model, which provides more diagenetic details and

quantitative data on porosity evolution than previous geological studies, was established and the favorable targets for further exploration of hydrocarbon reservoirs were pointed out. The main conclusion of this chapter are as follows.

The reflux dolomitization occurred mainly in the restricted-evaporative environment in the Ordos Basin, leading to a maximum porosity increment of 7.3% in the lagoon-facies micrite. Cyclic evolution of lithology and rock texture due to superimposition of multiple depositional sequences resulted in different brine fluxes and rock reactivities, and eventual varying degrees of dolomitization and heterogeneous distribution of dolomite zones. Although higher salinity and brine injection rate would promote the brine flux and dolomitization rate, the intercalated gypsum layers impeded downward seepage of brines and prevented the isolated dolomite bodies from merging into a larger dolomite zone.

The eogenetic karst developed mainly in the shoal-facies grainstone due to its relatively high paleo-topographic position in the basin and the Middle Ordovician high frequency sea level fluctuations. A dissolution lens was formed at the core part of the shoal during successive carbonate dissolution via meteoric water leaching. Based on a comparison of simulation results and measured data from drill core samples (e.g., reservoir thickness and porosities), the duration of subaerial exposure and karstification of shoal-facies grainstone in the sub-salt Majiagou Formation ranges mainly between 30–110 ka, leading to porosity increments of 1.5–6.7% (average 3.1%).

The hydrocarbon reservoirs in the sub-salt Majiagou Formation in the Ordos Basin display a typical characteristic of early diagenesis-control and the major reservoir porosities were formed during syngenetic to early diagenetic stage. The prediction of such carbonate reservoirs should particularly focus on the sedimentary environment and paleo-geomorphology that have significantly controlled the occurrence and distribution of dolomitization and karstification. Thus it can be inferred that the regional paleo-highlands (carbonate shoal facies) in the middle-eastern parts of Yishan Slope area should be favorable targets for further exploration of hydrocarbon reservoirs in the Ordos Basin.

6 Conclusions and outlook

Diagenesis research is an important basis for hydrocarbon reservoir characterization and exploration in sedimentary rocks. In the past few decades, great progress has been made in the theory and methodology of diagenesis, which contributes to numerous important achievements in guiding oil and gas exploration. The methodology of carbonate diagenesis is diverse, mainly including petrology, mineralogy, geochemistry, fluid inclusion petrography and laboratory physical experiments. Nevertheless, these diagenetic products-based methods have shortcomings in quantitative characterization of the evolution of diagenetic geo-bodies and the physical properties (porosity-permeability) of reservoirs at multiple spatial-temporal scales, which limits the prediction of precise diagenetic trends and thus introduces uncertainties into reservoir quality prediction. This thesis leverages reactive transport modeling (RTM), which is an emerging approach for diagenesis study, to forward simulate the two most important diagenetic processes of carbonate rocks (i.e., dolomitization and karstification), focusing on the mechanisms of diagenetic fluid-rock interactions, the spatial-temporal variations of diagenetic minerals and rock porosity as well as their potential controlling factors. Some controversies in carbonate diagenesis, which cannot be well explained by classical methods, have also been discussed. Based on investigation of two generic models, and a case study of hydrocarbon reservoir quality prediction in the Ordos Basin (North China) using integrated RTM and classical geological approaches, the following main conclusions are reached.

The fundamentals of the coupled thermo-hydro-chemical geo-processes are given in chapter 2. Three major fluid-rock interactions associated with carbonate diagenesis are considered in this thesis, i.e., carbonate dissolution, replacive dolomitization and concomitant gypsum/anhydrite cementation. The methodology and some representative mathematical/numerical models used for RTM studies in geological porous media are summarized, including chemical reactions, fluid flow and solute transport, and reaction-induced porosity and permeability changes. The simulations are performed using the reactive transport computer code TOUGHREACT, along which the coupling of thermo-hydro-chemical domains (THC) and solution method are also introduced.

The concentrated seawater-driven reflux dolomitization process is modeled in chapter 3. A simplified one-dimensional column model is used to simulate the mineral replacement reaction of calcite by dolomite. The kinetic process of dolomitization is modeled as a reaction network that comprises calcite dissolution followed by dolomite precipitation. Increased dolomite, decreased calcite and dynamic gypsum evolution (precipitation followed by dissolution) are observed during simulation. The gypsum precipitation is likely related to the combination of released Ca^{2+} during dolomitization (2 mole $CaCO_3$ replaced by 1 mole $MgCa(CO_3)_2$) and SO_4^{2-} in the solution. The rock porosity-permeability is collectively controlled by pore-increment via dolomitization and pore-infill by gypsum precipitation, displaying a dynamic variation of slight decrease followed by substantial increase. Sensitivity analyses suggest that the reaction rate and degree of dolomitization can be influenced by various hydrogeochemical conditions and rock fabrics (sediment reactivity and fluid mobility). Higher brine salinity, temperature, reactive surface area and brine injection rate accelerate the reaction rate, while the degree of dolomitization can only be enhanced under conditions of higher brine salinity and temperature, as well as fine-grained rock fabric such as micrite.

The eogenetic karst process of carbonate sediments in the meteoric diagenetic environment is modeled in chapter 4 using a one-dimensional generic model. In the vadose meteoric water-rock system, there is a downward decreasing trend in carbonate dissolution and rock porosity. The exposure time and rainfall recharge significantly determine the karst-affected depth and porosity increment. The amount of dissolution is also affected by a downward decrease in calcite solubility (temperature-dependent) and the enrichment of Ca^{2+} and HCO_3^- in the lower part. The promotional effect of calcite dissolution from increasing rainfall is more significant than increasing exposure time. The atmospheric carbon dioxide concentration is an important rate-determining factor of carbonate dissolution, because higher pCO_2 is conducive to higher dissolution rate, but has a minor impact on the extent of karst. The influence of atmospheric pCO_2 variation over geological time on porosity increment during eogenetic karst has also been reconstructed in a hypothetic base case scenario. Due to the different rate-determining reaction mechanisms, thermodynamically controlled calcite (limestone) tends to have a higher dissolution rate than kinetically controlled dolomite (dolostone) in a subaerial low-temperature

environment.

Following generic model studies, chapter 5 presents an integrated geological (petrographic and physical reservoir properties) and RTM study of hydrocarbon reservoir prediction in the Ordovician Majiagou Formation, Ordos Basin, China. RTM simulations are performed on the two key diagenetic processes, i.e., multistage reflux dolomitization and facies-controlled eogenetic karst. The reflux dolomitization occurred mainly in the restricted-evaporative environment, leading to a maximum 7.3% porosity increment of the lagoon-facies micrite. Cyclic evolution of lithology and rock texture due to superimposition of multiple depositional sequences resulted in different brine fluxes and rock reactivities, and eventually varying degrees of dolomitization and heterogeneous distribution of dolomite zones. The intercalated gypsum layers impeded downward seepage of brines and prevented the isolated dolomite bodies from merging into a larger dolomite zone. The eogenetic karst developed mainly in the shoal-facies grainstone due to its relatively high paleo-topographic position and high frequency sea level fluctuations. A dissolution lens was formed at the core part of shoal deposits during successive meteoric water leaching. Integrated simulation results and drill/measured data suggest that the duration of subaerial exposure and karstification of shoal-facies grainstone ranges mainly between 30–110 ka, leading to porosity increments of 1.5–6.7% (average 3.1%). In summary, the Majiagou Formation reservoir displays the typical characteristic of control by early diagenesis and the major reservoir porosities were formed during the syngenetic-early diagenetic stage. The prediction of such reservoirs should particularly focus on the sedimentary environment and paleo-geomorphology that have significantly controlled the occurrence and distribution of dolomitization and karstification. It can be thus inferred that the regional paleo-highlands (carbonate shoal facies) in the middle-eastern parts of Yishan Slope area should be favorable targets for further exploration of high quality reservoirs in the Ordos Basin.

As an expanding discipline in geosciences, numerical modeling of diagenetic fluid-rock interactions has achieved remarkable advances in the past 20 years, and has been proven to hold great potential for both academic interest and industrial applications. However, it must be acknowledged that the RTM approach still faces a few challenges before it can be routinely

used for practical reservoir prediction and development risk assessment. First, most of the models used in current studies are based on generic hydrological and geochemical mechanisms, while ignoring the complexity and heterogeneity of rock fabrics, textures and pore-throat sizes. Hence, an inevitable problem is that the fluid flow and solute transport processes in natural geological systems are more complex than that in simulated grid cells which always require necessary simplification and assumptions. This issue undermines the confidence of traditional geologists in the utility of the modeling approach. Second, a major challenge facing RTM simulation of diagenesis is that we are currently unable to validate the model or a particular diagenetic event at a geological spatial-temporal scale, which results in uncertainties in the extrapolation of the simulation results. For instance, the rate constant in Eq. 3.6 is obtained from the laboratory dolomite precipitation experiment conducted by Arvidson and Mackenzie (1999) under high-temperature conditions (115–196°C). In a near-surface low-temperature environment with reflux dolomitization, the applicability of this empirical rate constant remains uncertain. Besides, intense karstification is usually accompanied by rock structure changes, such as karst collapse, mixed infill and in situ brecciation, which result in significant complexity and uncertainty of the fluid flow. In this case, the current porosity-permeability relationship (Eq. 2.64), which is derived from the Kozeny-Carman equation, seems to be inapplicable.

Therefore, in follow-up work, the thermodynamic/kinetic mechanisms of more diagenetic geochemical reactions, especially under various environmental conditions, need to be explored, such as the different formation mechanisms of dolomite under high-temperature laboratory conditions and low-temperature natural conditions. Possible changes in rock structure during diagenesis with their feedback on rock reactivity and permeability should also be taken into consideration, such as the impact of rock collapse, brecciation and karst conduit on fluid flux and flow paths, and the impact of burial compaction on mineral reactive surface area. Overall, numerical modeling of diagenetic fluid-rock interactions requires further refinements in the fields of eliminating thermodynamic and kinetic uncertainties and coupling sedimentary (or diagenetic) heterogeneity and rock structure changes in the current thermo-hydro-chemical (THC) models. Integrating the use of classical geological methods (as many as possible) and

the RTM approach should be emphasized, especially with regard to the mutual verification of laboratory physical experiments and simulation results. These issues will likely become attractive venues of diagenesis research in the near future.

Through simplifying the complex geological processes into conceptual hydrological and geochemical models that are more accessible, RTM simulation is expected to be widely applied in future petroleum geology because it provides a faster and more economical approach to characterize and predict reservoir quality on a flexible spatial-temporal scale, especially in areas that are poorly explored or away from well control. Furthermore, RTM of fluid-rock interactions also has broad applications on other types of geo-energy development such as calcite/anhydrite/salt cementation in geothermal reservoirs and on CCUS research such as CO_2 underground sequestration and bio-methanation, and the karst-related carbon cycle.

References

Ajami, N.K., Gu, C., 2010. Complexity in microbial metabolic processes in soil nitrogen modeling: a case for model averaging. *Stochastic Environmental Research and Risk Assessment*, 24, 831–844.

Al-Helal, A., Whitaker, F., Xiao, Y.T., 2012. Reactive transport modeling of brine reflux: dolomitization, anhydrite precipitation, and porosity evolution. *Journal of Sedimentary Research*, 82, 196–215.

Armitage, P.J., Faulkner, D.R., Worden, R.H., Aplin, A.C., Butcher, A.R., Iliffe, J., 2011. Experimental measurement of, and controls on, permeability and permeability anisotropy of caprocks from the CO_2 storage project at the Krechba Field, Algeria. *Journal of Geophysical Research: Solid Earth*, 116, B12208.

Arora, B., Şengör, S.S., Spycher, N.F., Steefel, C.I., 2015. A reactive transport benchmark on heavy metal cycling in lake sediments. *Computational Geosciences*, 19, 613–633.

Arvidson, R.S., Ertan, I.E., Amonette, J.E., Luttge, A., 2003. Variation in calcite dissolution rates: A fundamental problem?. *Geochimica et Cosmochimica Acta*, 67, 1623–1634.

Arvidson, R.S., Mackenzie, F.T., 1999. The dolomite problem; control of precipitation kinetics by temperature and saturation state. *American Journal of Science*, 299, 257–288.

Azimi, G., Papangelakis, V.G., 2010. The solubility of gypsum and anhydrite in simulated laterite pressure acid leach solutions up to 250 C. *Hydrometallurgy*, 102, 1–13.

Badiozamani, K., 1973. The Dorag dolomitization model - application to the middle Ordovician of Wisconsin. *Journal of Sedimentary Research*. 43, 965–984.

Bai, X.L., Zhang, S.N., Huang, Q.Y., Ding, X.Q., Zhang, S.Y., 2016. Origin of dolomite in the Middle Ordovician peritidal platform carbonates in the northern Ordos Basin, western China. *Petroleum Science*, 13, 434–449.

Bear, J., 1972. Dynamics of fluids in porous media. Courier Corporation.

Berner, R.A., 1997. The rise of plants and their effect on weathering and atmospheric CO_2. *Science*, 276, 544–546.

Bethke, C.M., 1998. The geochemist's workbench: Hydrogeology program: Urbana, Illinois, University of Illinois, 224 p.

Bjørlykke, K., Jahren, J., 2012. Open or closed geochemical systems during diagenesis in

sedimentary basins: Constraints on mass transfer during diagenesis and the prediction of porosity in sandstone and carbonate reservoirsGeohorizon. *AAPG Bulletin*, 96, 2193–2214.

Bogan, R.A., Ohde, S., Arakaki, T., Mori, I., McLeod, C.W., 2009. Changes in rainwater pH associated with increasing atmospheric carbon dioxide after the industrial revolution. *Water, Air, and Soil Pollution*, 196, 263–271.

Borgia, A., Pruess, K., Kneafsey, T.J., Oldenburg, C.M., Pan, L., 2012. Numerical simulation of salt precipitation in the fractures of a CO_2-enhanced geothermal system. *Geothermics*, 44, 13–22.

Bouissonnié, A., Daval, D., Marinoni, M., Ackerer, P., 2018. From mixed flow reactor to column experiments and modeling: Upscaling of calcite dissolution rate. *Chemical Geology*, 487, 63–75.

Budd, D.A., Park, A.J., 2018. Formation of bed-scale spatial patterns in dolomite abundance during early dolomitization: Part I. Mechanisms and feedbacks revealed by reaction-transport modelling. *Sedimentology*. 65, 209–234.

Buhmann, D., Dreybrodt, W., 1985. The kinetics of calcite dissolution and precipitation in geologically relevant situations of karst areas: 1. Open system. *Chemical Geology*, 48, 189–211.

Burchette, T.P., 2012. Carbonate rocks and petroleum reservoirs: a geological perspective from the industry. *Geological Society, London, Special Publications*, 370, 17–37.

Charlton, S.R., Parkhurst, D.L., 2011. Modules based on the geochemical model PHREEQC for use in scripting and programming languages. *Computers & Geosciences*, 37, 1653–1663.

Chen, A.Q., Xu, S.L., Yang, S., Chen, H.D., Su, Z.T., Zhong, Y.J., Hu,S.H., 2018. Ordovician deep dolomite reservoirs in the intracratonic Ordos Basin, China: Depositional model and Diagenetic evolution. *Energy Exploration & Exploitation*, 36, 850–871.

Chen, A.Q., Yang, S., Xu, S.L., Ogg, J., Chen, H.D., Zhong, Y.J., Zhang, C.G., Li, F., 2019. Sedimentary model of marine evaporites and implications for potash deposits exploration in China. *Carbonates and Evaporites*, 34, 83–99.

Chen, A.Q., Zou, H., Ogg, J.G., Yang, S., Hou, M.C., Jiang, X.W., Xu, S.L., Zhang, Xiao.X., 2020. Source-to-sink of Late Carboniferous Ordos Basin: Constraints on crustal accretion margins converting to orogenic belts bounding the North China Block. *Geoscience*

Frontiers, 11, 2031–2052.

Chen, Y.H., Liu, Y., Sun, T., 1985. Change of pore volume in dolomitization. *Experimental Petroleum Geology*, 7, 29–37 (in Chinese with English abstract).

Cooper, K., Xiao, Y.T., Whitaker, F., Goldstein, R., Li, Z.Q., Franseen, E.K., Stafford, S., Jones, G., 2014. Reactive transport modeling of mixed fluid dolomitisation: Traditional coastal mixing zones and ascending mixing of fresh-mesohaline water. AAPG, April 4–9, Houston, USA.

Cramer, O., 1993. The variation of the specific heat ratio and the speed of sound in air with temperature, pressure, humidity, and CO_2 concentration. *The Journal of the Acoustical Society of America*, 93, 2510–2516.

de Periere, M.D., Durlet, C., Vennin, E., Caline, B., Boichard, R., Meyer, A., 2017. Influence of a major exposure surface on the development of microporous micritic limestones-Example of the Upper Mishrif Formation (Cenomanian) of the Middle East. *Sedimentary Geology*, 353, 96–113.

Daigle, H., Worthington, L.L., Gulick, S.P., Van Avendonk, H.J., 2017. Rapid sedimentation and overpressure in shallow sediments of the Bering Trough, offshore southern Alaska. *Journal of Geophysical Research: Solid Earth*, 122, 2457–2477.

Davis, J.A., Meece, D.E., Kohler, M., Curtis, G.P., 2004. Approaches to surface complexation modeling of uranium (VI) adsorption on aquifer sediments. *Geochimica et Cosmochimica Acta*, 68, 3621–3641.

Dupraz, C., Reid, R.P., Braissant, O., Decho, A.W., Norman, R.S., Visscher, P.T., 2009. Processes of carbonate precipitation in modern microbial mats. *Earth-Science Reviews*, 96, 141–162.

Dyer, B., Higgins, J.A., Maloof, A.C., 2017. A probabilistic analysis of meteorically altered $\delta^{13}C$ chemostratigraphy from late Paleozoic ice age carbonate platforms. *Geology*, 45, 135–138.

Ehrenberg, S.N., Nadeau, P.H., 2005. Sandstone vs. carbonate petroleum reservoirs: A global perspective on porosity-depth and porosity-permeability relationships. *AAPG Bulletin*, 89, 435–445.

Ehrenberg, S.N., Eberli, G.P., Keramati, M., Moallemi, S.A., 2006. Porosity-permeability relationships in interlayered limestone-dolostone reservoirs. *AAPG Bulletin*, 90, 91–114.

Ehrenberg, S.N., Walderhaug, O., 2015. Preferential calcite cementation of macropores in microporous limestones. *Journal of Sedimentary Research*, 85, 780–793.

Fan, M., Jiang, X.Q., Liu, W.X., Zhang, J.Y., Chen, H.Y., 2007. Dissolution of carbonate rocks in CO_2 solution under the different temperatures. *Acta Sedimentologica Sinica*, 25, 825–830.

Fattore, F., Bertolini, T., Materia, S., Gualdi, S., M'Bou, A.T., Nicolini, G., Valentini, R., Grandcourt, A.D., Tedesco, D., Castaldi, S., 2014. Seasonal trends of dry and bulk concentration of nitrogen compounds over a rain forest in Ghana. *Biogeosciences*, 11, 3069–3081.

Feng, Z.Z, Zhang, Y.S., Jin, Z.K., 1998. Type, origin, and reservoir characteristics of dolostones of the Ordovician Majiagou Group, Ordos, North China Platform. *Sedimentary Geology*, 118, 127–140.

Florea, L.J., Vacher, H.L., 2007. Eogenetic karst hydrology: insights from the 2004 hurricanes, peninsular Florida. *Groundwater*, 45, 439–446.

Fu, J.H., Wu, X.N., Sun, L.Y., Yu,Z., Huang, Z.L., Ding, Z.C., 2017. New understandings of the lithofacies paleogeography of the middle assemblage of Majiagou Fm in the Ordos Basin and its exploration significance. *Natural Gas Industry B*, 37, 9–16.

Fu, S.Y., Zhang, C.G., Chen, H.D., Chen, A.Q., Zhao, J.X., Su, Z.T., Yang, S., Wang, G., Mi, W.T., 2019. Characteristics, formation and evolution of pre-salt dolomite reservoirs in the fifth member of the Ordovician Majiagou Formation, mid-east Ordos Basin, NW China. *Petroleum Exploration and Development*, 46(6), 1153–1164.

Gabellone, T., Whitaker, F., 2016. Secular variations in seawater chemistry controlling dolomitization in shallow reflux systems: insights from reactive transport modelling. *Sedimentology*, 63, 1233–1259.

Gabellone, T., Whitaker, F., Katz, D., Griffiths, G., Sonnenfeld, M., 2016. Controls on reflux dolomitisation of epeiric-scale ramps: Insights from reactive transport simulations of the Mississippian Madison Formation (Montana and Wyoming). *Sedimentary Geology*, 345, 85–102.

Galamay, A.R., Meng, F., Bukowski, K., Lyubchak, A., Zhang, Y., Ni, P., 2019. Calculation of salt basin depth using fluid inclusions in halite from the Ordovician Ordos Basin in China. *Geological Quarterly*, 63, 619–628.

Cantrel, D.L., Swart, P., Hagerty, R.M., 2004. Genesis and characterization of dolomite, Arab-

D reservoir, Ghawarfield, SaudiArabia. *GeoArabia*, 9, 11–36.

Gradstein, F.M., Ogg, J.G., Schmitz, M.D., Ogg, G.M., 2012. The geologic time scale 2012. Elsevier.

Garcia-Fresca, B., Gabellone, T., Whitake, F.F., 2019. Reactive Transport Modeling Approach to Studying Silicification of Carbonates. In Proceedings of the AAPG Annual Convention and Exhibition, San Antonio, TX, USA (pp. 19-22).

Garcia-Fresca, B., Lucia, F.J., Sharp, J.M., Kerans, C., 2012. Outcrop-constrained hydrogeological simulations of brine reflux and early dolomitization of the Permian San Andres FormationHydrogeologic Model of Reflux Dolomitization of the San Andres Formation. *AAPG Bulletin*, 96, 1757–1781.

Genty, T., Bussière, B., Potvin, R., Benzaazoua, M., Zagury, G.J., 2012. Dissolution of calcitic marble and dolomitic rock in high iron concentrated acid mine drainage: application to anoxic limestone drains. *Environmental Earth Sciences*, 66, 2387–2401.

German, R. M., Park, S.J., 2009. Handbook of mathematical relations in particulate materials processing: ceramics, powder metals, cermets, carbides, hard materials, and minerals (Vol. 3). *John Wiley & Sons*.

Ghosh, P., Eiler, J., Campana, S.E., Feeney, R.F., 2007. Calibration of the carbonate 'clumped isotope' paleothermometer for otoliths. *Geochimica et Cosmochimica Acta*, 71, 2736–2744.

Given, R.K., Wilkinson, B.H., 1987. Dolomite abundance and stratigraphic age; constraints on rates and mechanisms of Phanerozoic dolostone formation. *Journal of Sedimentary Research*, 57, 1068–1078.

Gomez-Rivas, E., Corbella, M., Martín-Martín, J.D., Stafford, S.L., Teixell, A., Bons, P.D., Griera, A., Cardellach, E., 2014. Reactivity of dolomitizing fluids and Mg source evaluation of fault-controlled dolomitization at the Benicàssim outcrop analogue (Maestrat Basin, E Spain). *Marine and Petroleum Geology*, 55, 26–42.

Gong, Q.L., Li, F., Lu, C.J., Wang, H.Z., Tang, H., 2021. Tracing seawater-and terrestrial-sourced REE signatures in detritally contaminated, diagenetically altered carbonate rocks. *Chemical Geology*, 570, 120169.

Gong, X., Hou, W.J., Feng, D.L., Luo, Q.Z., Yang, X.Q., 2019. Modelling early karstification in future limestone geothermal reservoirs by mixing of meteoric water with cross-formational warm water. *Geothermics*, 77, 313–326.

Gregg, J.M., Bish, D.L., Kaczmarek, S.E., Machel, H.G., 2015. Mineralogy, nucleation and growth of dolomite in the laboratory and sedimentary environment: A review. *Sedimentology*, 62, 1749–1769.

Grimes, K.G., 2006. Syngenetic karst in Australia: a review. *Helictite*, 39, 27–38.

Hagemann, B., 2018. Numerical and analytical modeling of gas mixing and bio-reactive transport during underground hydrogen storage (Vol. 50). Cuvillier Verlag.

Hamon, Y., Bachaud, P., Granjeon, D., Bemer, E., Carvalho, A.M.A., 2021. Integration of diagenesis in basin-scale, stratigraphic forward models using reactive transport modeling: Input and scaling issues. *Marine and Petroleum Geology*, 124, 104832.

Hao, Y., Smith, M., Sholokhova, Y., Carroll, S., 2013. CO_2-induced dissolution of low permeability carbonates. Part II: Numerical modeling of experiments. A*dvances in Water Resources*, 62, 388–408.

Haq, B.U., Schutter, S.R., 2008. A chronology of Paleozoic sea-level changes. *Science,* 322, 64–68.

Hardie, L.A., 1987. Dolomitization; a critical view of some current views. *Journal of Sedimentary Research*, 57, 166–183.

Hardie, L.A., 1996. Secular variation in seawater chemistry: An explanation for the coupled secular variation in the mineralogies of marine limestones and potash evaporites over the past 600 my. *Geology*, 24, 279–283.

He, J., Fang, S.X., Hou, F.H., Yan, R.H., Zhao, Z.J., Yao, J., Tang, X.J., Wu, G.R., 2013. Vertical zonation of weathered crust ancient karst and the reservoir evaluation and prediction—A case study of $M5_5$-$M5_1$ sub-members of Majiagou Formation in gas fields, central Ordos Basin, NW China. *Petroleum Exploration and Development*, 40, 534–542.

He, X.Y., Shou, J.F., Shen, A.J., Wu, X.N., Wang, Y.S., Hu, Y.Y., Zhu, Y., Wei, D.X., 2014. Geochemical characteristics and origin of dolomite: a case study from the middle assemblage of Ordovician Majiagou formation member 5 of the west of Jingbian gas field, Ordos basin, north China. *Petroleum Exploration and Development*, 41, 417–427.

Hood, A.V.S, Planavsky, N.J., Wallace, M.W., Wang, X., 2018. The effects of diagenesis on geochemical paleoredox proxies in sedimentary carbonates. *Geochimica et Cosmochimica Acta*, 232, 265–287.

Huang, C.G., Guan, X., Ni, X.L., Chang, H.Y., Zhang, S.M., Yang, S., 2017. The characteristics

and major factors controlling on the E_3^2 dolomite reservoirs in saline lacustrine basin in the Yingxi area of Qaidam Basin. *Natural Gas Geoscience*, 28, 219–231.

Huang, D.J., Zhong, S.K., Zhang, D.F., Wang, B.B., Liao, J.C., Xie, K., Lu, Z.X., Tan, X.C., 2021. Datailed characterization and interpretation of sedimentary sequences under evaporitic environments: a case from the $Ma5_6$ submember of Middle Ordovician in central Ordos Basin. *Journal of Palaeogeography (Chinese Edition)*, 23, 735–755.

Huang, S.J., 2010. Carbonate diagenesis. Geological Publishing House, Beijing. pp. 1–288.

Hsu, K.J., 1967. Chemistry of dolomite formation. *In Developments in Sedimentology*, 9, 169–191.

Islam, A., Sun, A.Y., Yang, C., 2016. Reactive transport modeling of the enhancement of density-driven CO_2 convective mixing in carbonate aquifers and its potential implication on geological carbon sequestration. *Scientific Reports*, 6, 24768.

James, N.P., Choquette, P.W., (Eds.). 1987. Paleokarst. Springer Science & Business Media. pp. 1–416.

Jiang, L., Cai, C., Worden, R.H., Crowley, S.F., Jia, L.Q., Zhang, K., Duncan, I.J., 2016. Multiphase dolomitization of deeply buried Cambrian petroleum reservoirs, Tarim Basin, north-west China. *Sedimentology*, 63, 2130–2157.

Jones, G.D., 2000. Numerical modelling of saline groundwater circulation in carbonate platforms. Unpublished Ph. D., University of Bristol, England.

Jones, G.D., Whitaker, F.F., Smart, P.L., Sanford, W.E., 2004. Numerical analysis of seawater circulation in carbonate platforms: II. The dynamic interaction between geothermal and brine reflux circulation. *American Journal of Science*, 304, 250–284.

Jones, G.D., Xiao, Y.T., 2005. Dolomitization, anhydrite cementation, and porosity evolution in a reflux system: Insights from reactive transport models. *AAPG Bulletin*, 89, 577–601.

Kaczmarek, S.E., Gregg, J.M., Bish, D.L., Machel, H.S., Fouke, B.W., 2017. Dolomite, very-high magnesium calcite, and microbes: implications for the microbial model of dolomitization. *SEPM Special Publication*, 109, 1–14.

Kaczmarek, S.E., Sibley, D.F., 2007. A comparison of nanometer-scale growth and dissolution features on natural and synthetic dolomite crystals: implications for the origin of dolomite. *Journal of Sedimentary Research*, 77, 424–432.

Kaufmann, G., 2016. Modelling karst aquifer evolution in fractured, porous rocks. *Journal of*

Hydrology, 543, 796–807.

Kaufmann, G., Dreybrodt, W., 2007. Calcite dissolution kinetics in the system $CaCO_3$-H_2O-CO_2 at high undersaturation. *Geochimica et Cosmochimica Acta*, 71, 1398–1410.

Kaufmann, G., Romanov, D., Hiller, T., 2010. Modeling three-dimensional karst aquifer evolution using different matrix-flow contributions. *Journal of hydrology*, 388, 241–250.

Keshavarz, V., Taheri-Shakib, J., Khosravanian, R., Hosseini, S.A., Salimidelshad, Y., Saadati, P., 2019. Experimental investigation of rock-solvent interaction on the properties of carbonate reservoir rock. *Journal of Petroleum Science and Engineering*, 181, 106246.

Kong, H.M., Long, H.Y., 2014. The influence of elevated CO_2 on rain water PH value. *Science and Technology of West China*, 13, 57–58 (in Chinese with English abstract).

Kovalevych, V. M., Peryt, T. M., Zang, W., & Vovnyuk, S. V. (2006). Composition of brines in halite - hosted fluid inclusions in the Upper Ordovician, Canning Basin, Western Australia: new data on seawater chemistry. *Terra Nova*, 18, 95–103.

Lasaga, A.C., 1984. Chemical kinetics of water-rock interactions. *Journal of geophysical research: solid earth*, 89, 4009–4025.

Lasaga, A.C., Soler, J.M., Ganor, J., Burch, T.E., Nagy, K.L., 1994. Chemical weathering rate laws and global geochemical cycles. *Geochimica et Cosmochimica Acta*, 58, 2361–2386.

Lasaga, A.C., 1998. Kinetic theory in the earth sciences. Princeton, New Jersey: Princeton university press.

Land, L.S., 1998. Failure to precipitate dolomite at 25°C from dilute solution despite 1000-fold oversaturation after 32 years. *Aquatic Geochemistry*, 43, 361–368.

Li, F., Webb, G.E., Algeo, T.J., Kershaw, S., Lu, C., Oehlert, A.M., Gong, Q.L., Pourmand, A., Tan, X., 2019. Modern carbonate ooids preserve ambient aqueous REE signatures. *Chemical Geology*, 509, 163–177.

Li, M.L., Tan, X.C., Li, Y.J, Liu, Y.L., Jiang, L., Xia, J.W., 2020. Characteristics and main controlling factors of limestone reef-shoal reservoir: a case study of Upper Permian Changxing Formation, southern Sichuan Basin. *Fault-Block Oil and Gas Field*, 27, 585–590 (in Chinese with English abstract).

Li, P., Zou, H., Hao, F., Yu, X., Wang, G., Eiler, J.M., 2020. Using clumped isotopes to determine the origin of the Middle Permian Qixia Formation dolostone, NW Sichuan Basin, China. *Marine and Petroleum Geology*, 122, 104660.

Lippmann, F., 1982. Stable and metastable solubility diagrams for the system $CaCO_3$-$MgCO_3$-H_2O at ordinary temperature. *Bulletin de Mineralogie*, 105, 273–279.

Liu, H., Tan, X.C., Li, L., Ding, X., Cao, J., Yang, G., Ma, T., 2019. Eogenetic Karst in Interbedded Carbonates and Evaporites and Its Impact on Hydrocarbon Reservoir: A New Case from Middle Triassic Leikoupo Formation in Sichuan Basin, Southwest China. *Journal of Earth Science*, 30, 908–923.

Liu, H.J., Hou, Z.M., Were, P., Gou, Y., Xiong, L., Sun, X.L., 2015. Modelling CO_2-brine-rock interactions in the Upper Paleozoic formations of Ordos Basin used for CO_2 sequestration. *Environmental Earth Sciences*, 73, 2205–2222.

Liu, J., Yang, M., Wang, D., Zhang, J., 2018. Different bedding loaded coal mechanics properties and acoustic emission. *Environmental Earth Sciences*, 77, 1–11.

Liu, M.J., Xiong, Y., Xiong, C., Liu, Y., Liu, L., Xiao, D., Tan, X.C., 2020. Evolution of diagenetic system and its controls on the reservoir quality of pre-salt dolostone: The case of the Lower Ordovician Majiagou Formation in the central Ordos Basin, China. *Marine and Petroleum Geology*, 122, 104674.

Liu, X.S., Zhang, D.F., Dong, G.D., Wang, B.B., Xiao, D., 2019. Petrography and facies distribution of Middle Ordovician Ma 5_{1+2} tight dolomite reservoirs in the Ordos Basin, Central China. *Energy Exploration and Exploitation*, 37, 473–492.

Liu, Y., Tan, X.C., Liu, X.Y., He, W., Xiong, Y., Liu, L., Liu, M.J., Yang, Q.Y., 2018. Sedimentary characteristics and distribution of grain shoals of Ma57 submember in the Central Ordos Basin. *Acta Sedimentologica Sinica*, 36, 796–806 (in Chinese with English abstract).

Liu, Z., Yuan, D., Dreybrodt, W., 2005. Comparative study of dissolution rate-determining mechanisms of limestone and dolomite. *Environmental Geology*, 49, 274–279.

Liu, Z.G., Zhu, C., Li, S.M., Xue, J.Q., Gong, Q.S., Wang, Y.Q., Wang, P., Xia, Z.Y., Song, G.Y., 2017. Geological features and exploration fields of tight oil in the Cenozoic of western Qaidam Basin, NW China. *Petroleum Exploration and Development*, 44, 196–204.

Logan, B.W., 1987. The MacLeod evaporite basin, Western Australia: *AAPG Memoir*, 44, 140 p.

Lu, C.J., Liu, Z., Jia, H.B., Tian, H.Q., Zou, H.Y., Dai, Q.Q., Han, B., 2019. The eogenetic karst of the Cambrian Longwangmiao Formation in the Yangtze Platform: Implications

for the eustatic and stratigraphic correlations of Toyonian (Cambrian). *Geological Journal*, 54, 3720–3736.

Lu, P., Cantrell, D., 2016. Reactive transport modelling of reflux dolomitization in the Arab-D reservoir, Ghawar field, Saudi Arabia. *Sedimentology*, 63, 865-892.

Lu, P., Luo, P., Zhang, G., Zhang, S., Zhu, C., 2020. A mineral-water-gas interaction model of pCO2 as a function of temperature in sedimentary basins. *Chemical Geology*, 558, 119868.

Lucia, F.J., 1995. Rock-fabric/petrophysical classification of carbonate pore space for reservoir characterization. *AAPG Bulletin*, 79, 1275–1300.

Machel, H.G., 2004. Concepts and models of dolomitization: a critical reappraisal. *Geological Society, London, Special Publications*, 235, 7–63.

MacLean, W.H., Bonavia, F.F., Sanna, G., 1997. Argillite debris converted to bauxite during karst weathering: evidence from immobile element geochemistry at the Olmedo Deposit, Sardinia. Mineralium Deposita, 32, 607–616.

Maddah, S.M.M., Moghaddas, N.H., Ghafoori, M., 2020. Solubility variations of Tirgan limestone in Northeast of Iran with change of PH and temperature. *Carbonates and Evaporites*, 35, 1–10.

Maggi, F., Gu, C., Riley, W.J., Hornberger, G.M., Venterea, R.T., Xu, T.F, Spycher, N., Steefel, C., Miller, N.L., Oldenburg, C. M., 2008. A mechanistic treatment of the dominant soil nitrogen cycling processes: Model development, testing, and application. *Journal of Geophysical Research: Biogeosciences*, 113, G02016.

Markello, J.R., Koepnick, R.B., Waite, L.E., Collins, J.F., Lukasik, J., Simo, J.A., 2008. The carbonate analogs through time (CATT) hypothesis and the global atlas of carbonate fields—A systematic and predictive look at Phanerozoic carbonate systems. Controls on carbonate platform and reef development: *SEPM Special Publication*, 89, 15–45.

Mehrabi, H., Rahimpour-Bonab, H., Enayati-Bidgoli, A.H., Esrafili-Dizaji, B., 2015. Impact of contrasting paleoclimate on carbonate reservoir architecture: Cases from arid Permo-Triassic and humid Cretaceous platforms in the south and southwestern Iran. *Journal of Petroleum Science and Engineering*, 126, 262–283.

Mehrabi, H., Rahimpour-Bonab, H., Al-Aasm, I., Hajikazemi, E., Esrafili-Dizaji, B., Dalvand, M., Omidvar, M., 2018. Palaeo-exposure surfaces in the Aptian Dariyan Formation, offshore SW Iran: geochemistry and reservoir implications. *Journal of Petroleum Geology*, 41, 467–494.

Meng, F., Zhang, Y., Galamay, A.R., Bukowski, K., Ni, P., Xing, E., Ji, L., 2018. Ordovician seawater composition: evidence from fluid inclusions in halite. *Geological Quarterly*, 62, 344–352.

Meng, F.W., Zhang, Z.L., Yan, X.Q., Ni, P., Liu, W.H., Fan, F., Xie, G.W., 2019. Stromatolites in Middle Ordovician carbonate-evaporite sequences and their carbon and sulfur isotopes stratigraphy, Ordos Basin, northwestern China. *Carbonates and Evaporites*, 34, 11–20.

Menke, H.P., Maes, J., Geiger, S., 2021. Upscaling the porosity-permeability relationship of a microporous carbonate for Darcy-scale flow with machine learning. *Scientific Reports*, 11, 1–10.

Mitchum, R.M, Wagoner, J.C.V., 1991. High-frequency sequences and their stacking patterns: sequence-stratigraphic evidence of high-frequency eustatic cycles. *Sedimentary Geology*, 70, 131–160.

Morrow, D.W., 1982. Diagenesis 1. dolomite - part 1: the chemistry of dolomitization and dolomite precipitation. *Geoscience Canada*, 9, 5–13.

Morse, J.W., Arvidson, R.S., 2002. The dissolution kinetics of major sedimentary carbonate minerals. *Earth-Science Reviews*, 58, 51–84.

Moore, C.H., 2001. Carbonate reservoirs: porosity evolution and diagenesis in a sequence stratigraphic framework. developments in sedimentology. Elsevier Science B.V., Amsterdam, 55, 444p.

Murray, S.T., Swart, P.K., 2017. Evaluating formation fluid models and calibrations using clumped isotope paleothermometry on Bahamian dolomites. *Geochimica et Cosmochimica Acta*, 206, 73–93.

Nader, F.H., 2017. Multi-scale quantitative diagenesis and impacts on heterogeneity of carbonate reservoir rocks. Springer International Publishing. pp. 1–132.

Ning, M., Lang, X.G., Huang, K.J., Li, C., Huang, T., Yuan, H.Z., Yuan, H.L., Xing, C.C., Yang, R.Y., Shen, B., 2020. Towards understanding the origin of massive dolostones. *Earth and Planetary Science Letters*, 545, 116403.

Nordstrom, D.K., Plummer, L.N., Wigley, T.M.L., Wolery, T.J., Ball, J.W., Jenne, E.A., Bassett, R.L., Crerar, D.A., Florence, T.M., Fritz, B., Hoffman, M., Holdren, G.R., Lafon, G.M., Mattigod, S.V., McDuff, R.E., Morel, F., Reddy, M.M., Sposito, G., Thrailkill, J., 1979. A comparison of computerized chemical models for equilibrium calculations in aqueous systems. In: Chemical Modeling in Aqueous Systems - Speciation, Sorption, Solubility,

and Kinetics: Series 93 (Ed. E.A. Jenne), pp. 857–892. American Chemical Society, Washington.

Palandri, J.L., Kharaka, Y.K., 2004. A compilation of rate parameters of water-mineral interaction kinetics for application to geochemical modeling. Geological Survey Menlo Park CA.

Panday, S., Huyakorn, P.S., Therrien, R., Nichols, R.L., 1993. Improved three-dimensional finite-element techniques for field simulation of variably saturated flow and transport. *Journal of contaminant hydrology*, 12, 3–33.

Paterson, R.J., Whitaker, F.F., Smart, P.L., Jones, G.D., Oldham, D., 2008. Controls on early diagenetic overprinting in icehouse carbonates: Insights from modeling hydrological zone residence times using CARB3D$^+$. *Journal of Sedimentary Research*, 78, 258–281.

Perez-Fernandez, A., Berninger, U.N., Mavromatis, V., Von Strandmann, P.P., Oelkers, E.H., 2017. Ca and Mg isotope fractionation during the stoichiometric dissolution of dolomite at temperatures from 51 to 126°C and 5 bars CO_2 pressure. *Chemical Geology*, 467, 76–88.

Perrin, C., Marquez, X., Flores, J., Berthereau, G., 2020. Porosity Depth Saturation (PDS) model: Quantification of porosity preservation with burial in carbonate oil reservoirs, and application to infer oil charging time. *Marine and Petroleum Geology*, 120, 104515.

Pokrovsky, O.S., Golubev, S.V., Schott, J., 2005. Dissolution kinetics of calcite, dolomite and magnesite at 25°C and 0 to 50 atm pCO_2. *Chemical Geology*, 217, 239–255.

Pokrovsky, O.S., Golubev, S.V., Schott, J., Castillo, A., 2009. Calcite, dolomite and magnesite dissolution kinetics in aqueous solutions at acid to circumneutral pH, 25 to 150°C and 1 to 55 atm pCO_2: New constraints on CO_2 sequestration in sedimentary basins. *Chemical Geology*, 265, 20–32.

Poonoosamy, J., Klinkenberg, M., Deissmann, G., Brandt, F., Bosbach, D., Mäder, U., Kosakowski, G., 2020. Effects of solution supersaturation on barite precipitation in porous media and consequences on permeability: Experiments and modelling. *Geochimica et Cosmochimica Acta*, 270, 43–60.

Pruess, K., Oldenburg, C.M., Moridis, G.J., 1999. TOUGH2 user's guide version 2 (No. LBNL-43134). Lawrence Berkeley National Lab.(LBNL), Berkeley, CA (United States).

Rahimpour-Bonab, H., Mehrabi, H., Navidtalab, A., Izadi-Mazidi, E., 2012. Flow unit distribution and reservoir modelling in cretaceous carbonates of the Sarvak Formation,

Abteymour Oilfield, Dezful Embayment, SW Iran. *Journal of Petroleum Geology*, 35, 213–236.

Rameil, N., Immenhauser, A., Csoma, A.E., Warrlich, G., 2012. Surfaces with a long history: the Aptian top Shu'aiba Formation unconformity, Sultanate of Oman. *Sedimentology*, 59, 212–248.

Rasolofosaon, P.N., Zinszner, B.E., 2002. Comparison between permeability anisotropy and elasticity anisotropy of reservoir rocks. *Geophysics*, 67, 230–240.

Sarg, J.F., 1988. Sea-level changes: An integrated approach//in: Carbonate sequence stratigraphy. pp. 155–182.

Saller, A.H., Henderson, N., 1998. Distribution of porosity and permeability in platform dolomites: Insight from the Permian of west Texas. *AAPG Bulletin*, 82, 1528–1550.

Saller, A.H., Dickson, J.A.D., Matsuda, F., 1999. Evolution and distribution of porosity associated with subaerial exposure in upper Paleozoic platform limestones, west Texas. *AAPG Bulletin*, 83, 1835–1854.

Schmoker, J.W., Halley, R.B., 1982. Carbonate porosity versus depth: a predictable relation for south Florida. *AAPG Bulletin*, 66, 2561–2570.

Schwartz, M.O., 2012. Modelling groundwater contamination above a nuclear waste repository at Gorleben, Germany. *Hydrogeology Journal*, 20, 533-546.

Schwartz, M.O., 2015. Modelling the hypothetical methane-leakage in a shale-gas project and the impact on groundwater quality. *Environmental Earth Sciences*, 73, 4619–4632.

Seol, Y., Lee, K.K., 2007. Application of TOUGHREACT to performance evaluations of geothermal heat pump systems. *Geosciences Journal*, 11, 83–91.

She, M., Shou, J.F., Shen, A.J., Pan, L.Y., Hu, A.P., Hu, Y.Y., 2016. Experimental simulation of dissolution law and porosity evolution of carbonate rock. P*etroleum Exploration and Development*, 43 616–625.

Shen, A.J., Zhao, W.Z., Hu, A.P., She, M., Chen, Y.N., Wang, X.F., 2015. Major factors controlling the development of marine carbonate reservoirs. *Petroleum Exploration and Development*, 42, 597–608.

Shen, A.J., Hu, A.P., Cheng, T., Liang, F., Pan, W.Q., Feng, Y.X., Zhao, J.X., 2019. Laser ablation in situ U-Pb dating and its application to diagenesis-porosity evolution of carbonate reservoirs. *Petroleum Exploration and Development*, 46, 1127–1140.

Shen, Z.L., Wang, Y.X., 2002. Review and outlook of water-rock interaction studies. *Earth science-Journal of China university of Geosciences*, 27, 127–132.

Sonnenthal, E., Ito, A., Spycher, N., Yui, M., Apps, J., Sugita, Y., Conrad, M., Kawakami, S., 2005. Approaches to modeling coupled thermal, hydrological, and chemical processes in the Drift Scale Heater Test at Yucca Mountain. *International Journal of Rock Mechanics and Mining Sciences*, 42, 698–719.

Spycher, N.F., Reed, M.H., 1988. Fugacity coefficients of H_2, CO_2, CH_4, H_2O and of H_2O-CO_2-CH_4 mixtures: A virial equation treatment for moderate pressures and temperatures applicable to calculations of hydrothermal boiling. *Geochimica et Cosmochimica Acta*, 52, 739–749.

Stack, AG, Fernandez-Martinez, A., Allard, L.F., Bañuelo, J.L., Rother, G., Anovitz, L.M., Cole, D.R., Waychunas, G.A., 2014. Pore-size-dependent calcium carbonate precipitation controlled by surface chemistry. *Environmental Science and Technology*, 48, 6177–6183.

Stack, A.G., 2015. Precipitation in pores: A geochemical frontier. *Reviews in Mineralogy and Geochemistry*, 80, 165–190.

Steefel, C.I., Lasaga, A.C., 1994. A coupled model for transport of multiple chemical species and kinetic precipitation/dissolution reactions with application to reactive flow in single phase hydrothermal systems. *American Journal of Science*, 294, 529–592.

Steefel, C.I., Appelo, C.A.J., Arora, B., Jacques, D., Kalbacher, T., Kolditz, O., Lagneau, V., Lichtner, P.C., Mayer, K.U., Meeussen, J.C.L., Molins, S., Moulton, D., Shao, H., Simunek, J., Spycher, N., Yabusaki, S.B., Yeh, G.T., 2015. Reactive transport codes for subsurface environmental simulation. *Computational Geosciences*, 19, 445–478.

Steefel, C., 2018. Reactive Transport Modeling: Applications in Subsurface Energy and Environmental Problems. *John Wiley & Sons*.

Stoffers, P., Müller, G., 1979. Carbonate rocks in the Black Sea basin: indicators for shallow water and subaerial exposure during Miocene—Pliocene time. *Sedimentary Geology*, 23, 137–147.

Su, Z.T., Chen, H.D., Zhu, P., Zhao, J.X., Dong, S.F., Hao, Y., 2010. Pore Types and Evolution of Ordovician Majiagou Formation in the Southern Part of Ordos Basin. *Marine Origin Petroleum Geology*, 15, 6–13 (in Chinese with English abstract).

Sun, H., Vega, S., Tao, G., 2017. Analysis of heterogeneity and permeability anisotropy in carbonate rock samples using digital rock physics. *Journal of petroleum science and*

engineering, 156, 419–429.

Swart, P.K., Oehlert, A.M., 2018. Revised interpretations of stable C and O patterns in carbonate rocks resulting from meteoric diagenesis. *Sedimentary Geology*, 364, 14–23.

Tan, F., Zhang, Y.F., Wang, Z.Y., Dong, Z.X., Huang, Z.L., Wang, Q.P., Gao, J.W., 2017. Simulation experiment for the burial dissolution of different petrofabric carbonate rocks of Ordovician in the Ordos Basin. *Acta Sedimentological Sinica*, 35, 413–424 (in Chinese with English abstract).

Tan, X., Li, L., Liu, H., Cao, J., Wu, X., Zhou, S., Shi, X., 2014. Mega-shoaling in carbonate platform of the middle Triassic Leikoupo Formation, Sichuan basin, southwest China. *Science China Earth Sciences*, 57, 465–479.

Tan, X.C., Xiao, D., Chen, J.S., Li, L., Liu, H., 2015. New advance and enlightenment of eogenetic karstification. *Journal of Palaeogeography*, 17, 441–456 (in Chinese with English abstract).

Taron, J., Elsworth, D., Min, K.B., 2009. Numerical simulation of thermal-hydrologic-mechanical-chemical processes in deformable, fractured porous media. *International Journal of Rock Mechanics and Mining Sciences*, 46, 842–854.

Tingay, M.R., Hillis, R.R., Swarbrick, R.E., Morley, C.K., Damit, A.R., 2009. Origin of overpressure and pore-pressure prediction in the Baram province, Brunei. *AAPG Bulletin*, 93, 51–74.

Tostevin, R., Shields, G.A., Tarbuck, G.M., He, T., Clarkson, M.O., Wood, R.A., 2016. Effective use of cerium anomalies as a redox proxy in carbonate-dominated marine settings. *Chemical Geology*, 438 146–162.

Trotter, J.A., Williams, I.S., Barnes, C.R., Lécuyer, C., Nicoll, R.S., 2008. Did cooling oceans trigger Ordovician biodiversification? Evidence from conodont thermometry. *Science*, 321, 550–554.

Usdowski, E., 1994. Synthesis of dolomite and geochemical implications. *In*: Dolomites: A Volume in Honour of Dolomieu (Vol. 21, pp. 345-360). Blackwell Scientific Publications.

Vacher, H.L., Mylroie, J.E., 2002. Eogenetic karst from the perspective of an equivalent porous medium. *Carbonates and Evaporites*, 17, 182–196.

Vasconcelos, C., McKenzie, J.A., Bernasconi, S., Grujic, D., Tiens, A.J., 1995. Microbial mediation as a possible mechanism for natural dolomite formation at low temperatures.

Nature, 377, 220–222.

Varzina, A., Cizer, Ö., Yu, L., Liu, S., Jacques, D., Perko, J., 2020. A new concept for pore-scale precipitation-dissolution modelling in a lattice Boltzmann framework-Application to portlandite carbonation. *Applied Geochemistry*, 123, 104786.

Veizer, J., Ala, D., Azmy, K., Bruckschen, P., Buhl, D., Bruhn, F., Carden, G., Diener, A., Ebneth, S., Godderis, Y., Jasper, T., Korte, C., Pawellek, F., Podlaha, O.G., Strauss, H., 1999. $^{87}Sr/^{86}Sr$, $\delta^{13}C$ and $\delta^{18}O$ evolution of Phanerozoic seawater. *Chemical Geology*, 161, 59–88.

Verma, A., Pruess, K., 1988. Thermohydrological conditions and silica redistribution near high-level nuclear wastes emplaced in saturated geological formations. *Journal of Geophysical Research: Solid Earth*, 93, 1159–1173.

Wang, B.Q., Al-Aasm, I.S., 2002. Karst-Controlled Diagenesis and Reservoir Development: Example from the Ordovician Main-Reservoir Carbonate Rocks on the Eastern Margin of the Ordos Basin, China. *AAPG Bulletin*, 86, 1639–1658.

Wang, L.C., Hu, W.X., Wang, X.L., Cao, J., Chen, Q., 2014. Seawater normalized REE patterns of dolomites in Geshan and Panlongdong sections, China: Implications for tracing dolomitization and diagenetic fluids. *Marine and Petroleum Geology*, 56, 63–73.

Wang, Y., Liu, S.N., Zhang, L.W., Gan, M.G., Miao, X.X., Wei, N., Cheng, X.W., Liu, H.J., Li, X.C., Li, J., 2021. Evidence of self-sealing in wellbore cement under geologic CO_2 storage conditions by micro-computed tomography (CT), scanning electron microscopy (SEM) and Raman observations. *Applied Geochemistry*, 128, 104937.

Warren, J., 2000. Dolomite: occurrence, evolution and economically important associations. *Earth-Science Reviews*, 52, 1–81.

Warren, J.K., 2010. Evaporites through time: Tectonic, climatic and eustatic controls in marine and nonmarine deposits. *Earth-Science Reviews*, 98, 217–268.

Wei, W., Chen, D., Qing, H., Qian, Y., 2017. Hydrothermal Dissolution of Deeply Buried Cambrian Dolomite Rocks and Porosity Generation: Integrated with Geological Studies and Reactive Transport Modeling in the Tarim Basin, China. *Geofluids*, 2017, 9562507.

Weyl, P.K., 1960. Porosity through dolomitization: Conservation-of-mass requirements. *Journal of Sedimentary Research*, 30, 85–90.

Whelan, J.F., Paces, J.B., Peterman, Z.E., 2002. Physical and stable-isotope evidence for

formation of secondary calcite and silica in the unsaturated zone, Yucca Mountain, Nevada. *Applied Geochemistry*, 17, 735–750.

Whitaker, F.F., Smart, P.L., 2007a. Geochemistry of meteoric diagenesis in carbonate islands of the northern Bahamas: 1. Evidence from field studies. *Hydrological Processes: An International Journal*, 21, 949–966.

Whitaker, F.F., Smart, P.L., 2007b. Geochemistry of meteoric diagenesis in carbonate islands of the northern Bahamas: 2. Geochemical modelling and budgeting of diagenesis. *Hydrological Processes: An International Journal*, 21, 967–982.

Whitaker, F.F., Xiao, Y., 2010. Reactive transport modeling of early burial dolomitization of carbonate platforms by geothermal convection. *AAPG Bulletin*, 94, 889–917.

Whitaker, F.F., Al-Helal, A., Gabellone, T., Griffiths, G., 2012. Integrated reactive transport modelling: challenges and opportunities for improved prediction of diagenetic impact on reservoir quality. Lawrence Berkeley National Laboratory, Berkeley, California, September, pp. 17–19.

White, W.B., 1988. Geomorphology and Hydrology of Karst Terrains. Oxford University Press: New York.

Wilson, A.M., Sanford, W., Whitaker, F., Smart, P., 2001. Spatial patterns of diagenesis during geothermal circulation in carbonate platforms. *American Journal of Science*, 301, 727–752.

Witt, K.J., Brauns, J., 1983. Permeability-anisotropy due to particle shape. *Journal of geotechnical engineering*, 109, 1181–1187.

Wolery, T.J., 1992. EQ3/6, a software package for geochemical modeling of aqueous systems: package overview and installation guide (version 7.0) (No. UCRL-MA--110662-PT. 1). Lawrence Livermore National Lab.

Worthington, S.R., Davies, G.J., Alexander Jr, E.C., 2016. Enhancement of bedrock permeability by weathering. *Earth-Science Reviews*, 160, 188–202.

Wu, D.X., Wu, X.N., Cao, R.R., Yu, Z., 2014. Reservoir Characteristics and Evolution of Majiagou Middle Assemblage on East Side of Ordovician Central Paleouplift, Ordos Basin. *Marine Origin Petroleum Geology*, 19, 38–44 (in Chinese with English abstract).

Xiao, D., Tan, X.C., Xi, A.H., Liu, H., Shan, S.J., Xia, J.W., Cheng, Y., Lian, C.B., 2016. An inland facies-controlled eogenetic karst of the carbonate reservoir in the Middle Permian

Maokou Formation, southern Sichuan Basin, SW China. *Marine and Petroleum Geology*, 72, 218–233.

Xiao, D., Tan, X.C., Zhang, D.F., He, W., Li, L., Shi, Y.H., Chen, J.P., Cao, J., 2019. Discovery of syngenetic and eogenetic karsts in the Middle Ordovician gypsum-bearing dolomites of the eastern Ordos Basin (central China) and their heterogeneous impact on reservoir quality. *Marine and Petroleum Geology*, 99, 190–207.

Xiao, Y., Jones, G.D., 2006. Reactive transport modeling of carbonate and siliciclastic diagenesis and reservoir quality prediction. In Abu Dhabi International Petroleum Exhibition and Conference. OnePetro.

Xiao, Y.T., Whitaker, F., Xu, T.F., Steefel, C., 2018. Reactive transport modeling. John Wiley & Sons, Incorporated.

Xie, K., Tan, X.C., Feng, M., Wang, B.B., Zhong, S.K., Yang, M.Y., Nie, W.C., Qiao, Z.F., Zeng, W., 2020. Eogenetic karst and its control on reservoirs in the Ordovician Majiagou Formation, eastern Sulige gas field, Ordos Basin, NW China. *Petroleum Exploration and Development*, 47, 1246–1261.

Xiong, Y., Tan, X.C., Zuo, Z.F., Zou, G.L., Liu, M.J., Liu, Y., Liu, L., Xiao, D., Zhang, J., 2019. Middle Ordovician multi-stage penecontemporaneous karstification in North China: Implications for reservoir genesis and sea level fluctuations. *Journal of Asian Earth Sciences*, 183, 103969.

Xiong, Y., Tan, X.C., Dong, G.D., Wang, L.C., Ji, H.K., Liu, Y., Wen, C.X., 2020a. Diagenetic differentiation in the Ordovician Majiagou Formation, Ordos Basin, China: Facies, geochemical and reservoir heterogeneity constraints. *Journal of Petroleum Science and Engineering*, 191, 107179.

Xiong, Y., Tan, X.C., Wu, K.Y., Wang, X.F., 2020b. Research advances, geological implication and application in Ordos Basin of the “pore-size controlled precipitation” in diagenesis of carbonate rock reservoir. *Journal of Palaeogeography* 22(4): 744–760. (in Chinese with English abstract).

Xiong, Y., Hou, Z.M., Tan, X.C., Luo, J.S., Yue, Y., Wu, K.Y., 2021a. Constraining fluid-rock interactions during eogenetic karst and their impacts on carbonate reservoirs: insights from reactive transport modeling. *Applied Geochemistry*, 131, 105050.

Xiong, Y., Tan, X.C., Wu, K.Y., Xu, Q., Liu, Y., Qiao, Y.P., 2021b. Petrogenesis of the Eocene lacustrine evaporites in the western Qaidam Basin: Implications for regional tectonic and

climate changes. *Sedimentary Geology* 416, 105867.

Xiong, Y., Wang, L.C., Tan, X.C., Liu, Y., Liu, M.J., Qiao, Z.F., 2021c. Dolomitization of the Ordovician subsalt Majiagou Formation in the central Ordos Basin, China: fluid origins and dolomites evolution. *Petroleum Science* 18(2): 362–379.

Xiong, Y., Tan, X.C., Zhong, S.K., Xiao, D., Wang, B.B., Yang, M.Y., Nie, W.C., Cao, J. 2022. Dynamic paleokarst geochemistry within 130 Myr in the Middle Ordovician Shanganning carbonate platform, North China. *Palaeogeography, Palaeoclimatology, Palaeoecology*, 110879.

Xu, T.F., Pruess, K., 1998. Coupled modeling of non-isothermal multiphase flow, solute transport and reactive chemistry in porous and fractured media: 1. Model Development and Validation. Lawrence Berkeley National Laboratory Report (No. LBNL-42050), Berkeley, California.

Xu, T.F, Sonnenthal, E., Bodvarsson, G., 2003. A reaction-transport model for calcite precipitation and evaluation of infiltration fluxes in unsaturated fractured rock. *Journal of contaminant hydrology*, 64, 113–127.

Xu, T.F., Sonnenthal, E., Spycher, N., Pruess, K., 2004. TOUGHREACT user's guide: A simulation program for non-isothermal multiphase reactive geochemical transport in variable saturated geologic media (No. LBNL-55460). Lawrence Berkeley National Lab.(LBNL), Berkeley, CA (United States).

Xu, T.F., Sonnenthal, E., Spycher, N., Pruess, K., 2006. TOUGHREACT—a simulation program for non-isothermal multiphase reactive geochemical transport in variably saturated geologic media: applications to geothermal injectivity and CO_2 geological sequestration. *Computers & Geosciences*, 32, 145–165.

Xu, T.F., Apps, J.A., Pruess, K., Yamamoto, H., 2007. Numerical modeling of injection and mineral trapping of CO_2 with H_2S and SO_2 in a sandstone formation. *Chemical Geology*, 242, 319–346.

Yang, J.J., Huang, S.J., Zhang, W.Z., Huang, Y.M., Liu, G.X., Xiao, L.P., 1995. Experimental simulation of dissolution for carbonate with different composition under the conditions from epigenesist to burial diagenesis environment. *Acta Sedimentological Sinica*, 13, 49–54 (in Chinese with English abstract).

Yang, L.L., Xu, T.F., Wei, M.C., Feng, G.H., Wang, F.G., Wang, K.R., 2015. Dissolution of arkose in dilute acetic acid solution under conditions relevant to burial diagenesis. *Applied*

Geochemistry, 54, 65–73.

Yang, L.L., Xu, T.F., Liu, K.Y., Peng, B., Yu, Z.C., Xu, X.M., 2017. Fluid-rock interactions during continuous diagenesis of sandstone reservoirs and their effects on reservoir porosity. *Sedimentology*, 64, 1303–1321.

Yang, L.L., Chen, D.H., Yu, L.J., Liu, J.L., 2020a. Effect of atmospheric freshwater leaching on carbonate reservoirs during the early diagenetic stage: A case study of carbonates in the Shunnan area, Tarim Basin. *Bulletin of Mineralogy, Petrology and Geochemistry*, 39, 843–852 (in Chinese with English abstract).

Yang, L.L., Yu, L.J., Chen, D.H., Liu, K.Y., Yang, P., Li, X.W., 2020b. Effects of dolomitization on porosity during various sedimentation-diagenesis processes in carbonate reservoirs. *Minerals*, 10, 574.

Yang, W., 2001. Estimation of duration of subaerial exposure in shallow-marine limestones: an isotopic approach. *Journal of Sedimentary Research*, 71, 778–789.

Yang, X.Y, Mei, Q.Y, Wang, X.Z, Dong, Z.X, Li, Y., Huo, F., 2018. Indication of rare earth element characteristics to dolomite petrogenesis--A case study of the fifth member of Ordovician Majiagou Formation in the Ordos Basin, central China. *Marine and Petroleum Geology*, 92, 1028–1040.

Yin, J., Yan, D.H., Yang, Z.Y., Yuan, Z., Yuan, Y., Wang, H., Shi, X.L., 2016. Research on historical and future spatial-temporal variability of precipitation in China. *Advances in Meteorology*, 9137201.

Yu, Z., Ding Z.C., Wang, L.H., Zhang, D.F., Luo, C., Wei, Y., Guo, W., Wei, L.B., 2018. Main factors controlling formation of dolomite reservoir underlying gypsum-salt layer in the 5th member of Ordovician Majiagou Formation, Ordos Basin. *Oil & Gas Geology*, 39, 1214–1218 (in Chinese with English abstract).

Zeng, L., Lyu, W., Li, J., Zhu, L., Weng, J., Yue, F., Zu, K., 2016. Natural fractures and their influence on shale gas enrichment in Sichuan Basin, China. *Journal of Natural Gas Science and Engineering*, 30, 1–9.

Zengler, D.H., Dunham, J.D., Ethington, R.L., 1980. Concepts and models of dolomitization. *SEPM Special Publication*. 28.

Zhang, B.M., Liu, J.J., 2009. Classification and characteristics of karst reservoirs in China and related theories. *Petroleum Exploration and Development*, 36, 12–29.

Zhang, F., Xu, H., Konishi, H., Shelobolina, E.S., Roden, E.E., 2012. Polysaccharide-catalyzed nucleation and growth of disordered dolomite: A potential precursor of sedimentary dolomite. *American Mineralogist*, 97, 556–567.

Zhang, G., Lu, P., Luo, P., Sonnenthal, E., Huang, Y., Zhu, C., 2019. Effects of natural gas acidic components on local porosity generation in a carbonate reservoir: Insights from reactive transport modeling. *AAPG Bulletin*, 103, 2975–3001.

Zhang, Y.D., Zhan, R.B., Zhen, Y.T., Wang, Z.H., Yuan, W.W., Fang, X., Ma, X., Zhang, J.P., 2019. Ordovician integrative stratigraphy and timescale of China. *Science China Earth Sciences*, 62, 61–88.

Zhao, W.Z., Shen A J, Zheng, J.F., Qiao, Z.F., Wang, X.F., Lu, J.M., 2014. The porosity origin of dolostone reservoirs in the Tarim, Sichuan and Ordos basins and its implication to reservoir prediction. *Science China Earth Sciences*, 44, 1925–1939.

Zhang, X.F., Liu, B., Cai, Z.X., Hu, W.X., 2010. Dolomitization and carbonate reservoir formation. *Geological Science and Technology Information*, 29, 79–85.

Zhang, X.F, Shi, K.B., Liu, B., Yang, Y.K., Wang, J.Q., 2014. Retention processes and porosity preservation in deep carbonate reservoirs. *Geological Science and Technology Information*, 33, 80–85.

Zhong, Y., Tan, X.C., Zhao, L.M., Guo, R., Li, F., Jin, Z.M., Chen, Y.T., Xiao, D., 2019. Identification of facies-controlled eogenetic karstification in the Upper Cretaceous of the Halfaya oilfield and its impact on reservoir capacity. *Geological Journal*, 54, 450–465.